A HEMISPHERICAL ACOUSTIC RESONATOR FOR THE MEASUREMENT OF THE SPEED OF SOUND IN GASES

A thesis submitted to the

University of London

for the Degree of Doctor of Philosophy

by

Jeanette Louise Angerstein

Department of Chemistry

Christopher Ingold Laboratories

20 Gordon Street

University College London

London WC1H 0AJ

December 1999

Abstract

A hemispherical acoustic resonator is described which was designed and constructed for the measurement of the speed of sound in gases, at pressures up to 40 MPa and at temperatures in the range from 300 K to 400 K. The hemispherical geometry retains many of the advantages characteristic of the spherical geometry but affords a major advantage at high pressures because one of the transducers may be placed at a position of maximum acoustic density for the radial modes and so loss of signal strength is minimised. A detailed description is given of the resonator and pressure vessel, the thermostat and the various measurement techniques employed.

Characterisation of the resonator was achieved using a prototype equatorial plate for which the sound source could be moved over the radius of the cavity. Using the prototype plate, measurements performed in air at room temperature and pressure allowed the transducer configuration to be optimised. Calibration of the resonator was possible by comparison of the values of $u/a(p,T)$ obtained isothermally in nitrogen with data obtained previously using a spherical resonator. These measurements allowed the resonator's geometry to be characterised and the dependence of the radius on temperature and pressure to be modelled.

The semi-empirical model developed using the results of the calibration was tested using measurements obtained in argon; results were obtained simultaneously from the hemispherical resonator and a well-characterised spherical resonator.

Measurements on propene together with the results from nitrogen allowed the halfwidths to be modelled and enabled useful information about the loss mechanisms occurring to be extracted from the measured halfwidths. Tetrafluoromethane was subsequently studied and the acoustic virial coefficients and vibrational relaxation times were measured and compared with literature values.

Acknowledgements

Firstly, I would like to thank Dr. M. B. Ewing for his supervision and guidance throughout the time I have spent at University College London. I would also like to thank the staff at UCL for providing excellent technical support, with particular thanks to Dave Morfett and his colleagues in the mechanical workshop and to Dick Waymark and his colleagues in the electronics section.

I am indebted to Darryl and all my family and friends for their support, encouragement and patience. I am particularly grateful to my fellow colleagues, Damian Royal and Jesus Sanchez for their help and for providing many useful suggestions and interesting discussions, but most of all for making the time I spent in lab131 enjoyable.

Very special thanks must be given to my mum for her support and encouragement throughout the duration of this work and in particular for caring for Natalie during some of the research.

Finally, I would like to thank EPSRC for financial support.

CONTENTS

3 Acoustic Theory

4 Apparatus

LIST OF TABLES

LIST OF FIGURES

CHAPTER 1 Introduction

(1.1) The Speed of Sound

The Maxwell equation which relates the speed of sound u, in a non-relaxing gas to its thermophysical properties is given by

$$u^2 = \left(\frac{\partial p}{\partial \rho}\right)_S \tag{1.1.1}$$

Where p is the pressure, ρ is the gas density and S denotes entropy. This expression is exact in the limits of low frequency and small amplitude [1]. Combination with the viral equation of state,

$$\frac{pV_m}{RT} = 1 + \frac{B}{V_m} + \frac{C}{V_m} + \ldots, \tag{1.1.2}$$

where B, C, ... are the second, third, ... virial coefficients, leads to the pressure explicit series expansion:

$$u^2 = A_0 + A_1 p + A_2 p^2 + \ldots, \tag{1.1.3}$$

where, γ^{pg} is the ratio of the perfect-gas heat capacities,

$$A_0 = \left(\frac{RT\gamma^{pg}}{M}\right) \tag{1.1.4}$$

and the second and third acoustic virial coefficients are given by

$$\beta_a = \left(\frac{M}{\gamma^{pg}}\right) A_1 \tag{1.1.5}$$

and

$$\gamma_a = \left(\frac{M}{\gamma^{pg}}\right) A_2 \tag{1.1.6}$$

The acoustic virial coefficients are functions of temperature and are related to the virial coefficients (of the equation of state) by second order differential equations. The second acoustic virial coefficient is given by

$$\beta_a = 2B + 2T\left(\gamma^{pg} - 1\right)\left(dB/dT\right) + T^2\left(d^2B/dT^2\right)\left[\left(\gamma^{pg} - 1\right)/\gamma^{pg}\right] \tag{1.1.7}$$

and the third by

$$\gamma_a = \left[\left(\gamma^{pg}-1\right)/\gamma^{pg}\right]\times\left[B+2\left(\gamma^{pg}-1\right)T\left(\mathrm{d}B/\mathrm{d}T\right)+\left(\gamma^{pg}-1\right)T^2\left(\mathrm{d}^2B/\mathrm{d}T^2\right)\right]^2$$
$$+\left(1/\gamma^{pg}\right)\times\left\{\left(1+2\gamma^{pg}\right)C+\left[\left(\gamma^{pg}\right)^2-1\right]T\left(\mathrm{d}C/\mathrm{d}T\right)+\left(\tfrac{1}{2}\right)\left(\gamma^{pg}-1\right)^2T^2\left(\mathrm{d}^2C/\mathrm{d}T^2\right)\right\} \quad (1.1.8)$$

The second virial coefficient B is related to the potential energy function U for a pair of molecules [2]. When U is dependent only on the distance r between the molecules, B is given, according to classical mechanics, by

$$B = 2\pi L\int_0^\infty\left[1-\exp\left(\frac{-U}{kT}\right)\right]r^2\mathrm{d}r \quad (1.1.9)$$

In which L is Avogadro's constant and k is Boltzmann's constant.

At non-zero pressures there are deviations from perfect-gas behaviour as a result of intermolecular forces, but in the limit of zero pressure,

$$u^2 = \left(\frac{RT\gamma^{pg}}{M}\right) \quad (1.1.10)$$

since all gases behave perfectly in the limit where $p \to 0$. Extrapolation to zero pressure of the isothermal sound speeds at a number of pressures may therefore yield valuable information. Application of equation (1.1.10) enables extremely accurate measurements of any of the properties on the right-hand-side of the equation to be determined, provided the others are also known. An accurate re-determination of the gas constant was performed by Moldover *et al.* using a spherical acoustic resonator [3]. The equation has been utilised in the field of primary thermometry [4 - 9] and the molar perfect-gas heat capacities $C_{p,m}^{pg}$ and $C_{v,m}^{pg}$ [10 - 12] and the composition of binary mixtures [13] have also been successfully obtained through the use of equation (1.1.10). Away from the perfect gas limit, the density of real fluids as a function of temperature and pressure may also be provided by acoustic measurements [14].

(1.2) Kinetic Effects

The sound speed is determined by the equilibrium properties when the frequencies are sufficiently low. Sound is absorbed, however, as a result of kinetic effects in the gas as these are non-

equilibrium properties. Transport of heat and momentum and vibrational and rotational relaxation are examples of such kinetic processes. Quantitative information about the timescale of various relaxation processes may be provided under conditions where the sound speed is not determined solely by the equilibrium properties (i.e. at sufficiently high frequencies). The local equilibrium of the fluid is disturbed by sound waves: in the approach to zero frequency the cyclic fluctuations imposed by the sound field occur reversibly and adiabatically. As the frequency is increased some of the sound energy is dissipated and over a wide frequency range the absorption coefficient α rises smoothly. However, when the period of the sound wave becomes comparable with a timescale characterising one of the kinetic mechanisms, more dramatic effects occur and acoustic measurements are very difficult to determine precisely as the quality factors of the resonances become severely reduced.

Classical absorption is always present and its magnitude is controlled by the coefficients of the thermal conductivity κ and the shear viscosity η. Its contribution to the absorption coefficient is given by

$$\alpha_{cl} = \left(\frac{\omega}{2u^3}\right)\left[\left(\frac{4D_s}{3}\right) + (\gamma - 1)D_h\right] \qquad (1.2.1)$$

where ω is the angular frequency, γ is the ratio of the perfect-gas heat capacities and D_s and D_h are the viscous and thermal diffusivities.

In practice, at sufficiently low frequencies all the other absorption mechanisms can be accounted for through the frequency-independent bulk viscosity η_b, whose contribution to the absorption coefficient is given by

$$\alpha_b = \left(\frac{\omega}{2u^3}\right)\left(\frac{\eta_b}{\rho}\right) \qquad (1.2.2)$$

The absorption coefficient α is the sum of equations (1.2.1) and (1.2.2) and the quantity $(\alpha - \alpha_{cl})$ can be obtained from measurement of the bulk viscosity and this enables the characteristic relaxation time (if there is one) that dominates the non-classical absorption to be deduced.

(1.3) The Acoustic Technique

The acoustic technique, employed in this work, to measure the speed of sound relies on the resonance within a fixed volume cavity. A sound field is excited to produce resonance frequencies which are characteristic of the cavity and of the fluid under study. The most simple geometry that may be utilised is a sphere and for this it was proposed by Rayleigh that the speed of sound is related to the radius of the cavity by

$$f = \frac{u\nu}{2\pi a} \tag{1.3.1}$$

Where a is the radius of the cavity, f is the frequency of the normal modes and ν is an eigenvalue known exactly. This simple model, however, cannot explain the finite linewidths which are observed experimentally. A first-order perturbation theory developed later by Mehl and Moldover [15] makes corrections to the frequency and explains the observed linewidths. Thus, the measured frequencies differ from the unperturbed frequencies given by equation (1.3.1) and can be represented by the complex quantity

$$F = (f + ig) = \left(\frac{u\nu}{2\pi a}\right) + \Sigma_j (\Delta f + ig)_j \tag{1.3.2}$$

where the sum represents the perturbations in the cavity, which will be discussed in more detail in chapter 3.

(1.4) Spherical Geometry

Measurements of the speed of sound using spherical acoustic resonators have been made up to pressures of about 20 MPa [16] and for a wide range of gases [17 - 29]. The spherical geometry yields particularly precise speed of sound measurements as it has a favourable surface area to volume ratio minimising perturbations caused by the gas-shell interface. Furthermore, the radially symmetric modes (radial modes) of a sphere have several salient features: they are non-degenerate and are therefore easily resolved; the acoustic density is concentrated towards the centre of the sphere thereby minimising energy losses and the gas motion is normal to the cavity wall so there is no viscous damping [30]. The radial modes therefore have exceptionally high quality factors ($Q = f/2g$) and allow the speed of sound to be measured very precisely. Furthermore, it is possible

with a spherical geometry to be able to solve shifts in frequency due to coupling of the motion of the gas and of the cavity wall [31].

Spherical resonators have also found application in the determination of phase boundaries [32, 33]; to determine the effect of light hydrocarbons on the wax appearance points in a well fluid [34]; for the development and optimisation of equations of state [35, 36]; the determination of composition [37, 38] and, for polyatomic gases, information has been extracted about the timescale of relaxation processes [17, 18, 39 - 41].

(1.5) Hemispherical Geometry

The hemispherical resonator was designed for the measurement of the radial acoustic modes at pressures up to 40 MPa. This geometry retains many of the advantages characteristic of the sphere [42], but is more effective for use at high pressures. The boundary conditions which must be satisfied at the gas-shell interface lead to a single equation which determines the complex eigenfrequencies from their unperturbed values $f_{l,n}^{0}$

$$F_N = f_{l,n}^{0} + \Delta f_{\mathrm{h}} + \Delta f_{\mathrm{v}} + \Delta f_{\mathrm{sh}} + i\left(g_{\mathrm{h}} + g_{\mathrm{v}} + g_{\mathrm{b}}\right) \tag{1.5.1}$$

This condition may be solved exactly for a perfect sphere and for the radial modes the viscous boundary layer perturbation $\left(\Delta f_{\mathrm{v}} + i g_{\mathrm{v}}\right)$ vanishes. Although in the hemisphere there is a perturbation from the shear waves at the equatorial surface this is not as important at high pressures and the appropriate corrections can be made. Furthermore, the effects of shell motion Δf_{sh} , the most important correction at high pressures, should be somewhat reduced by the thick walls employed and the high acoustic admittance of stainless steel. In practice, further corrections may be applied for the effects of holes and slots.

At pressures exceeding 10 MPa the transducers in the sphere suffer substantial attenuation due to the large loads on the membrane. The greatest advantage of the hemispherical geometry however, exploits the fact that a transducer may be placed at the centre of the equatorial plate ($r/a = 0$); a position corresponding to maximum acoustic density for the radial modes. Even at high pressures the signal strengths are still very intense and enables the use of small inefficient transducers.

Though not exploited in this work, the hemispherical geometry is potentially very useful for the determination of the thermal conductivities and shear viscosities of a gas. The radial modes of the hemisphere suffer from shear losses at the equatorial wall in addition to thermal losses at the spherical and plane boundaries and this allows the contributions of the thermal and viscous loss mechanisms at the cavity wall to be separated; this is not the case for radial modes in a sphere because there are only thermal losses at the gas-shell interface.

(1.6) Cylindrical Geometry

The relative ease with which a cylindrical cavity may be fabricated (compared with a spherical vessel) means a large number of measurements have been performed using interferometers with cylindrical geometry [43 - 51]. In terms of accuracy, cylindrical cavities have been superceded largely by the spherical geometry. The resonances observed in a cylinder are much less sharp than for the spherical geometry due to both thermal and viscous damping at the gas-shell interface and the less favourable surface area to volume ratio and therefore results in a less precise determination of the resonance frequencies. An extra degree of freedom, however, is afforded by the cylinder in the ratio b/L (where b is the internal radius and L is the length) and this may be chosen to suit the particular application [52].

The cylinder is particularly useful for the determination of the thermal conductivities and shear viscosities as the thermal and viscous loss mechanisms at the cavity wall may be separated due to the existence of modes of differing symmetry. The cylindrical geometry has been utilised by Colgate to determine diffusion coefficients [53].

(1.7) Annular Geometry

Consisting of two concentric cylinders the annulus affords an additional degree of freedom to the cylinder in the radius ratio, that is, the ratio of the inner and outer radii. However, it has a less favourable surface area to volume ratio giving rise to broader resonance linewidths. The geometry becomes favourable for low pressure measurements of the speed and absorption of sound in relaxing gases, with large bulk viscosities. This is due to the long pathlengths which may be attained for the azimuthal modes of an annulus and hence low frequencies, for which sharp

resonances are observed. It is possible using an annular resonator to study relaxing gases at pressures a factor of ten lower than for a practical sphere [54, 55].

(1.8) Acoustic Theory

It can be shown that the eigenvalues for the ideal sphere and the ideal hemisphere of the same radius are identical, see section (3.13). In this case the resonance frequencies are given by

$$f_{l,n} = \nu_{l,n}\left(\frac{u}{2\pi a}\right) \tag{1.8.1}$$

and the only contribution to the half-widths is through the bulk absorption. However, the perturbations in a sphere and a hemisphere are not identical. For the radial modes in a sphere or hemisphere, there is a perturbation to the resonance frequencies as a result of thermal waves at the interface between the gas and the spherical wall. The magnitude of the thermal boundary layer losses in a spherical cavity are twice those of a hemisphere with an identical radius. Additional perturbations to the resonance frequencies occur in the hemispherical cavity due to thermal and shear waves at the interface between the gas and the equatorial surface.

Other perturbations also differ for the two geometries and as such, the corrections applied for holes in the resonator's wall and for the smaller effects arising from molecular slip and temperature jump at the boundary are not identical. The corrections to the resonance frequencies and halfwidths of the radial modes are discussed in more detail in chapter 3.

The motion of the cavity was assumed to be similar to that of a sphere or even a cylinder for design purposes, but it was not possible to calculate accurately, as the motion of a hemisphere is not known exactly. A breathing frequency was expected because one is observed for a spherical resonator, where the correction is dependent on the ratio of the particular resonance frequency to the breathing frequency. The correction relies on the assumption that the breathing frequency occurs at a much higher frequency than the resonances studied and this is usually the case. For a cavity which employs wall thicknesses as large as those of the hemisphere, the calculated breathing frequency was expected to be extremely high and well above the frequency range of the first few radial modes. For the hemispherical cavity, however, it is likely that the dominant features of shell motion are due to resonances of the equatorial plate, which behaves like an edge-clamped plate [52]. However, the non-isotropic geometry of the cavity means the shell frequencies are extremely

difficult to predict accurately. Proximity of shell resonance frequencies to those of the gas leads to severe losses which are so large it is impossible to make precise corrections for the behaviour using perturbation theory, which is valid only for small perturbations [56 - 58].

(1.9) Measurements

The hemispherical resonator designed was initially characterised using a prototype equatorial plate. This confirmed the existence of radial modes in the cavity. The effect on the resonance frequencies and halfwidths of the radial modes of the position of the source transducer on the equatorial plate with respect to the radius was investigated. The hole size of the active area of the source transducer on the measured frequencies and half-widths was also probed and the results are reported in chapter 5.

Calibration of the hemisphere was performed by comparison of the data obtained from six isotherms performed in nitrogen with the acoustic virial coefficients reported in reference [59]. These measurements enabled effective eigenvalues to be calculated for the radial modes and the temperature and pressure dependency of the cavity to be modelled. Propene was studied to assess the loss mechanisms occurring in the resonator and an appropriate model was developed using the nitrogen and propene data. Testing of the model describing the resonance frequencies and halfwidths of the radial modes was carried out by performing measurements in both the hemispherical resonator and the spherical resonator discussed in section (4.16). Measurements were made along two isotherms using both resonators filled with the same sample gas (argon). The gas line and pressure gauges were shared in order to eliminate errors arising from sample purity and systematic errors.

Tetrafluoromethane was studied to assess the ability of the resonator to perform at lower pressures and enabled the calculation of thermal relaxation effects. The much lower sound speed of CF_4 was also of interest as the gas resonance frequencies were substantially lower than those of the other gases reported and this allowed the effects of shell resonance to be studied.

CHAPTER 2 Equations of State

(2.1) Introduction

A function which is used to relate the pressure, density, temperature and composition of a system is generally known as an *equation of state.* Empirically derived, an equation of state allows the prediction of the thermodynamic properties of pure fluids and fluid mixtures to be ascertained. There are a number of categories of equations of state which will be discussed in more detail below; some are able to adequately represent the gas phase only, some just the liquid phase, but the most important equations of state may be applied simultaneously to both the liquid and gaseous phases.

Equations of state have been largely developed by combining a theoretical analysis of the molecular interactions with parameterisation arrived at empirically from experimental data.

The simplest equation of state is that of a perfect-gas mixture

$$p = \left(\sum_i n_i \right) R\,T\,/\,V \tag{2.1.1}$$

and was deduced from the various works of Boyle, Charles, Gay-Lussac and Dalton [1]. Equation (2.1.1) however, only describes gases (not liquid phase) in the limit $p \rightarrow 0$, although it sometimes serves as a useful approximation.

Pioneering experimental work in the nineteenth century eventually led van der Waals to postulate the so-called van der Waals equation [60]

$$p = \frac{RT}{V_{\mathrm{m}} - b} - \frac{a}{V_{\mathrm{m}}^2} \tag{2.1.2}$$

which incorporates terms for excluded volume and intermolecular interactions. The van der Waals equation formed the basis for the development of more detailed equations of state. It was the first equation able to predict both the gaseous and liquid phases. Further rigorous theoretical analysis and experimental work (by many notable workers in this field)

has led to a large body of equation of state models which, in the majority, are empirical modifications of the van der Waals equation.

The diversity of equations that have been and continue to be developed is borne out of a need for the accurate prediction of the thermodynamic properties of many fluids and fluid mixtures. The functional form, the empiricism and the predictive capabilities of specific equations of state vary. The use of any particular model depends largely on the application and the accuracy required. It is usual practice, therefore, to classify the equations of state according to their functional form. A brief discussion of the various functional forms is given below together with the most important and widely used equations of that type.

(2.2) Standard PVT Forms

For a pure fluid the equation of state may be written

$$p = p\left(\mathrm{T}, \mathrm{V_m}\right) \quad \text{or} \quad \mathrm{Z} = \mathrm{Z}\left(\mathrm{T}, \mathrm{V_m}\right) \tag{2.2.1}$$

and for a mixture of n components, there are a further (n-1) independent composition variables. The standard PVT forms may be classified according to the structure of the function p or Z.

(2.3) The Virial Equation of State

The virial equation of state, may be rigorously derived from statistical mechanics [64]. It may be expressed with the pressure given by a polynomial in $1/V_m$, with temperature dependent coefficients

$$Z_m = \frac{pV_m}{RT} = 1 + \frac{B}{V_m} + \frac{C}{V_m^2} + \cdots, \tag{2.3.1}$$

or in terms of a pressure-explicit expansion

$$Z_m = \frac{pV_m}{RT} = 1 + \left(\frac{B'}{RT}\right)p + \left(\frac{C'}{RT}\right)p^2 + \cdots, \tag{2.3.2}$$

where R is the gas constant and the second, third, ... virial coefficients are given by B, C, ... and are related to B' and C' by

$$\mathrm{B'} = \mathrm{B} \tag{2.3.3}$$

$$C' = \frac{\left(C - B^2\right)}{RT} \tag{2.3.4}$$

The virial coefficients B, C, ..., are related to the intermolecular energies of clusters of two, three, ..., molecules [119]. The second virial coefficient is related to the pair-wise intermolecular energy function $U(r)$ and the intermolecular separation r by

$$B(T) = 2\pi L \int_0^\infty \left[1 - \exp\left\{-U(r)/kT\right\}\right] r^2 \mathrm{d}r \tag{2.3.5}$$

The non-pairwise addivity of intermolecular potential energies complicates the expressions for the higher order virial coefficients. For a multi-component gas mixture, the second virial coefficients are given by

$$B\left(T, x_\mathrm{A}, x_\mathrm{B}, \cdots\right) = \sum_i \sum_j x_i x_j B(T)_{ij} \qquad \left(i, j = \mathrm{A}, \mathrm{B}, \cdots\right) \tag{2.3.6}$$

where, in particular, for the binary gas mixture $\{(1\text{-}x)\mathrm{A} + x\mathrm{B}\}$

$$B(T,x) = (1-x)^2 B_{\mathrm{AA}} + 2(1-x)xB_{\mathrm{AB}} + x^2 B_{\mathrm{BB}} \tag{2.3.7}$$

where the virial coefficients arising from interactions of pure A or pure B are given by B_{AA} and B_{BB} respectively. The cross virial coefficient is given by B_{AB} and arises through interactions of A and B.

To represent a given set of measurements both equations (2.3.1) and (2.3.2) must be truncated and the criteria for determining the number of coefficients that can be justified is discussed in the literature [61, 63, 65]. Determination of accurate values of the coefficients is a more subtle problem. For example, the definition of the second virial coefficient, is

$$B = \lim_{p \to 0} \left\{ \frac{pV_\mathrm{m}}{RT} - 1 \right\} V_\mathrm{m} \tag{2.3.8}$$

which relies on measurements being obtained at sufficiently low pressures that the expression is realised [63, 118].

(2.4) Cubic equations

Cubic equations of state are those which are cubic in the molar volume. Rearranging terms in the vdW equation of state gives

$$V_\mathrm{m}^3 - \left(b + \frac{RT}{p}\right) V_\mathrm{m}^2 + \frac{a}{p} V_\mathrm{m} - \frac{ab}{p} = 0 \tag{2.4.1}$$

The two parameters a and b may be adjusted to reproduce the critical temperature and pressure for a pure fluid. The first term of equation (2.4.1) contains the parameter b, which is the volume excluded by the molecules and it represents the effect of repulsive interactions. The second term, containing the parameter a represents the effect of attractive interactions.

The semi-theoretical basis on which the equation is based leads to predictions which are qualitatively correct but fail quantitatively. It is still a vast improvement on the ideal gas equation though because it encompasses vapour liquid equilibrium; it describes the coexistence curve which delineates the two phase region and it predicts the existence of a critical point. Predictions of volumetric properties, however, are accurate only to about 25 to 30 per cent. The equation, like all analytic equations of state breaks down at the critical point where it lacks the appropriate singularity. The quantitative failings of the (vdW) equation can, at least, be partially rectified by fairly simple modifications which retain the cubic form.

The van der Waals equation loses its universality by including the parameters a and b. Substitution of the principle of corresponding state into the vdW equation gives the reduced form of the van der Waals equation

$$p_{\mathrm{r}} + \frac{3}{V_{\mathrm{r}}^{2}}\left(3V_{\mathrm{r}} - 1\right) = 8T_{\mathrm{r}} \tag{2.4.2}$$

If a pure fluid obeys the principle of corresponding states then the compression factor Z_m may be written

$$Z_{\mathrm{m}} = \frac{pV_{\mathrm{m}}}{RT} = \phi\left(p/p^{\mathrm{c}}, T/T^{\mathrm{c}}\right) \tag{2.4.3}$$

in which p^c is the critical pressure, T^c is the critical temperature and ϕ is the same function for each fluid. Equation (2.4.3) may be extended to three variables to include substances which do not obey the principle of corresponding states, as in Pitzer's equation [120]

$$Z_{\mathrm{m}} = \frac{pV_{\mathrm{m}}}{RT} = \phi_{\omega}\left(p/p^{\mathrm{c}}, T/T^{\mathrm{c}}, \omega\right) \tag{2.4.4}$$

in which the acentric factor ω is defined by

$$\omega = \log_{10}\left[\mathrm{p}^{\mathrm{c}}/\mathrm{p}^{\mathrm{l+g}}\left(T/T^{\mathrm{c}} = 0.7\right)\right] - 1 \tag{2.4.5}$$

The acentric factor was chosen such that $\omega \approx 0$ for argon, krypton and xenon.

(2.5) Carnahan-Starling

Replacement, in equation (2.4.1), of the repulsive term in the pressure by the correct one for hard spheres (which may be accurately represented by rational polynomials in the density) leads to greatly improved accuracy on the vdW equation. The equation proposed by Carnahan and Starling [121] combines the simple mean-field attractive term of van der Waals with the function for hard spheres. The virial expansion for a hard sphere fluid correct to sixth order in y is

$$Z_{\mathrm{H}} = \frac{pV_{\mathrm{m}}}{RT} = 1 + 4y + 10y^2 + 18.365y^3 + 28.26y^4 + 39.5y^5 + 57y^6 + \cdots, \quad (2.5.1)$$

where y is given by

$$y = \frac{b}{4V_{\mathrm{m}}} \quad (2.5.2)$$

Carnahan and Starling developed a closed form expression

$$Z_{\mathrm{H}} = \frac{\left(1 + y + y^2 - y^3\right)}{\left(1 - y\right)^3} \quad (2.5.3)$$

$$= 1 + 4y + 10y^2 + 18y^3 + 28y^4 + 40y^5 + 54y^6 + \cdots,$$

that is a much better approximation to equation (2.5.1) than the van der Waals expansion

$$Z_{\mathrm{H}} = 1 + 4y + 16y^2 + 64y^3 + \cdots, \quad (2.5.4)$$

which is correct only to first order in y by comparison.

(2.6) General Cubic Equations

In many applications of equation of state the shortcomings of the attractive term are thought to be of more importance than the failure of the simple vdW repulsive term. Improvements concentrated on the attractive term and retaining the vdW repulsive term lead to a general cubic equation given by

$$p = \frac{RT}{V_{\mathrm{m}} - b} - \frac{\mathrm{a}(T)}{\left\{\left(V_{\mathrm{m}}^2 + V_{\mathrm{m}}cb - \left(c-1\right)b^2\right)\right\}} \quad (2.6.1)$$

The modified cubic equations are characterised by integer values of the parameter c and all except van der Waals have a as a function of temperature containing fixed parameters, in addition to critical constants, which were determined by fitting experimental vapour pressure data for a range of substances.

(2.7) Redlich-Kwong (RK)

The Redlich-Kwong equation of state is an empirical modification of its predecessors and although a great improvement it gives useful results for only a few rather simple fluids [122]. In terms of the general cubic equation (2.6.1), the RK equation has

$$a(T) = \frac{a\left(T^{c}\right)}{T^{\frac{1}{2}}} \tag{2.7.1}$$

and $c = 1$ and $Z^{c} = 1/3$. The usefulness of the equation is limited because the parameters of the equation are based entirely on the two critical constants T^{c} and p^{c} and do not incorporate the acentric factor. However, the PVT properties of compressed gases are described more accurately and the saturation line is better modelled , although still not well.

(2.8) Soave (RKS)

The Soave equation is a modification of the RK equation in which a more complicated function of the temperature has replaced $a\,(T)$ which incorporates the acentric factor; this is designed to reproduce the vapour pressures of hydrocarbons and light gases [123].

$$\mathrm{a}(T) = \mathrm{a}(T)\alpha\left(T/T^{c}\right) = \mathrm{a}\left(T^{c}\right)\left[1+\left(e+f\omega+g\omega^{2}\right)\left\{1-\left(T/T^{c}\right)^{\frac{1}{2}}\right\}\right]^{2} \tag{2.8.1}$$

The RKS equation can reproduce the vapour pressure curves of most hydrocarbons and light gases within 1 to 2 per cent, so is practical for engineering applications. Its major weakness is in its under prediction of liquid density values.

(2.9) Peng-Robinson (PR)

This equation has a different choice of the integer parameter ($c = 2$), compared to the Soave equation, which results in an improved prediction of the critical compression factor to $Z^c = 0.307$ and generally improved predictions of liquid density [124]. The term $a\,(T)$ is identical to that for the RKS equation.

(2.10) Complex Empirical Equations

Simultaneous modifications to both the attractive and repulsive terms in the vdW equation of state leads to equations which are no longer cubic in the molar volume. Beattie and Bridgeman [125] developed the following equation

$$p = \frac{RT}{V_{\mathrm{m}}} + \frac{\left(B_0 RT - A_0 - Rc/T^2\right)}{V_m^2} + \frac{\left(aA_0 - B_0 bRT - RB_0 c/T^2\right)}{V_{\mathrm{m}}^3} + \frac{RB_0 bc}{V_{\mathrm{m}}^4 T^2} \tag{2.10.1}$$

where a, b, c, A_0 and B_0 are adjustable parameters. The expression only provides a representation of fluids below the critical density. The Beattie and Bridgeman equation was modified by Benedict, Webb and Rubin [126] to extend its range of applicability up to densities twice the critical value by use of two additional parameters α and γ:

$$p = \frac{RT}{V_{\mathrm{m}}} + \frac{\left(B_0 RT - A_0 - C_0/T^2\right)}{V_{\mathrm{m}}^2} + \frac{(bRT - \mathrm{a})}{V_{\mathrm{m}}^3} + \frac{(a\alpha)}{V_{\mathrm{m}}^6} + \frac{\left(c\left(\gamma - 1/V_{\mathrm{m}}^2\right)\exp\left(-\gamma/V_{\mathrm{m}}^2\right)\right)}{V_{\mathrm{m}}^3 T^2} \tag{2.10.2}$$

Experimental PVT data on gases, critical properties and vapour pressures were employed in the evaluation of the eight parameters in the original BWR equation. Coefficients were obtained for fewer than fifty substances, mostly hydrocarbons and as each substance required its own set of parameters, this was a major limitation. Han and Starling later generalised the equation to permit wider application of the equation. The generalised version, BWR(HS), contains coefficients in terms of the critical constants and acentric factors of pure substances together with the combining rules which allows the equation to

also be applied to mixtures. Schouten *et al.* [127 - 130] also developed a virial equation truncated at the third virial coefficient valid for mixtures. The fully developed BWRS equation of state is able to accurately predict properties as low as $T_r = 0.3$ and reduced densities as large as $\rho_r = 3.0$. One of the most accurate equations of state is the Lee-Kesler equation of state which employs two reference fluids in its formulation. The more complex equations of state have the advantage of representing the volumetric properties of real fluids accurately over wide ranges of temperature and pressure, but require vastly increased computer time.

The vdW, RK, SRK and PR equations may be implemented very efficiently because nearly all phase equilibrium calculations are performed at defined pressures and temperatures and therefore the equation of state only needs to be solved for volume, which is simple in the case of the vdW, RK, SRK and PR equations of state.

(2.11) Mixtures

There is usually considerably less data available to determine values of coefficients to ensure an equation of state that can accurately represent a mixture. The best choice of equation of state is one which adequately combines the properties of the pure components of the mixture. The critical constants of the component fluids could be combined in a plausible way *i.e.* a linear combination or in principle, the critical properties of the mixture could be measured to obtain the corresponding a and b parameters for the mixture.

(2.12) Measurement of the Second Virial Coefficient

The second virial coefficient may be extracted from (p,V_m,T) measurements made over large ranges of pressure. However, as mentioned previously the definition of B (equation 2.3.5) relies on measurements being made close to the limit where $p \rightarrow 0$ and consequently the most reliable values are usually obtained from measurements made at low pressures in apparatus designed for the purpose. Boyle's tube or a Burnett apparatus are just such examples.

A Boyle's tube consists of a fixed amount of substance contained at a constant temperature T, within a variable volume, V, confined by mercury which is used to calculate the sample pressure, p. The amount of substance is given by $\lim_{p\to 0}\{pV/RT\}$. The apparatus may be calibrated using a gas with a known equation of state or the experimental volumes may be determined by measuring the mass of mercury required to fill each one. The use of mercury limits the use of Boyle's tubes to the range over which mercury is a liquid with an acceptably low vapour pressure.

(2.13) Calorimetric methods

Indirect methods [66] of measuring PVT properties include the measurement of the isothermal Joule-Thomson coefficient given by

$$\phi = \left(\frac{\partial H}{\partial p}\right)_T = \mu C_p \tag{2.13.1}$$

where C_p is the heat capacity at constant pressure and

$$\mu = \left(\frac{\partial T}{\partial p}\right)_H \tag{2.13.2}$$

is the isenthalpic Joule-Thomson coefficient. A typical experiment would consist of passing gas at pressure p_1 through an adjustable throttle after which it assumes a pressure p_2. The Joule heat required to keep the temperature of the gas the same on both sides of the throttle is measured. In the limit of a very small pressure drop the measured quantity becomes the isothermal Joule-Thomson coefficient. The advantages of this method over direct PVT measurements are firstly, that direct measurement of the extent of gas imperfection is more easily detectable than the small difference between two large quantities and secondly, the experiment is not complicated by the effects of adsorption.

(2.14) Speed of Sound Measurements

Equations of state may be written in the form

$$u^2 = u^2(T, p) \tag{2.14.1}$$

as an alternative to (p,V_m,T) relations and should be immune to the effects of adsorption since u is formally independent of the amount of substance. However at pressures greater than 0.6 of the vapour pressure anomalous effects have been observed, which have been explained by precondensation theory [67] whereby the surface admittance is greatly enhanced as the pressure of the gas approaches saturation.

In the absence of relaxation, the speed of sound is given by the Maxwell equation given in chapter 1 (equation 1.1.1). This may also be written as the expansion given by equation (1.1.3) where the second and third acoustic virial coefficients are related to the (p,V_m,T) virial coefficients, B and C in equation (1.1.2), through

$$\beta_a = 2B + 2\left(\gamma^{pg}-1\right)T\left(\frac{dB}{dT}\right)+\frac{\left(\gamma^{pg}-1\right)^2}{\gamma^{pg}}T^2\left(\frac{d^2B}{dT^2}\right) \qquad (2.14.2)$$

and

$$\gamma_a = \frac{\left(\gamma^{pg}-1\right)}{\gamma^{pg}}\times\left\{B+2\left(\gamma^{pg}-1\right)T\left(\frac{dB}{dT}\right)+\left(\gamma^{pg}-1\right)T^2\left(\frac{d^2B}{dT^2}\right)\right\}^2$$
$$+\frac{1}{\gamma^{pg}}\times\left\{\left(1+2\gamma^{pg}\right)C+\left[\left(\gamma^{pg}\right)^2-1\right]T\left(\frac{dC}{dT}\right)+\tfrac{1}{2}\left(\gamma^{pg}-1\right)^2T^2\left(\frac{d^2C}{dT^2}\right)\right\} \qquad (2.14.3)$$

The determination of B and C from the acoustic virial coefficients is discussed in greater detail in the literature [8].

For a binary gaseous mixture $u(T, p)$ measurements contain sufficient information to determine the mole fraction, provided that $C_{p,m}^{pg}$ and M are known for the pure components.

(2.15) Sonic Nozzles

A tube of variable cross-section through which the steady flow of a gas out of a large vessel occurs is known as a sonic nozzle [116]. The simplicity, lack of moving parts and easy maintenance of sonic nozzles recommends their use as flow metering standards to the gas industry. The calculation of mass flow rates through nozzles invariably requires the use of an equation of state combined with a method of predicting the perfect-gas heat

capacity. The evaluation of equations of state, by comparison with speed of sound results are important for the reliable estimates of flow rates. Accurate sonic speeds on multi-component mixtures can be used to test the validity of models and guide efforts to fine tune them if necessary. Studies on methane and a binary mixture of methane and ethane were performed by Boyes [59] in which comparisons were made with the BWRS, PR and RKS equations of state discussed previously as well as a number of other relevant equations. For methane and the binary mixture, he found that all equations of state produced zero-pressure values of u to within about 0.1 % of those determined experimentally. For the whole temperature and pressure ranges studied, the deviations of u from the predicted values were less than 1 % and generally better than 0.5 %. Acoustic resonance determinations of the sonic speed and dew points in a natural-gas mixture and retrograde condensate have also been compared with equation of state models [32] where the agreement has been found to be very good.

CHAPTER 3 Acoustic Theory

(3.1) Propagation in an Ideal Fluid

In order to derive a wave-equation describing the propagation of sound in a fluid several assumptions are made to obtain a simple model. The first of the assumptions is that the fluid is ideal *i.e.* the mechanisms that result in dissipation are ignored. The second is that local thermodynamic equilibrium is established instantaneously in the fluid, and the third, that the fluid is at rest, except for the motion due to the passage of sound. In the presence of sound the pressure exerted by the fluid may be expressed by $p + p_a(\boldsymbol{r},t)$, the temperature is denoted by $T + T_a(\boldsymbol{r},t)$ and the mass density by $\boldsymbol{\rho} + \boldsymbol{\rho}_a(\boldsymbol{r},t)$. Each of these sums represents the contribution from the equilibrium value and the much smaller acoustic value.

The acoustic contributions are small compared with the equilibrium values and this allows us to neglect squares, cross-products and higher powers of these quantities, the fluid velocity u is also a small acoustic quantity.

The wave equation appropriate to the model described above is given by

$$\left[\nabla^2 - \left(\frac{1}{u_0^2}\right)\left(\frac{\partial^2}{\partial t^2}\right)\right] p_a(r,t) = 0 \tag{3.1.1}$$

Where $\nabla^2 = \nabla \cdot \nabla$ is the Laplacian operator and $u_0^2 = \left(\partial p / \partial \rho\right)_S$ as given by equation (1.1.1).

Equation (3.1.1) is valid in the limiting case, which requires that the amplitude of the disturbance be small.

Equation (3.1.1) is derived, through various manipulations, from Euler's equation for motion in a fluid which is,

$$-\nabla \rho_a = (\rho + \rho_a)\left[\left(\frac{\partial \upsilon}{\partial t}\right) + (\upsilon \cdot \nabla)\upsilon\right] \tag{3.1.2}$$

(where υ represents the fluid velocity) and from the equation of continuity for mass density, given in the Cartesian coordinate system, by

$$\left(\frac{\partial \rho_a}{\partial t}\right) = -(\rho + \rho_a)\nabla \cdot \upsilon - (\upsilon \cdot \nabla)\rho_a \tag{3.1.3}$$

where

$$\nabla = \boldsymbol{i}\left(\frac{\partial}{\partial x}\right) + \boldsymbol{j}\left(\frac{\partial}{\partial y}\right) + \boldsymbol{k}\left(\frac{\partial}{\partial z}\right) \tag{3.1.4}$$

A particular solution of the wave equation is given by $p_a = f(\boldsymbol{q})$ where $\boldsymbol{q} = \boldsymbol{r} + u\boldsymbol{th}$ which describes a wave travelling in a direction parallel to that of the unit vector $\boldsymbol{h}$ at speed u. If f is substituted into the wave equation then the speed of sound u is equal to $\boldsymbol{u}_0 = \left(\partial p / \partial \rho\right)_S^{1/2}$, where u_0 is called the ideal speed of sound.

(3.2) Propagation in a Dissipative Fluid

A modified wave equation is now derived which includes some of the effects of dissipation. In real fluids dissipation occurs as a result of the effects of thermal conduction and friction and is also due to molecular and chemical relaxation processes (considered in chapter 8). The effect of thermal conduction is that, in the presence of sound, the acoustic cycle fails to be perfectly isentropic because gradients in temperature cause irreversible flow of energy from regions of high temperature to regions of low temperature. The effects of friction are contained in the transport properties, the shear and bulk viscosities (η and η_b respectively) and enter directly into the equations of motion.

The acoustic model now contains six quantities: the acoustic pressure, temperature and density (p_a, T_a and ρ_a respectively) and the three components of the fluid velocity υ. Six equations are therefore required to specify a solution. The first of these is the equation of mass-density continuity,

$$\left(\frac{\partial \rho_a}{\partial t}\right) + \rho \nabla \cdot \upsilon_l = 0 \tag{3.2.1}$$

The second, the thermodynamic equation of state (which is used to interrelate the acoustic contributions to the temperature, pressure and density),

$$\rho_a = \left(\frac{\gamma}{u_0^2}\right)\left(p_a - \beta T_a\right) \tag{3.2.2}$$

The third is the second-order diffusion equation, describing thermal conduction

$$D_{\mathrm{h}}\nabla^2 T_{\mathrm{a}} = \left(\frac{\partial}{\partial t}\right)\left\{T_{\mathrm{a}} - \left(\frac{\gamma - 1}{\gamma\beta}\right)p_{\mathrm{a}}\right\} \tag{3.2.3}$$

where the thermal diffusivity is given by $D_{\mathrm{h}} = k/(\rho C_p)$ and the thermal conductivity and isobaric heat capacity are denoted by k and C_p respectively. The remaining three quantities are the three components of the linearised Navier-Stokes equation, for the longitudinal flow of a compressible fluid, equation (3.2.4). These are derived from the Navier-Stokes equation, which may be written correct to first order in the acoustic variables in the form

$$\left(\frac{\partial \upsilon}{\partial t}\right) = -\left(\frac{1}{\rho}\right)\nabla p_{\mathrm{a}} + \left[\left(\frac{4D_{\mathrm{s}}}{3}\right) + \left(\frac{\eta_{\mathrm{b}}}{\rho}\right)\right]\nabla(\nabla\cdot\upsilon) - D_{\mathrm{s}}\nabla\times(\nabla\times\upsilon) \tag{3.2.4}$$

where $D_s = \eta_b/\rho$ is the viscous diffusivity. The fluid velocity υ is a vector function of position and can be resolved into the sum of a longitudinal component υ_l for which $\nabla\times\upsilon_l = 0$ and a rotational component υ_{r} for which $\nabla\cdot\upsilon_r = 0$. The longitudinal component may be represented in terms of a velocity potential and ∇p_{a} contributes only to longitudinal fluid flow since the gradient of a scalar function is entirely longitudinal.

The linear Navier-Stokes equation (3.2.4) may be written as two uncoupled equations:

$$\left(\frac{\partial \upsilon_{\mathrm{l}}}{\partial t}\right) = -\left(\frac{1}{\rho}\right)\nabla p_{\mathrm{a}} + D_{\mathrm{v}}\nabla\times\left(\nabla\cdot\upsilon_{\mathrm{l}}\right) \tag{3.2.5}$$

and

$$\left(\frac{\partial \upsilon_{\mathrm{r}}}{\partial t}\right) = -D_{\mathrm{s}}\nabla\times\left(\nabla\cdot\upsilon_{\mathrm{r}}\right) \tag{3.2.6}$$

where

$$D_{\mathrm{v}} = \left(4D_{\mathrm{s}}/3\right) + \left(\eta_{\mathrm{b}}/\rho\right) \tag{3.2.7}$$

It may be noted that equation (3.2.6) is independent of the acoustic pressure and hence may be neglected in the bulk of the fluid, but transverse flow may be important when there are boundary conditions to be satisfied.

The modified wave equation;

$$\nabla^2 p_{\mathrm{a}} = \left(\frac{\gamma}{u_0^2}\right)\left[\left(\frac{\partial^2}{\partial t^2}\right) - D_{\mathrm{v}}\left(\frac{\partial}{\partial t}\right)\nabla^2\right]\left(p_{\mathrm{a}} - \beta T_{\mathrm{a}}\right) \tag{3.2.8}$$

is obtained by taking the divergence of equation (3.2.5) and eliminating υ_1 using the equation of mass-density continuity and eliminating ρ_a using equation (3.2.2).

This equation (3.2.8) may be solved simultaneously with equation (3.2.3) for T_a and p_a.

(3.3) Boundary Conditions

It is a necessary practicality of the experimental work presented in chapters 7 and 8 that any fluid under study is bound by some vessel. When the fluid is contained to a particular region by a surface, the solutions of the wave equation must satisfy certain boundary conditions at that surface as well as the fundamental equations given above that describe the propagation of sound in an infinite fluid medium.

An acoustic impedance Z_a is assigned to the boundary, which is dependent on the acoustic pressure acting there. It is useful to define a specific acoustic admittance y_0 of the surface by

$$y_0 = \frac{\rho u}{Z_a} \tag{3.3.1}$$

where ρu is the acoustic impedance of the adjacent fluid which is assumed uniform for practical purposes.

(3.4) Thermal and Viscous Boundary Layers

In the bulk, only the propagational waves are important. However, at an interface, the thermal and shear waves in the boundary layer give rise to significant loss mechanisms in the fluid. The detailed theory given in reference [52] leads to the following expressions for the specific acoustic admittance of the thermal y_h and shear y_s boundary layers,

$$y_h = (1+i)(\gamma-1)\left(\frac{\omega}{2u}\right)\delta_h \tag{3.4.1}$$

and

$$y_s = (1+i)\left(\frac{k_t}{k}\right)^2\left(\frac{\omega}{2u}\right)\delta_s \tag{3.4.2}$$

where k_t is the tangential propagation constant. A measure of the distance over which the boundary layer effects are important is given by the thermal δ_h and viscous δ_v penetration lengths,

$$\delta_h = \left(\frac{2D_h}{\omega} \right)^{1/2} \tag{3.4.3}$$

and

$$\delta_s = \left(\frac{2D_s}{\omega} \right)^{1/2}. \tag{3.4.4}$$

The viscous effects on the sound wave near the wall depend on the angle of incidence but the effects of heat flow at the wall are independent of k_t.

(3.5) Absorption and Dispersion of the Speed of Sound

The transport of heat and momentum, vibrational and rotational relaxation and chemical and structural rearrangements are kinetic processes that do not affect the low-frequency speed of sound since this is determined by the equilibrium properties. The absorption and dispersion of sound occurs when the frequency is sufficiently high that the fluid is unable to maintain local equilibrium and the period of the sound wave becomes comparable with a timescale characterising one of the kinetic mechanisms.

(3.6) The Acoustic Absorption Coefficient

The acoustic absorption coefficient α is a measure of absorption which arises because the sound wave disturbs the local state of the fluid. A small contribution to the total absorption results from the flow of heat and momentum which are always present in a fluid; this leads to classical absorption the magnitude of which is determined by the thermal conductivity κ and the shear viscosity η. The classical absorption coefficient denoted by α_{cl} is given by

$$\alpha_{cl} = \left(\frac{\omega}{2u^3} \right) \left[\left(\frac{4D_s}{3} \right) + (\gamma - 1) D_h \right] \tag{3.6.1}$$

where ω is the angular frequency given by $\omega = 2\pi f$, γ is the ratio of the perfect gas heat capacities given by $\gamma = C_p / C_v$ and D_s and D_h are the viscous and thermal diffusivities, given by $D_s = \eta / \rho$ and $D_h = \kappa / \rho C_p$ respectively.

Once corrections for the classical absorption have been made, other dissipation mechanisms which are usually significantly greater may be investigated.

(3.7) Relaxation

Thermal relaxation in a fluid is the result of the exchange of energy between translational and other internal degrees of freedom of the molecules. The existence of rotational and vibrational energy levels leads to possible modes of energy transfer within a polyatomic fluid. These are translational $\rightarrow$ vibrational (T-V) and translational $\rightarrow$ rotational (T-R) modes of energy exchange. At the temperatures at which most acoustic experiments are usually performed many of the closely spaced rotational levels are populated. The T-R transitions can be included in the bulk viscosity through

$$\eta_b = (\gamma - 1)(\rho u^2)\tau_{rot}\Delta_{rot} \tag{3.7.1}$$

where τ_{rot} is the rotational relaxation time and $\Delta_{rot} = C_{rot}/C_p$ is the fraction of the heat capacity that is relaxing. As T-R transfer occurs at nearly every collision, equilibrium of the rotational levels is not much greater than for translational motion and so τ_{rot} is usually negligible.

The vibrational energy levels, however, are usually much wider spaced and only a few are populated so the vibrational relaxation time is related to the probability of transitions from one vibrational state to another and it is this that usually dominates the bulk absorption.

$$\eta_b = (\gamma - 1)(\rho u^2)\tau_{vib}\Delta_{vib} \tag{3.7.2}$$

where τ_{vib} is the vibrational relaxation time and $\Delta_{vib} = C_{vib}/C_p$ is the fraction of the heat capacity that is relaxing. It is assumed that the vibrational modes couple strongly to each other so that the vibrational contribution to the heat capacity C_{vib} relaxes with a single apparent relaxation time τ_{vib}. The effect of the relaxation time depends on the timescale of the energy exchange compared with the period of the sound wave. At low enough frequencies, when the characteristic timescale of thermal relaxation (τ) is small compared with the frequency of sound

i.e. $1/\omega >> \tau$, the (T-R) and (T-V) transfers are not important in attenuating sound and the effects are contained in the frequency-independent bulk viscosity η_b assigned to the fluid. Thus, the total absorption, which includes classical effects and those contained in the bulk absorption is now given by the absorption coefficient

$$\alpha = \left(\frac{\omega}{2u^3}\right)\left[\left(\frac{4D_s}{3}\right) + (\gamma - 1)D_h + \left(\frac{\eta_b}{\rho}\right)\right] \tag{3.7.3}$$

When the relaxation time is comparable to the period of the sound wave *i.e.* $1/\omega \sim \tau$ the sound speeds will be severely attenuated and the resulting dispersion is given by

$$\left(\frac{u}{u_0}\right)^2 = 1 + \left\{\frac{(\omega/\rho)^2(\tau\rho)^2(\gamma-1)(1-\gamma\Delta)\Delta}{1+(\omega/\rho)^2(\tau\rho)^2(1-\gamma\Delta)^2}\right\} \tag{3.7.4}$$

and the absorption per wavelength μ by

$$\mu = 1 + \left\{\frac{\pi(\omega/\rho)(\tau\rho)(\gamma-1)\Delta}{1+(\omega/\rho)^2(\tau\rho)^2(1-\Delta)(1-\gamma\Delta)}\right\} \tag{3.7.5}$$

The product $\tau\rho$ is expected to be nearly independent of density along an isotherm and may be extracted from an analysis of the resonance halfwidths and is discussed in more detail in chapter 8.

At high frequencies, some or all of the internal degrees of freedom cease to participate in the acoustic cycle and for this limiting behaviour there is no longer any heat capacity contribution from the vibrational mode to the effective heat capacity and the dispersion of the speed of sound is very large.

However, when the dispersion is not too severe the fractional perturbations of absorption on the resonance frequencies and halfwidths of the system are given respectively by

$$\frac{\Delta f}{f} \approx \left(\frac{(\gamma-1)\Delta\omega^2\tau^2}{2}\right)\left(1 - \frac{\Delta(1+3\gamma)}{4}\right) \tag{3.7.6}$$

which is small at low frequencies and more importantly,

$$\frac{g_b}{f} = \left(\frac{u}{2\pi}\right)\alpha \tag{3.7.7}$$

Equations (3.7.6) and (3.7.7) suggest higher order terms in the loss mechanisms.

The dispersion and absorption of sound has been widely studied in both gases and liquids [68 - 73] and has successfully lead to information about the relaxation properties occurring in the fluid.

(3.8) Cavities

Simple-harmonic standing wave motion is maintained in a cavity by the continuous generation of sound. Resonance conditions are satisfied when the source frequency coincides with a natural frequency of the system. For a simple geometry and for a cavity with known wall properties, solutions to the appropriate wave equation may be found which satisfy the boundary conditions. This enables expressions which relate the frequency and halfwidth of a resonance to the speed and absorption of sound in a medium.

(3.9) Normal Modes of an Acoustic Cavity

The velocity potential for the region of the cavity $\mathbb{R}$ with simple-harmonic time dependence is given by the product

$$\Psi(r,T) = A\Phi(r)\exp(i\omega t) \tag{3.9.1}$$

where $\omega = 2\pi f$ is the angular frequency, $\Phi(r)$ is a dimensionless wavefunction that gives the spatial variation of the wave field, and A is a constant that determines its overall amplitude. The wave equation,

$$\left[\nabla^2 + \left(\frac{k}{\omega}\right)^2\left(\frac{\partial^2}{\partial t^2}\right)\right]\Psi(r,t) = 0 \tag{3.9.2}$$

will be satisfied when

$$\nabla^2\Phi(r) = -k^2\Phi(r) \tag{3.9.3}$$

where the propagation constant is given by

$$k = (\omega / u) - i\alpha \tag{3.9.4}$$

The solutions of equation (3.9.3) that are allowed within the closed region $\mathbb{R}$ are the eigenfunctions of ∇^2, represented by $\Phi_N(\mathbf{r},\omega)$, and satisfy the boundary conditions at the

surface of the enclosure. These solutions are collectively known as the normal modes of the cavity and form the infinite set of solutions that are mutually orthogonal, finite and continuous within the closed region. The corresponding eigenvalues are the allowed values of $-k^2$. Each of the normal modes will obey the orthogonality condition, and the boundary conditions at the surface. The boundary condition restricts the propagation constant k to a discrete set of values $K_N(\omega)$, where N is the set of three indices n_1, n_2, n_3 required to specify the solution in three dimensions. The propagation constant has also to satisfy equation (3.9.4) so the complex natural frequencies of the system are given by

$$F_N = \left(f_N + ig_N\right) = \left(\frac{u}{2\pi}\right)\left(K_N + i\alpha\right) \tag{3.9.5}$$

Free oscillations may occur only at these discrete natural frequencies of the system. The N-th mode will oscillate in proportion to $\exp(2\pi i\, F_N\, t)$ and decay with a time constant $1/2\pi g_N$.

(3.10) Forced Oscillations

The steady state response of the acoustic cavity to the source of sound can be derived from the information contained in the normal-mode solutions. The response to a source of finite size may be obtained by summing the effects of infinitesimal sources, each giving a simple-harmonic and continuous wave field. The response of the driven cavity and the source are not necessarily in phase so the acoustic pressure (p_ω) is a complex quantity. When the modes are well resolved, a single component (or group of degenerate components) dominates near resonance and will always have a finite linewidth due to dissipation in the bulk of the fluid and at the boundary. At low frequencies the response of the driven cavity is punctuated by more or less well resolved resonances and a mode may be studied in near isolation, with the background contribution of the other modes expanded in a Taylor series about the frequency f_0 of interest.

$$p_\omega = \left\{\frac{A_N}{\left(F_N / f\right)^2}\right\} + B + C\left(f - f_0\right) + \ldots \tag{3.10.1}$$

where A_N, B, C, ... are complex constants for a fixed location of source and detector. As the frequency increases so too does the mode density, consequently, at higher frequencies the chance of overlap between neighbouring modes is increased. Measurements of the amplitude

and phase of the acoustic pressure over a small frequency band near to resonance allow the complex natural frequencies and other constants to be determined.

The quality factor $Q_N = f_N/2g_N$ of a particular mode gives an indication of the precision with which a particular mode may be measured; high Q_N correspond to precise measurements.

A Lorentzian lineshape is given for a sharp singlet without background by

$$p_\omega = \frac{ia_N}{\left[g_N + i\left(f - f_N\right)\right]} \tag{3.10.2}$$

When the source frequency is coincident with the resonance frequency, the response of the cavity reaches a maximum value of a_N/g_N. The amplitude is reduced to $1/\sqrt{2}$ of its maximum value at $f = f_N \pm g_N$ and consequently g_N is referred to as the resonance halfwidth; with $2g_N$ as the usual measure of the linewidth.

(3.11) Ideal Cavities

The Helmholtz equation is a fourth order partial differential equation, which, when separated into the product of the acoustic and thermal modes is given by the following expression

$$\left(\nabla^2 + k_{\mathrm{p}}^2\right)\left(\nabla^2 + k_{\mathrm{t}}^2\right)T_{\mathrm{a}}(\mathbf{r}) = 0 \tag{3.11.1}$$

where k_{p} and k_{t} are referred to as the propagation parameters for the acoustic and thermal modes, and k_{p}^2 and k_{t}^2 are the roots of the bi-quadratic equation, T_{a} is the acoustic temperature.

An ideal cavity is one which has a perfect geometry and zero surface admittance. For a particular cavity there will be characteristic boundary conditions which are satisfied by a Helmholtz operator; the eigenfunctions of which can be used to exploit the results of the general response of a cavity to a continuous simple-harmonic source of sound. Once solutions have been found for the ideal cavity, perturbation theory may be used to evaluate the effects of deviations from an ideal cavity, thereby extending the treatment to real cavities.

For the ideal case, the boundary conditions, called the homogeneous Neumann conditions are,

$$\left(\nabla^2 + k^2\right)\phi(r) = 0 \tag{3.11.2}$$

within $\mathbb{R}_0$, the region of the ideal cavity and

$$(\partial/\partial n)\phi(r)\big|_{r=r_s} = 0 \tag{3.11.3}$$

on $\mathbb{S}_0$, the surface of the ideal cavity. The eigenfunctions of the Helmholtz operator are denoted by ϕ_N (**r**) and $-k_N^2$ are the corresponding eigenvalues which are purely real quantities independent of frequency. The normalisation constants are denoted by Λ_N^2. The wavefunctions are defined as zero outside the cavity.

(3.12) Real Cavities

Real cavities will suffer perturbations as a result of non-zero and non-uniform surface admittance. A general perturbation treatment allows solutions to be found for any cavity for which the corresponding idealized cavity is solvable. To calculate the effects of perturbations, solutions of the homogeneous wave equation

$$\left(\nabla^2 + k^2\right)\Phi(r) = 0 \tag{3.12.1}$$

within $\mathbb{R}$, the region of the real cavity are found subject to the inhomogeneous boundary conditions that prevail on the surface $\mathbb{S}$ of the real cavity

$$(\partial / \partial n)\,\Phi(r)\Big|_{r=r_S} = -i\,(\omega / u)\Phi(r)y(r) \tag{3.12.2}$$

Green's functions are employed to express the solutions in terms of those for the idealized cavity with surface $\mathbb{S}$, not necessarily coincident with $\mathbb{S}_0$. The unperturbed wave functions ϕ_N form the basis set from which Φ_N is expanded. Since the unperturbed wavefunctions ϕ_N are, by definition, zero outside the surface $\mathbb{S}_0$, the surface $\mathbb{S}$ must be chosen to be entirely enclosed by $\mathbb{S}_0$. Hence, for the case of perfect geometry but non-zero effective specific acoustic admittance y ($\boldsymbol{r}_s$) of the surface, the eigenvalue is

$$K_N = k_N + \left(\frac{\omega}{uk_N}\right)\left(\frac{i}{2V\Lambda_N^0}\right)\iint_S y(r_S)\left|\phi_N(r_S)\right|^2 dS \tag{3.12.3}$$

Assuming that the perturbation of non-zero acoustic admittance is a small quantity, in a first-order approximation ϕ_N may be substituted for Φ_N; (ω / uk_N) replaced by unity for oscillations at resonance and

$$\iiint_R \left|\phi_N\right|^2 dV = V\Lambda_N^0 . \tag{3.12.4}$$

Perturbation theory may be extended to include imperfect geometry using this method and a detailed description is given elsewhere [74, 75]; this effect is not usually one of the principal corrections however. Other principal corrections include the coupling of fluid and shell motion (see section 3.19) and bulk dissipation in the fluid, discussed in section (3.7). Other corrections may also arise due to holes, slots and cracks in the resonator's wall [15, 50].

By the application of a suitable coordinate system appropriate to the boundary shape of the idealized cavity and exploiting the results of the perturbation theory given above, expressions may be derived which predict the resonance frequencies and halfwidths for a given cavity.

(3.13) Spherical and Hemispherical Cavities

It is useful to consider the case of the hemispherical cavity alongside that of the spherical cavity, since the treatments are very similar and spherical polar coordinates are used for both (figure 3.13.1). The region of the spherical cavity is defined by a sphere of radius a centred at the origin and the region of the hemispherical cavity is defined as the northern hemisphere of this.

Figure (3.13.1): Coordinate system for the spherical and hemispherical geometries

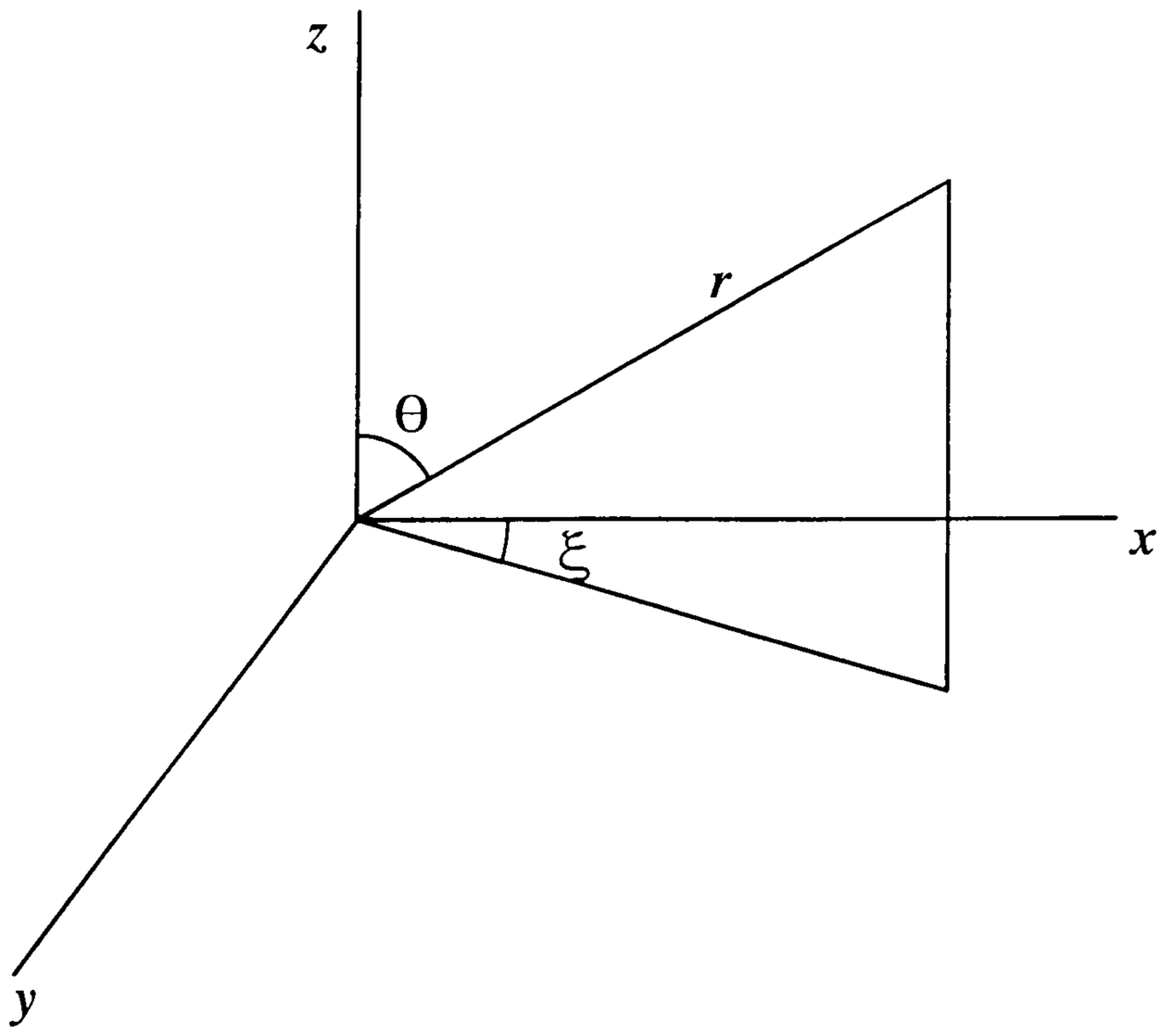

The spherical polar coordinates (r, θ, ξ) are related to the cartesian coordinates by

$$x = r\sin\theta\cos\xi \tag{3.13.1}$$

$$y = r\sin\theta\sin\xi \tag{3.13.2}$$

$$z = r\cos\theta \tag{3.13.3}$$

Where r is the radius, θ is the colatitude and ξ is the azimuthal angle, see figure (3.13.1). Perfect geometry is assumed throughout the derivation in this section and, for the ideal case, zero surface admittance is also assumed.

Rayleigh showed in the 19th century, that the wavefunction could be separated into the product:

$$\Psi(r,\theta,\xi) = \Psi_r\Psi_\theta\Psi_\xi \tag{3.13.4}$$

By substitution into the Helmholtz equation,(3.11.1), three independent equations are obtained the solutions of which are given by (3.13.5), (3.13.6), and (3.13.7),

$$\Psi_r = j_l\left(\upsilon_{l,n}\, r/a\right) \tag{3.13.5}$$

$$\Psi_\theta = P_l^m(\cos\theta) \tag{3.13.6}$$

$$\Psi_\xi = \exp(im\xi) \text{ or } \Psi_\xi = (\cos m\xi + \sin m\xi) \tag{3.13.7}$$

For the radial wavefunction, j_l is the spherical Bessel function of order l and ν_{ln} is the n-th turning point of j_l. The set of eigenvalues k_N follows from the equation for the radial boundary condition

$$(d/dr)\, j_l(kr)\Big|_{r=a} = 0 \tag{3.13.8}$$

successive roots of which, $k_N = \nu_{ln}/a$ are labelled by $n = 1, 2, 3, \ldots$ Values of ν_{ln} may be found in the literature [30, 50].

The polar function $P_l^m(\cos\theta)$ is the associated Legendre polynomial of order l. Combining the two angular functions defines the set of spherical harmonics $Y_{l,m}$ (θ, ξ);

$$Y_{lm}(\theta,\xi) = \exp(im\xi)\, P_l^m(\cos\theta) \tag{3.13.9}$$

as the solution. However, it is necessary to separate the functions for θ and ξ to evaluate the volume integral, so it is not always convenient to use $Y_{l,m}$. The full solution for the ideal spherical or hemispherical cavity may therefore be given as

$$\phi_N(r,\theta,\xi) = j_l\left(\nu_{ln} r/a\right) Y_{lm}(\theta,\xi) \tag{3.13.10}$$

The allowed values are $l = 0,\ 1,\ 2,\ ...,\ m = 0,\ \pm 1, \pm 2\ ...\pm\ l$, and $n = 1,\ 2,\ 3,\ ...$; there is $(2l + 1)$-fold degeneracy for states with a given value of l.

The orthogonality of the set of normal modes may be verified using the appropriate properties of the spherical Bessel and spherical harmonic functions. The normalization constants for the spherical and hemispherical cases are identical as shown below.

(3.14) Normalisation

The volume integral is given by

$$\iiint \Psi^* \Psi dV = I_r I_\theta I_\xi \tag{3.14.1}$$

As the limits of the radius and the azimuthal angle are the same for a sphere and a hemisphere *i.e.*

$$0 \le r \le a \tag{3.14.2}$$

$$0 \le \xi \le 2\pi \tag{3.14.3}$$

the radial integral (equations 3.14.4 and 3.14.5) is identical for a sphere or a hemisphere

$$I_r = \int_0^a r^2 j_l^2 \left(\nu_{ln} r / a\right) dr \tag{3.14.4}$$

$$= \left(\frac{a^3}{2}\right)\left(1 - \frac{l(l+1)}{\nu_{l,n}^2}\right) j_l^2\left(\nu_{l,n}\right) \tag{3.14.5}$$

and so is the azimuthal integral (equations 3.14.6 and 3.14.7) given for the spherical and hemispherical cases by

$$I_\xi = \int_0^{2\pi} e^{-im\xi} e^{im\xi}\, d\xi \tag{3.14.6}$$

$$= 2\pi \tag{3.14.7}$$

The radial integral can be obtained from a standard Bessel function integral and the definition of spherical Bessel functions.

The polar integral is different, however, for the spherical and hemispherical cases. For the sphere the limits of the polar or co-latitudinal angle are $0 \le \theta \le \pi$ and so the polar integral, which is a standard integral for associated Legendre polynomials, is given by,

$$I_\theta = \int_0^\pi \sin\theta \left\{P_l^m(\cos\theta)\right\}^2 d\theta \tag{3.14.8}$$

$$I_\theta = \left(\frac{2(l+m)!}{(2l+1)(l-m)!} \right) \tag{3.14.9}$$

but for a northern hemisphere, the polar angle has the limits $0 \le \theta \le \pi/2$, so now the polar integral is given by

$$I_\theta = \int_0^{\pi/2} \sin\theta \left\{ P_l^m(\cos\theta) \right\}^2 d\theta \tag{3.14.10}$$

$$= \left(\frac{1(l+m)!}{(2l+1)(l-m)!} \right) \tag{3.14.11}$$

which is a factor of 2 smaller than for the sphere. The normalization integral is given by,

$$V\Lambda_0 = I_r I_\theta I_\xi \tag{3.14.12}$$

So for a sphere

$$V\Lambda_0 = 2\pi a^3 \, j_l^2(\nu_{ln}) \left\{ 1 - \frac{l(l+1)}{\nu_{ln}^2} \right\} \frac{1(l+m)!}{(2l+1)(l-m)!} \tag{3.14.13}$$

with $V = 4\pi a^3/3$, and for a hemisphere

$$V\Lambda_0 = \pi a^3 \, j_l^2(\nu_{ln}) \left\{ 1 - \frac{l(l+1)}{\nu_{ln}^2} \right\} \frac{1(l+m)!}{(2l+1)(l-m)!} \tag{3.14.14}$$

with $V = 2\pi a^3/3$. The polar integral and the volume of a hemisphere are half those for a sphere, so a sphere and a hemisphere have the same normalisation constant given by,

$$\Lambda_0 = \frac{3 j_l^2(\nu_{ln})}{2} \left\{ 1 - \frac{l(l+1)}{\nu_{ln}^2} \right\} \frac{(l+m)!}{(2l+1)(l-m)!} \tag{3.14.15}$$

The shapes of the characteristic functions for modes of various symmetries are shown in reference [52]. Modes with given values of l and n are characterized by the same total angular momentum and by the same radial factor in the wavefunction; they differ, through the value of m, in the alignment of the angular momentum vector in space. The purely radial modes (figure (4.5.1)) concentrate the acoustic energy near the centre of the sphere and are the only non-degenerate modes in a perfect sphere. The modes with $l > 0$ but $m = 0$ retain axial symmetry and tend to concentrate the energy near to the wall when $l > n$. When both l and n are large, the wave energy is distributed, on average, more evenly throughout the sphere.

(3.15) Non-zero Surface Admittance

The perturbations to the propagation constant due to non-zero surface admittance are obviously different for a sphere and a hemisphere. Both the sphere and the hemisphere experience a perturbation due to the spherical surface but in the hemispherical case there is an additional term due to the equatorial surface, for which there are contributions from both thermal and shear waves at the wall.

(3.16) Perturbation on the Spherical Surface

To determine the perturbation on the spherical surface of a sphere or a hemisphere, we need the volume element dV, given by

$$dV = dr\, r \sin\theta\, d\xi \cdot r d\theta \tag{3.16.1}$$

$$= -r^2 dr\, d(\cos\theta)\, d\xi \tag{3.16.2}$$

By omitting the term dr from dV, the surface-area element dA at the radius $r = a$ is obtained,

$$dA = a \sin d\xi a d\theta \tag{3.16.3}$$

$$= -a^2 d(\cos\theta)\, d\xi \tag{3.16.4}$$

If y_s is the admittance on the spherical surface, then the perturbation to the propagation constant is

$$\delta k = \frac{i}{2} \frac{\iint \Psi^* y_s \Psi dA}{\iiint \Psi^* \Psi dV} \tag{3.16.5}$$

with the surface element $dA = -a^2 d(\cos\theta)\, d\xi$, given by (3.16.4). On the surface at $r = a$, the wavefunction is

$$\Psi(a, \theta, \xi) = j_l(\nu_{ln}) \Psi_\theta \Psi_\xi \tag{3.16.6}$$

and, if we assume that y_s is uniform over the surface, then the perturbation may be written as

$$\delta k = \frac{i}{2 y_s} \left\{ \frac{a^2 j_l^2(\nu_{ln}) I_\theta I_\xi}{I_r I_\theta I_\xi} \right\} \tag{3.16.7}$$

The factor of two difference between the sphere and the hemisphere is contained in the polar integral I_θ which cancels exactly giving for both geometries

$$\delta k = \frac{i}{2y_s}\left\{\frac{a^2 j_l^2(\nu_{l,n})}{I_r}\right\} \tag{3.16.8}$$

and using equation (3.14.5) for I_r ,we have

$$\delta k = \frac{iy_s}{a}\left\{\frac{1-l(l+1)}{\nu_{ln}^2}\right\}^{-1} \tag{3.16.9}$$

In general, the admittance is related to the thermal δ_h and viscous δ_s penetration lengths by

$$y = (1+i)\frac{k}{2}\left\{(\gamma-1)\delta_h + \left(\frac{k_t}{k}\right)^2 \delta_s\right\} \tag{3.16.10}$$

where k_t is the tangential propagation constant at the wall and k is the propagation constant in the bulk of the fluid. Using (3.16.9), the fractional perturbation is

$$\frac{\delta k}{k} = \left\{\frac{i(1+i)}{2a}\right\}\left\{(\gamma-1)\delta_h + \left(\frac{k_t}{k}\right)^2 \delta_s\right\}\left\{\frac{1-l(l+1)}{\nu_{ln}^2}\right\}^{-1} \tag{3.16.11}$$

In a sphere,

$$k = \frac{\nu_{ln}}{a} \tag{3.16.12}$$

and

$$k_t = \frac{\sqrt{l(l+1)}}{a} \tag{3.16.13}$$

so that

$$\left(\frac{k_t}{k}\right)^2 = \frac{l(l+1)}{\nu_{ln}^2}. \tag{3.16.14}$$

Consequently, the perturbation caused by the non-zero admittance of the spherical surface in a sphere is

$$\frac{\delta k}{k} = \left\{\frac{i(1+i)}{2a}\right\}\left\{(\gamma-1)\delta_h + \frac{l(l+1)}{\nu_{ln}^2}\delta_s\right\}\left\{1-\frac{l(l+1)}{\nu_{ln}^2}\right\}^{-1} \tag{3.16.15}$$

For a radial mode, $l = 0$ and because tangential motion is absent there is no viscous loss and the perturbation is particularly simple,

$$\frac{\delta k}{k} = \frac{i(1+i)(\gamma-1)\delta_h}{2a} \tag{3.16.16}$$

This gives the specific acoustic admittance of the surface as

$$y_s = (1+i)\left(\frac{\omega}{2u}\right)(\gamma-1)\delta_h + y_{sh} \tag{3.16.17}$$

where y_{sh} is the admittance of the shell.

(3.17) Perturbation on the Equatorial Surface

The perturbation on the equatorial surface obviously applies only to the hemispherical cavity. For a hemispherical surface at the equator, the surface area element is obtained from dV by omitting the term $rd\theta$.

$$dA = dr\, r\, sin\theta\, d\xi \qquad \left(\theta = \pi/2,\ sin(\pi/2) = 1\right) \tag{3.17.1}$$

$$= r\, dr\, d\xi \tag{3.17.2}$$

The surface at the equator gives rise to a perturbation

$$\delta k = \frac{i}{2}\frac{\iint \Psi^* y_e \Psi\, dA}{\iiint \Psi^* \Psi\, dV} \tag{3.17.3}$$

where the surface element $dA = rdrd\xi$ is given above and y_e is the admittance on the equatorial surface. The wavefunction at the equator ($\theta = \pi/2$ where $\cos\theta = 0$) is

$$\Psi(r, \pi/2, \xi) = \psi_r P_l^m(0)\psi_\xi \tag{3.17.4}$$

So the perturbation for the equatorial surface is given by

$$\delta k = \left(\frac{i}{2}\right) y_e \frac{\left\{P_l^m(0)\right\}^2 \int_0^a r\, j_l^2\left(\nu_{ln}\, r/a\right) dr\, I_\xi}{\int_0^a r^2 j_l^2\left(\nu_{ln}\, r/a\right) dr \int_0^{\pi/2} \sin\theta \left\{P_l^m(\cos\theta)\right\}^2 d\theta\, I_\xi} \tag{3.17.5}$$

The radial integral in the numerator gives,

$$\int_0^a r\, j_l^2\left(\nu_{ln}\, r/a\right) dr = \frac{a^2}{2}\left\{\frac{1-l(l+1)}{\nu_{ln}^2}\right\} j_l^2\left(\nu_{ln}\right) \tag{3.17.6}$$

which differs from I_r given for a spherical surface (equation 3.14.5) by a factor of a. The angular integral in the denominator gives

$$\int_0^{\pi/2} \sin\theta \left\{P_l^m(\cos\theta)\right\}^2 d\theta = -\int_{\cos 0}^{\cos(\pi/2)} \left\{P_l^m(\cos\theta)\right\}^2 d(\cos\theta) \tag{3.17.7}$$

$$\int_0^{\pi/2} \sin\theta \left\{ P_l^m(\cos\theta) \right\}^2 d\theta = \frac{(l+m)!}{2l+1\,(l-m)!} \tag{3.17.8}$$

Equation (3.17.18) is obtained using a standard integral for associated Legendre polynomials. The perturbation is obtained by combining equations (3.17.5), (3.17.6) and (3.17.8),

$$\delta k = \frac{i}{2a} y_e \left\{ P_l^m(0) \right\}^2 \frac{(2l+1)(l-m)!}{(l+m)!} \tag{3.17.9}$$

With equation (3.16.10) this gives the fractional perturbation for the equatorial surface as

$$\frac{\delta k}{k} = i(1+i)\frac{1}{4a}\left\{ P_l^m(0) \right\}^2 \left\{ (\gamma-1)\delta_h + \left(\frac{k_t}{k}\right)^2 \delta_s \right\} \frac{(2l+1)(l-m)!}{(l+m)!} \tag{3.17.10}$$

For radial modes, $l = 0$, $P_0^0(\cos\theta) = 1$ and $k_t = k$; consequently the perturbation for the equatorial surface is

$$\frac{\delta k}{k} = i(1+i)\frac{1}{4a}\left\{ (\gamma-1)\delta_h + \delta_s \right\} \tag{3.17.11}$$

and the total perturbation to the radial modes due to the surface admittance of the spherical and equatorial surfaces in a hemisphere is

$$\frac{\delta k}{k} = i(1+i)\left[\frac{1}{2a}(\gamma-1)\delta_h + \frac{1}{4a}\left\{ (\gamma-1)\delta_h + \delta_s \right\} \right] \tag{3.17.12}$$

or

$$\frac{\delta k}{k} = i(1+i)\frac{1}{4a}\left\{ 3(\gamma-1)\delta_h + \delta_s \right\} \tag{3.17.13}$$

With the specific acoustic admittance of the hemispherical surface y_{hem} given by

$$y_{hem} = (1+i)\left(\frac{\omega}{4u}\right)\left\{ 3(\gamma-1)\delta_h + \delta_s \right\} + y_{sh} \tag{3.17.14}$$

The first-order expression for the resonance frequencies and halfwidths of the radial modes in a sphere is given by,

$$f_{0n} + ig_{0n} = \left(\frac{u}{2\pi a}\right)\left(\nu_{0n} + iy_s + ia\alpha\right) \tag{3.17.15}$$

$$= \left(\frac{u}{2\pi a}\right)\nu_{0n} + \left(\Delta f_h + \Delta f_{sh}\right) + i\left(g_h + g_{sh} + g_b\right) \tag{3.17.16}$$

and for a hemisphere by

$$f_{0n} + ig_{0n} = \left(\frac{u}{2\pi a}\right)\left(\nu_{0n} + iy_{\text{hem}} + ia\alpha\right) \tag{3.17.17}$$

$$= \left(\frac{u}{2\pi a}\right)\nu_{0n} + \left(\Delta f_{\text{h}} + \Delta f_{\text{v}} + \Delta f_{\text{sh}}\right) + i\left(g_{\text{h}} + g_{\text{v}} + g_{\text{sh}} + g_{\text{b}}\right) \tag{3.17.18}$$

For an unperturbed cavity, the surface admittance is zero and the terms y_s and y_{hem} vanish, giving the unperturbed frequencies and halfwidths in a sphere or a hemisphere as

$$f_{0n} + ig_{0n} = \left(\frac{u}{2\pi a}\right)\left(\nu_{0n} + ia\alpha\right) \tag{3.17.19}$$

where the only contribution to the imaginary part is through the bulk absorption as given by equation (3.7.3). The shifts in resonance frequencies, from their unperturbed values are given by Δf_{h} , Δf_{v} and Δf_{sh} and are the contributions from the thermal and viscous boundary layers and from the coupling of fluid and shell motion. The corresponding contributions to the resonance halfwidths are denoted by g_{h}, g_{v} and g_{sh} .

(3.18) Molecular Slip and Temperature Jump

The boundary layer theory presented in the previous sections assumes that the thermal conductivity of the gas near the interface is equal to that of the bulk fluid. Real gases, however, exhibit the so-called temperature jump effect where an apparent discontinuity exists between the temperature of the gas, T_{g}, and the temperature of the wall at the interface, T_{s} [76]. This apparent discontinuity is given by

$$\left(T_{\text{g}} - T_{\text{s}}\right) = \frac{J_{\text{h}}\, l_{\text{h}}}{\kappa} \tag{3.18.1}$$

where J_{h} is the magnitude of the heat current density in the wall, κ is the thermal conductivity of the gas and the thermal accommodation length l_{h} is given by

$$l_{\text{h}} = \left(\frac{\kappa}{p}\right)\left(\frac{\pi M T_{\text{g}}}{2R}\right)^{1/2}\left(\frac{2 - h_{\text{h}}}{h_{\text{h}}}\right)\left\{\left(\frac{C_{V,\text{m}}}{R}\right) + \left(\frac{1}{2}\right)\right\}^{-1} \tag{3.18.2}$$

where h_{h} is the thermal accomodation coefficient and is typically close to unity. The thermal accomodation length modifies the specific acoustic admittance of the thermal boundary layer by a factor of $\left[1 - (1+i)\left(l_{\text{h}}/\delta_{\text{h}}\right)\right]$, giving

$$y_h = \left(\frac{(\gamma-1)\omega\delta_h}{2u}\right)\left\{(1+i)-2i\left(\frac{l_h}{\delta_h}\right)\right\} \tag{3.18.3}$$

for the spherical case and

$$y_h = \left(\frac{3(\gamma-1)\omega\delta_h}{4u}\right)\left\{(1+i)-2i\left(\frac{l_h}{\delta_h}\right)\right\} \tag{3.18.4}$$

for the thermal boundary layer of the hemispherical case, both correct in leading order to (l_h/δ_h).

An analogous effect occurs in the shear boundary layer of real fluids. It was assumed in the previous section that the shear viscosity of the gas near the interface was equal to that of the bulk fluid but real gases exhibit molecular slip where there is a discontinuity of momentum current in the gas and near the interface. The slip velocity is given by

$$\upsilon_0 = \frac{J_P\, l_s}{\eta} \tag{3.18.5}$$

where J_P is the magnitude of the momentum current density in the wall and η is the shear viscosity of the gas. The momentum accommodation length is given by

$$l_s = \left(\frac{\eta}{p}\right)\left(\frac{\pi R T_g}{2M}\right)^{1/2}\left(\frac{2-h_s}{h_s}\right) \tag{3.18.6}$$

where h_s is the momentum accomodation coefficient and, like h_h, is typically unity. It is not possible to determine either h_s or h_h *a priori*. The momentum accomodation length modifies the specific acoustic admittance of the shear boundary layer by a factor of $\left[1-(1+i)\left(l_s/\delta_s\right)\right]$, giving

$$y_s = \left(\frac{\omega\delta_s}{4u}\right)\left\{(1+i)-2i\left(\frac{l_s}{\delta_s}\right)\right\} \tag{3.18.7}$$

for the shear boundary layer of the hemispherical case, correct in leading order to (l_s/δ_s). The spherical case is not included as we are interested only in the radially symmetric modes, so there is no tangential motion and the shear boundary layer is not important.

It is notable that, since both l_h and l_s are proportional to p^{-1}, the thermal and momentum accomodation lengths are important only at low pressures where hydrodynamic theory fails to describe adequately the boundary conditions. With this in mind it is clear that these

second-order corrections are not important for the majority of this work but they are included here for completeness.

(3.19) Shell Motion

The shell motion of an isotropic spherical shell has been considered in great detail in the literature [31, 77]. In the ideal case the shell is perfectly rigid, uniform and unsupported and there is no radiation from the outside of the shell into the surrounding fluid. In this case, and at low pressures, the effects on the eigenfrequencies is small unless the acoustic and shell eigenfrequencies accidentally coincide. At high pressures, however, the effects of shell motion dominate the corrections to the observed resonance frequencies and these need to be estimated in order to achieve internal consistency on the order of a few parts in 10^{-5} in u^2 [78]. Since the correction due to the coupling of fluid and shell motion is approximately linear in density, adequate corrections to the observed resonance frequencies may be made when the radial acoustic frequencies are sufficiently removed from the shell resonances. The specific acoustic admittance is then given by

$$y_{\mathrm{sh}} = \left(\frac{-i2\pi a f \left(\rho_{\mathrm{g}} u_{\mathrm{g}}^2 / \rho_{\mathrm{s}} u_{\mathrm{s}}^2 \right)}{1 - \left(f / f_{\mathrm{br}} \right)^2} \right) \tag{3.19.1}$$

and the corresponding corrections to the resonance frequencies and halfwidths are

$$\frac{\Delta f_{\mathrm{sh}} + i g_{\mathrm{sh}}}{f} = -\left(\frac{\rho_{\mathrm{g}} u_{\mathrm{g}}^2 / \rho_{\mathrm{s}} u_{\mathrm{s}}^2}{1 - \left(f / f_{\mathrm{br}} \right)^2} \right) \tag{3.19.2}$$

where ρ_{g} and u_{g} are the density and sound speed in the gas, ρ_{s} is the density of the shell material and u_{s} is the speed of longitudinal waves in the shell material[1]. The breathing frequency, denoted by f_{br}, is the lowest radial frequency and may be calculated approximately by

$$f_{\mathrm{br}} = \frac{u_{\mathrm{s}}}{a} \left\{ \frac{t^3 - 1}{2\pi^2 (t-1)\left(1 + t^3\right)} \right\}^{1/2} \tag{3.19.3}$$

where t is the ratio of outer and inner radii *i.e.* $t = b/a$.

---

[1]For stainless steel u_{s} is approximately 5980 ms^{-1}

The theory described above is for an isotropic spherical shell; further corrections may be made for radiation from the external surface and for the presence of mechanical supports [31, 77], though these terms are small and often unnecessary when the uncertainty in other corrections is considered.

The shell of the hemispherical resonator is far from being an isotropic sphere and can be described as hemispherical only on its internal surface, with the external surface more closely resembling a cylinder. However, an analogous form of equations (3.19.1) to (3.19.3) would still be expected to exist even though an exact solution is not possible. Measurements at high pressures with a well-characterised gas, such as argon, may be used to assess the effects of shell motion. As the thickness of the cavity walls is very large the lowest radial frequency of the shell would be expected to be much higher than the radial modes of the fluid and it is the bending modes of the equatorial plate that are more likely to cause problems due to their proximity in frequency to the radial modes.

(3.20) Deflection and Fundamental Frequency of a Circular Plate

A stiff circular plate subject to a uniform acoustic pressure, p_a, on one side will undergo static deflections at low frequencies and for circularly symmetric vibrations the displacement amplitude is given by

$$\zeta(r) = \left\{\frac{3p_a\left(1-\sigma^2\right)}{16Yd^3}\right\}\left(a^2 - r^2\right)^2 \qquad (3.20.1)$$

where the plate material is characterised by Young's modulus Y and Poisson's ratio σ, and d is the thickness of the undamped plate. The boundary condition imposed at the circumference of the plate requires ζ and $\partial\zeta/\partial r$ to vanish at $r = a$, this is referred to as an edge-clamped plate. The resonance frequencies of the plate are given by

$$f_n = \left(\frac{d\nu_n^2}{4\pi a^2}\right)\left\{\frac{Y}{3\rho\left(1-\sigma^2\right)}\right\}^{1/2} \qquad (3.20.2)$$

where $\nu_1 = 1.015\pi$ $\nu_2 = 2.007\pi$ $\nu_3 = 3.000\pi$ $\nu_n \xrightarrow[n\to\infty]{} n\pi$. The mean surface displacement amplitude of the plate is given by

$$\langle\zeta\rangle \xrightarrow[\omega\to 0]{} \left(\frac{\left(1-\sigma^2\right)a^4}{16Yd^3}\right)p_a \tag{3.20.3}$$

For the stainless steel plate which forms the equatorial surface of the hemisphere if $a = 66$ mm, $d = 45$ mm, $Y = 200$ GPa and $\sigma = 0.27$, the fundamental resonance frequency would be expected to occur at 33 kHz and the low frequency displacement is about 0.06 pm Pa^{-1} which is just 2.4 μm at 40 MPa. With a fundamental frequency at about 33 kHz the radial modes of the gas are sufficiently removed from f_1 to be largely unaffected and the correction given by equation (3.19.2) is valid. However, the equatorial plate is not uniform (holes are required to accommodate the source transducer and gas inlet pipe), so the shell resonance could occur at a much lower frequency near frequencies of the low order modes rendering equations (3.19.1) and (3.19.2) invalid.

(3.21) Holes in Resonator Wall

A hole in the wall of a resonator will cause a perturbation to the resonance modes of a gas due to the difference in the specific acoustic admittance over the area of the opening to that of the shell wall, given by equation (3.16.17). The microphone and source transducers and the gas inlet tube are necessary holes in the wall of the resonator and may be regarded as tubes that form small waveguides. The type of tube will normally fall into one of the following categories; an open flanged tube, an open unflanged tube, or a closed tube which may or may not be terminated by a small volume; the specific acoustic admittance will be different for each, as shown by equations (3.21.10), (3.21.13) and (3.21.14).

For a hole in the wall of a spherical surface $r/a = 1$ always, so the wavefunction is constant over the area of the opening and the correction is simple. However, for a hole in the equatorial wall of a hemispherical shell, the wavefunction varies over the area of the hole (because r/a is changing) and so the correction is more complicated.

For the general case, the shift in resonance frequency Δf_o and contribution to the halfwidth g_o caused by a hole is given by

$$\Delta f_o + ig_o = \frac{iy_o \iint_{S_o} \left|\phi_N(r_s)\right|^2 dS_o}{2V\Lambda_N^0} \tag{3.21.1}$$

where y_o is the specific acoustic input admittance of the opening and S_o is the surface of the hole. The surface integral for the opening may be evaluated and for a hole in a spherical wall, where $r/a = 1$ over all S_o,

$$y_o \iint_{S_o} \left|\phi_N(r_s)\right|^2 dS_o = y_o a^2 j_0^2(\nu_{0n}) \int_0^{2\pi} d\xi \int_0^{\pi} \sin\theta \, d\theta \tag{3.21.2}$$

$$= 4\pi a^2 y_o \, j_0^2(\nu_{0n})$$

Using the normalisation constant given by equation (3.14.15), and the corrections to the resonance frequencies and halfwidths

$$\Delta f_o + ig_o = iy_o \frac{4\pi a^2 \, j_0^2(\nu_{0n})}{4\pi a^3 \, j_0^2(\nu_{0n})} \tag{3.21.3}$$

$$= \frac{iy_o}{a}$$

yields

$$\Delta f_o + ig_o = \left(\frac{u}{2\pi a}\right)\left(\frac{\Delta S}{4\pi a^2}\right) iy_o \tag{3.21.4}$$

Where $(\Delta S/4\pi a^2)$ is the ratio of the area of the hole to the surface area of the shell. For an opening in the equatorial surface, the surface integral is given by

$$y_o \iint_{S_o} \left|\phi_N(r_s)\right|^2 dS_o = y_o \left\{P_l^m(0)\right\}^2 \int_0^a r \, j_l^2(\nu_{ln} \, r/a) \, dr \int_0^{2\pi} d\xi \tag{3.21.5}$$

$$= 2\pi \, y_o \left\{P_l^m(0)\right\}^2 \frac{a^2}{2} \left\{\frac{1 - l(l+1)}{\nu_{ln}^2}\right\} j_l^2(\nu_{ln} \, r/a)$$

For radial modes where $l = 0$ and $P_0^0(cos\theta) = 1$, the surface integral is given by

$$y_o \iint_{S_o} \left|\phi_N(r_s)\right|^2 dS_o = y_o \, \pi a^2 \left\{\frac{j_0^2(\nu_{0n} \, r/a)}{\nu_{0n}^2}\right\} \tag{3.21.6}$$

The normalisation constant is given by equation (3.14.15), and by combination with equations (3.21.1) and (3.21.6) the correction to the resonance frequencies and halfwidths is

$$\Delta f_o + ig_o = \left(\frac{i\ y_o}{2a\ \nu_{0n}^2}\right)\left\{\frac{j_0^2(\nu_{0n}\ r/a)}{j_0^2(\nu_{0n})}\right\} \tag{3.21.7}$$

By comparison with the sphere this gives the correction to frequencies and halfwidths for a hole in the equatorial plate as

$$\Delta f_o + ig_o = \left(\frac{u}{2\pi a}\right)\left(\frac{\Delta S}{\pi a^2}\right)\left(\frac{1}{2\nu_{0n}^2}\right)\left\{\frac{j_0^2(\nu_{0n}\ r/a)}{j_0^2(\nu_{0n})}\right\} i\ y_o \tag{3.21.8}$$

Where $(\Delta S/\pi a^2)$ is the ratio of the area of the hole to the surface area of the equatorial plate. The value taken for $j_0^2(\nu_{0n}\ r/a)$ for a hole with finite size is given by the integration of this function over the area ΔS_o.

As mentioned previously, the specific acoustic admittance of the opening y_o depends on conditions at the termination of the tube. In the regime where only plane waves can propagate, the specific acoustic admittance is constant over any cross-section of the tube and y_o may be expressed in terms of the propagation constant of plane waves and the value of the specific acoustic admittance at the termination of the tube, denoted by y_L. Consideration of the standing wave pattern and imposition of the boundary conditions at the ends of the tube gives the admittance at the end of the tube as

$$y_L = -i\ tan(i\Phi_L) \tag{3.21.9}$$

and that at the opening as

$$y_o = i\ \tan(\kappa_{KH} L - i\Phi_L) \tag{3.21.10}$$

where the parameter Φ_L characterises the terminal admittance. The Kirchoff-Helmholtz propagation constant, is given by

$$\kappa_{KH} = (\omega/u) + (1-i)\alpha_{KH} \tag{3.21.11}$$

with the Kirchoff-Helmholtz tube attenuation constant, for a tube of radius r_o, being given by

$$\alpha_{KH} = \frac{(\gamma-1)\delta_h + \delta_s}{r_o} \tag{3.21.12}$$

The microphone transducer in the spherical wall and the source transducer in the equatorial wall are considered to be closed tubes. In this case, the end remote from the

resonator is required to be closed by a rigid termination at which the reflection coefficient is unity so that the specific acoustic admittance is zero at the end but at the opening it is

$$y_o = i \tan\left(\kappa_{KH} L\right) \tag{3.21.13}$$

A small correction may also be made to this expression to account for a tube which is terminated by a small volume [52].

The gas inlet tube is an open tube which is flanged at the end remote from the resonator. In this case the specific acoustic admittance at the opening is approximated by

$$y_o = -i \cot\left(\kappa_{KH} L\right) \tag{3.21.14}$$

which is applicable for a tube open to free space. Small corrections may be made for flanged or unflanged conditions at the end of the tube and this is discussed in detail in reference [52]. It was noted by Goodwin [77] that for an open tube of length $1.023a$, that the radial acoustic resonances lie between resonances of the tube, and so by careful choice of tube length the inherent perturbations may be minimised.

(3.22) Annular Slots

Correction terms due to slots are used to estimate the effects of annular slots surrounding plugs and transducers fitted closely in the cavity wall or to estimate the effect of a small opening at the junction of two hemispheres (for a spherical resonator) or between a hemisphere and an equatorial plate (for the hemispherical resonator). An annular slot may be modelled as parallel semi infinite plates separated by a distance d and extending to a depth L where they are closed by a rigid wall.

The perturbation to the resonance frequencies and halfwidths of the radial modes from an annular slot is given by

$$\Delta f_o - i g_o = \frac{-i y_{o,s} S_o}{4\pi a^2}\left(\frac{u}{2\pi a}\right) \tag{3.22.1}$$

for an opening in a spherical wall and by

$$\Delta f_o - i g_o = \frac{-i y_{o,s} S_o}{\pi a^2}\left(\frac{u}{2\pi a}\right) \tag{3.22.2}$$

for an opening in an equatorial plate. The specific acoustic admittance of the resonator surface at $r = b$ (where b is the radius of the slot) is then given by

$$y_{o,s} = \left\{ \frac{(1+i)(3\gamma)^{\frac{1}{2}}}{(6\delta_s/d)} \right\} \tanh\left[(1+i)(\delta_s/d)\, kL(3\gamma)^{\frac{1}{2}} \right] \qquad (3.22.3)$$

In contrast with the sharp resonances of a tube, the resonances in a narrow slot are highly damped and $y_{o,s}$ varies slowly with frequency.

The effect of an annular slot between the hemispherical shell and its equatorial plate is discussed in detail in chapter 7.

CHAPTER 4 Apparatus

(4.1) The Hemispherical Resonator

A hemispherical acoustic resonator with a nominal radius of 37 mm was turned from a billet of austenitic stainless steel 321, chosen for its ability to withstand high pressures and for its high acoustic impedance. The interior of the resonator was hand polished with emery paper to remove tooling marks and fine polished with alumina paste to achieve a near-mirror finish. Holes for the gas inlet tube and for the source transducer were drilled into the top plate and a hole for the microphone transducer was drilled into the bottom of the hemisphere; the positioning of the holes is discussed in more detail in section (4.5) and details of the transducer assemblies are reported in sections (4.6) and (4.7). Figure (4.1.1) shows a cross-section through the acoustic resonator.

(4.2) Pressure Vessel Design

The pressure vessel formed an integral part of the resonator which was designed in accordance with a number of pressure vessel codes and safety regulations [79 -101, 105, 107], in order that it could be operated at pressures up to 40 MPa.

A simple arrangement for the pressure vessel is for an end plate to be bolted to a hemispherical base. This is classified as a blind flange with the gasket positioned entirely within the bolt circle; as illustrated by figure (4.2.1).

Based on this arrangement, calculations were made to determine the minimum required thickness of the shell and the flange. The minimum bolt area required and the adequacy of the threads were also assessed.

Working with a nominal internal radius of 40 mm for the hemisphere, several preliminary calculations were performed. These calculations are in accordance with the unfired pressure vessel code, section viii, 1962 [101]. According to the code, the analysis for the hemispherical shell, in this case, is identical to that of the corresponding spherical shell.

Figure (4.1.1): Cross-section through the hemispherical acoustic resonator

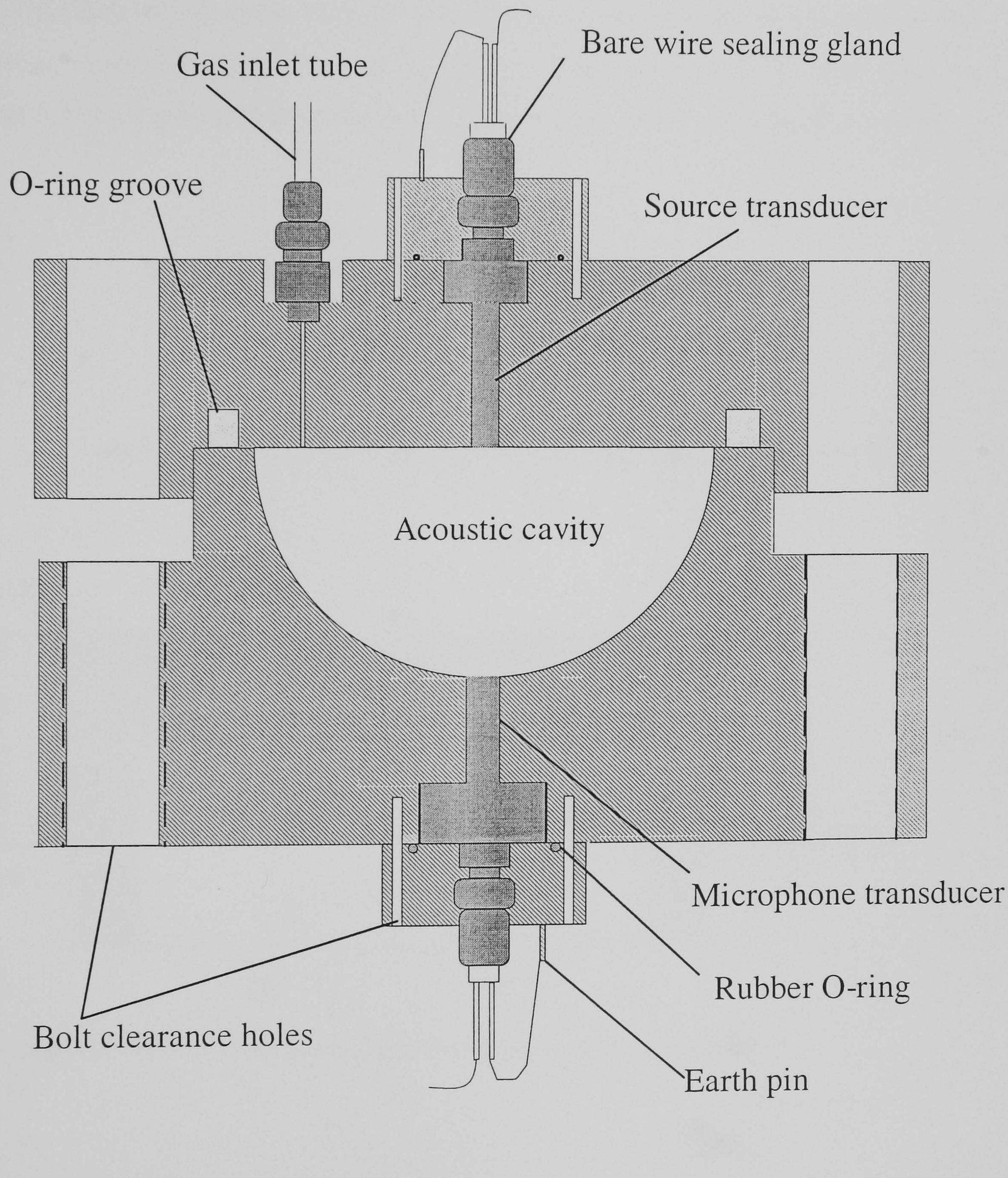

For spherical vessels when the thickness of the shell does not exceed $0.356a$ or p does not exceed $(0.665\ S_{FO} E_J)$, the following formula applies,

$$t = \frac{pa}{(2S_{FO}E_J - 0.2p)} \tag{4.2.1}$$

Here t is the minimum required thickness of the shell, p is the proposed internal pressure, a is the inside radius of shell course under consideration, S_{FO} is the maximum allowable stress value at design temperature and E_J is a joint efficiency factor (which will be unity since the hemisphere has no joints). With $p = 40$ MPa, $a = 40$ mm, $S_{FO} = 207.9$ MPa and $E_J = 1$ a wall

Figure (4.2.1): Blind flange entirely within gasket circle

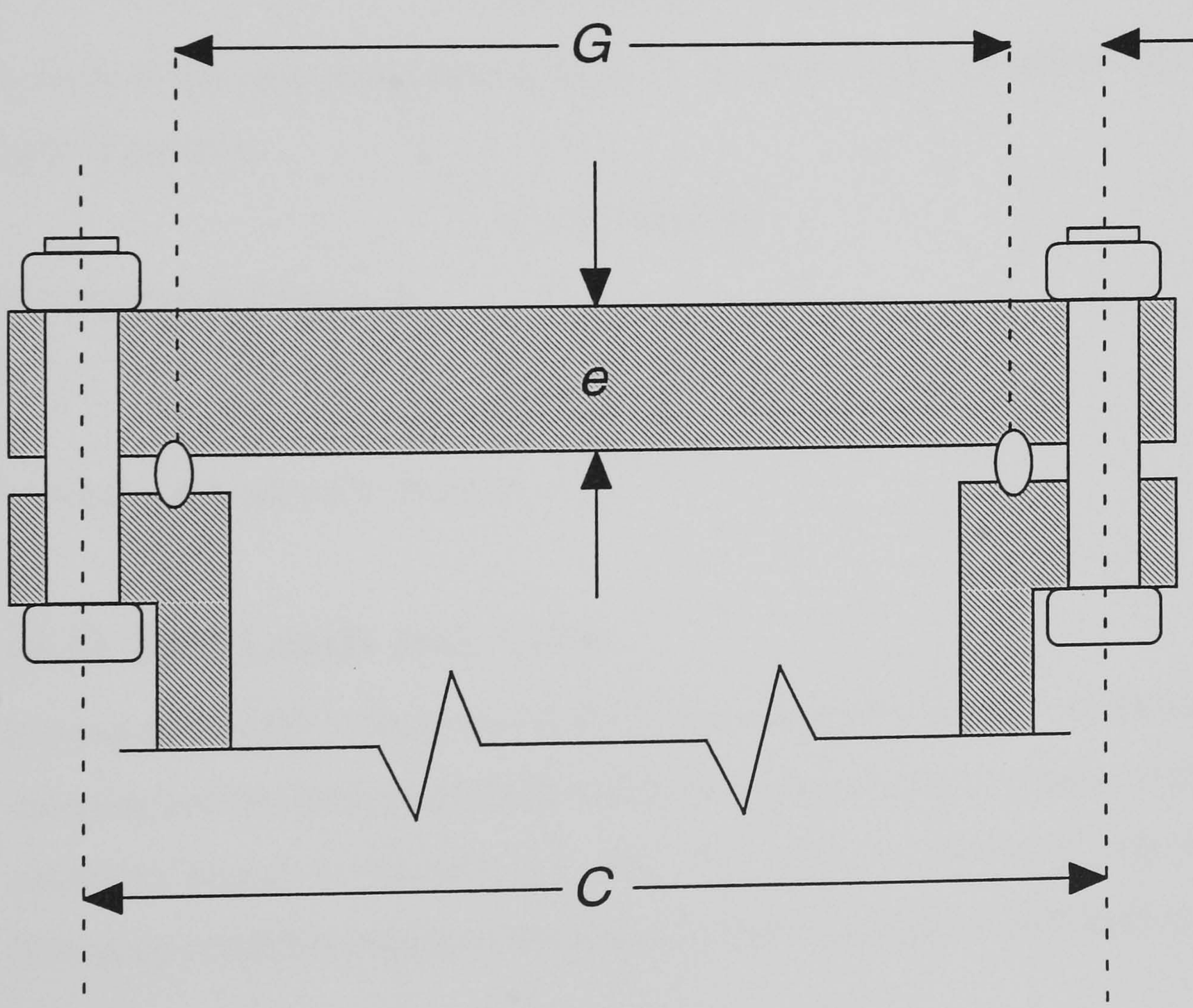

thickness of at least 4 mm is required. In practice, the wall was much thicker to compensate for holes in the resonator wall [86, 93] and to accomodate the threaded bolt holes.

For a bolted flange arrangement, the minimum thickness for a circular end plate, in accordance with BS 5500, is given by the following equation,

$$e = \left\{ \frac{0.3G^2 p}{S_{FO}} + \frac{1.909 W_{m1} h_G}{G S_{FO}} \right\} \tag{4.2.2}$$

Here e is the minimum thickness of the end plate, G is the diameter at the location of gasket load reaction, W_{m1} is the minimum required bolt load for operating conditions, computed from equation (4.2.3) and h_G is the radial distance from the gasket load reaction to the bolt circle, defined by equation (4.2.6).

$$W_{m1} = H_p + H \tag{4.2.3}$$

where H_p is the compression load on the gasket to ensure a tight joint and is given by

$$H_p = 2b \times 3.14 G m p \tag{4.2.4}$$

in terms of the basic gasket seating width b[1], the gasket factor m and the total hydrostatic end force H given by,

$$H = 0.785 G^2 p \tag{4.2.5}$$

The equation defining h_G is,

$$h_G = \frac{(C - G)}{2} \tag{4.2.6}$$

where C is the bolt circle diameter.

(4.3) Bolt Loads and Areas

It is required by BS 5500 section (3.8.3.2) that bolt loads and areas be calculated for both the operating and the bolting-up conditions for the design of a safe pressure vessel. The operating conditions require a minimum bolt load W_{m1} which is calculated from equation (4.2.3). Bolting-up conditions require a minimum bolt load W_{m2} which is calculated from the following equation

$$W_{m2} = 3.14 b G y \tag{4.3.1}$$

---

[1] $b = b_0$ when $b_0 \leq 6.3$ mm; $b = 2.52 \sqrt{b_0}$ when $b_0 > 6.3$ mm.

where y is the gasket or joint-contact-surface minimum design seating stress, (see table 4.3.1 for suggested values).

The minimum bolt area A_m is then determined for W_{m1} or W_{m2} using the nominal bolt stress at the temperature appropriate to the two conditions, *i.e.* A_m is the greater of A_{m1} or A_{m2} where,

$$A_{m1} = \frac{W_{m1}}{S_b} \tag{4.3.2}$$

and

$$A_{m2} = \frac{W_{m2}}{S_a}. \tag{4.3.3}$$

S_b and S_a are the bolt nominal design stresses at the design temperature and atmospheric temperature respectively. It is sufficient for our temperature range to take $S_a = S_b$ .The actual bolt area A_b should not be less than A_m.

In order to minimise the plate thickness and the bolt loads a viton O-ring was deemed most suitable for the proposed experimental conditions.

The maximum number of bolts B_{max} possible was calculated from

$$B_{max} = \frac{\pi C}{B_{sp}} \tag{4.3.4}$$

where B_{sp} is the bolt spacing. For a given bolt there is a nominal root area based on the mean of its major and minor diameters. If the calculated minimum required bolt area A_m is divided by the root area the minimum number of bolts of this type is calculated. Tables of these root areas for various bolts are given in reference [92].

Various dimensions describing the bolts and their corresponding nuts was also required for the calculations, these dimensions may be found in reference [85]. The most suitable bolts were found to be metric M20 (2.5 mm) bolts. For the design conditions stated previously, the total required minimum bolt area is $A_m = 1222.5$ mm^2 which implies a minimum of six M20 bolts. It is possible to fit nine M20 bolts on this bolt circle and the actual bolt area $A_b = 2027$ mm^2 provided an additional safety factor of 1.7.

Table (4.3.1): Gasket properties

Facing Sketch	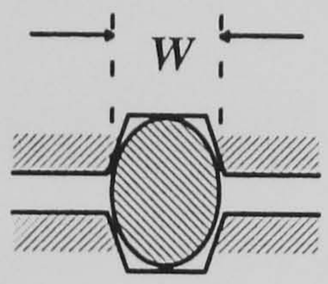	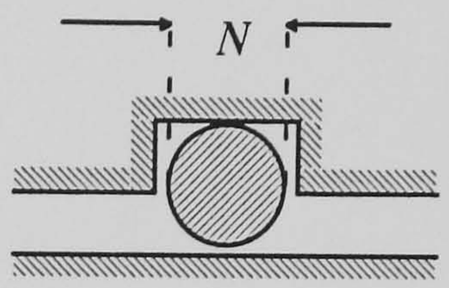
Gasket Material	Iron or soft steel Monel or chrome Stainless steels	Rubber O-rings
Gasket Factor m	5.50, 6.00 and 6.50 respectively	0 to 0.25
Min. Design Seating Stress y	124, 150 and 179 respectively	0.7 to 1.4
Basic Gasket Seating Width b_0	$W/8$	$N/2$

The adequacy of the thread was assessed by the following equation

$$p = \left\{ \frac{8 N d_B L_t \sigma_y G}{G^2 C} \right\} \tag{4.3.5}$$

where N is the number of bolts, d_B is the diameter of the bolt and L_t is the length of engaged thread; ideally this is taken as the length of one thread, because most of the stress is concentrated here. It has been estimated that the stress in the first thread is *3.5* times that of the average [92, 106]. With $N = 9$, $d_B = 20$ mm, $\sigma_y = 207.9$ MPa, $G = 87$ mm, $C = 137$ mm and $L_t = 2.5$ mm, this gave a maximum working pressure of 64 MPa, which is well above the proposed working pressure and gave confidence in the ability of the bolts to perform at 40 MPa.

Further constraints were placed on the final design by keeping the overall size to a minimum (and hence the mass and the heat capacity) but the internal radius to a maximum (to achieve optimum surface area to volume ratio in the resonator).

(4.4) Dilation of the Pressure Vessel

The dilation, or radial growth, of a pressure vessel is given in reference [88] by,

$$\delta = a\left\{\frac{\sigma_2}{E} - \frac{\mu\sigma_1}{E}\right\} \tag{4.4.1}$$

where δ is the total dilation, σ_1 and σ_2 are the principle stresses, E is the modulus of elasticity, μ is Poisson's ratio and a is the internal radius. An approximation to the principal stresses in the hemispherical resonator may be given by the following equations

$$\sigma_1 = \frac{pa}{2h} \tag{4.4.2}$$

and

$$\sigma_2 = \frac{pa}{h} \tag{4.4.3}$$

where h is the wall thickness. Substituting into equation (4.4.1) gives,

$$\delta = \left(\frac{pa^2(2-\mu)}{2hE}\right) \tag{4.4.4}$$

This is the formula appropriate for a cylindrical pressure vessel which was considered closer geometrically to our pressure vessel than a spherical vessel. It is not intended to give an accurate measurement of the actual dilation of the hemisphere but rather, an approximate order of magnitude. At 40 MPa the hemisphere may be estimated to dilate by approximately 0.01 mm. This corresponds to changes in frequency of 295 ppm at 40MPa (for the (0,2) mode in Argon at 300 K). Corrections to the frequency back to the zero-pressure radius are made to account for the dilation and this is discussed more fully in chapter 7.

(4.5) Positioning of Inlet Tube and Transducers

The hemispherical resonator retains many of the advantages characteristic of the sphere. An additional feature, however, which makes it more suitable for high pressure measurements of

the speed of sound is the possible location of the transducers. In particular, one of the transducers (and it doesn't matter which) may be placed in the centre of the equatorial surface *i.e.* at $r/a = 0$. The significance of this position may clearly be seen by considering the radial wavefunctions of the modes it is intended to study; that is, the first four radial modes. The wavefunctions give us a representation of the spatial distribution of acoustic energy in the cavity. The squared wavefunctions of the first four radial modes $(0,n)$; n = 2,3,4,5 and their average is shown in figure (4.5.1). The acoustic pressure is proportional to ϕ_N^2, so by positioning the source transducer at $r/a = 0$, very intense signal strengths are observed. The microphone transducer was placed directly opposite in the spherical wall (*i.e.* at $r/a = 1$), which is a position where the acoustic density is much lower for all the radial modes (and is conventionally the position in a spherical resonator).

Figure (4.5.1): Spatial distribution of acoustic energy for the first four radial modes

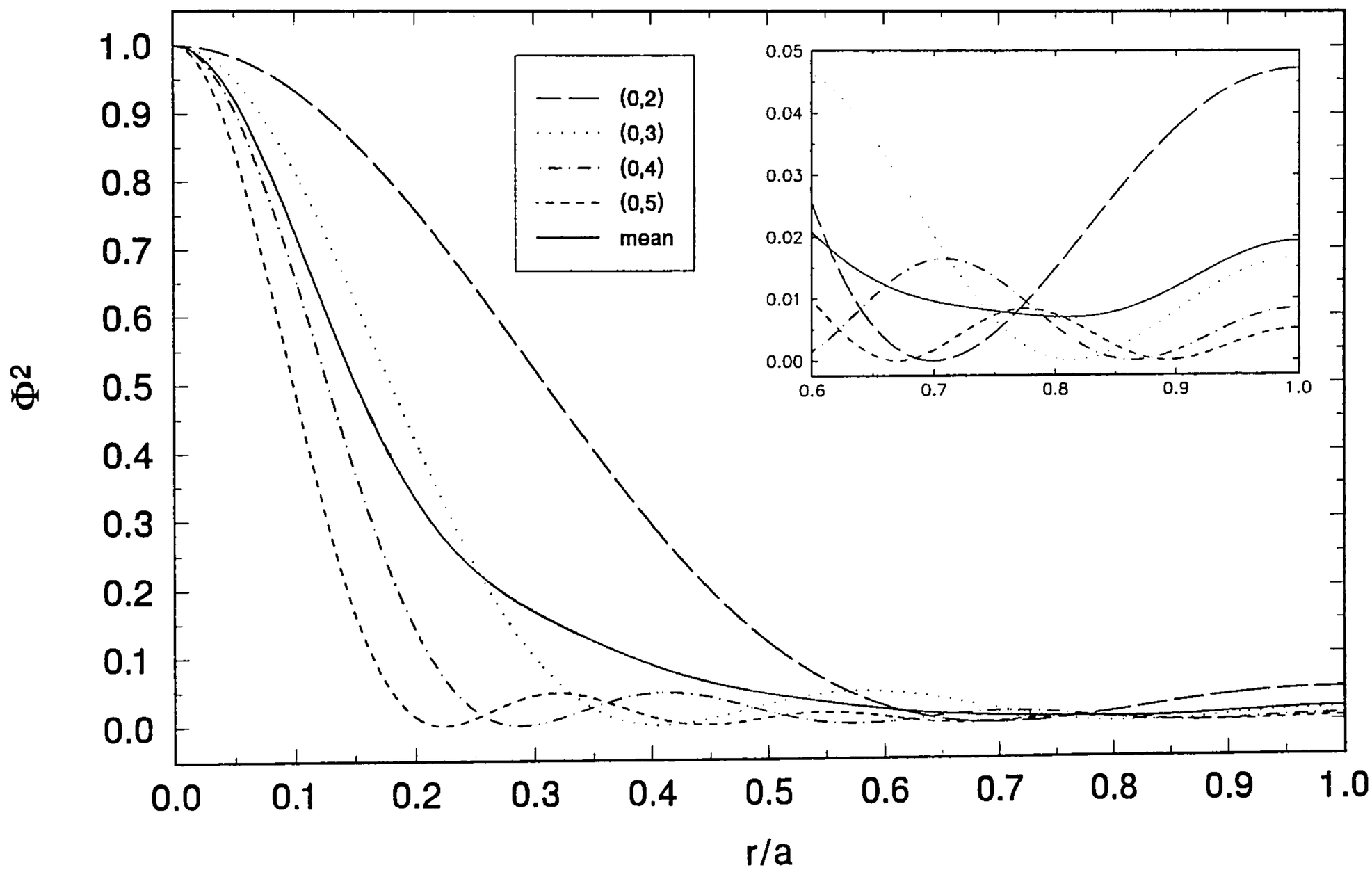

The position of the gas inlet tube is chosen to cause minimum perturbation and should therefore be placed at a position where ϕ_N^2 is a minimum for all modes. Figure (4.5.1) suggests that the inlet tube should be placed at $r/a \approx 0.8$ where the average of ϕ_N^2 is at its smallest. In order to reduce the perturbation from the inlet tube still further its length was chosen to be identical to the radius of the hemisphere. This exploits the fact that the eigenvalues are approximately equal to $(n - \frac{1}{2})\pi$; so when $L = a$, $Re\,(iy_0)$ vanishes near to the frequency of each radial mode. The actual length may be modified to take account of departures of the eigenvalues from their unperturbed values.

Wide-bandwidth transducers were employed as the design incorporates the transducers to form parts of the wall of the resonator. Thus a high acoustic impedance is required so that the properties of the cavity are not perturbed too much.

(4.6) Source Transducer

The source transducer, pictured in figure (4.6.1) consisted of a brass housing (**H**) which screwed into the top plate of the resonator so that the surface was flush with the interior of the resonator. The face of this housing had a 3.0 mm diameter hole drilled through it onto which a thin polarised membrane (**M**) was clamped into position by means of a Teflon insert (**T**) and a threaded ring (**R**). The backplate (**B**), which was the same diameter as the hole in the housing, had five holes 0.5 mm deep and 0.3 mm diameter drilled into its surface to allow pressure equalisation on either side of the membrane, thereby increasing the compliance of the element and ensuring that the normal modes of the cavity were not perturbed by natural resonances of the membrane. The electret membrane consisted of aluminized polyester, the metal layer of which was held in contact with the brass housing, this in turn was held at ground potential. Tension of the membrane on the backplate was achieved by means of a spring (**S**) which had a spring constant of approximately 0.3 Nm^{-1}. The tension may be varied by turning the insulated nut (**N**) and feedthrough (**F**) to optimise the signal. The feedthrough was specially shaped so that the wire could be easily threaded into position from the sealing gland. The back electrode was excited with an a.c. signal of about 60 V rms with a d.c. bias of approximately 300 V. In this way the membrane was driven by the electrostatic force to produce sound at the frequency

of excitation. The whole ensemble was pressure sealed using a bolted flange with viton O-ring into which a bare-wire sealing gland (supplied by 'Conax') was mounted via a tapered thread.

Figure (4.6.1): Source transducer assembly

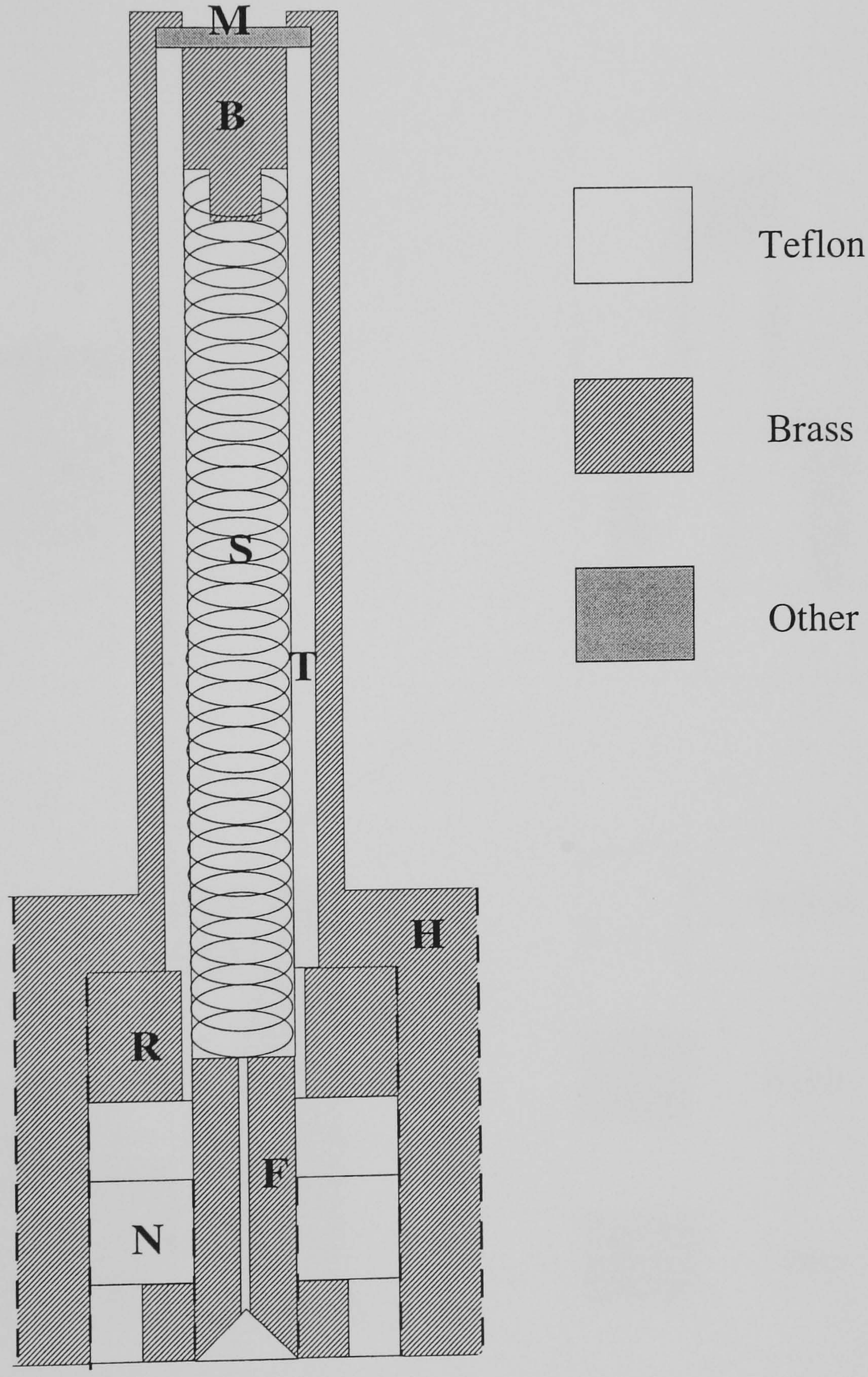

(4.7) Microphone Transducer

The microphone transducer consisted of a brass housing which screwed into the base of the resonator. Its upper surface had the same radius of curvature as the interior of the resonator so that it was flush with the spherical surface when in position; it also had an aperture of 6 mm

Figure (4.7.1): Microphone transducer assembly (inset shows alternative arrangement)

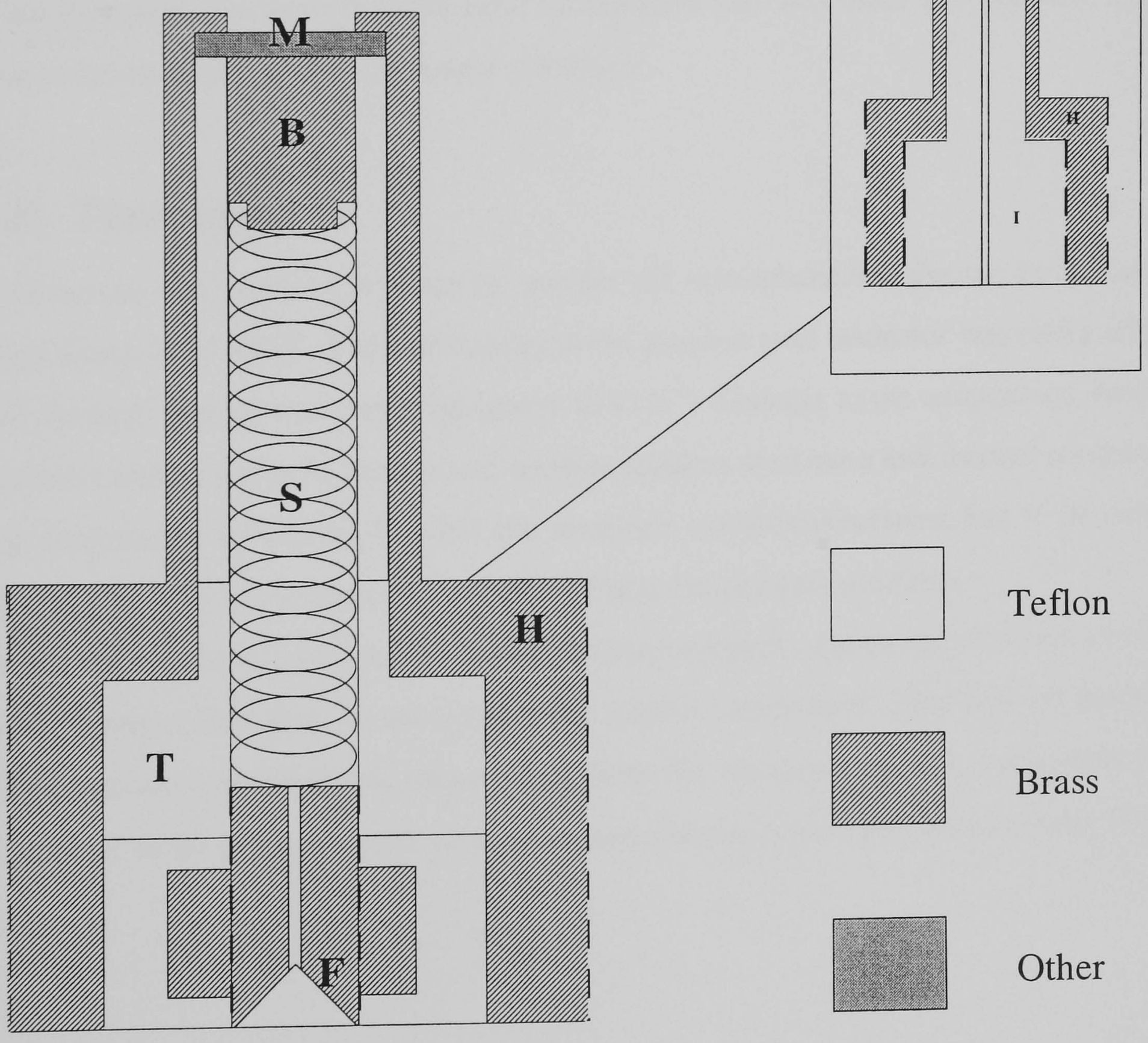

diameter through which the membrane (**M**) distended. The membrane material had a permanent dielectric polarisation so that no d.c. bias was required and the active area was deliberately kept large so there would not be large attenuation of the sound amplitudes at high pressures. Tensioning of the membrane, as in the source transducer, was acheived by a spring (**S**) which rested on the backplate (**B**), the tension could be varied by tightening the feedthrough (**F**). A preamplifier was required very close to the transducer to prevent division of the signal by the coaxial cable and a simple JFET circuit was soldered directly to the electrical feedthrough pin. The housing was also designed so that it could directly contain a small commercial microphone (see inset of figure 4.7.1): these microphone inserts consist of a permanently polarised polyvinylidene fluoride disc as a membrane and a JFET preamplifier within a small casing and are therefore very efficient and easily assembled in the housing. For the measurements discussed it is this latter arrangement that was used. The pressure seal was made in the same way as with the source transducer.

(4.8) Thermostat

A thermostat was required in order to operate the hemispherical resonator isothermally at temperatures up to 400 K. Thermal stability in the stainless steel resonator was easily achieved since the heat capacity was very large (about 10 kJ K^{-1}). Changes to the temperature, however, required relatively powerful heaters and, because stainless steel has a low thermal conductivity, large temperature differences between the resonator and its environment had to be carefully controlled in order to avoid the development of large temperature gradients.

The thermostat consists of a series of nested aluminium shells, the design of which was based on the theory of heat flow in and between the various components. Heat flow by conduction and convection constituted the major losses from the resonator and the components of the thermostat, whilst radiation losses were eliminated; the results are summarised in table (4.12.2).

(4.9) Construction of thermostat

The configuration of the thermostat is shown in figure (4.9.1) while the relevant dimensions are given in table (4.9.1). The two innermost shields (① and ②) were constructed from aluminium tube but the outermost shield (shield ③) was rolled from 1.6 mm thick aluminium sheet because its overall dimensions were so large. The endplates for all the shields were made using 6.35 mm thickness aluminium plate and were each bolted into place onto the ends of each cylinder. Aluminium was chosen for the shields of the thermostat as it has a high thermal conductivity and high thermal diffusivity, which gave even temperature distribution throughout the material and minimised the thermal time constants; aluminium also has a relatively low density which kept the total mass of the shields to a minimum.

Due to the substantial weight of the resonator a conventional suspended arrangement was not employed as this would be very difficult to assemble. Instead, the endplate of the outermost shield rested directly on the frame and heat bricks were then used as supports for the endplate of shield ②. High density polypropylene tubing was then utilised as support between the second and the first shields and also between the first shield and the resonator. This arrangement considerably eased the assembly of the thermostat and eliminated potential heat leaks resulting from metal supports. The shields were each positioned concentrically around the resonator; with expanded polystyrene as the insulation between each shield. The thermal conductivities of all the materials used are given in table (4.9.2).

	Resonator	**Shield ①**	**Shield ②**	**Shield ③**
O.D. / mm	165.5	190.5	279.4	533.4
Length / mm	116.5	254.0	342.9	596.9
Thickness / mm	------	6.4	12.7	1.6
Axial Spacing / mm	68.8	44.5	127.0	------
Radial Spacing / mm	6.2	44.5	127.0	------

Table (4.9.1): Thermostat dimensions

Figure (4.9.1): Thermal environment of the hemispherical resonator

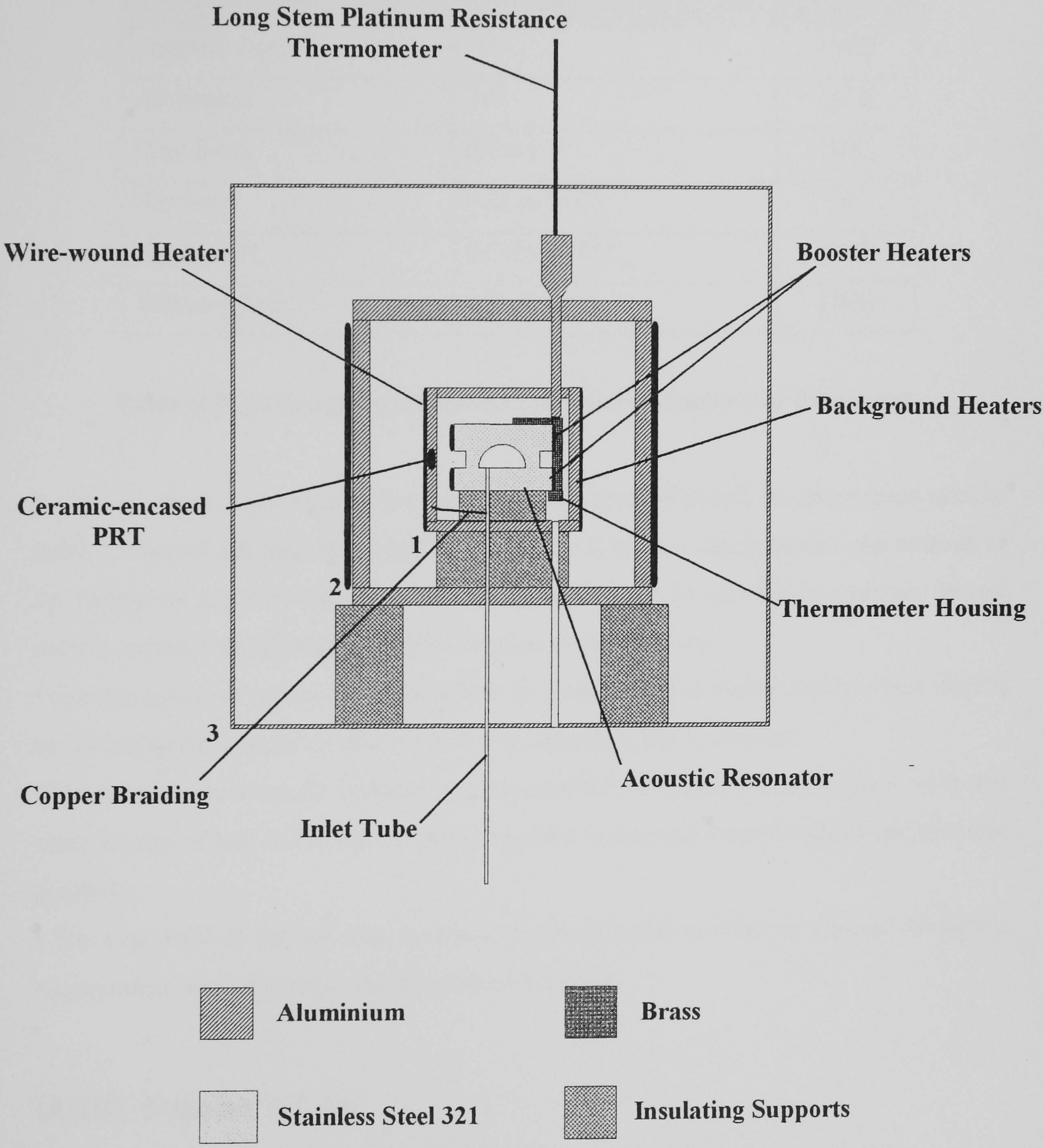

Material	Thermal Conductivity at Operating Conditions / $Wm^{-1}K^{-1}$	Reference
Stainless Steel 321	19	[102]
Aluminium	150	[102]
Heat Brick	0.8 to1.2	[103]
Kaowool	0.04 to 0.078	[6]
Polystyrene	0.035 to 0.055	[103]
Polypropylene	0.2	[104]

Table (4.9.2): Thermal conductivities of materials used in the thermostat

In order to obtain a precision of about 10 ppm in the speed of sound, the temperature must be stable to about 6 mK although a stability of 1 or 2 mK is obviously preferable. An estimate of the thermostat's performance and the criteria which must be satisfied to maintain thermal stability on this scale is provided by consideration of the following.

- The attenuation of radial and axial gradients by passive isolated shields, that is, where there is no controlled heating and no allowance for any connecting pipes, wires etc.
- The heat flow between the various components of the thermostat (including pipes, wires and other sources of heat leaks) and the power required to maintain thermal stability and eliminate gradients.
- The evaluation of thermal time constants in the resonator in order to evaluate the power requirements when changes to the temperature are made.

(4.10) Fourier's Law

Fourier's law of heat flow for a perfectly lagged system, in one dimension, is given by

$$J = \frac{-kA}{L}\Delta T \qquad (4.10.1)$$

where J is the heat transfer rate, κ is the thermal conductivity of the material, A is the cross-sectional area through which conduction is occurring, L is the conductor length and ΔT is the temperature difference across its ends. The attenuation of axial and radial gradients through the thermostat may be assessed using this equation. Since Fourier's law for heat flow is analogous to the equations for electrical current a corresponding thermal resistance may be given by

$$R_t = \frac{L}{k\,A} \qquad (4.10.2)$$

for axial heat flow, and

$$R_t = \frac{\ln\left(r_2/r_1\right)}{2p\,L\,k} \qquad (4.10.3)$$

for radial heat flow. The thermal resistances obey the same laws of summation as electrical resistors do when arranged in series and parallel. Each shell may be regarded as a combination of thermal resistors in series and parallel as illustrated by figure (4.10.1).

The temperature drop across any component may then be calculated from the equivalent thermal circuit. Calculations were performed assuming that

(i) The algebraic sum of heat flow into a junction is zero.

(ii) In any closed loop the algebraic sum of the ΔT's is equal to the algebraic sum of the products of heat flow and thermal resistance.

(iii) Thermal resistors in parallel have the same temperature drop across them.

(4.11) Axial Temperature Gradients

Equations (4.10.1) and (4.10.2) together with the rules given above and the thermal circuit given in figure (4.11.1) enabled the attenuation of axial temperature gradients between subsequent shields to be calculated and the results are summarised in table (4.11.1). The temperature gradient per unit length is denoted by ∇.

Figure (4.11.1): Thermal resistances

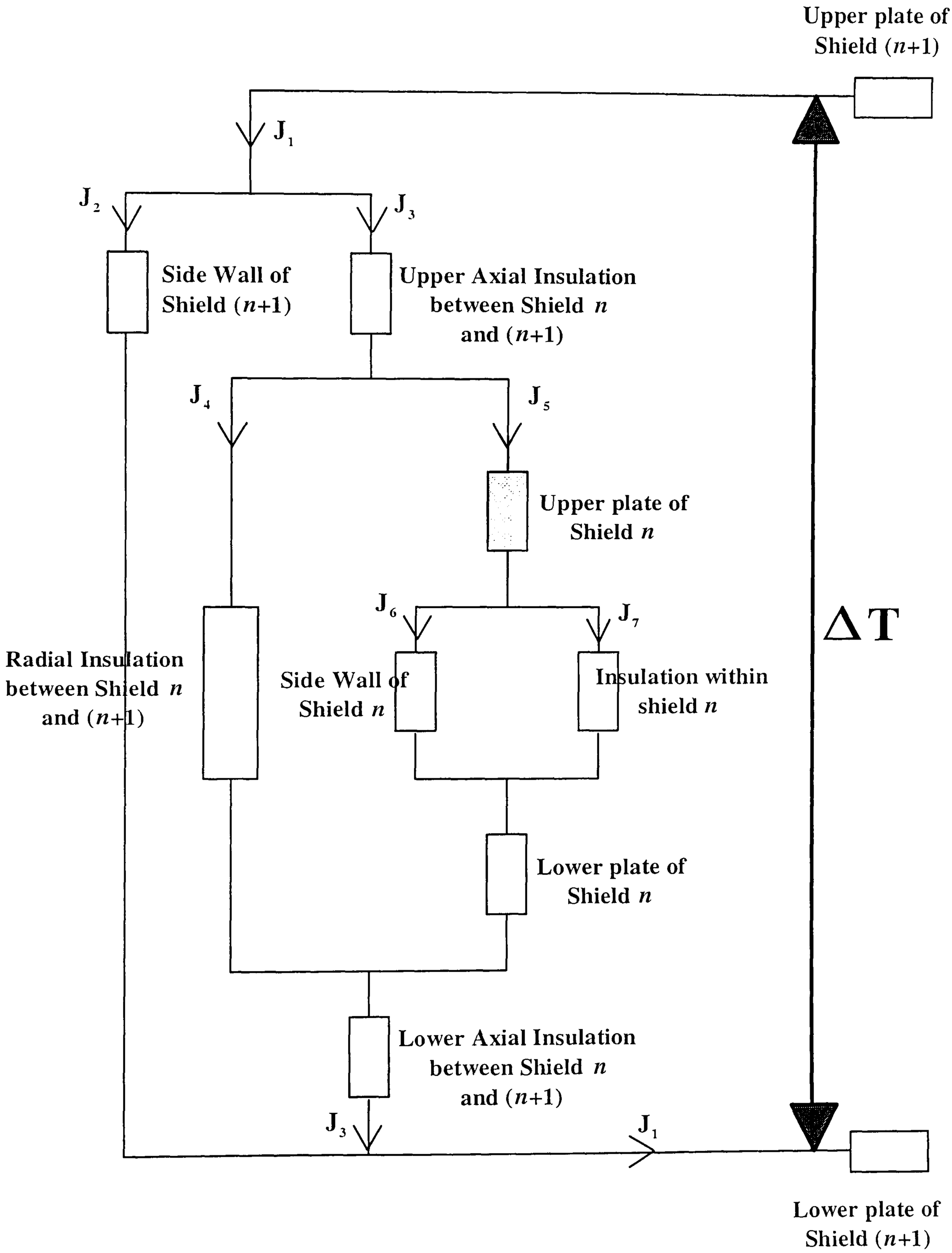

	Shield ③	Shield ②	Shield ①	Resonator
∇ / (K·m^{-1})	16.75	0.648	0.026	0.00012
ΔT / K	10	0.181	0.005	0.02×10^{-3}
Attenuation	26	25	218	2

Table (4.11.1): Axial temperature gradients

The calculations assume an axial temperature gradient of 10 K across the end-plates of shield ③ and assumes the radial temperature to be independent of the axial heat flow. This assumption is not strictly true and a more detailed analysis in three dimensions is possible [54], although several one-dimensional calculations performed in different directions are still useful for three-dimensional bodies especially in the case of thin shells. The attenuation quoted in the table refers to that provided by shield *n* and the insulation between shield *n* and (*n*-1). A further attenuation of at least a factor of 2 is expected between the surface of the resonator and the acoustic cavity.

(4.12) Power Requirements

The large heat capacities, which are given in table (4.12.1) for the various components, required considerable heater powers if changes in set-point temperature were to be achieved in a reasonable time.

Powerful booster heaters were attached directly to the surface of the hemispherical resonator in order to quickly achieve the setpoint temperature. These heaters were flexible silicone rubber heaters (25.4 mm by 510 mm) with a power input of 100 W at 240 V ('Watlow' 010200C2); they were attached to the cylindrical surface of the resonator using an RTV compound designed for this purpose.

In order to estimate the power requirements of the different components of the thermostat the heat flow between active shields was considered. The power requirements to maintain thermal equilibrium once the resonator had reached the set-point temperature were calculated by

Components	Heat Capacity/ kJ · K^{-1}
Resonator	10.1
Insulation between resonator & shield ①	6.4
Shield ①	2.4
Insulation between shield ① & shield ②	8.5
Shield ②	9.7
Insulation between shield ② & shield ③	151.9
Shield ③	31.9
TOTAL	**220**

Table (4.12.1): The heat capacities of the components of the thermostat

considering the worst case scenario, *i.e.* a temperature difference of approximately 60 K between the resonator and the local environment of the system. To maintain the resonator at this temperature without introducing it to unacceptable gradients, there needs to be an attenuation of the temperature between the resonator and its environment. Consideration of the heat flow between coupled active shields provides the basis of the discussion of the thermostat operation. The results for the total heat losses Q (radial (q_r) + axial (q_x)) are summarised in table (4.12.2) for temperature differences of 10 K between each component.

	Q / W	q_r / W	q_z / W
Resonator	1.24	0.38	0.86
Shield ①	1.36	1.20	0.16
Shield ②	1.46	1.32	0.14
Shield ③	2.52	2.20	0.32

Table (4.12.2): Heat losses in the thermostat

(4.13) Power Requirements Due to Heat Leaks

It was important to consider heat losses from pipes and electrical wires leaving the resonator as these may cause unacceptably large temperature gradients in the system. An estimate of the losses due to the stainless steel inlet tube (o.d.= 6.35 mm, i.d.= 3.86 mm) revealed non-negligible heat flow at temperature differences of 100 K and gradients across the resonator.

Copper braiding was used to isothermally link the inlet tube to shield ① and further up to shield ②, effectively heating the pipe. Additional heaters were also positioned on the underside of the endplate of shield ② in order to reduce the axial gradient.

Primary temperature control took place on shield ①. A ceramic encapsulated platinum resistance thermometer mounted on the shield acted as the primary control thermometer, whilst a wire wound element acted as the heat source. The wire-wound heater was mounted to the cylindrical surface of the shield by winding tightly to the surface and then held in position by aluminium strips screwed into the surface of the shield at six points along its length. To achieve a uniformity of 1 mK on the surface of the resonator then the maximum allowable gradient on shield ① is 0.98 $K\,m^{-1}$, restricting the power to about 6 W. Basic temperature control was provided by shield ② operated a few Kelvin below shield ① and controlled to 0.3 K. Background heating could be provided by shield ③ for the highest temperatures but was not always required and was used primarily as a passive shield and to hold the insulation in position.

The controller gave proportional and integral control which minimised overshoot and the temperature once at setpoint was stable to less than 1mK.

Due to electrical noise the temperature controller had to be switched off during the measurement of a data set but even at the highest temperatures the temperature was unchanged by at worst 2 mK as indicated by the thermometer, and was probably much less than this as the thermal time constants in the resonator were greater than those of the thermometer.

(4.14) Thermal Time Constants

The thermal time constants give us an estimate of the time required for a system to reach thermal equilibrium and is an important consideration after changes to the system are made (e.g. after an isentropic expansion of the gas to reduce the pressure). The time constant is given by

$$\tau/\mathrm{s} = \frac{1}{\alpha k_z^2} \tag{4.14.1}$$

where

$$k_z = \left(\frac{l\pi}{L}\right)^2 + \left(\frac{\chi_{mn}}{b}\right)^2 \tag{4.14.2}$$

and α is the thermal diffusivity of the material, which is 3.48×10^{-6} $m^2 s^{-1}$ for stainless steel 321 and 73×10^{-6} $m^2 s^{-1}$ for aluminium. For longitudinal flow,

$$k_z = \frac{l\pi}{L} \tag{4.14.3}$$

and so the time constant for longitudinal heat flow in the stainless steel resonator is approximately 352 s.

For the radial heat flow, from the edge of the resonator to the centre it is the (0,0,2) mode which is of interest. In this case

$$\chi_{02} = kb = 3.832 \tag{4.14.4}$$

and so the time constant for radial heat flow is about 148 s. The thermal time constants for the components of the thermostat were also calculated in this way and the results are summarised in table (4.14.1).

Components	τ_{rad} /s	$\tau_{end\text{-}end}$ /s	$\tau_{mid\text{-}end}$ /s
Shield ③	66.4	450.8	112.7
Shield ②	18.2	163.2	40.8
Shield ①	8.5	89.5	22.4
Resonator	148.1	352.3	88.1

Table (4.14.1): Thermal time constants

(4.15) Measurement of Temperature Gradients

The temperature gradients were measured in practice by placing type K thermocouples at strategic positions on the resonator and shields. The temperature difference on shield ① were never more than 20 mK; *i.e.* if there were temperature gradients across shield ① they were not detectable using 'type K' thermocouples. Additional thermocouples capable of detecting temperature differences of 1 mK were attached to various positions on the walls of the acoustic resonator. One such thermocouple was attached to a position on the resonator's external surface nearest to the acoustic cavity and which therefore most closely matched the 'true' temperature of the gas. Another was located on the thermometer well and a further two were attached at opposite poles of the resonator body. The temperature differences between these thermocouples was generally undetectable and even at the highest temperatures was never greater than 4 mK. These measurements provided a useful check of the ability of the thermostat to maintain stable conditions within the required accuracy.

(4.16) Spherical Acoustic Resonator

The spherical resonator employed for some of the measurements (chapter 8) was the 45 mm stainless steel resonator described in detail by Boyes in reference [59] and illustrated in figure (4.16.1). A brief description is included here for completeness.

The spherical cavity consisted of two hemispherical components, machined from stainless steel 321, which were welded together to form a pressure and vacuum tight seal. The resonator was pressure compensated *i.e.* the internal and external pressures were approximately equal. The pressure vessel [77] consisted of a cylinder with a threaded end closure and was designed to withstand pressures up to 20 MPa and temperatures up to 373 K. The sealing gasket used to seal the vessel was a viton O-ring suitable for the experimental conditions reported in chapter 8. Silver goop was used on the end-cap to prevent seizure and cold-welding of the threads.

Figure (4.16.1): The spherical acoustic resonator [59] used for the argon measurements reported in chapter 8

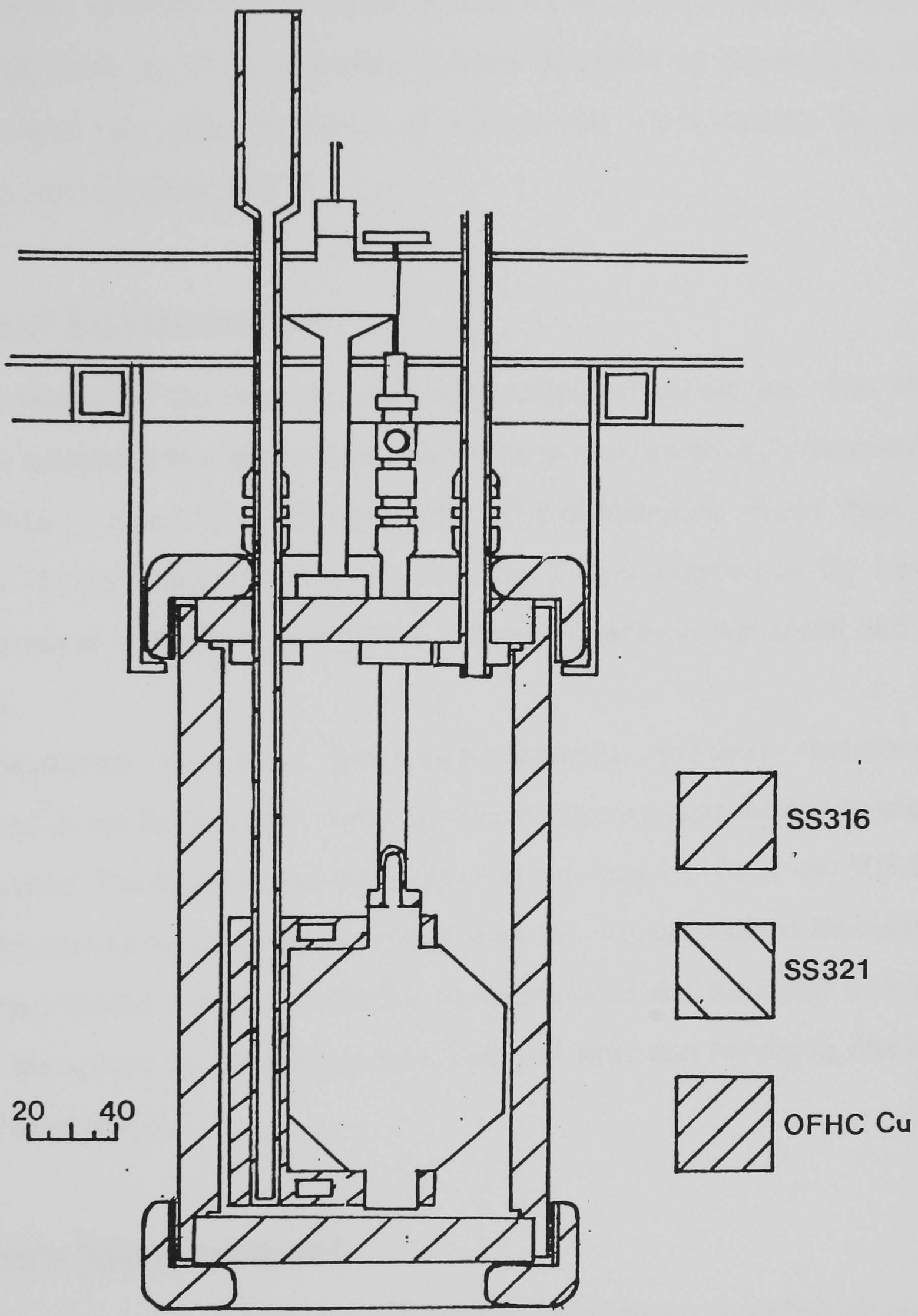

(4.17) Transducers used in Spherical Resonator

The source transducer employed and detailed in reference [59] was of the type described in section (4.6) and was used without modification to its design. The detector housing, however, was modified in order that it could accommodate a commercially available insert, rather than be made up of the assembly of parts described by Boyes [59]. Both transducers were sealed into place by means of indium wire which limited the upper temperature limit to approximately 150 ° C.

(4.18) Thermal Environment

The sphere was contained in the pressure vessel containing the ballast gas. The whole apparatus was then suspended in a stirred water-filled thermostat insulated by kaowool, as shown in figure (4.16.1) taken from reference [59]. The temperature of the bath was controlled using a 'Tronac' temperature controller. The power supplied to the heaters attached to the resonator was determined by the difference between the actual and set-point temperatures.

Temperature measurement was by a long stem platinum resistance thermometer (LN 780308) housed in the thermometer well such that its sensing element was located at the resonator's equator. The thermometer was calibrated between 90.188 K and 903.89 K by the National Physical Laboratory and was used with the instrumentation described in section (6.7). Copper blocks were fixed directly to the walls of the resonator and these blocks connected the sphere to the thermometer-well and provided mounting blocks to which the heaters were attached.

(4.19) Pressure Measurement

The pressure was measured by the digiquartz pressure transducer described in section (6.8) and a differential pressure transducer which was operated as a null-reading device. The differential pressure transducer (Schaevitz P642-0001; serial no. 83911) was previously calibrated [59] such that the d.c. output, Φ, is represented for the positive span,

up to 100 kPa by,

$$\Delta_+ \, p/\mathrm{kPa} = 19.699\left(\Phi/\mathrm{V}\right) + 6.27\times10^{-3}\left(\Phi/\mathrm{V}\right)^3 \qquad (4.19.1)$$

with a standard deviation of 9 Pa and for the negative span up to 31 kPa by

$$\Delta_- \, p/\mathrm{kPa} = 19.696\left(\Phi/\mathrm{V}\right) \qquad (4.19.2)$$

with a standard deviation of 4 Pa. The shift in the zero pressure drift reading Φ_z as a function of line pressure could be represented up to 0.2 mV by

$$\Phi_z/\mathrm{V} = -7.89\times10^{-6}\left(p/\mathrm{kPa}\right) \qquad (4.19.3)$$

(4.20) Characterisation of Spherical Resonator

The resonator geometry was characterised using microwave measurements and the technique described in references [108 -110]. The radius was calibrated by means of argon measurements performed by Boyes [59] along seven isotherms at temperatures between 250 and 350 K and at pressures up to 10 MPa. The results of this calibration are given in equation (7.4.2).

CHAPTER 5

Characterisation of the Resonator

(5.1) Introduction

As mentioned previously (chapter 4), the source transducer, was placed at a position in the hemisphere corresponding to maximum acoustic density. Although this arrangement is advantageous in that very strong signals are observed, large perturbations to the complex frequencies may also occur.

When testing of the hemispherical resonator began, the disagreement between modes was found to be unacceptable and so, a prototype equatorial plate was used to determine how the performance of the resonator could be optimised. The perturbation caused by the transducer at the centre of the plate was investigated experimentally in two ways. Firstly, the hole size of the transducer housing was changed and its effect on the observed resonance frequencies and halfwidths measured (section 5.4). Secondly, the position of the hole along the radius (*i.e.* from $r/a = 0$ to $r/a = 1$) was changed and again measurements of the resonance frequencies and halfwidths were measured (section 5.5). In the second experiment, the signal strengths were also measured as a function of r/a and the location of the nodes and anti-nodes confirmed that the modes were indeed radial modes (section 5.3).

(5.2) Comparison of original and prototype plates

The prototype equatorial plate was constructed from 1/2″ aluminium sheet. Two parallel slots were cut along opposite edges of the plate in positions which allowed at least two of the bolts to be bolted into the resonator's base. A recessed hole was drilled at a position which would correspond to the centre of the equatorial surface. The source transducer designed for the original plate fitted snugly into this hole and, by virtue of the design, the signal was propagated through a very short waveguide (approximately 1.0 mm in length). The slots allowed the hole

at the centre to be moved along a radius of the resonator and then clamped in position using the bolts. This was necessary in order to achieve a good acoustic seal between the equatorial plate and the hemispherical base.

Two millimetre scales were fixed to the apparatus, one to the resonator's base, the other to one side of the prototype plate. These were aligned at zero when the hole was at the centre of the resonant cavity's diameter. This fairly crude technique allowed the radius to be measured within approximately 0.3 mm.

The original plate gave resonance frequencies which agreed to about 3.5 per cent. This was obviously unacceptable and worse agreement, in fact, than the prototype plate, for which the resonance frequencies agreed to within 350 ppm, as shown by figure (5.2.1).

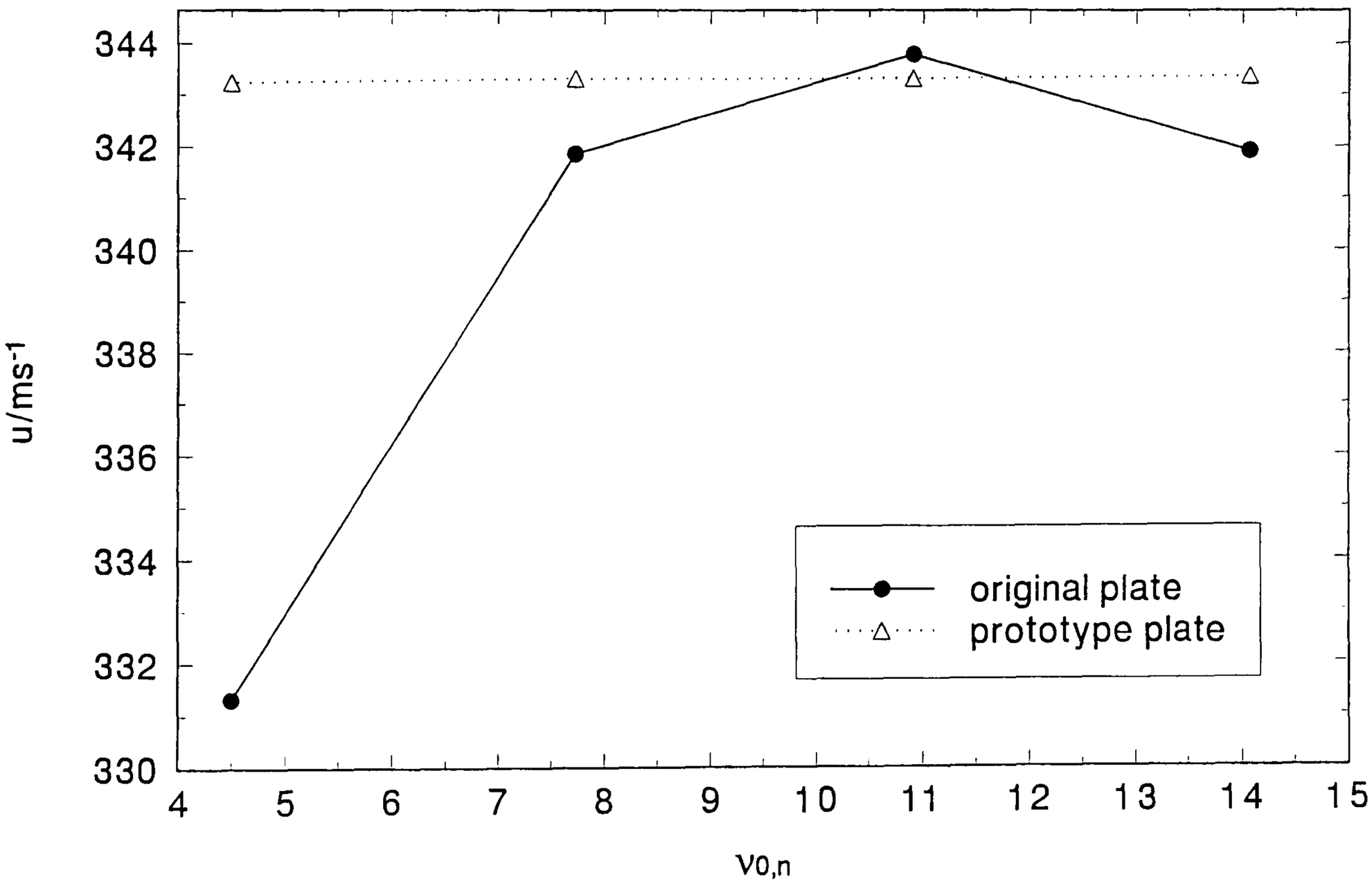

Figure (5.2.1): Comparison of agreement between first four radial modes for the original and prototype plates

Although initially it was thought this anomaly was due to the size of the source transducer in the equatorial plate it was subsequently discovered that the very large disagreement between the radial modes was due to a mismatch between the end plate and the hemispherical part of the resonator. Effectively, the acoustic cavity had a slot of 1.5 mm width around its equator (illustrated by figure 5.2.2).

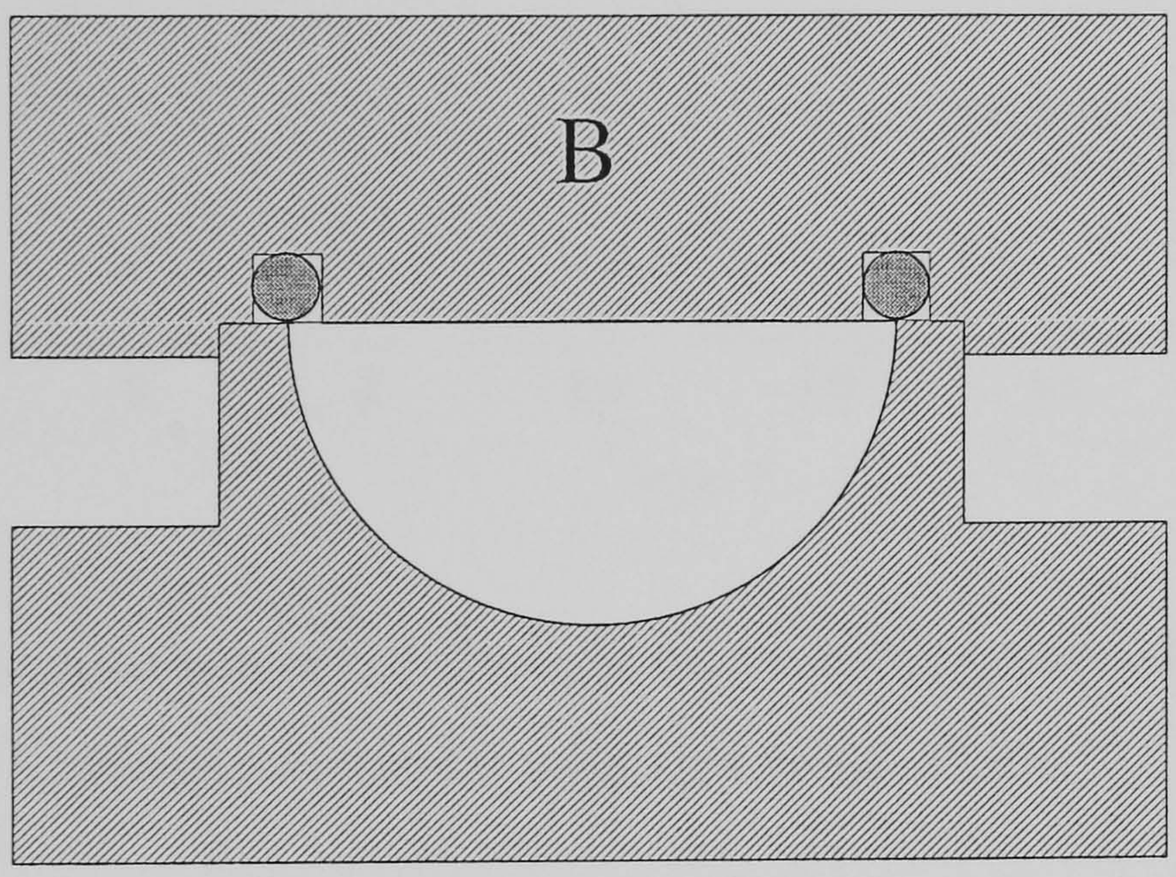

Figure (5.2.2): Hemispherical acoustic resonator with slot around equator

This problem was solved by placing a ring around the top plate (**B**) which was then polished to its previous quality. The vast improvement may be seen by figure (5.2.3). However, compared to the prototype plate there was still appreciable disagreement as shown by figure (5.2.4).

Figure (5.2.3): Agreement between radial modes for hemispherical resonator with and without the slot illustrated by figure (5.2.2)

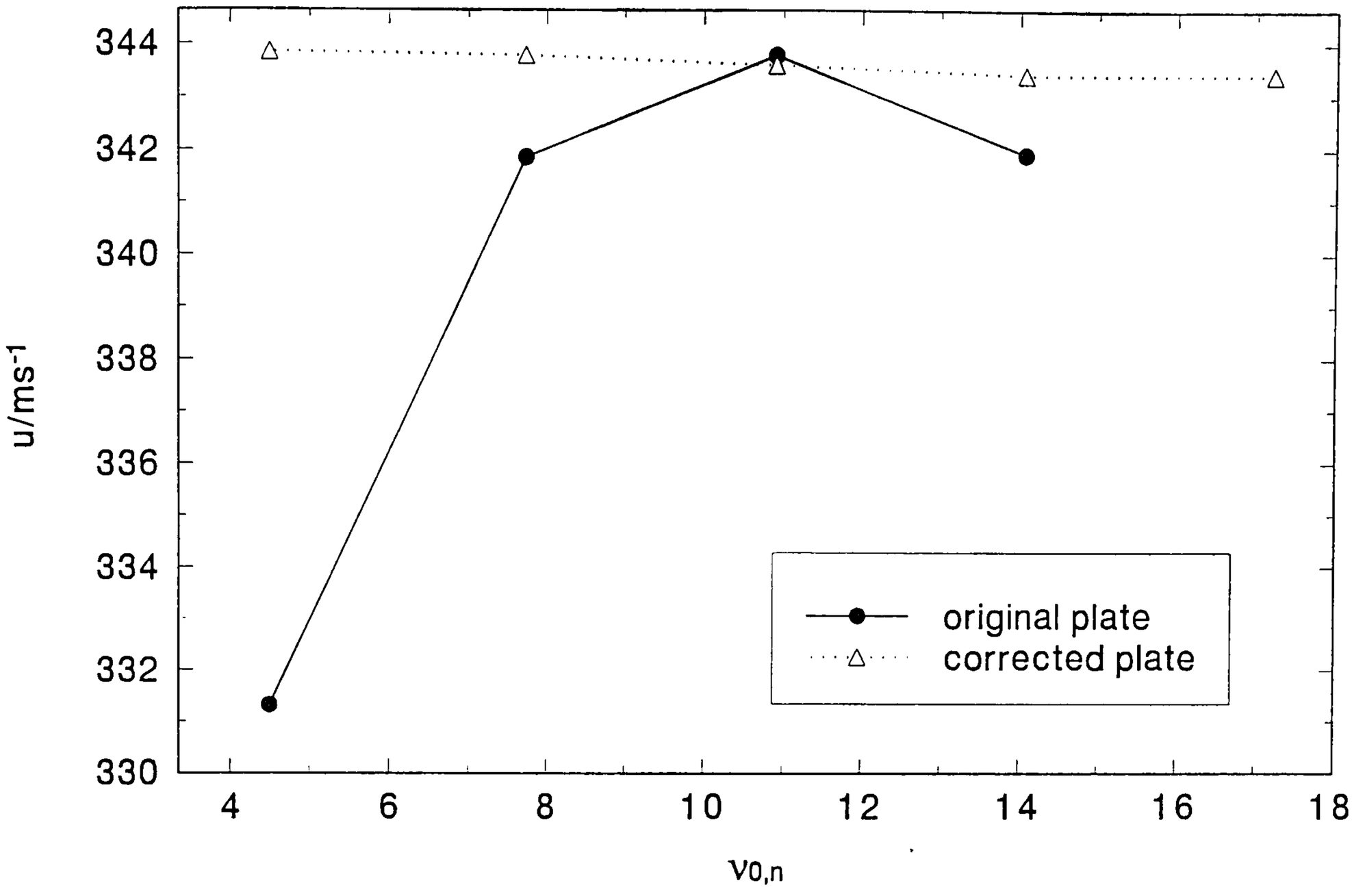

Figure (5.2.4): Comparison of radial modes for prototype plate with various hole dimensions and for improved original plate

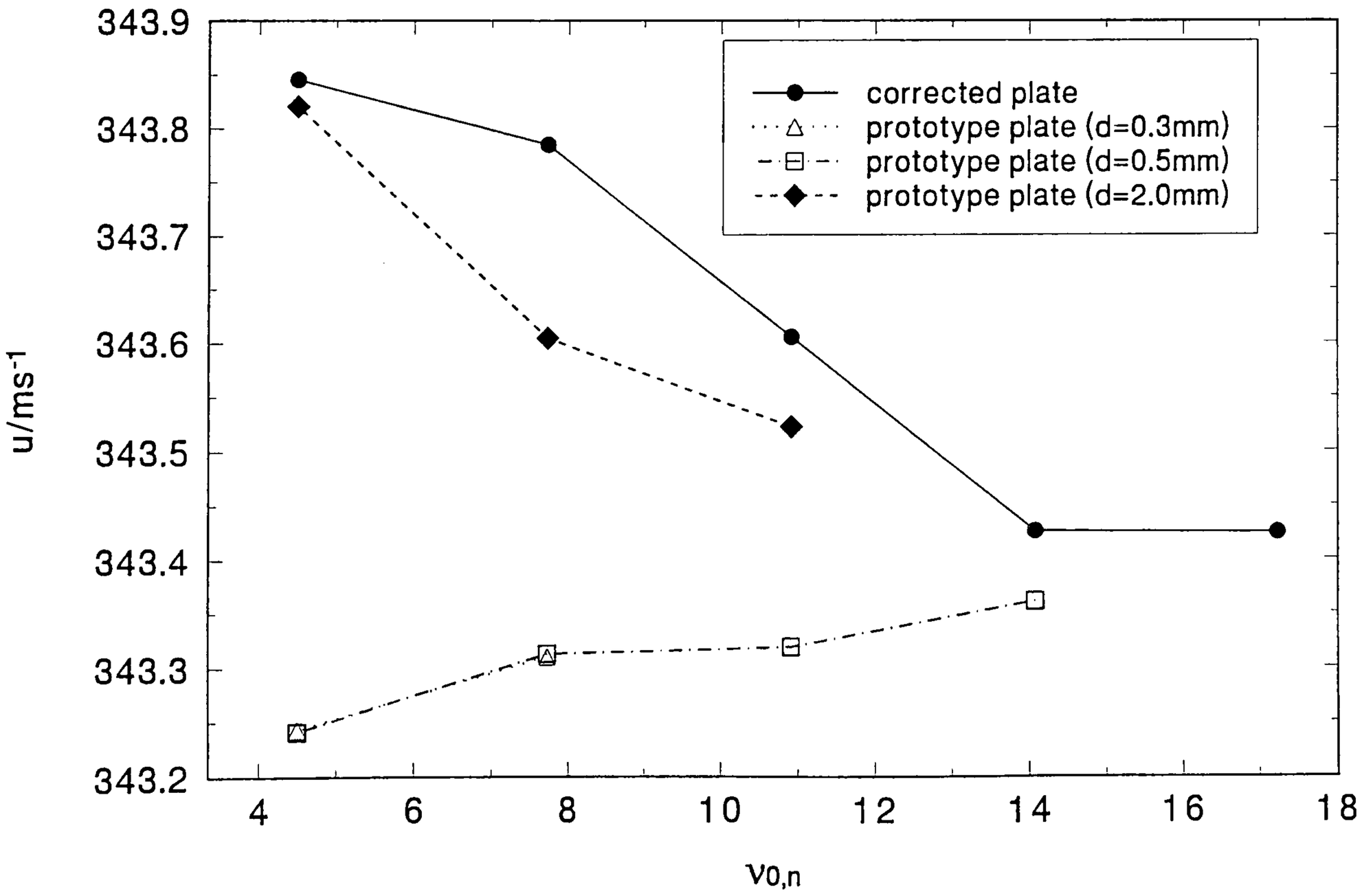

The disagreement between the modes was much less severe; the fractional agreement in the speed of sound was on the order of 0.1 per cent for the original plate compared with about 300 ppm for the prototype plate. The difference between the two plates was attributable to the size of the active area of the transducer; for the original plate the active area had a diameter of 3 mm, whilst for the prototype plate, the agreement of 300 ppm, refers to an active area of 1 mm diameter. The effect of hole size on the resonance frequencies and halfwidths of the radial modes is discussed in more detail in section (5.4).

(5.3) Observation of nodes and anti-nodes

The relative signal intensity along a radius was measured in order to locate the position of the nodes and anti-nodes for each resonance. The position of the nodes for the first four radial modes (0,n); $n = 2, 3, 4, 5$, is clearly illustrated by figure (5.3.1) which shows the wavefunction ϕ for each mode. However, since the acoustic pressure varies as ϕ^2 (figure 4.5.1), the measured signal in dB varies as log (ϕ^2). The theoretical curves for the first four radial modes can be seen in figures (5.3.2), (5.3.3), (5.3.4) and (5.3.5) together with the experimental points. The prototype plate was used for the measurements of signal intensity and the hole size through which the sound was coupled was 0.5 mm diameter. The experimental points for the (0,2) mode were obtained by first measuring the signal strength at $r/a = 1$ at the resonance frequency. The position of the transducer was then moved by about 2 mm and, without altering the frequency, the signal intensity was re-measured; this procedure was then repeated at approximately 2 mm intervals until $r/a = 0$. Further measurements of the signal intensity were then made for positions of the transducer as it traversed the radius from $r/a = 0$ to $r/a = 1$. Measurements of the signal intensity as a function of r/a were made for the (0,3), (0,4) and (0,5) modes using the method outlined for the (0,2) mode. The signal for the (0,6) mode was not sufficiently strong for differences in signal intensity to be resolved. The results were unchanged for any radius across the hemisphere.

This evidence confirms the theory given in chapter (3) that the radial modes in the hemisphere are of the type characteristic of the sphere.

Figure (5.3.1): Variation of the wavefunction ϕ with *r/a*

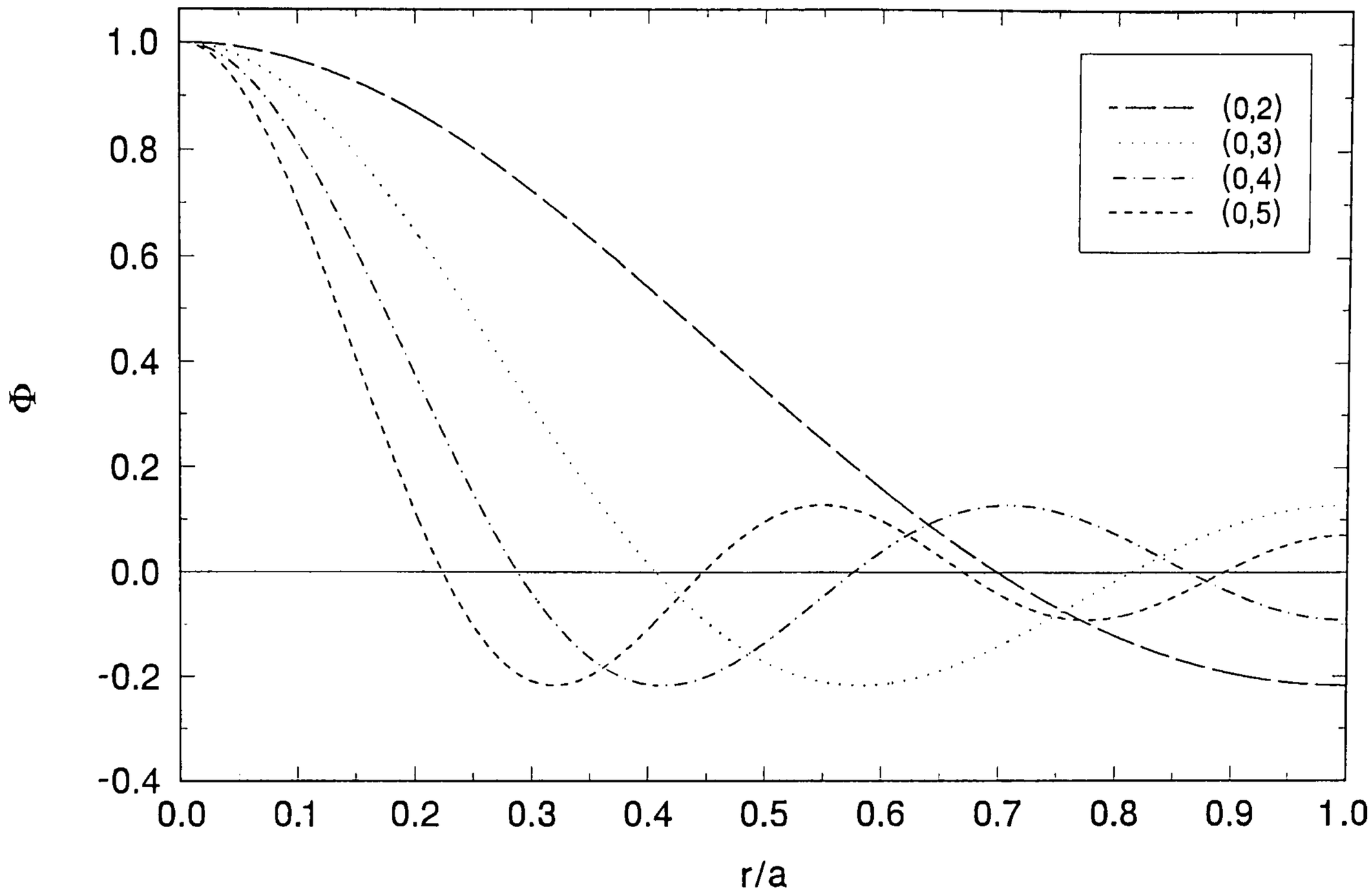

Figure (5.3.2): Variation of signal strength as a function of *r/a* for the (0,2) mode

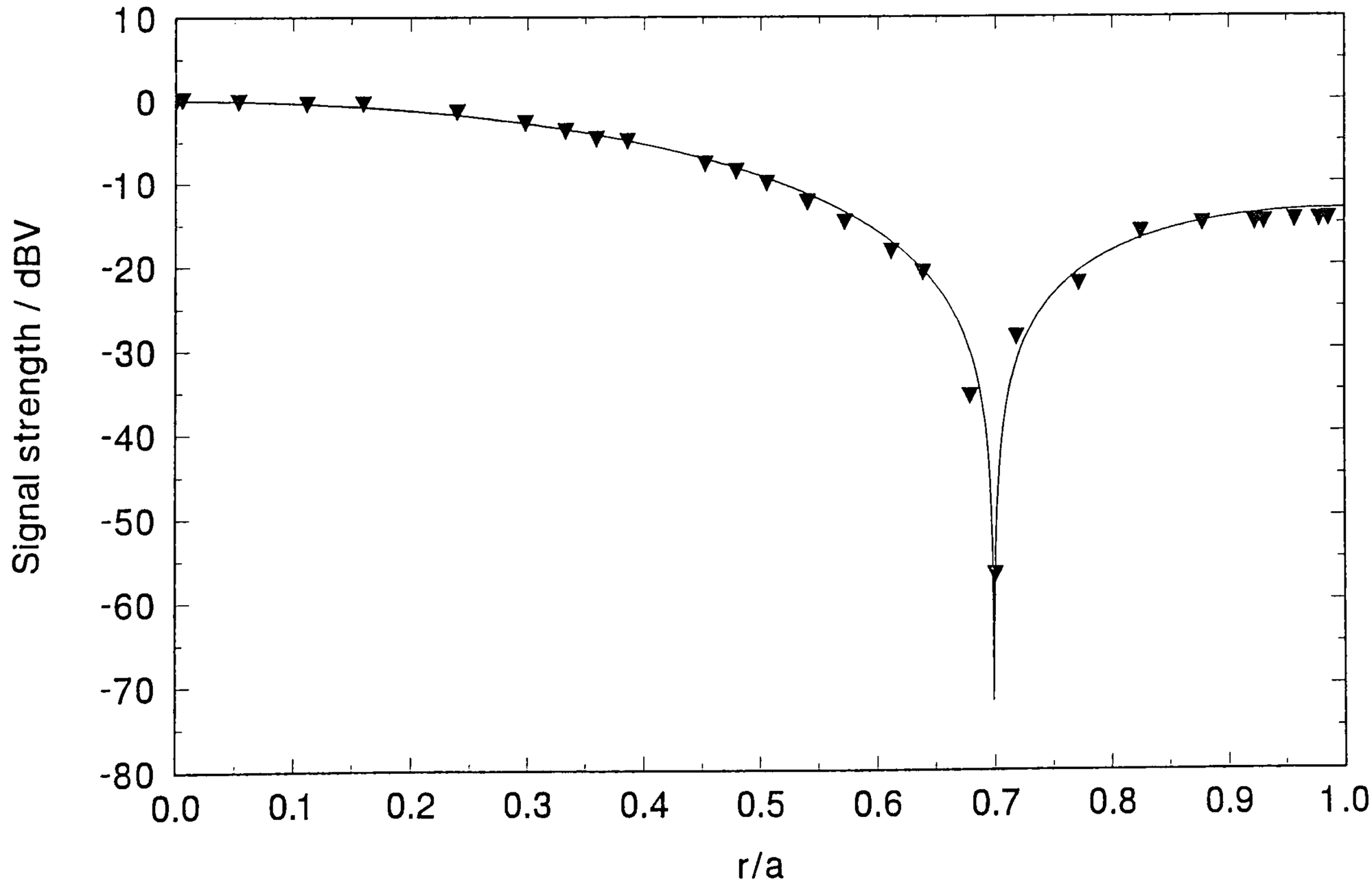

Figure (5.3.3): Variation of signal strength as a function of *r/a* for the (0,3) mode

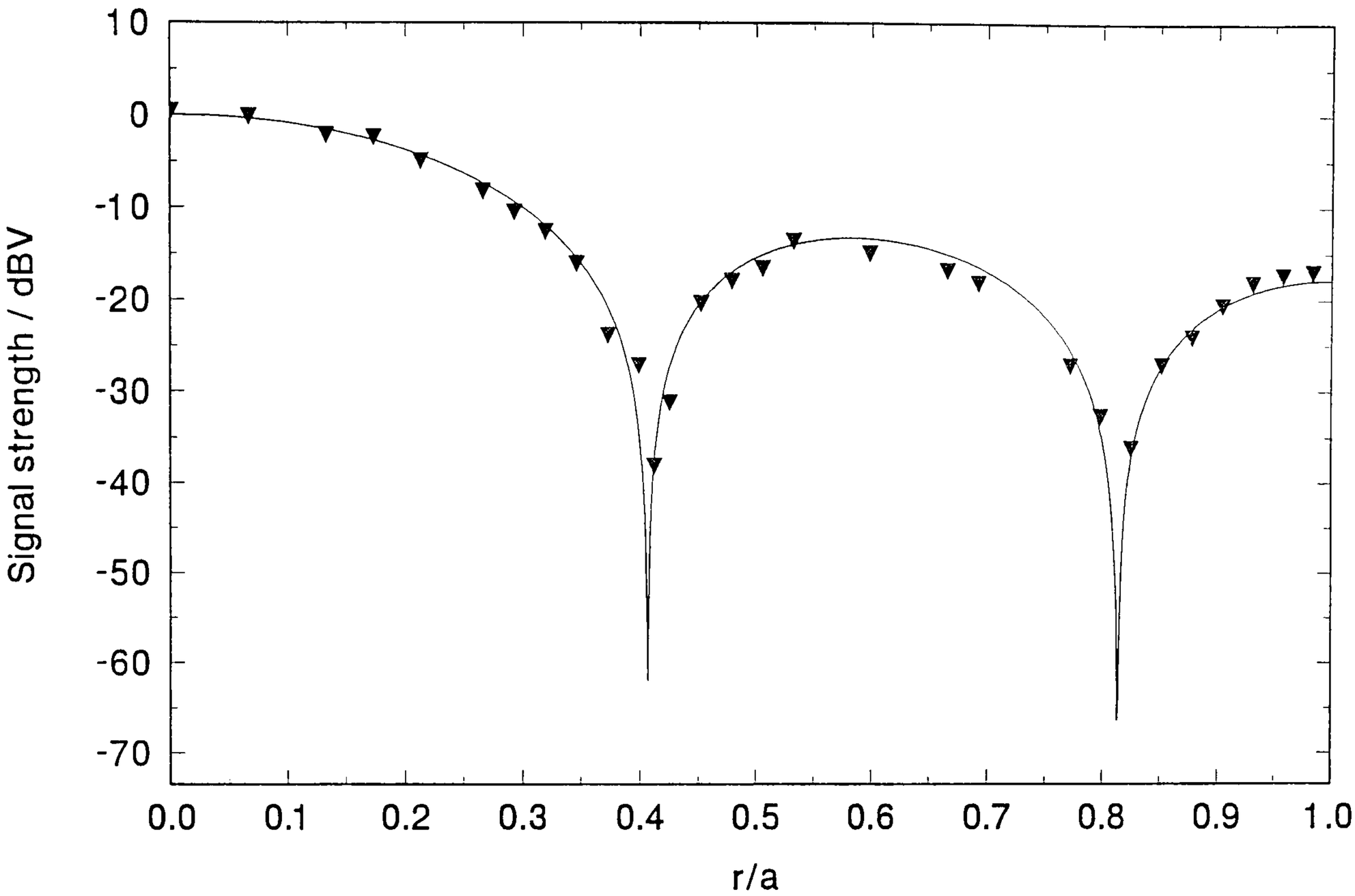

Figure (5.3.4): Variation of signal strength as a function of *r/a* for the (0,4) mode

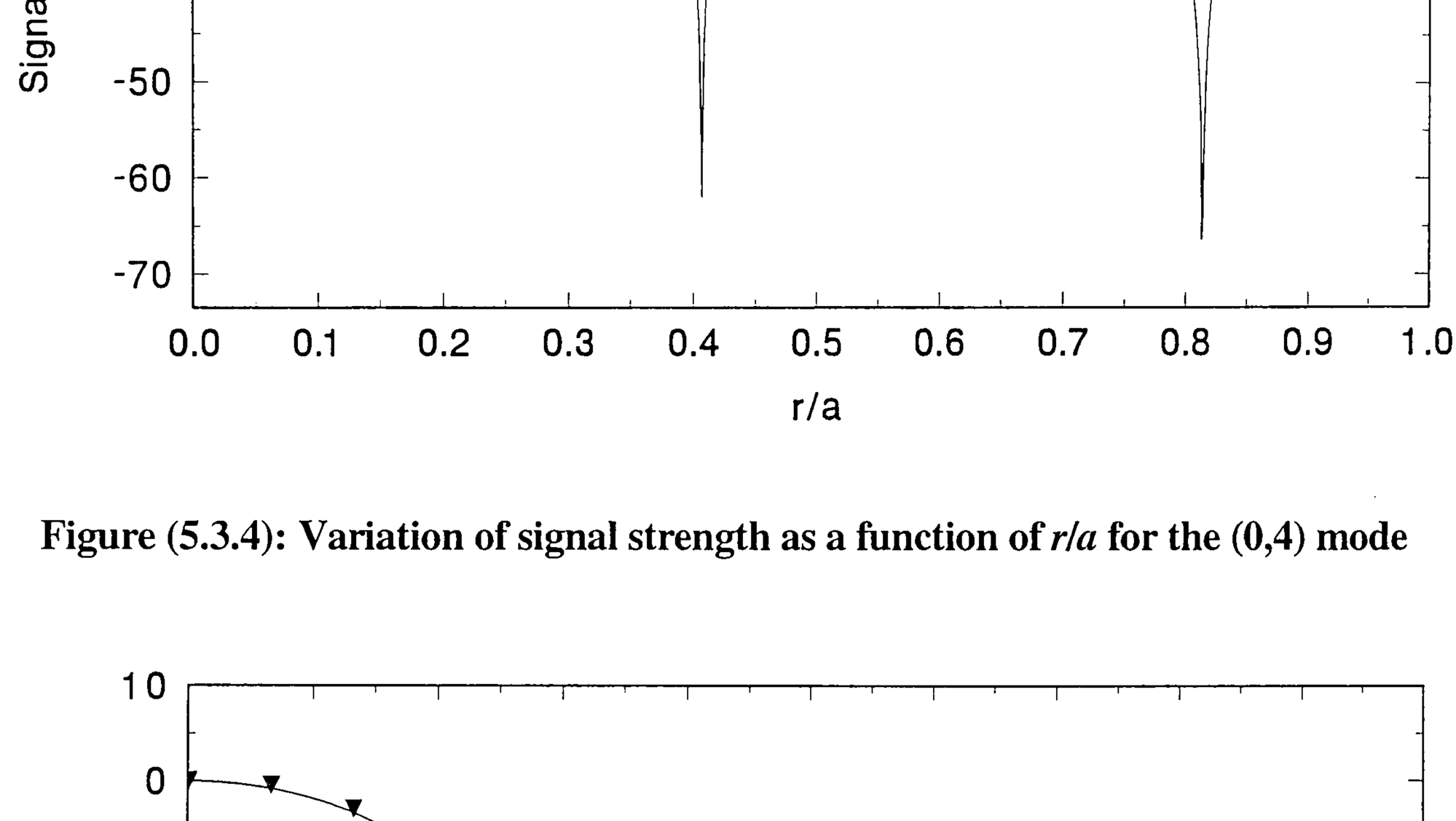

Figure (5.3.5): Variation of signal strength as a function of *r/a* for the (0,5) mode

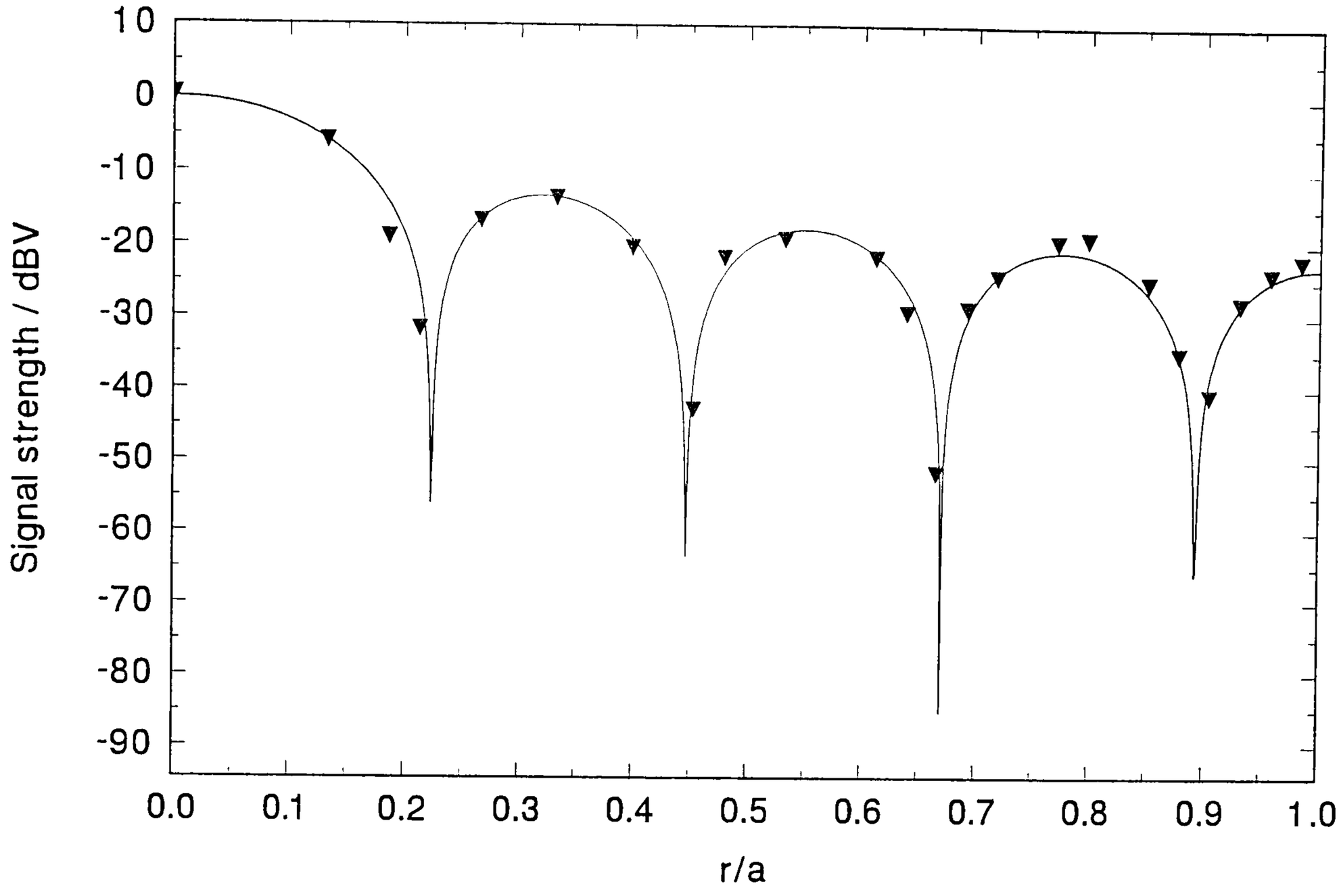

(5.4) Effect of hole size on ($\Delta f + ig$)

Clearly, the magnitude of the perturbation caused by the transducer at $r/a = 0$ will increase as the active area of the transducer increases (in other words, as the diameter of the hole size of the transducer housing increases). For a hole in the equatorial surface, we recall from chapter 3, that the specific acoustic admittance of the surface will differ from that given by equation (3.16.10) over the area ΔS of the hole and in leading order the shift Δf_o in the resonance frequency and contribution to the halfwidth g_o of a radial mode caused by the opening is,

$$\Delta f_o + ig_o = \left\{\frac{j^2(\upsilon_{0,n}(r/a))}{j^2(\upsilon_{0,n})}\right\}\left(\frac{1}{2\upsilon_{0,n}^2}\right)\left(\frac{u}{2\pi a}\right)\left(\frac{\Delta S}{\pi a^2}\right)iy_o \ . \qquad (5.4.1)$$

The factor $\left(1/2\upsilon_{0,n}^2\right)$ is valid only for a hemisphere and arises because the radial integrals of the hemispherical and spherical geometries are different. In a spherical resonator the position of the transducers is conventionally at the wall (*i.e* at $r/a = 1$) and provided y_o is constant over the area ΔS, the contributions Δf_o and g_o to the resonance frequencies and halfwidths are linear with respect to the area of the opening. In other words, the additional factor $\left(j^2(\upsilon_{0,n}(r/a))/j^2(\upsilon_{0,n})\right)$ seen for the equatorial plate is always unity, for a hole in a spherical wall because the magnitude of the wavefunction is constant over the area of the hole. Consequently the contribution to the resonance frequencies and halfwidths for a hole in the wall of a sphere is given by

$$\Delta f_o + ig_o = \left(\frac{u}{2\pi a}\right)\left(\frac{\Delta S}{4\pi a^2}\right)iy_o \qquad (5.4.2)$$

and for a hole in the spherical wall of a hemisphere,

$$\Delta f_o + ig_o = \left(\frac{u}{2\pi a}\right)\left(\frac{\Delta S}{2\pi a^2}\right)iy_o \ . \qquad (5.4.3)$$

When the transducer is centred in the wall of the equatorial plate (at $r/a = 0$) the factor $\left\{j^2\left(\upsilon_{0,n}\left(r/a\right)\right)/j^2\left(\upsilon_{0,n}\right)\right\}$ does not reduce to unity because the wavefunction is changing over the area of the hole. Figure (5.4.1) shows the functional form of the first two terms of equation (5.4.1), valid for perturbations to the resonance frequencies caused by an opening centred at $r/a = 0$ in the equatorial plate. It is clear then that Δf_o and g_o in the equatorial wall are proportional to $\Delta S\int \Gamma \, dr$, where

$$\Gamma = \left(\frac{j^2\left(\upsilon_{0,n}\left(r/a\right)\right)}{j^2\left(\upsilon_{0,n}\right)}\right)\left(\frac{1}{2\upsilon_{0,n}^2}\right) \qquad (5.4.4)$$

and this is illustrated (over the region of the position of the hole), by figure (5.4.2) together with the experimental points for g_o.

For each of the first four radial modes an estimate of g_o was made using,

$$g_o = g_m - g_{(r/a=0)} \tag{5.4.5}$$

where g_m is the measured halfwidth. Since g_m was fairly constant in the range where $r/a \approx 0$ to 0.007 (*i.e.* for hole diameters of $d \leq 0.5$ mm) a good estimate of $g_{(r/a=0)}$ was given by g_m at $r/a = 0.004$ (*i.e.* when $d = 0.3$ mm).

Figure (5.4.1): Variation of Γ with respect to radius for an opening in the equatorial surface of a hemisphere

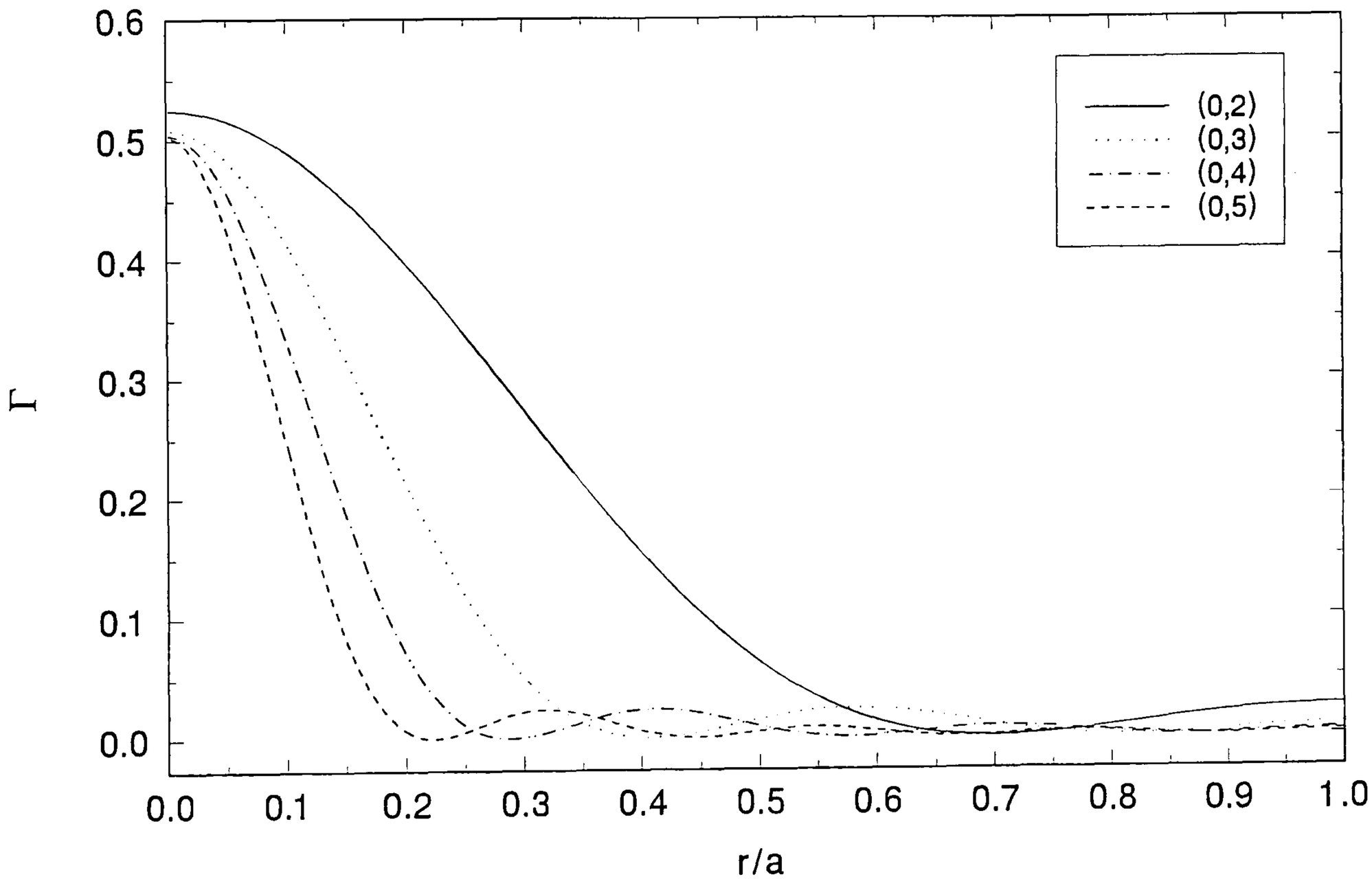

Figure (5.4.2): Halfwidth contribution as a function of transducer active area when centred at *r/a* = 0 in the equatorial surface of the hemisphere

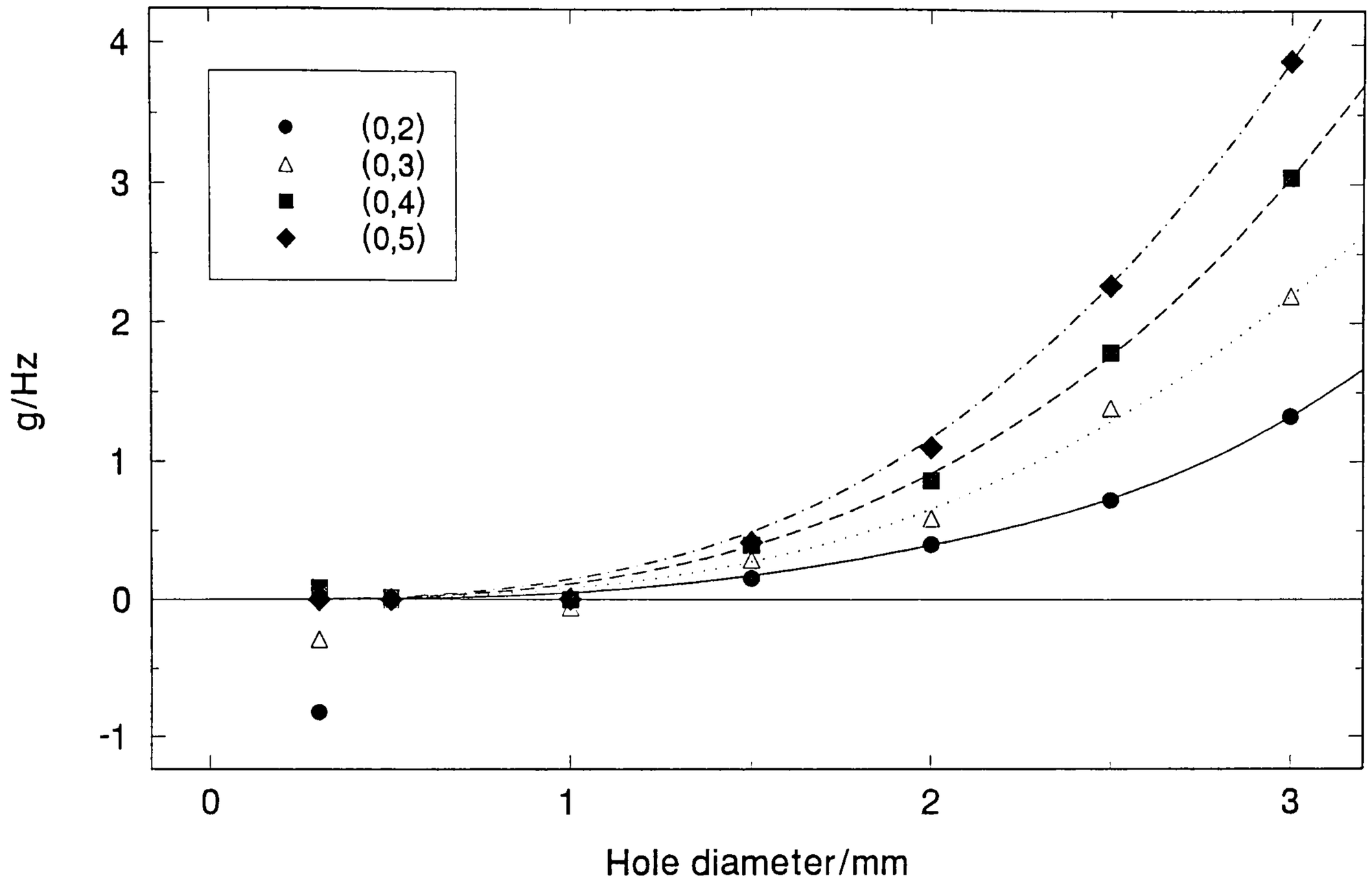

(5.5) Effect of (*r/a*) on (Δf + *ig*)

Qualitatively the effect of *r/a* on the resonance halfwidth is that a minimum is exhibited when the source is placed near a node. It is obvious that when an infinitesimally small transducer is positioned at a node the perturbation it will cause is zero but the sound field will fail to be excited. However, a practical transducer has a finite size positioned at a node the perturbation will take on a non-zero but minimum value and the sound field will be excited.

Referring again to equation (5.4.1) and figure (5.4.1) it is clear how the contribution to Δf_o and g_o varies across the radius of the resonator. To measure the resonance halfwidths g_m of each mode the following steps were taken: (1) The transducer was centred at $r/a = 0$ and the resonance frequency of the (0,*n*) mode located. (2) At this position four measurements of the resonance frequency and halfwidth were made and the mean halfwidth calculated. (3) The

position of the transducer was moved by approximately 5 mm and step (2) was repeated. (4) Step (3) was repeated until $r/a \approx 1$ and then steps (1) and (2) were repeated. Experimental g_o's at r/a for each mode were estimated by subtracting the value of the halfwidth at a node g_{node} from the corresponding measured halfwidth $g_m(r/a)$ *i.e.*

$$g_o(r/a) = g_m(r/a) - g_{node} \tag{5.5.1}$$

The theoretically predicted form for each of the first four radial modes is shown by figures (5.5.1), (5.5.2), (5.5.3) and (5.5.4) together with the experimental points calculated from equation (5.5.1).

Figure (5.5.1): Contribution to the resonance halfwidth of the (0,2) mode from the opening in the equatorial surface of the hemispherical resonator as a function of *r/a*

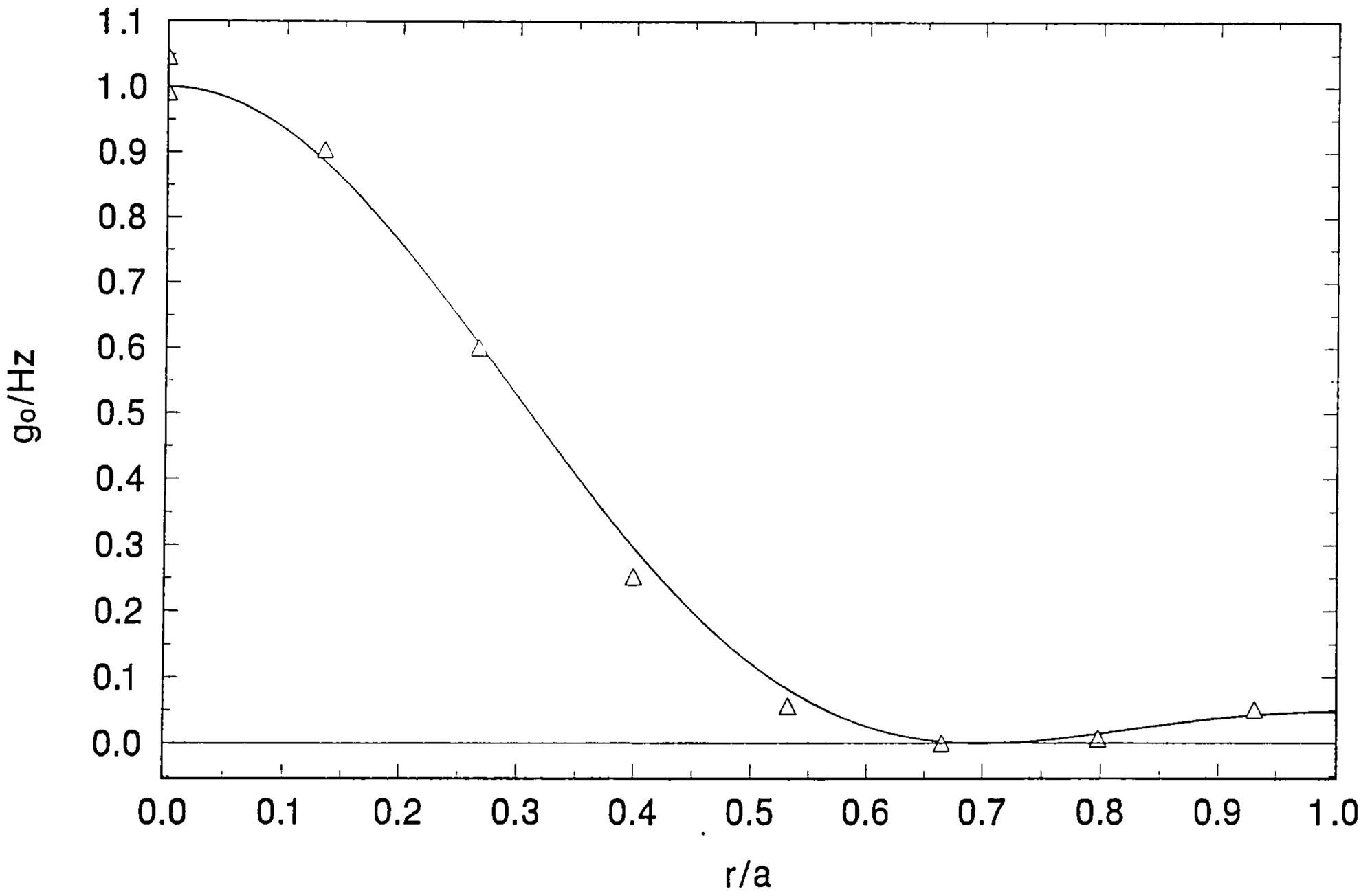

Figure (5.5.2): Contribution to the resonance halfwidth of the (0,3) mode from the opening in the equatorial surface of the hemispherical resonator as a function of *r/a*

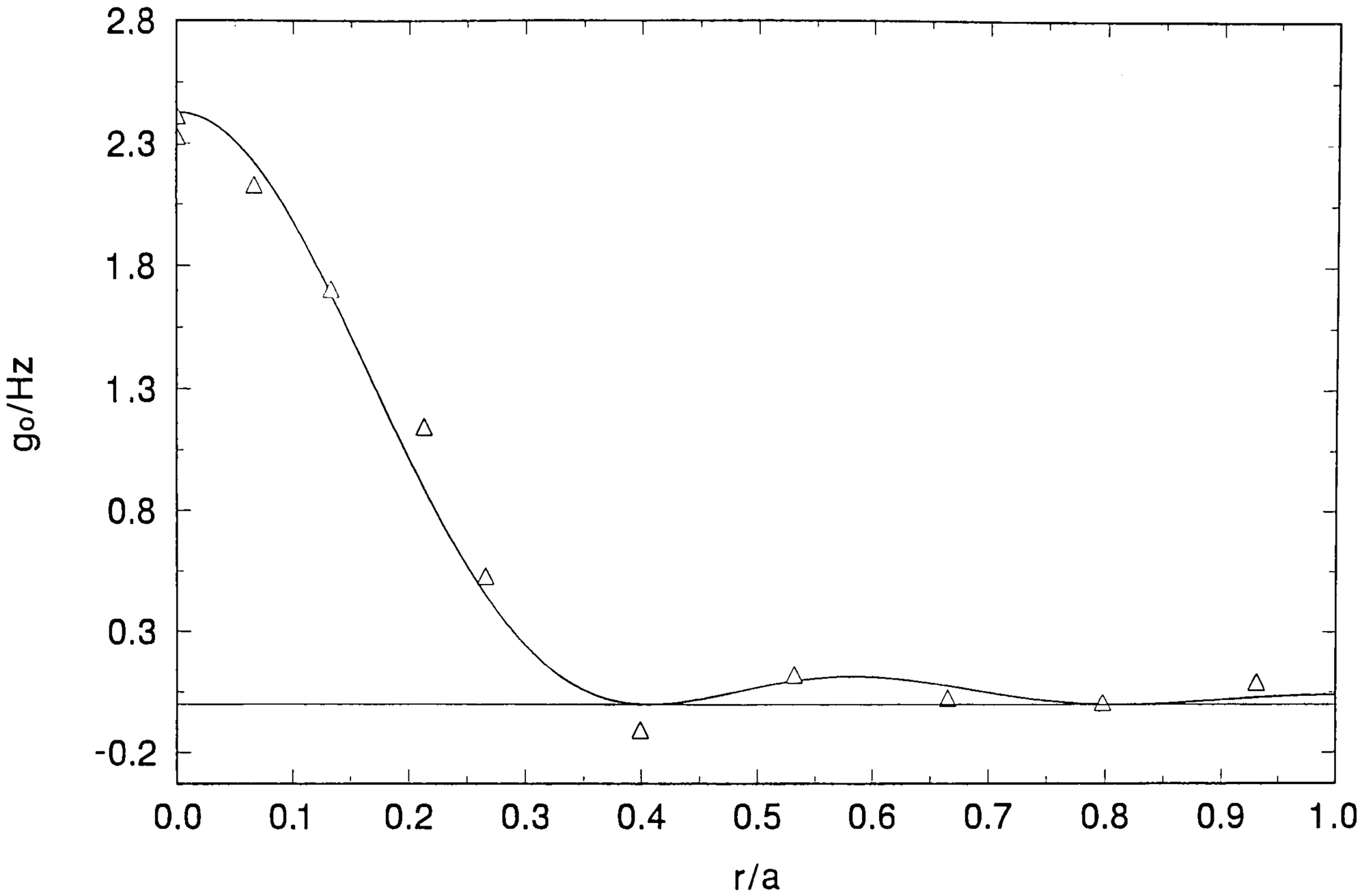

Figure (5.5.3): Contribution to the resonance halfwidth of the (0,4) mode from the opening in the equatorial surface of the hemispherical resonator as a function of *r/a*

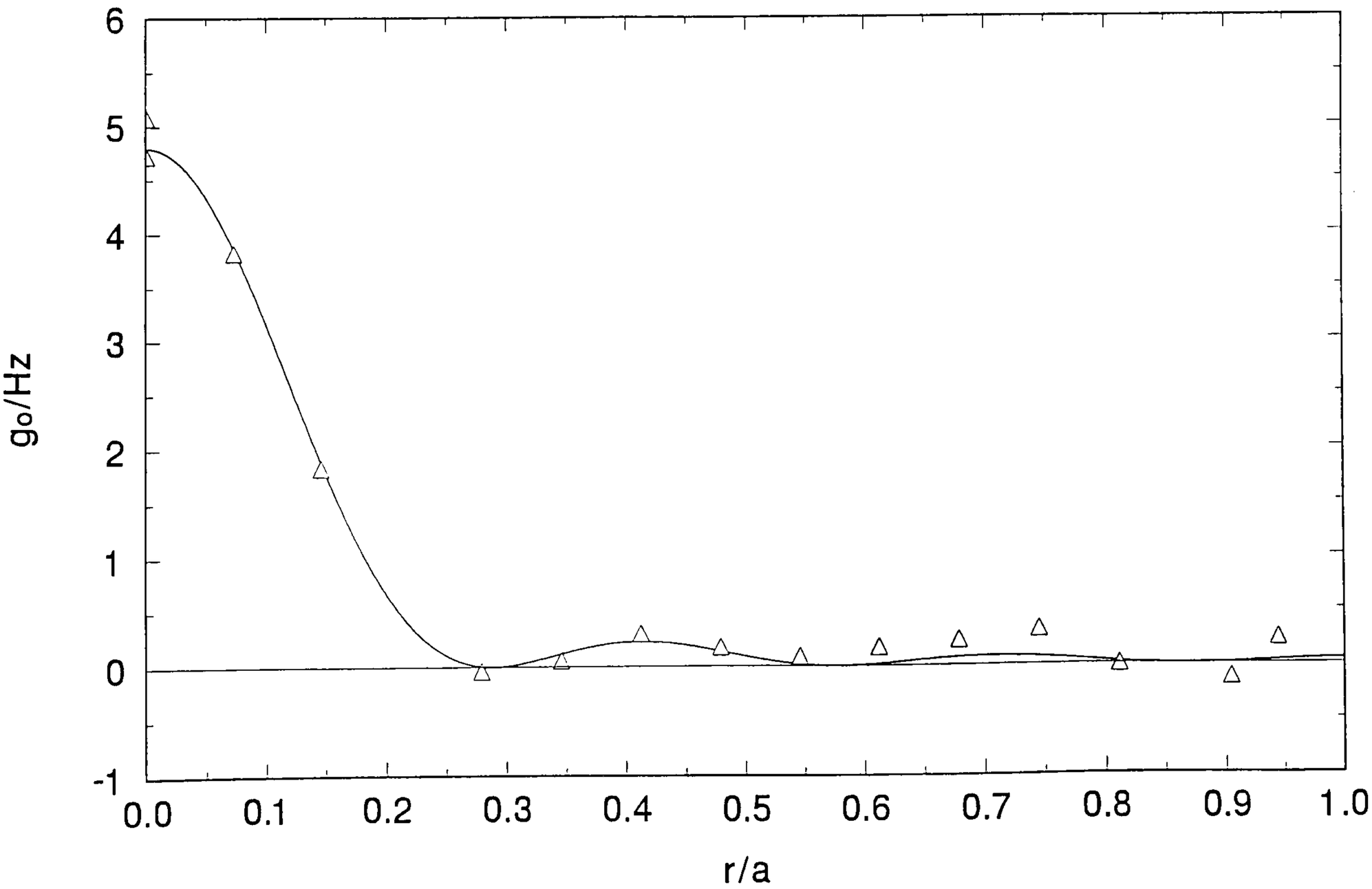

Figure (5.5.4): Contribution to the resonance halfwidth of the (0,5) mode from the opening in the equatorial surface of the hemispherical resonator as a function of *r/a*

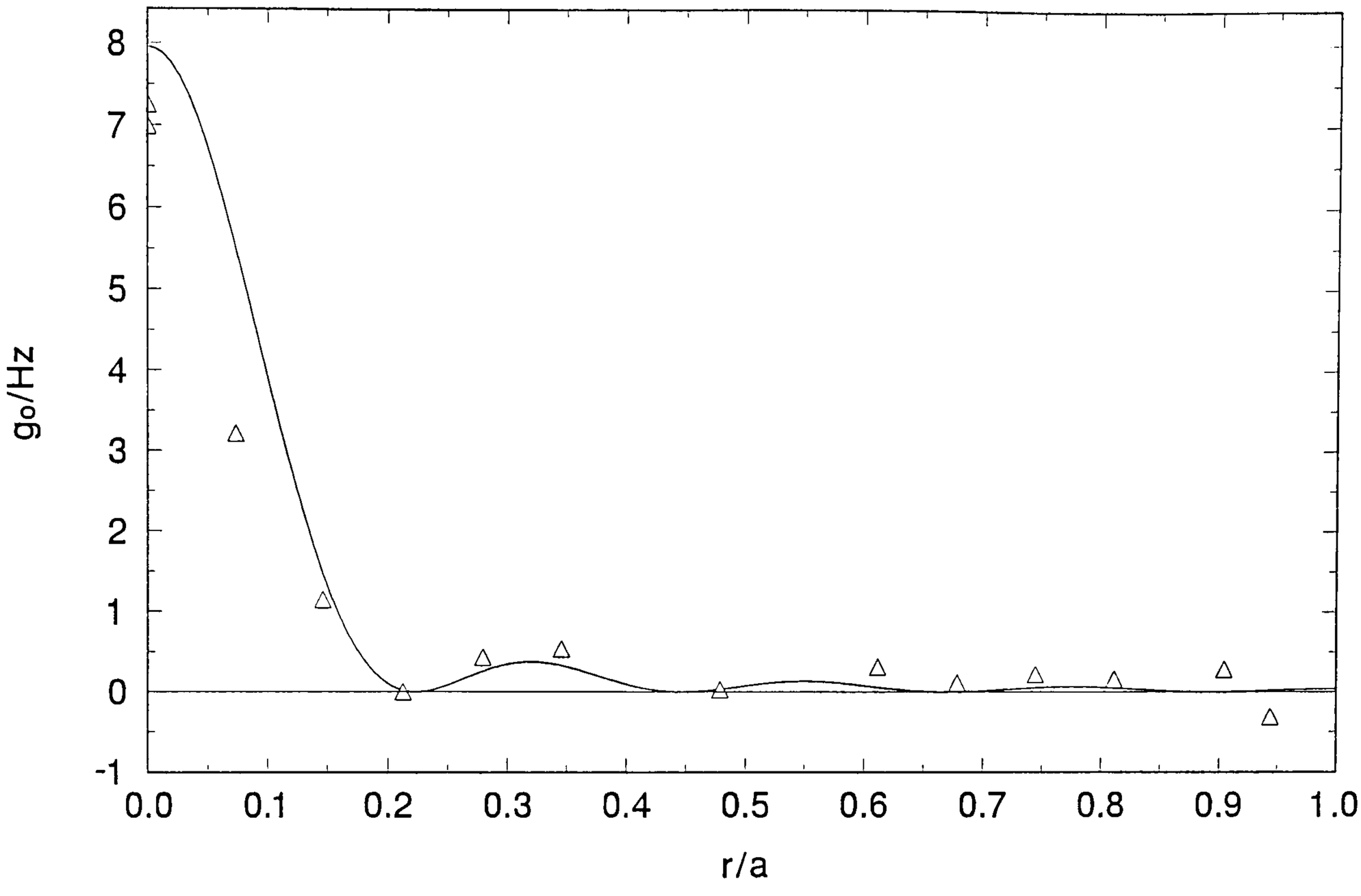

(5.6) Summary

With the results obtained using the prototype plate, the design of the original transducer housing was altered in order to optimise the play-off between the signal strengths and the perturbation caused by the positioning of the source transducer and its active area. As the theory suggests the signal strength is proportional to the active area b of the transducer the final arrangement used $b = 0.3$ mm but this was clearly a compromise. The active area (*i.e.* the hole size) was reduced by insertion of a small brass plug mounted against the face of the transducer. This had a hole of 0.3 mm diameter drilled through it which acted as a small waveguide through which the signal could be propagated. The perturbation to the resonance

Figure (5.6.1): Speed of sound obtained from the first five radial modes with diameter *d* of the active area and length *L* of waveguide

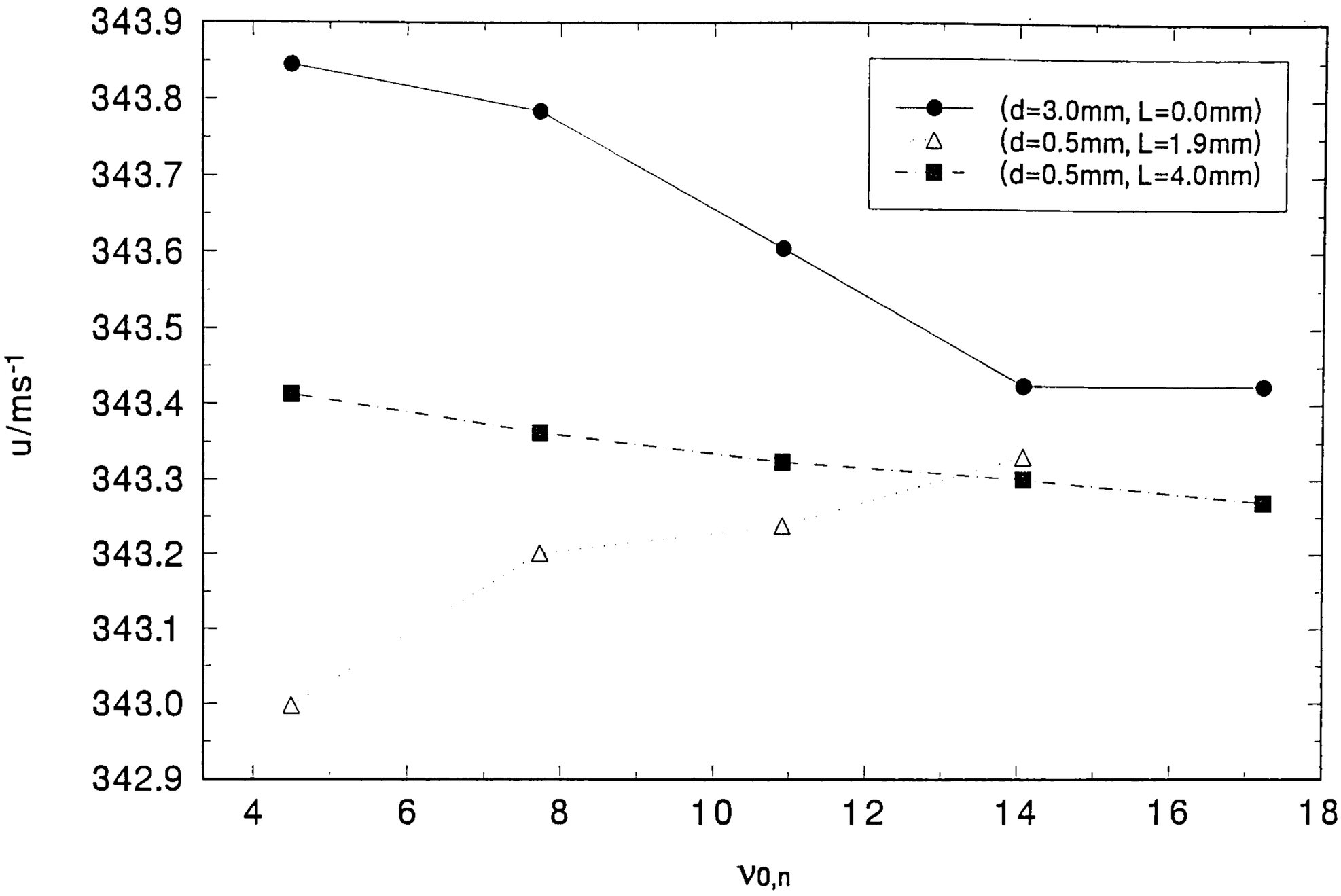

frequencies was reduced still further by fixing the length (L) of the waveguide so that $Re(\kappa_{KH} L)$ was near $n\pi$ with integer n; the effect is shown in by figure (5.6.1).

The signal strengths were attenuated somewhat by the new arrangement, but because the waveguide projects an acoustic image of the termination on the opening at $r/a = 0$, the signals were still very intense and the perturbations much smaller.

CHAPTER 6

Experimental Techniques

(6.1) Introduction

Resonators may be divided into those of variable geometry (for example, a cylinder with a moving piston) or fixed geometry. For the measurements reported here spherical and hemispherical cavities were operated under steady state conditions using wide-bandwidth transducers for the generation and detection of sound. The low frequency operation of the wave-source enabled the lowest four radially symmetric modes to be studied in isolation, without overlap from other modes. The resonance frequencies and halfwidths of the modes under study were measured and analysed as described below and the speed of sound and the thermophysical properties of the gas were extracted from the resulting data. The temperature of the hemispherical and spherical cavities was maintained as described in chapter 4. This allowed measurements of the resonance frequencies and halfwidths to be made at a number of state points along an isotherm. Once thermal and hydrostatic equilibrium had been reached the temperature was measured by means of PRT's attached to the walls of the cavities and the pressure was measured using a digiquartz pressure gauge. For measurements involving the spherical resonator a differential pressure transducer was also utilised.

(6.2) Instrumentation

Although the procedures for measuring resonance frequencies, temperature and pressure have been described previously by former workers of this laboratory [50, 54, 59, 77] brief descriptions are included here for completeness and to define precisely the techniques used. The discussion which follows is summarised by the block diagram given in figure (6.2.1).

The generation and detection of sound took place using two wide-bandwidth transducers embedded in the walls of the resonator. The continuous wave-source was generated by a network analyser (Hewlett-Packard HP4192A, serial number 820031) which was controlled via an IEEE interface. It was ensured that the fractional accuracy of the signals was better than 10^{-7} by phase-locking the impedance analyser to the 10 MHz time-base of a counter (Hewlett-Packard 5315B option 004). The frequency output from the impedance analyser was variable between 5 Hz and 13 MHz and could be set with a resolution of 10^{-7}, whilst the voltage output could be varied between 0.005 and 1.1 V r.m.s. with increments of 0.001 V r.m.s. Although the maximum voltage output was usually required for measurements in the sphere, no more than 0.6 V r.m.s was required for measurements in the hemisphere. The signal was passed through a power amplifier and D.C. bias to amplify the output of the impedance analyser to 60 V r.m.s. and mix it with a D.C. bias of 300 V. A variable resistance attenuator was required for the output of the signal before it passed into the source transducer of the hemispherical cavity as it was extremely efficient; this also cleaned the signal of random noise. A resistive-potential divider was placed in parallel with the output of the power amplifier, supplying a reference signal to the analyser. The output from the detector was fed to a low noise differential amplifier, which had a forward gain of 1000. Further amplification was achieved using a bandpass amplifier with a potential difference gain variable between 10 and 30, this served to remove low frequency (below 1 kHz) and high frequency (above 100 kHz) noise. Generally a gain of only 10 was used, higher amplifications leading to unacceptable levels of noise. The amplified signal was then fed to the test input channel of the impedance analyser. The amplitude A and phase ϕ of the measured signal could be resolved to 0.01 % and 0.0002 rad, with a time constant of 1 s.

Data collection took place by comparative measurements of the amplitude and phase of the transmitted and received signals. Initially, an estimate of the centre-frequency f_N of each mode was made using an oscilloscope connected to the input and the output of the impedance analyser and by manually scanning the appropriate frequency range. The excitation frequency was increased through eleven synthesised discrete frequencies from $(f_N - g_N)$ to $(f_N + g_N)$ with increments of $g_N / 5$ and at each point the in-phase and

Figure (6.2.1): Block diagram of instrumentation

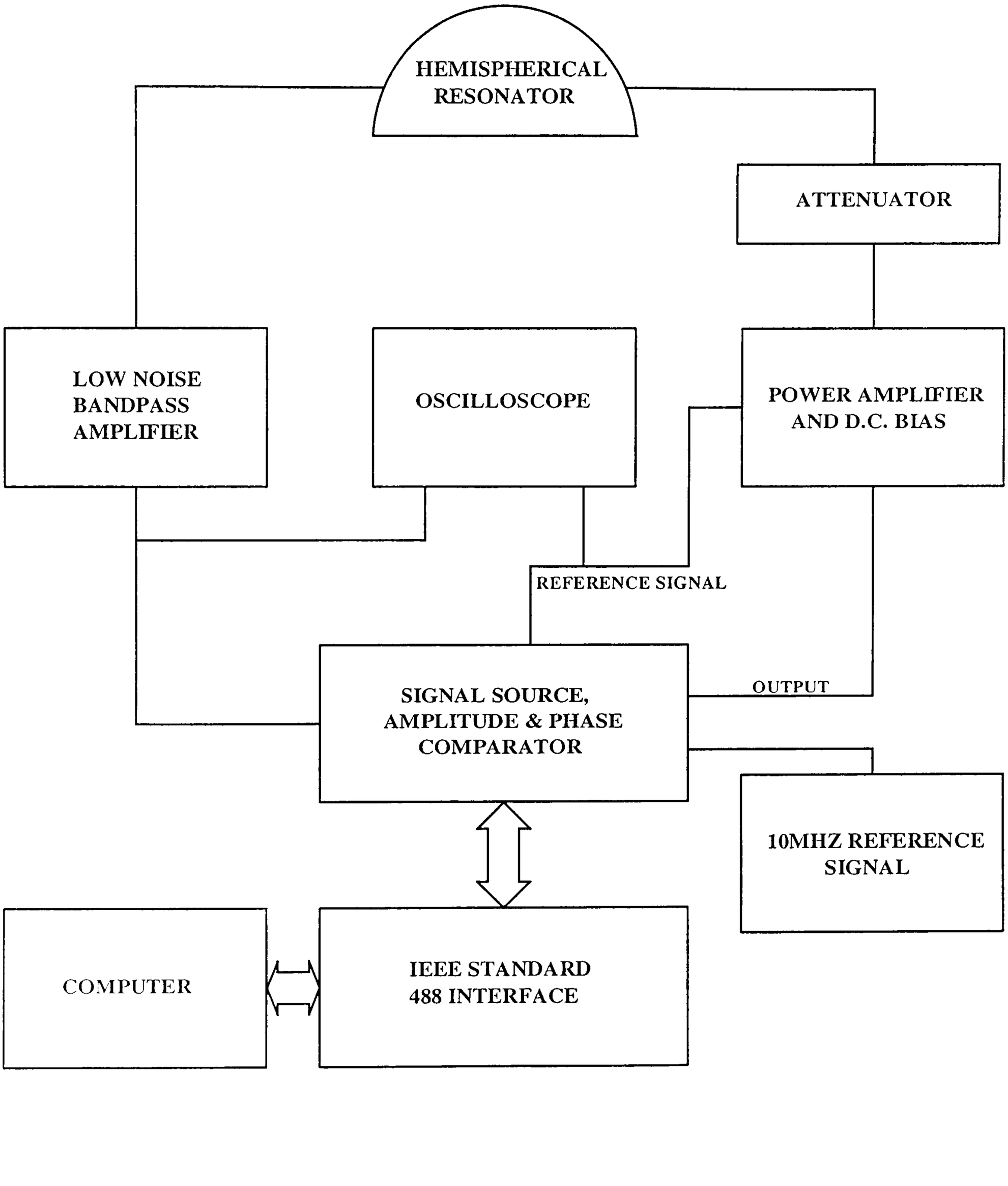

quadrature components of the transmitted and received signals were measured. Each resonance was scanned with increasing then decreasing frequency to compensate against any drifts in temperature. After each point, a short pause was necessary to allow the acoustic pressure to stabilise, before the amplitude and phase of the next point could be recorded. To obtain values of A and ϕ constant to 0.02 %, which is the accuracy of the impedance analyser, a pause of $\tau = 1.4/g$ is required, since this is the time required for the acoustic response to be within $\exp(-2\pi g\tau)$ of its steady state value.

Measurements of the amplitude and phase of the received and transmitted signals were expressed in terms of the real and imaginary parts of the complex potential difference ratio

$$\omega = \langle a \rangle \cos(\phi) + i \langle a \rangle \sin(\phi) = u + i\nu \tag{6.2.1}$$

The complex voltages were then fitted to a function of the theoretically predicted form,

$$\omega = \frac{A}{\left(F_{0n}^2 - f^2\right)} + B + Cf \tag{6.2.2}$$

where A is the complex amplitude and where

$$F_{0n} = \left(f_{0n} + ig_{0n}\right) \tag{6.2.3}$$

Any background signal due to overlap and other mechanisms is represented by the two leading terms of a Taylor's series. The data for each mode was then fitted to either a 6 parameter (f_{0n}, g_{0n} and complex A and B) or 8 parameter (complex C is also considered) equation. A detailed description for fitting $\omega(f)$ to equation (6.2.2) is given in reference [111]. For measurements in the hemisphere only a 6 term fit was ever required due to the intense signals received and the absence of a frequency dependent background. For measurements obtained using the spherical resonator an 8 term fit was generally required especially at the lowest pressures where the signal-noise ratio was so poor as to require 8 terms.

(6.3) Temperature Measurement in the Hemisphere

The temperature of the hemisphere was measured using a long stem platinum resistance thermometer encased in stainless steel (SDL long). This was mounted in a brass housing that was bolted into position on the external surface of the resonator. The thermal contact was

improved by filling the thermometer well with vacuum grease. The depth of immersion of the thermometer within the well was 110 mm which should provide adequate immersion for the precision required [112].

A comparison of this thermometer with one calibrated on the International Temperature Scale of 1990 (ITS-90) was carried out by Royal and Sanchez [113] and is outlined below.

(6.4) Calibration of Platinum Resistance Thermometer (SDL Long)

The temperature range over which the thermometer was employed was from room temperature to about 370 K. In this range the International Temperature Scale of 1990 is defined by means of platinum resistance thermometers calibrated at specified sets of defining fixed points and using specified interpolation procedures.

For the calibration in the range from the triple point of equilibrium hydrogen (13.8033 K) to the freezing point of silver (961.78 °C) the temperatures are determined in terms of the ratio of the resistance $R(T_{90})$ and at a temperature T_{90} and the resistance R (273.16 K) at the triple point of water. The ratio, $W(T_{90})$, is

$$W(T_{90}) = R(T_{90})/R(273.16\,K) \tag{6.4.1}$$

The temperature, T_{90} is then obtained from the appropriate reference function and the deviation function

$$\begin{aligned} W(T_{90}) - W_r(T_{90}) = a\left[W(T_{90})-1\right] + b\left[W(T_{90})-1\right]^2 + c\left[W(T_{90})-1\right]^3 \\ + d\left[W(T_{90}) - W(660.323°C)\right]^2 \end{aligned} \tag{6.4.2}$$

For calibration of the entire range, the fixed points used are the triple point of water (0.01 °C) and the freezing points of tin (231.928 °C), zinc (419.527 °C), aluminium (660.323 °C) and silver (961.78 °C). The calibrations performed for our purposes did not cover the full range but were comparable to accepted sub-range calibrations.

(6.5) Sub-range calibration from 0 °C to 150 °C

The thermometer was calibrated at the triple point of water and at a temperature of approximately 150 °C. As measurements at the freezing point of indium were not readily accessible, they were replaced by comparative ebulliometry measurements at temperatures close to 150 °C. The comparative ebulliometry technique [114] allows temperatures to be obtained with a very high constancy and measured to an accuracy of better than 1 mK. The thermometers used to measure the temperature of the ebulliometric technique were long stem platinum resistance thermometers previously calibrated on ITS-90 by the National Physical Laboratory (NPL). For this temperature range, the deviation function is given by equation (6.4.2), where $b = c = d = 0$ and the appropriate reference function is given by

$$W_r(T_{90}) = C_0 + \sum_{i=1}^{9} C_i \left[\frac{(T_{90}/K) - 754.15}{481} \right]^i \qquad (6.5.1)$$

where the coefficients, C_0 and C_i are given in reference [112]. Measurements at the defining fixed points then allowed a to be determined and hence $W(T_{90})$ and T_{90} itself at intermediate temperatures.

(6.6) Sub-range calibration from the triple point of mercury (-38.8344 °C) to the melting point of gallium (29.7646 °C)

The thermometer was calibrated at the triple points of mercury and water and at the melting point of gallium. The deviation function for this range is again given by equation (6.4.2). For this temperature range $c = d = 0$ and the values of a and b are obtained from measurements at the defining fixed points. The reference function for the range 13.8033 K to 273.16 K is given by

$$\ln[W_r(T_{90})] = A_0 + \sum_{i=1}^{12} A_i \left[\frac{\ln(T_{90}/273.16\,K) + 1.5}{1.5} \right]^i \qquad (6.6.1)$$

where the coefficients, A_0 and A_i are given in reference [112]. This equation (6.4.2) allowed the calculation of $W_r(T_{90})$ at the mercury triple point and together with the previous sub-range calibration and $W_r(T_{90})$ for the melting point of gallium (from the previous reference function

given by equation (6.5.1)), values of a and b were obtained. Calculation of all intermediate temperatures (T_{90}) was then possible from the measurement of their corresponding resistances.

(6.7) Temperature Measurement in the Sphere

The temperature of the sphere was measured using a long stem PRT calibrated on the International Practical Temperature Scale of 1968 (IPTS-68). The details of which have been reported previously in reference [59]. Calibration of the thermometers used for the sphere and the hemisphere were based on IPTS-68 and ITS-90 respectively. However, IPTS-68 corrections to ITS-90 are easily made and the temperatures reported here refer to ITS-90.

The resistance of both PRTs was measured to a precision and resolution of 10 μΩ using an a.c. bridge (Tinsley type 5840, serial number 830037) operating at 375Hz and a current of 1 mA. A standard Wilkins Resistor (Wilkins type 5685A, serial number 236201) was used to monitor any drifts in the bridge.

(6.8) Pressure Measurement

The gas lines of the spherical and hemispherical resonators were connected as shown in figure (8.2.1). This arrangement allowed measurements to be made on the two systems simultaneously, which was extremely useful during the check of the calibration of the hemisphere's radius and allowed differences due to the pressure measurement technique to be eliminated.

Pressure measurement up to 7 MPa was by a temperature compensated, digiquartz pressure gauge (supplied by Paroscientific, model no. 2900-AT serial no. 31285). The quartz crystal used in the gauge exploits the piezoelectric and thermoelectric properties of the crystal. Oscillations of the crystal are measured using a universal counter (Hewlett Packard 5315B) giving the time periods of the pressure signal (τ_p) and the temperature signal (τ_t) in microseconds. The temperature is represented by

$$T/^{\circ}C = Y_1 U + Y_2 U^2 + Y_3 U^3 \qquad (6.8.1)$$

where $U = \tau_t - U_0$ and the pressure is given by

$$P / kPa = C\left(1-\frac{T_0^2}{\tau_p^2}\right)\left\{1- D\left(1-\frac{T_0^2}{\tau_p^2}\right)\right\} \qquad (6.8.2)$$

where

$$C = C_1 + C_2U + C_3U^2 \qquad (6.8.3)$$

$$D = D_1 + D_2U \qquad (6.8.4)$$

$$T_0 = T_1 + T_2U + T_3U^2 \qquad (6.8.5)$$

the coefficients of which are given in table (6.8.1).

Coefficient	**Value**	**Coefficient**	**Value**
U_0 /μs	5.877146	C_3/ kPa μs^{-2}	107466.83
Y_1 /(°C μs^{-1})	-3881.938	D_1	0.0267322
Y_2 /(°C μs^{-2})	-9586.934	D_2	-0.3599045
Y_3 /(°C μs^{-3})	16600.28	T_1/μs	24.94856
C_1/kPa	33876.052	T_2	0.1861965
C_2/ kPa μs^{-1}	2432.6106	T_3/μs	14.93324

Table (6.8.1): Coefficients used to determine the pressure from the digiquartz pressure transducer

The gauge was previously calibrated by Boyes [59] by comparison with an oil lubricated pressure balance. Large deviations from the manufacturers calibration and hysteresis over a closed loop in pressure were found. The results of the calibration are included here for convenience. The pressure (p) indicated by the digiquartz, using equation (6.8.2) deviates from that given by the pressure balance, to 100 Pa, by

$$\delta \mathrm{P} = j\,\mathrm{p} + k\,\mathrm{p}^4 + l\,\mathrm{p}^5 + m\,\mathrm{p}^6 + n\sin\left(\frac{2\pi\,\mathrm{p}}{\mathrm{p}^*}\right) \qquad (6.8.6)$$

where $j = 0.14188$, $k = -0.1515\times10^{-1}$, $l = 0.4244\times10^{-2}$, $m = -0.2771\times10^{-3}$, $n = 0.25024$ and $\mathrm{p}^* = 4228.51$ kPa. At the highest pressures of about 7 MPa the deviation is as much as 2.5 kPa, giving a fractional imprecision of 3.6×10^{-4}.

For measurements involving the sphere and the hemisphere both gas lines to the digiquartz pressure transducer were opened. The sphere was pressure compensated and because purity of the gas sample was not important it was possible to use the same (low-grade) argon as both the ballast in the sphere's pressure vessel and as the sample gas. The whole system could then be opened initially to ensure equal pressure in both the sphere and the hemisphere and also in the sphere pressure vessel. When using research grade argon for the measurements, the gas filling the pressure vessel was isolated from that filling the resonator and lower-grade 'pureshield' argon was used as the ballast gas. After equilibr ation the valve at the top of the sphere could be closed off and the pressure in both the sphere and the hemisphere measured using the digiquartz. The differential pressure transducer (DPT) was operated as a null-reading device as described previously and was utilised only to check that the pressure difference between the sphere and its pressure vessel remained zero. The details and calibration of the DPT have been discussed previously (section 4.19).

CHAPTER 7

Calibration of Hemispherical Resonator

PART I The Speed of Sound

(7.1) Introduction

Measurements of the resonance frequencies and halfwidths of the radial modes in the hemispherical resonator allow highly accurate, precise values of the speed of sound to be calculated for a particular gas. However, initial analysis of the measured frequencies and halfwidths directly yields values of (u/a), since the speed of sound is given by,

$$\left(\frac{u}{a}\right)(T,p)=\left(\frac{2\,\pi\,F_N}{\nu_{0,n}}\right) \tag{7.1.1}$$

where F_N is the corrected resonance frequency, u is the speed of sound, a is the cavity radius and $\nu_{0,n}$ is the eigenvalue of the $(0,n)$ mode. In order to obtain the more useful quantity u it was therefore essential to determine the absolute value of the radius of the cavity at any temperature and pressure *i.e.* $a\,(T, p)$.

It would be expected that the hemispherical geometry, and hence the radius, were dependent on both the temperature and the internal pressure. These dependencies had not been investigated previously for a hemispherical shell and no exact formalism exists. The dilation of the cavity, when subjected to internal pressure, is likely to be similar to that of a sphere for the spherical wall, but like the end-plate of a cylinder for the equatorial surface and it is therefore difficult to model mathematically. It is likely that the equatorial surface undergoes some bending, particularly at high pressures, and it is not known how this will affect the symmetry of the radial modes. This geometry change further complicates the

development of a useful theoretical approach and it was therefore necessary to determine the radius empirically by obtaining measurements over the full range of temperature and pressure.

The precision with which the speed of sound in the hemispherical cavity may be calculated is limited by the precision with which the radius is known. At any state point, to calculate the radius within the required accuracy, it was necessary to perform measurements in a well-characterised gas in which the speed of sound is well known; the resulting values of $a(T, p)$ were then fitted accordingly.

(7.2) Reference Data

Argon is the usual choice of calibration gas as it is non-relaxing and its thermophysical properties are known with a very high degree of accuracy. However, nitrogen was also suitable for calibration purposes because although it is a relaxing gas, its thermophysical properties are also very well known. The speed of sound in nitrogen was calculated from the acoustic virial coefficients given in reference [59]. These measurements were obtained using the stainless steel spherical resonator described in section (4.16) and were sufficiently accurate for calibration purposes. The reference data were also collected over temperature and pressure ranges similar to those used for our calibration measurements.

The zero grade nitrogen, supplied by BOC plc. with a stated mole fraction purity of 0.99999, was used without any attempt at additional purification. The nitrogen gas from which the reference data were obtained was also zero grade, from the same supplier and also underwent no further purification.

Six isotherms were studied at temperatures close to 304 K, 314 K, 322 K, 330 K, 340 K and 349 K. The resonance frequencies and halfwidths of the first four radial modes were measured for each isotherm using the procedure set out in section (6.2). For each isotherm, the initial pressure p_1 was limited to the highest pressure obtainable from the cylinder which was approximately 7 MPa. Subsequent points were taken at decrements in pressure of approximately $(p_1/10)$ until the measured pressure was $(p_1/10)$ or, in practice,

about 1 MPa, at which stage two or three further points were taken at about 500 kPa, 200 kPa and 100 kPa.

(7.3) Analysis

It is usual practice to obtain the corrected resonance frequencies F_N by summing the measured resonance frequency $f_{0,n}$, and the various contributions *i.e.*

$$F_N = f_{0,n} + \Delta f_{\mathrm{v}} + \Delta f_{\mathrm{h}} + \Delta f_{\mathrm{t}} + \Delta f_{\mathrm{sh}} \qquad (7.3.1)$$

where the losses which arise through the thermal and viscous boundary layers are denoted by Δf_{h} and Δf_{v} respectively; perturbations to the resonance frequency caused by openings in the cavity wall are denoted by Δf_{t} and the losses due to shell motion are given by Δf_{sh}. The first three correction terms (Δf_{v}, Δf_{h} and Δf_{t}) may be easily modelled theoretically for a hemispherical cavity as seen in chapter 3. However, as mentioned previously, it is difficult to model the dilation of a hemisphere and therefore to predict the behaviour of Δf_{sh}. So that predictions about Δf_{sh} can be made the corrected resonance frequency is initially approximated by the first four terms of equation (7.3.1).

To assess the model, it is useful to look at the excess halfwidths of the individual modes. The fractional excess halfwidths are given by,

$$\frac{\Delta g}{f_{0,n}} = \left(\frac{g_{0,n} - g_{\mathrm{h}} - g_{\mathrm{v}} - g_{\mathrm{b}} - g_{\mathrm{t}}}{f_{0,n}} \right) \qquad (7.3.2)$$

where the measured frequency and halfwidth are given by $f_{0,n}$ and $g_{0,n}$ respectively and g_{h}, g_{v}, g_{b} and g_{t} are the contributions to the halfwidth from the thermal and viscous boundary layers, through bulk dissipation in the gas and from openings in the resonator wall.

The fractional excess halfwidths of all the modes, are shown as a function of temperature and pressure in figures (7.3.1) to (7.3.4). For all the modes ($\Delta g/f_{0,n}$) is always positive by a fairly significant amount. The (0,2) mode is the most severely affected, showing a different pressure and temperature dependence to that exhibited by the (0,3), (0,4) and (0,5) modes and will be discussed separately. Since equation (7.3.1) fails to predict adequately the resonance halfwidths it was decided that it would be more reliable to obtain

the corrected resonance frequency, of individual modes, from the sum of the measured frequency and halfwidth *i.e.*

$$F_N = f_{0,n} + g_{0,n} \tag{7.3.3}$$

The approach taken by equation (7.3.3) has the advantage that it allows for unknown or under-estimated losses which nevertheless perturb the resonance frequencies to be included in the corrected frequency F_N. This is particularly important if unaccounted correction terms give significantly large excess halfwidths.

As the effects of shell motion are expected to contribute only to the real component of the complex frequency, it is possible by combining equations (7.1.1) and (7.3.3) and comparing with known values of $u\,(T,\ p)$ to assess these effects. It may be, that the derived shell motion is in keeping with the expected behaviour of the geometry based on the theory of elasticity, in which case a useful approximation to Δf_{sh} could be developed based on equation (3.19.2). Otherwise, when the effects of shell motion are deemed to be too dissimilar to this model, an empirical approach is more useful.

Figure (7.3.1): Fractional excess halfwidths of the (0,2) mode in nitrogen as a function of pressure

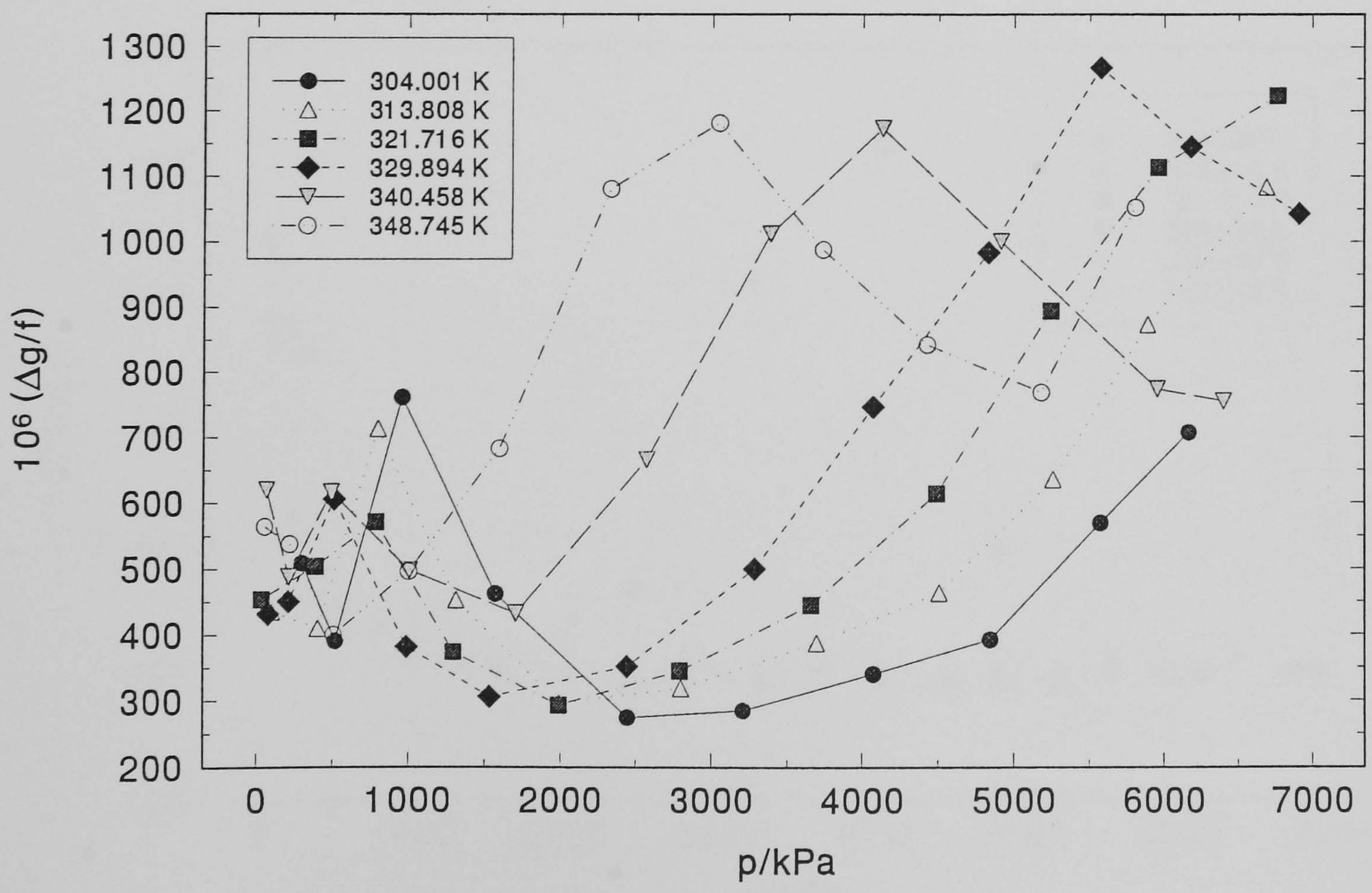

Figure (7.3.2): Fractional excess halfwidths of the (0,3) mode in nitrogen as a function of pressure

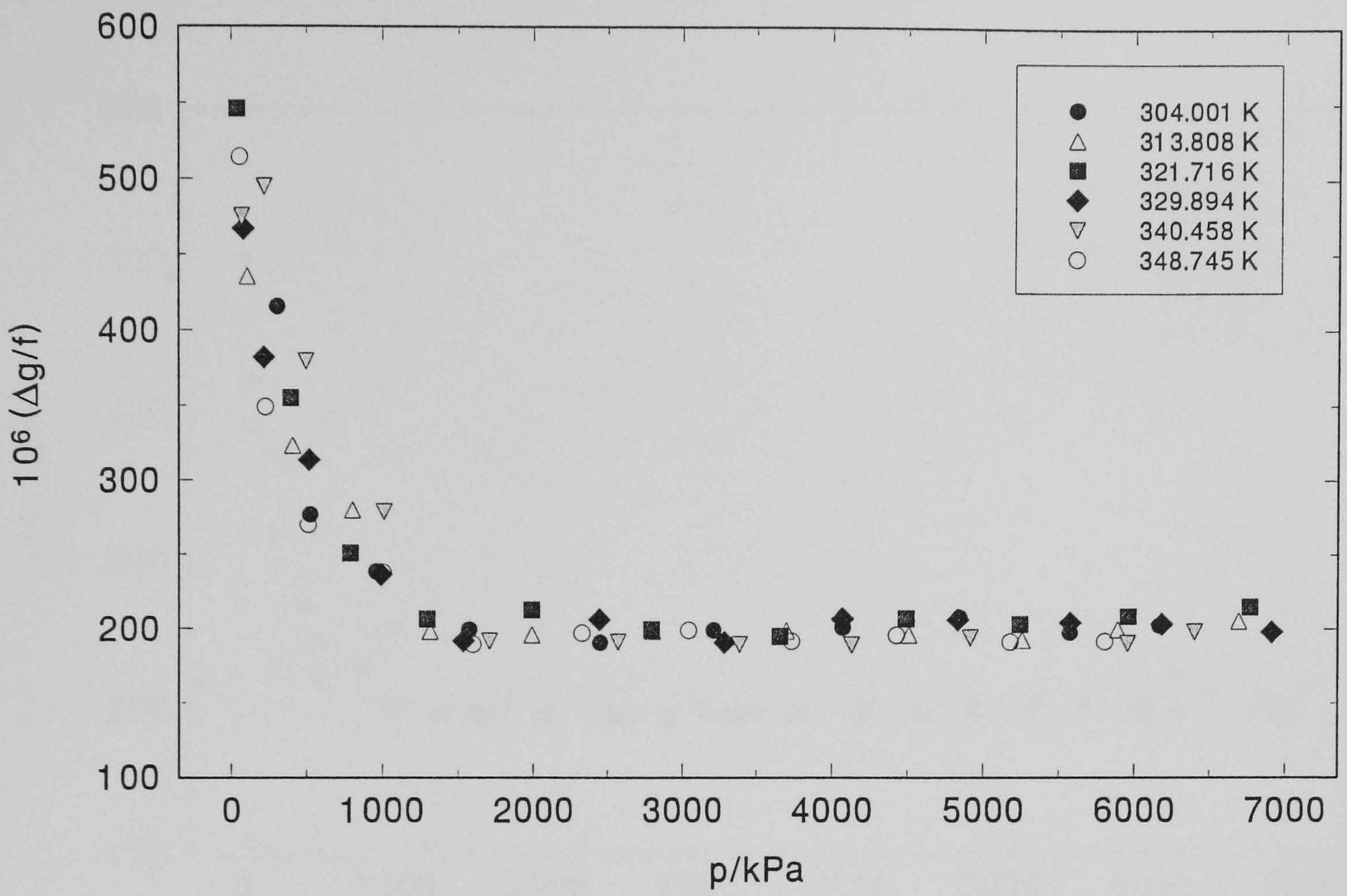

Figure (7.3.3): Fractional excess halfwidths of the (0,4) mode in nitrogen as a function of pressure

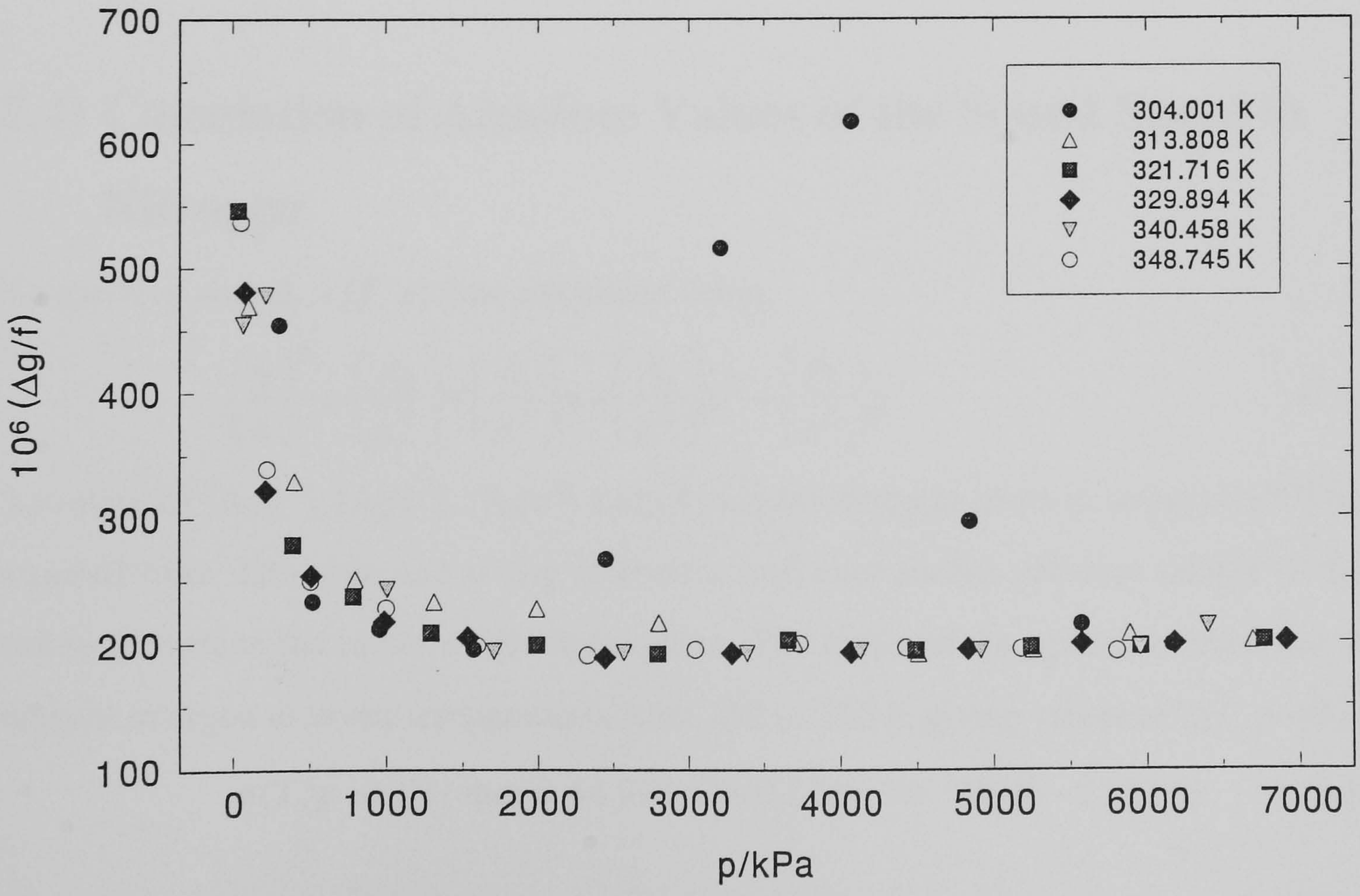

Figure (7.3.4): Fractional excess halfwidths of the (0,5) mode in nitrogen as a function of pressure

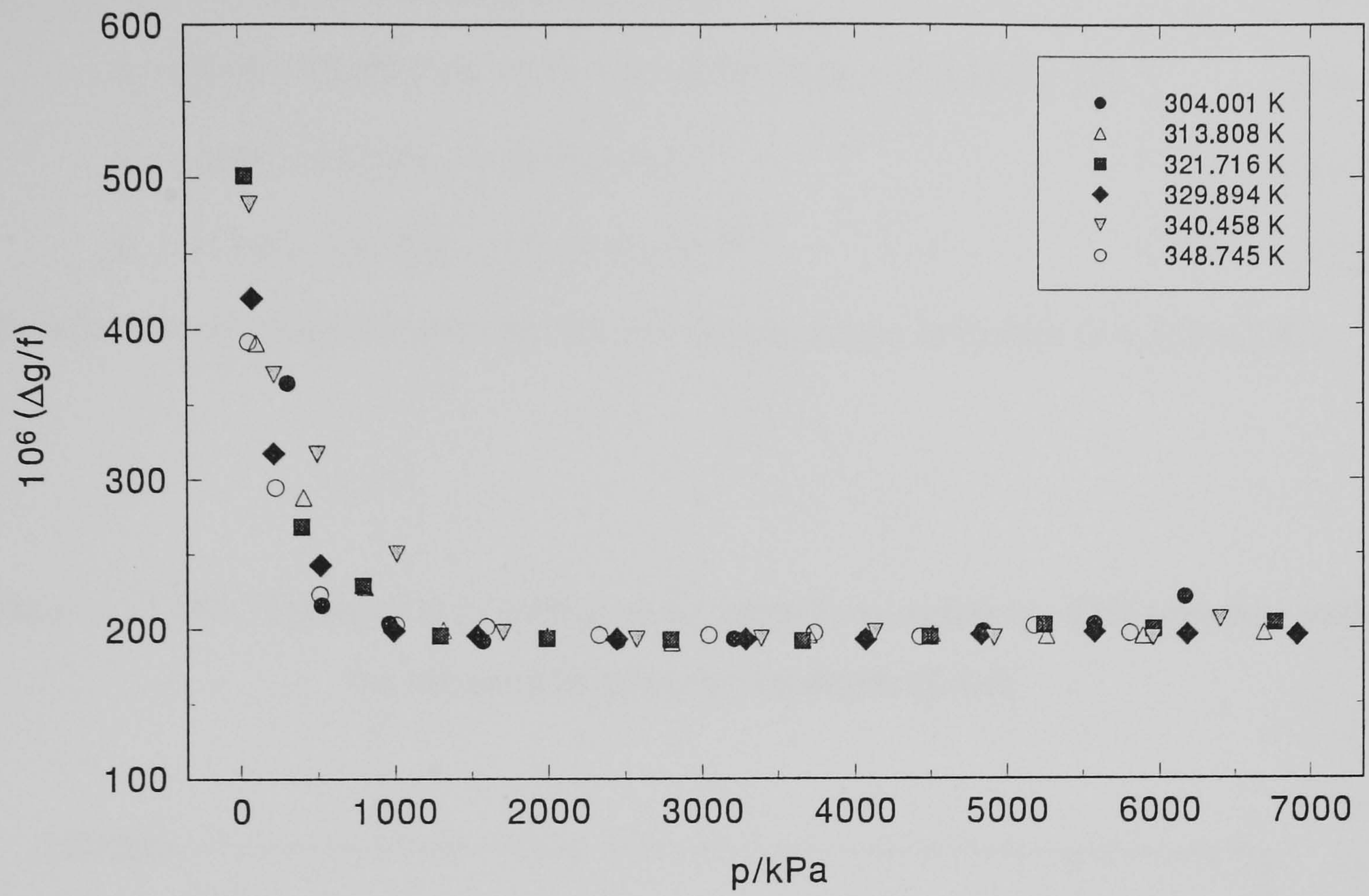

(7.4) Calculation of Absolute Values of the Sound Speed in Nitrogen

The speed of sound, u (T, p) was calculated using,

$$\left(\frac{u}{a}\right)^2 = \left(\frac{A_0}{a^2}\right) + \left(\frac{A_1}{a^2}\right)p + \left(\frac{A_2}{a^2}\right)p^2 + \left(\frac{A_3}{a^2}\right)p^3 \qquad (7.4.1)$$

The values of (A_0/a^2), (A_1/a^2), (A_2/a^2) and (A_3/a^2) for nitrogen given in reference[59] were extracted from data obtained at five isotherms and over similar pressure ranges to those used to determine the radius of the hemisphere. The radius of the spherical resonator was obtained in argon at seven temperatures from 250 to 350 K giving values of $a(T, p\rightarrow 0)$ as,

$$a(T, p \rightarrow 0)/\text{mm} = 44.97142 + 0.738\times10^{-3}(T/\text{K} - 273.16) \qquad (7.4.2)$$

Values of A_0, A_2 and A_3 were each fitted against temperature using a simple linear regression, whilst the values of A_1 quoted were fitted using a second order polynomial giving,

$$A_0 = 113492 + 415.64\,(T/\mathrm{K} - 273.16) \tag{7.4.3}$$

$$A_1 = \left\{696 + 15.45\,(T/\mathrm{K} - 273.16) - 0.058\,(T/\mathrm{K} - 273.16)^2\right\} \times 10^{-6} \tag{7.4.4}$$

$$A_2 = \left\{940 - 4.1(T/\mathrm{K} - 273.16)\right\} \times 10^{-13} \tag{7.4.5}$$

$$A_3 = \left\{1400 - 32\,(T/\mathrm{K} - 273.16)\right\} \times 10^{-21} \tag{7.4.6}$$

The reference data together with the adopted fits are shown in figures (7.4.1) to (7.4.4).

Figures (7.4.1): Values of the coefficient A_0 taken from reference [59] together with the adopted fit given by equation (7.4.3)

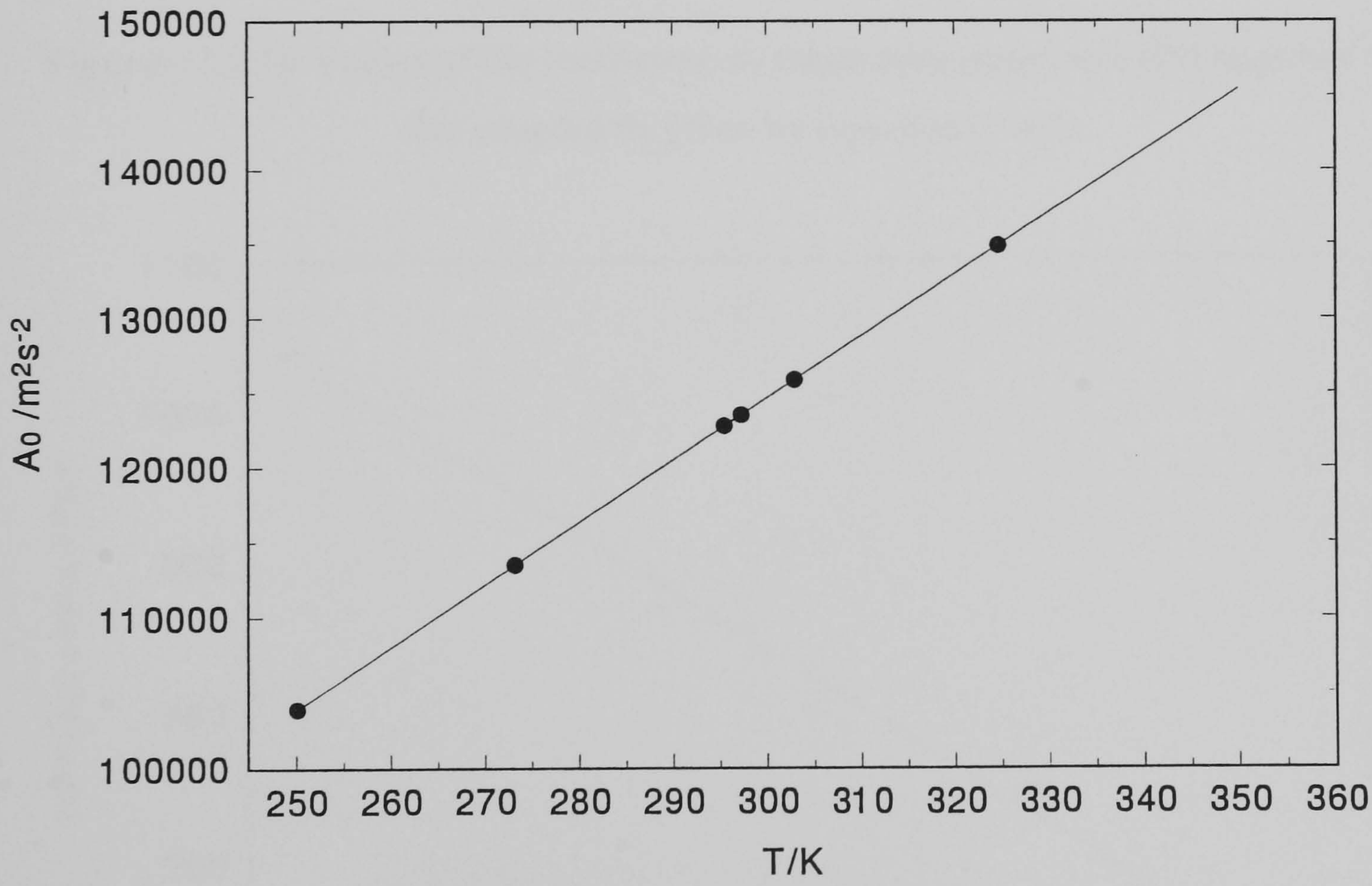

Figures (7.4.2): Values of the coefficient A_1 taken from reference [59] together with the adopted fit given by equation (7.4.4)

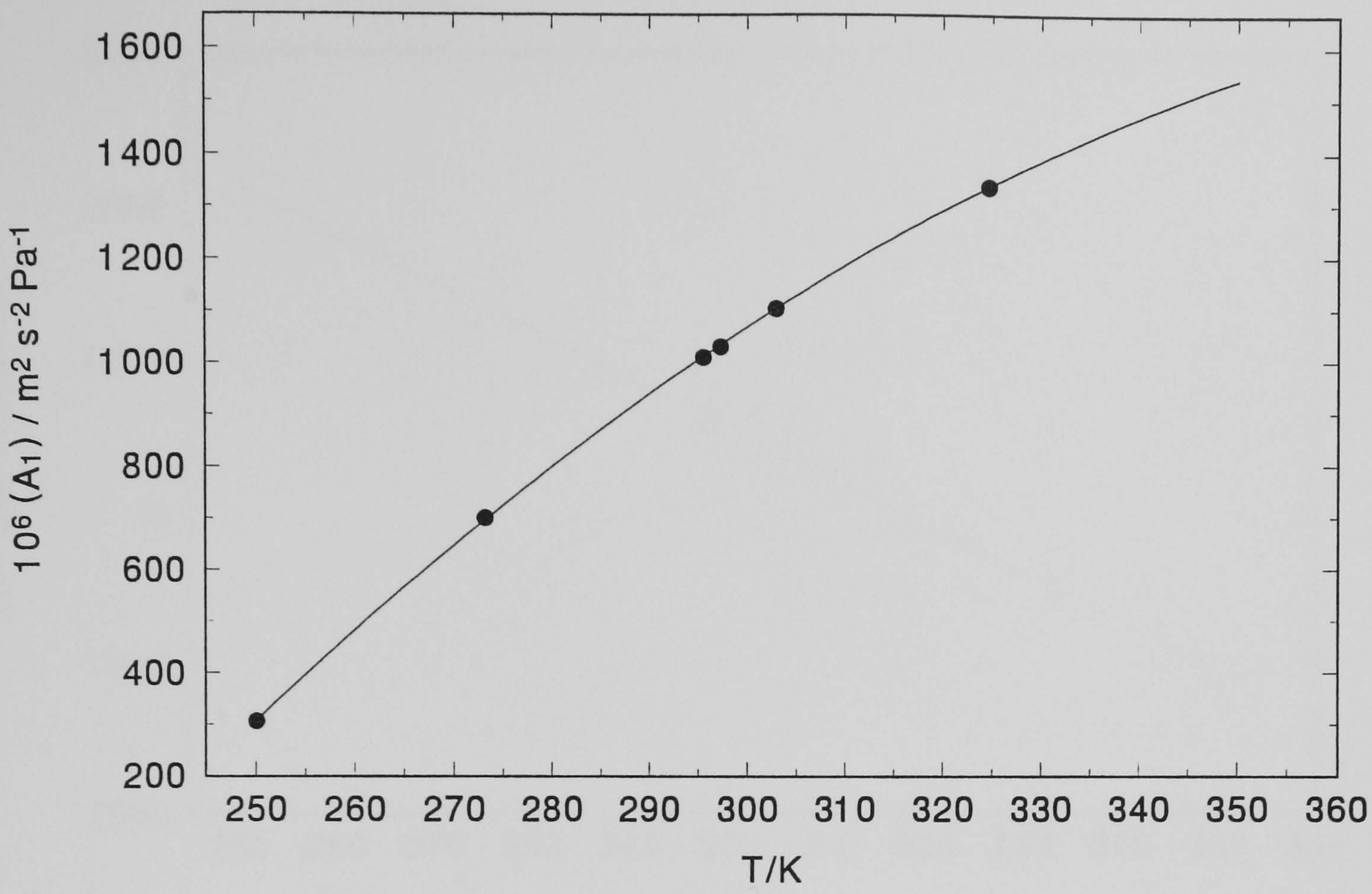

Figures (7.4.3): Values of the coefficient A_2 taken from reference [59] together with the adopted fit given by equation (7.4.5)

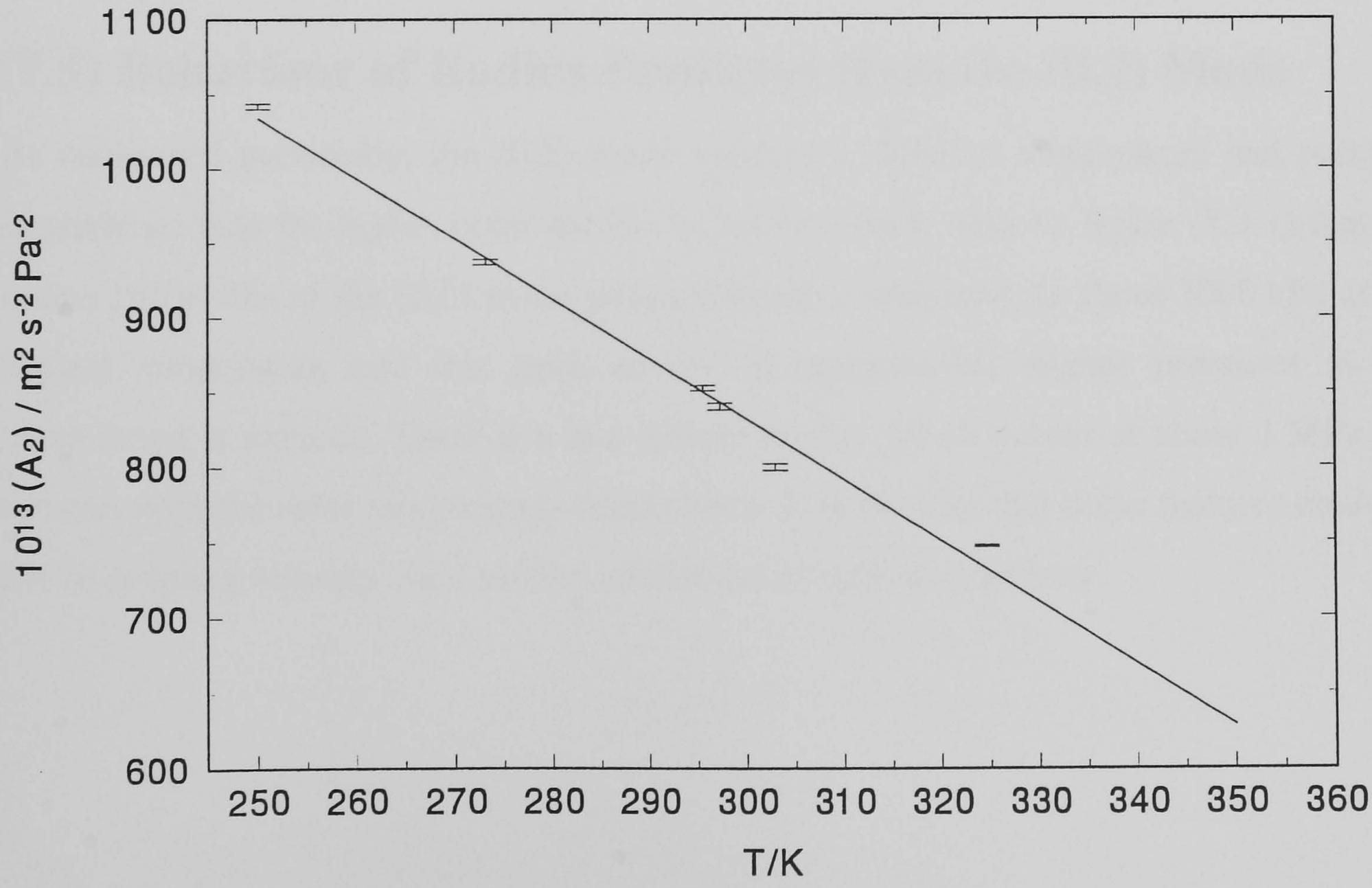

Figures (7.4.4): Values of the coefficient A_3 taken from reference [59] together with the adopted fit given by equation (7.4.6)

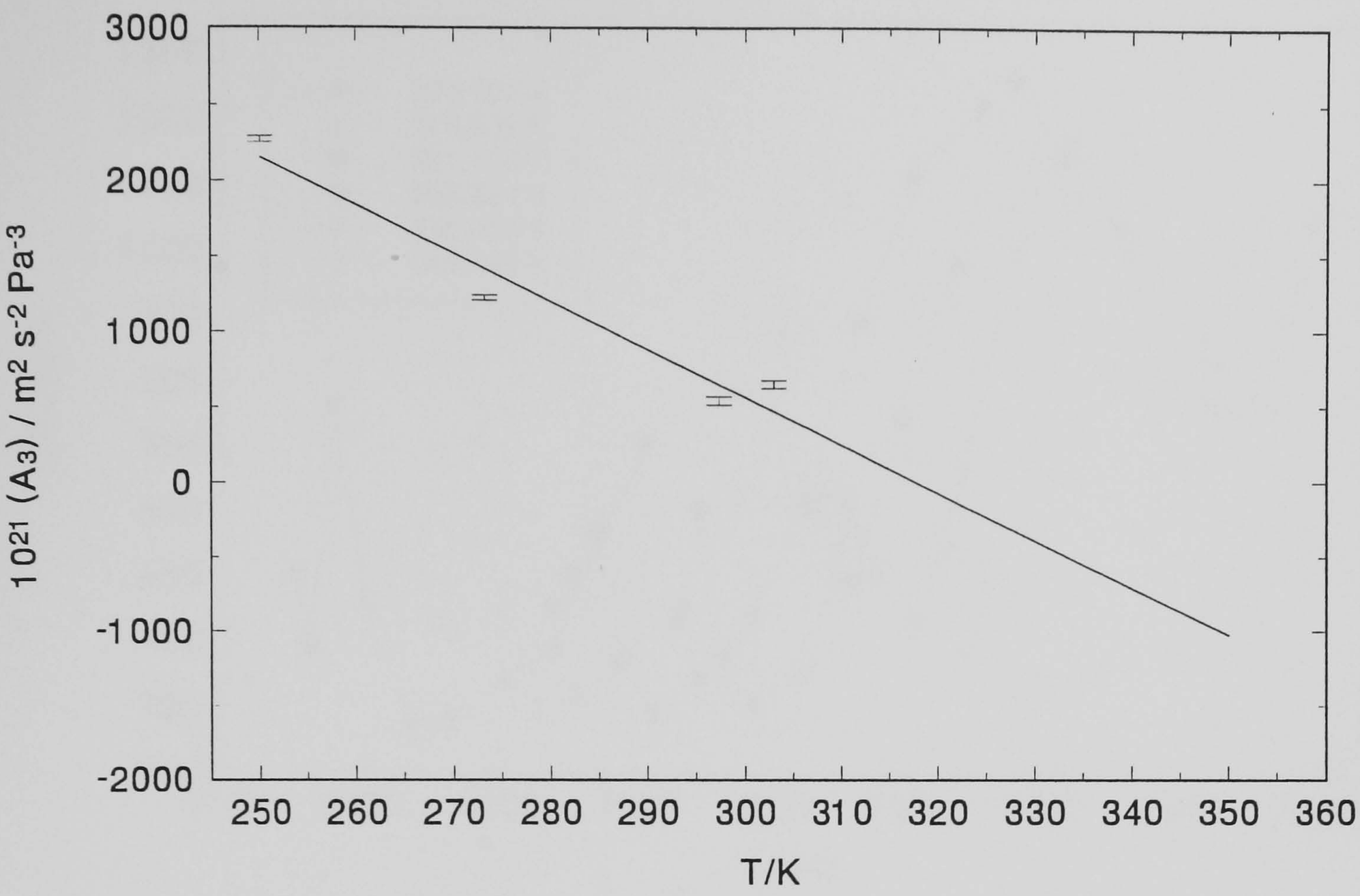

(7.5) Behaviour of Radius Predicted from the (0,2) Mode

As mentioned previously, the (0,2) mode exhibits a different temperature and pressure dependence than the higher order modes. It can be clearly seen by figure (7.3.1) that the excess halfwidths of the (0,2) mode passes through a maximum at about 3000 kPa at the highest temperature and this peak occurs at progressively higher pressures as the temperature is reduced. There is a less intense feature which occurs at about 1 MPa and behaves with the same temperature dependence. It is thought that these features could be due to coupling between shell motion and modes of similar symmetry.

Figure (7.5.1): Fractional excess halfwidths of the (0,2) mode in nitrogen as a function of frequency

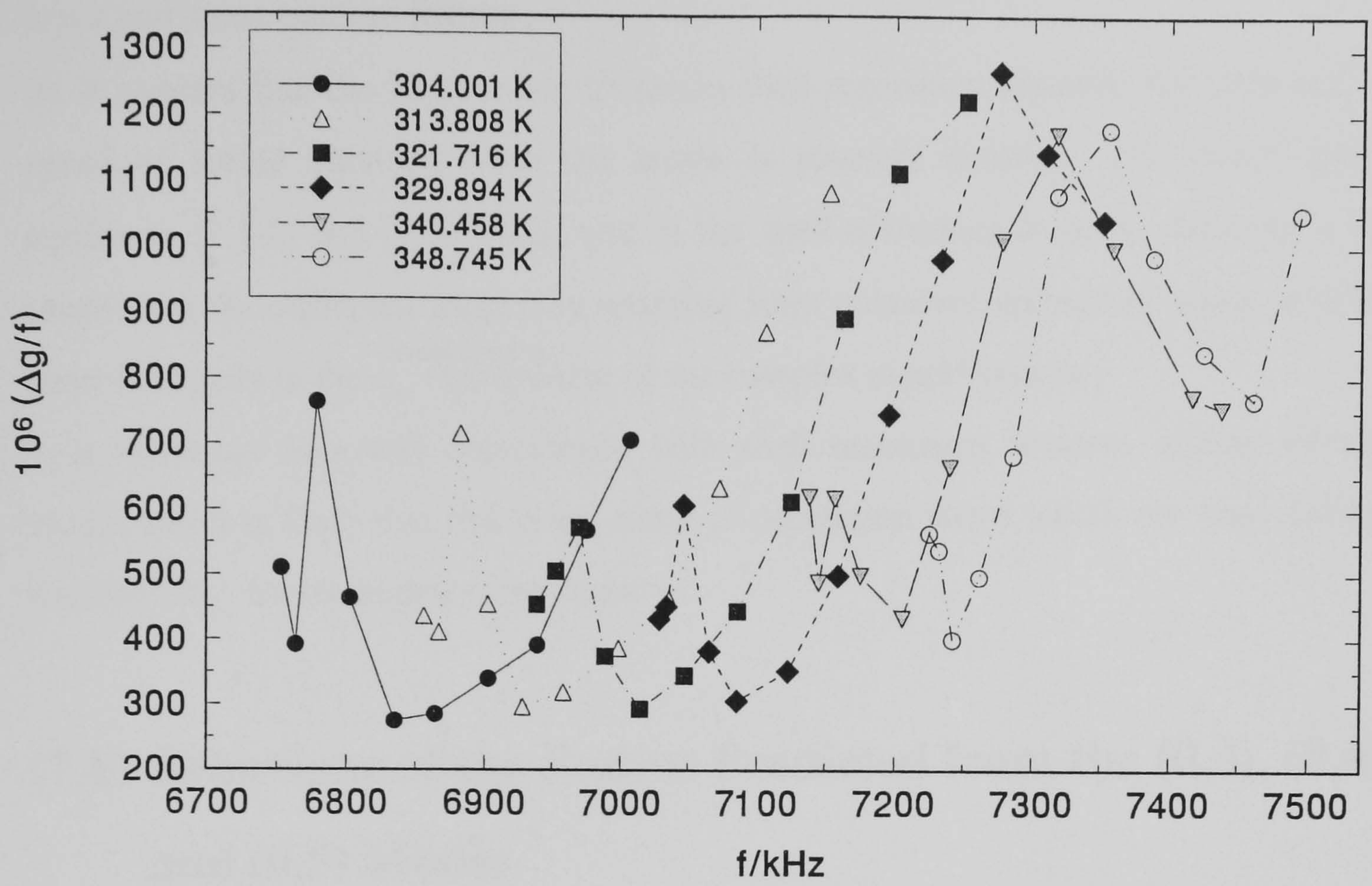

Figure (7.5.2): Frequencies at which maximum excess halfwidths occur for the (0,2) mode in nitrogen

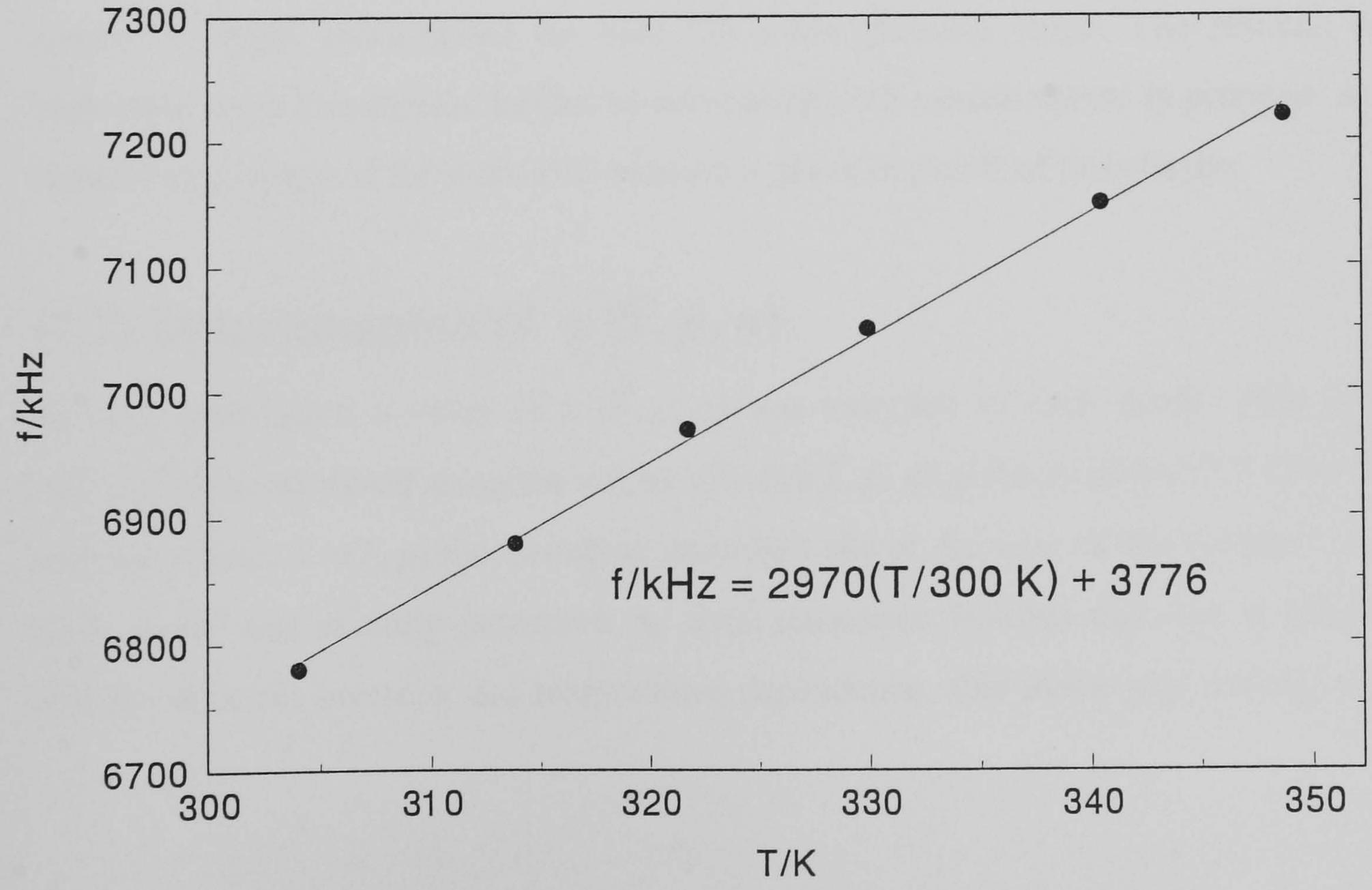

The temperature dependency of the pressure (and hence frequency) at which these maxima in $\Delta g^{ex}(0,2)$ occur is simple as shown by figures (7.5.1) and (7.5.2) and confirms that this is not just some random feature.

As it appears that the (0,2) mode traverses shell resonance features the accuracy of the speed of sound obtained from this mode is severely reduced. The model given by equations (7.1.1) and (7.3.3) fails and at the shell resonance there is obviously a severe shortfall in the corrected frequency resulting from unknown correction terms which must contribute only to the imaginary component of the complex eigenfrequency.

It is uncertain how this coincidence with shell resonance features affects subsequent modes and it is likely that this is the cause of correction terms which are unaccounted for theoretically, for the higher order modes.

(7.6) Behaviour of the Radius Predicted from the (0,3), (0,4) and (0,5) Modes

The excess halfwidths of these higher order modes show a fairly obvious trend, with the model failing most severely at the lowest pressures. The failure at low pressures could be due to slots or holes which have not been accounted for, but the pressure dependence observed implies that it is unsatisfactory to use equation (7.3.1) as there are obviously correction terms unaccounted for over the entire pressure range. The residual excess halfwidths were investigated further by comparing with measurements in propene. A more detailed description of the halfwidth analysis is given in part II of this chapter.

(7.7) Determination of $a\,(T, p, n)$

At each state point a value of $a\,(T, p, n)$ was assigned to each mode. This value of $a\,(T,p,n)$ was calculated using the values of $(u/a)(T, p, n)$ given in tables (7.7.1) to (7.7.6) and the values of $u(T, p)$ calculated as described above. In view of the evidence that the (0,2) mode was severely perturbed by shell resonance features and that it exhibits an entirely different pressure and temperature dependence, this mode was initially rejected

Table (7.7.1): Values of a (p, T) determined from calibration using nitrogen at temperature 304.001 K and at pressures p

T = 304.001 K					
p/kPa	Mode index n	a/mm	p/kPa	Mode index n	a/mm
6165.99	2	37.646843	3209.19	2	37.642239
	3	37.631439		3	37.629005
	4	37.632023		4	37.629101
	5	37.632889		5	37.628880
5572.44	2	37.648628	2446.77	2	37.631184
	3	37.630890		3	37.626938
	4	37.630920		4	37.626678
	5	37.631062		5	37.626225
4841.40	2	37.646721	1570.61	2	37.613625
	3	37.629021		3	37.624531
	4	37.630135		4	37.624538
	5	37.630177		5	37.624573
4072.06	2	37.637547	958.83	2	37.609444
	3	37.629822		3	37.624386
	4	37.629868		4	37.624790
	5	37.629929		5	37.624554

Table (7.7.2): Values of a (p, T) determined from calibration using nitrogen at temperature 313.808 K and at pressures p

T = 313.808 K					
p/kPa	Mode index n	a/mm	p/kPa	Mode index n	a/mm
6689.93	2	37.633415	2801.50	2	37.649776
	3	37.637753		3	37.636158
	4	37.637455		4	37.635998
	5	37.637630		5	37.636086
5889.39	2	37.646767	1990.47	2	37.638306
	3	37.637505		3	37.634403
	4	37.637630		4	37.634872
	5	37.637547		5	37.634274
5258.64	2	37.655331	1311.85	2	37.624573
	3	37.637436		3	37.633720
	4	37.637684		4	37.633423
	5	37.637711		5	37.633877
4507.99	2	37.655674	802.55	2	37.620853
	3	37.636604		3	37.633675
	4	37.636234		4	37.633682
	5	37.636578		5	37.633656
3696.70	2	37.648739			
	3	37.635918			
	4	37.636242			
	5	37.636002			

Table (7.7.3): Values of a (p, T) determined from calibration using nitrogen at temperature 321.716 K and at pressures p

T = 321.716 K					
p/kPa	Mode index n	a/mm	p/kPa	Mode index n	a/mm
6763.41	2	37.619984	2793.53	2	37.649139
	3	37.645535		3	37.640839
	4	37.645527		4	37.640926
	5	37.645512		5	37.640854
5959.22	2	37.639584	1987.55	2	37.647572
	3	37.643581		3	37.640717
	4	37.643597		4	37.640263
	5	37.643597		5	37.640533
5242.36	2	37.649914	1292.95	2	37.634026
	3	37.643536		3	37.640320
	4	37.643005		4	37.640320
	5	37.643044		5	37.640343
4490.51	2	37.659508	788.39	2	37.623634
	3	37.642151		3	37.639503
	4	37.642056		4	37.639809
	5	37.642159		5	37.639378
3656.90	2	37.657040			
	3	37.641415			
	4	37.641518			
	5	37.641998			

Table (7.7.4): Values of a (p, T) determined from calibration using nitrogen at temperature 329.894 K and at pressures p

T = 329.894 K					
p/kPa	Mode index n	a/mm	p/kPa	Mode index n	a/mm
6911.95	2	37.639957	3284.22	2	37.665127
	3	37.654736		3	37.649609
	4	37.654720		4	37.649540
	5	37.654716		5	37.649567
6180.48	2	37.633488	2443.06	2	37.655499
	3	37.653088		3	37.648109
	4	37.653023		4	37.649242
	5	37.653095		5	37.648724
5573.71	2	37.632092	1533.50	2	37.652679
	3	37.653965		3	37.647572
	4	37.654099		4	37.647320
	5	37.654018		5	37.647999
4830.84	2	37.656071	989.96	2	37.640072
	3	37.651402		3	37.647221
	4	37.652122		4	37.648396
	5	37.652016		5	37.647511
4069.06	2	37.663898	513.21	2	37.629784
	3	37.651115		3	37.646030
	4	37.651051		4	37.646095
	5	37.651119		5	37.646046

Table (7.7.5): Values of a (p, T) determined from calibration using nitrogen at temperature 340.458 K and at pressures p

T = 340.458 K					
p/kPa	Mode index n	a/mm	p/kPa	Mode index n	a/mm
6399.71	2	37.671658	2569.54	2	37.671532
	3	37.670189		3	37.660210
	4	37.670773		4	37.660164
	5	37.670631		5	37.660156
5956.47	2	37.658577	1704.62	2	37.661037
	3	37.669128		3	37.658558
	4	37.669247		4	37.658562
	5	37.669331		5	37.658604
4913.27	2	37.652401	1009.42	2	37.661812
	3	37.667660		3	37.657345
	4	37.666710		4	37.657230
	5	37.666924		5	37.657322
4129.77	2	37.645309	493.42	2	37.645927
	3	37.664288		3	37.656094
	4	37.664509		4	37.656078
	5	37.664387		5	37.656139
3385.87	2	37.665562			
	3	37.662598			
	4	37.663029			
	5	37.662689			

Table (7.7.6): Values of a (p, T) determined from calibration using nitrogen at temperature 348.745 K and at pressures p

T = 348.745 K					
p/kPa	Mode index n	a/mm	p/kPa	Mode index n	a/mm
5804.43	2	37.677708	2326.88	2	37.663963
	3	37.681393		3	37.667721
	4	37.681374		4	37.668633
	5	37.681412		5	37.668259
5179.31	2	37.683090	1594.98	2	37.669510
	3	37.678120		3	37.666100
	4	37.678570		4	37.666222
	5	37.678371		5	37.666183
4426.80	2	37.659122	1003.72	2	37.667183
	3	37.675468		3	37.663815
	4	37.675236		4	37.664654
	5	37.675453		5	37.664200
3732.90	2	37.659039	509.08	2	37.660912
	3	37.673702		3	37.662941
	4	37.673820		4	37.663773
	5	37.673805		5	37.663017
3042.82	2	37.642216			
	3	37.670536			
	4	37.670547			
	5	37.671047			

from the analysis to determine the radius. The remaining three modes were the (0,3), (0,4) and (0,5) modes.

It can be seen by figures (7.7.1 to 7.7.6) that the radius increases with pressure as expected but the rate of increase changes with temperature. This variation in pressure dependency could be due, in part, to the change of Young's modulus with temperature although this does not change sufficiently quickly with temperature to account fully for this observation. It is more likely that this change in pressure dependency occurs because the shell resonance frequency decreases as the temperature increases and this leads to an apparent increase in the radius. It can also be seen that there is significant disagreement between modes at the same state points although the difference seems to be fairly independent of temperature. If the (0,2) mode does traverse a shell resonance, subsequent modes will be less severely affected as their frequency increases. Indeed, the (0,3) mode shows a considerable separation from the other modes with the (0,4) and (0,5) modes agreeing much more closely as their resonance frequencies become further removed from the suspected shell resonance frequency. This separation is dealt with in section (7.8). At low pressures (those below 500 kPa) the behaviour is less well defined as in most cases the radius would have to fall dramatically in order to yield the correct value of the speed of sound. This anomalous behaviour is due to inadequate modelling of the correction terms in the system at low pressures as has already been demonstrated by the large excess halfwidths in this regime. The data was therefore truncated at pressures below about 500 kPa and all the resulting values of $a\,(T, p, n)$ were fitted using non-linear regression analysis. Terms describing the temperature and pressure dependence of the radius were selected from a bank of 29 terms in p^x and T^x where x = -3, -2, -1, 0, 1, 2, 3 and from the cross terms P^yT^z where y, z = -2, -1, 0, 1, 2. Terms were selected only when the F-level by including the term in the fit was greater than about 10, since the data consisted of about 200 points, this corresponds to terms significant at a probability of 99.95 per cent [115].

Figure (7.7.1): Pressure dependence of radius of hemisphere predicted from the first four radial modes at a temperature of 304.001 K

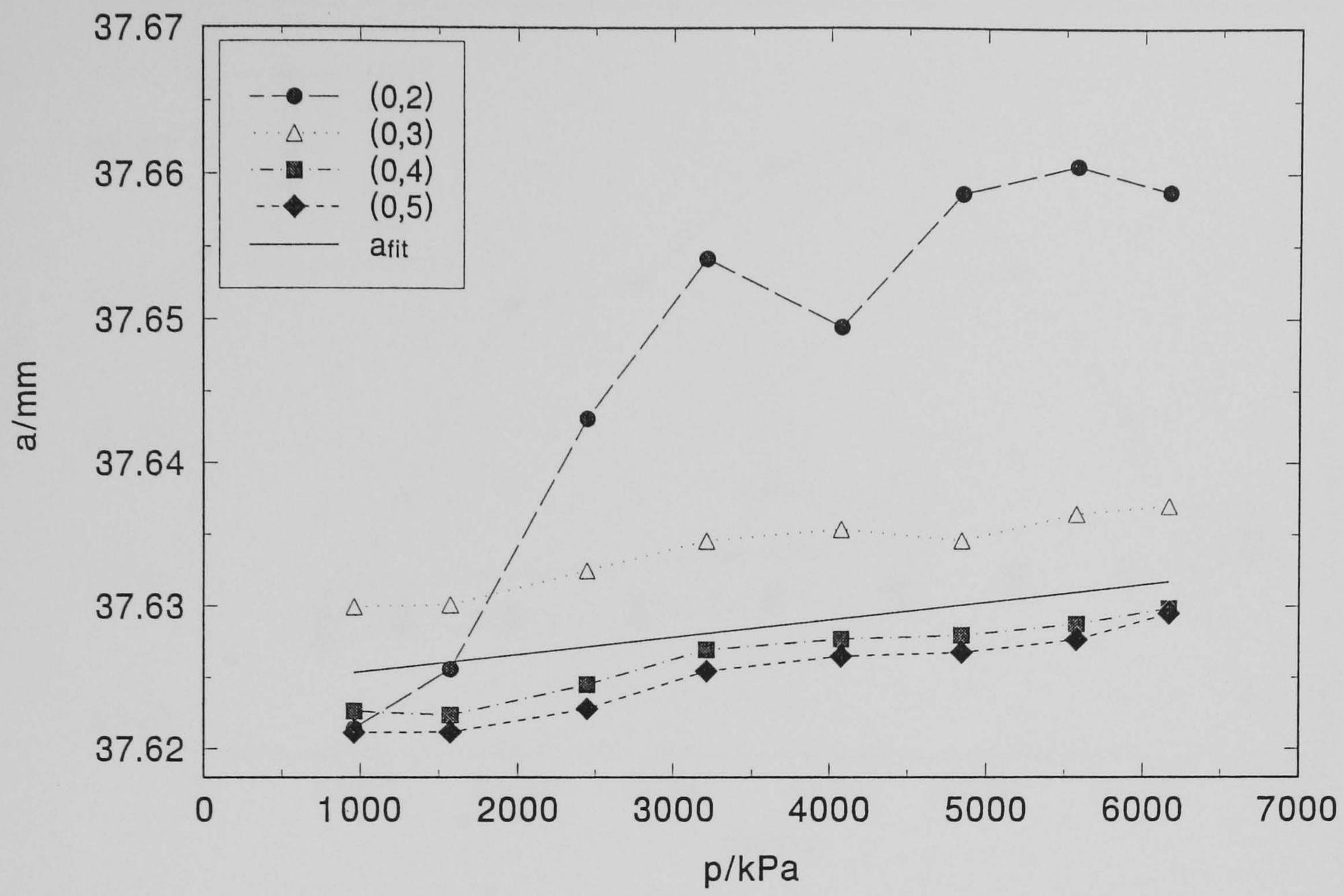

Figure (7.7.2): Pressure dependence of radius of hemisphere predicted from the first four radial modes at a temperature of 313.808 K

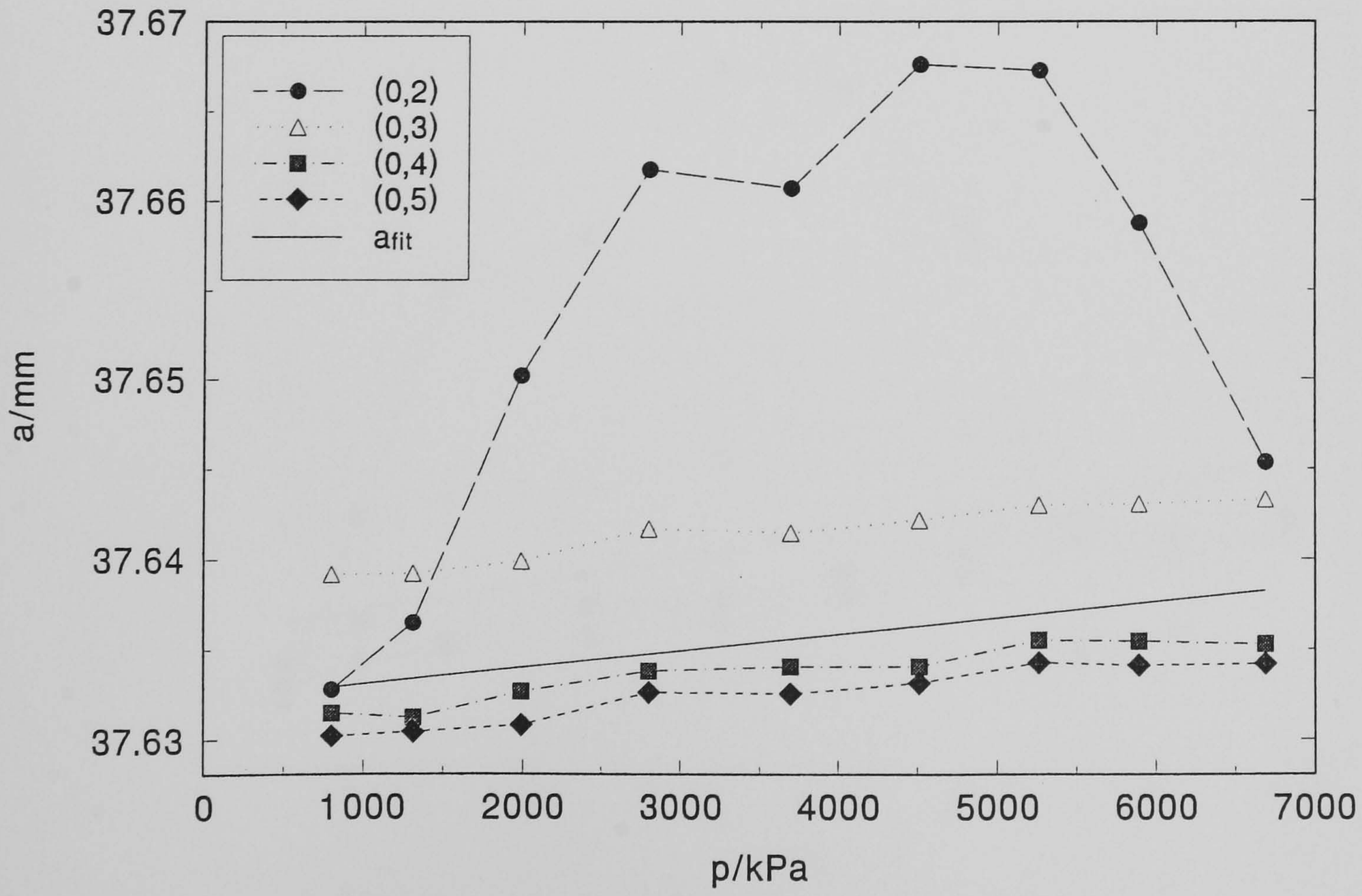

Figure (7.7.3): Pressure dependence of radius of hemisphere predicted from the first four radial modes at a temperature of 321.716 K

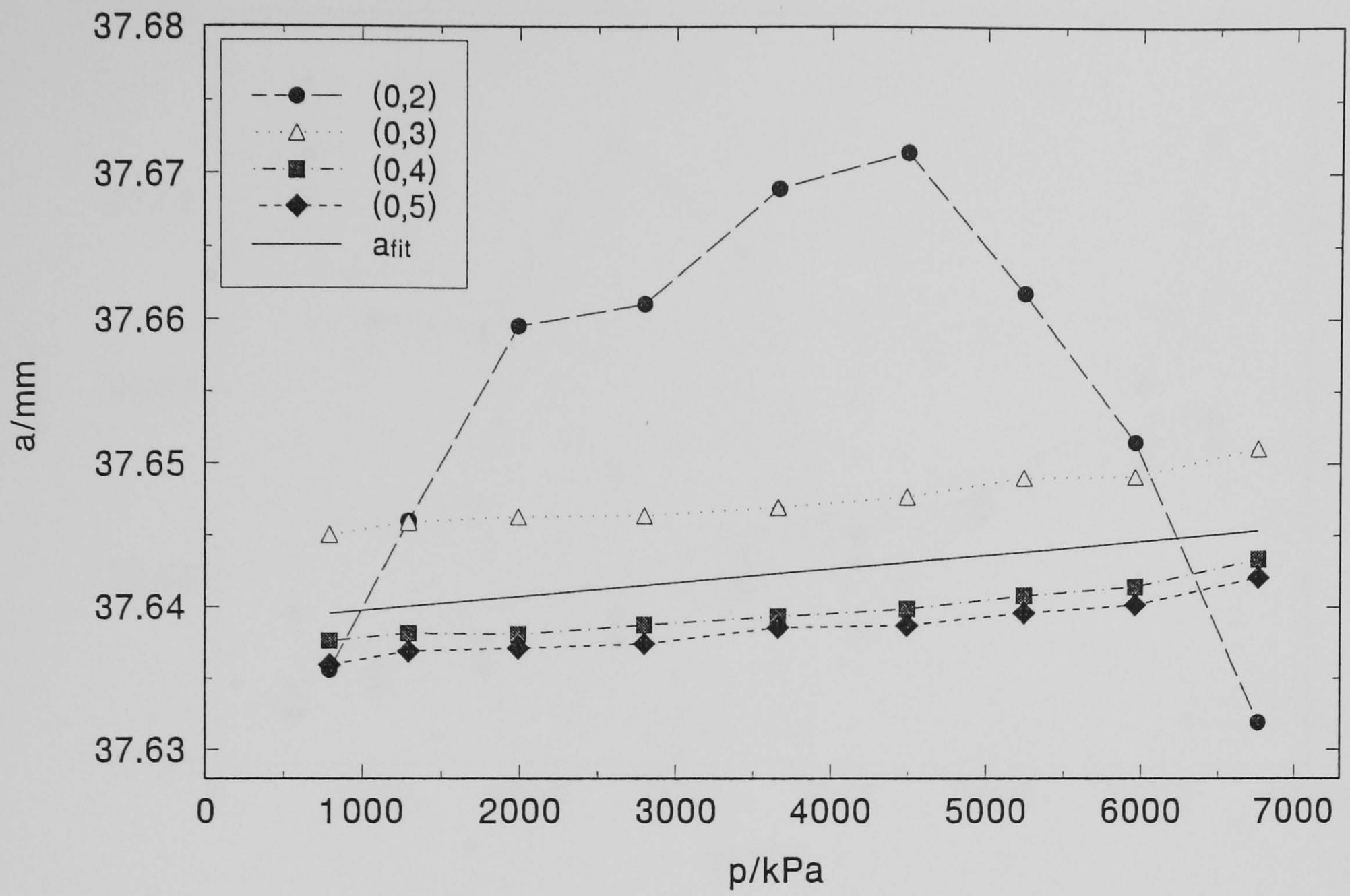

Figure (7.7.4): Pressure dependence of radius of hemisphere predicted from the first four radial modes at a temperature of 329.894 K

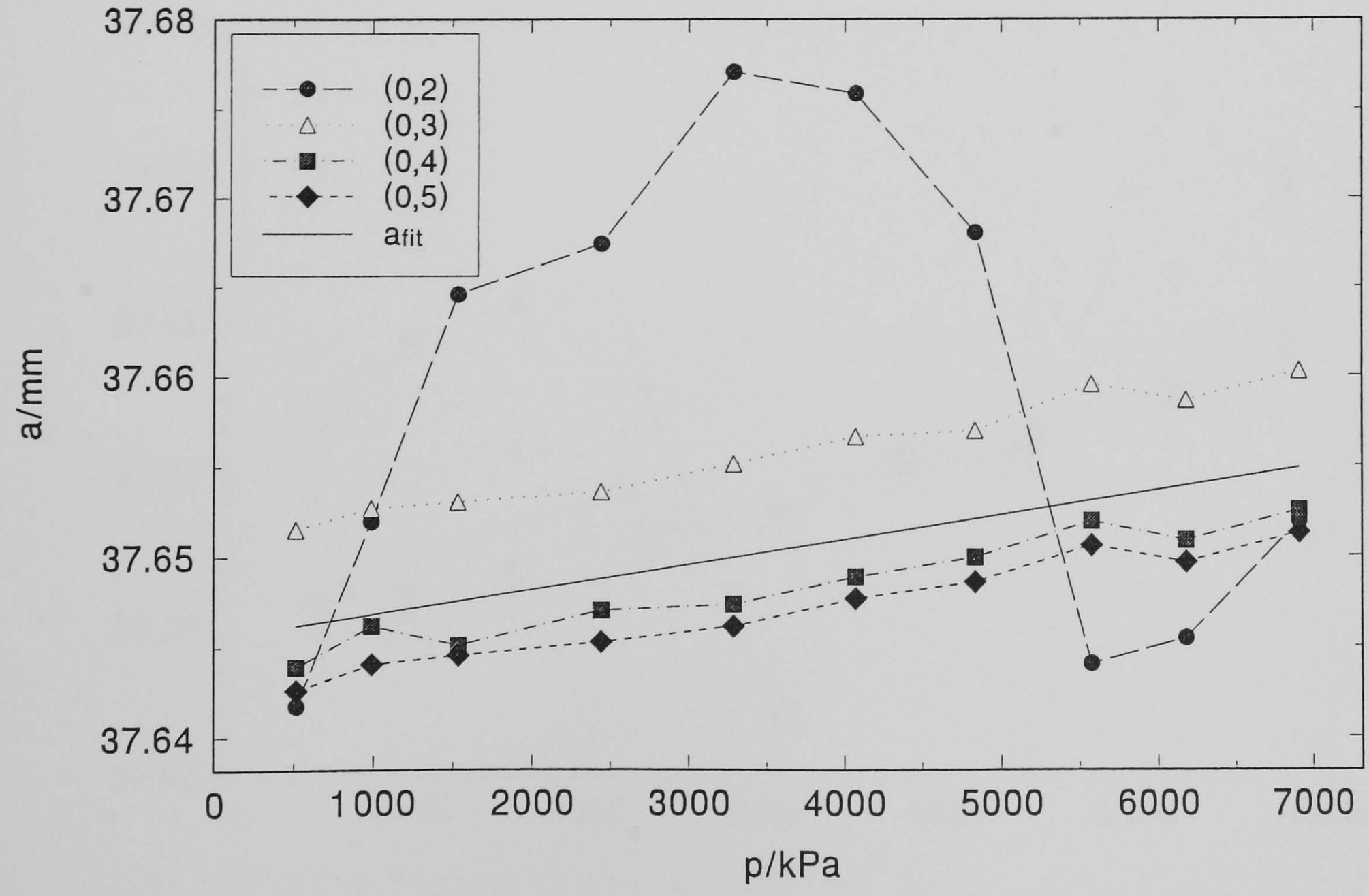

Figure (7.7.5): Pressure dependence of radius of hemisphere predicted from the first four radial modes at a temperature of 340.458 K

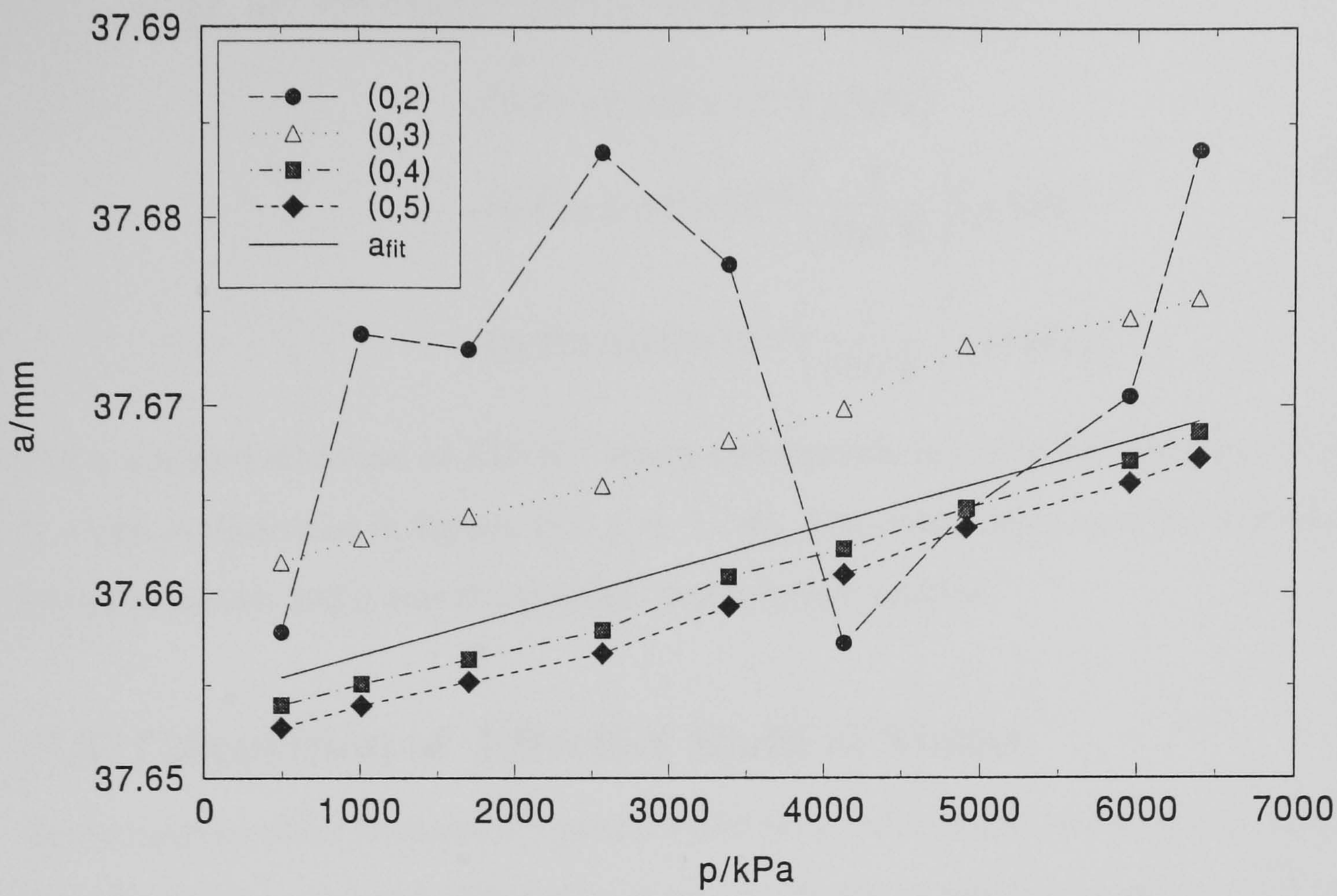

Figure (7.7.6): Pressure dependence of radius of hemisphere predicted from the first four radial modes at a temperature of 348.745 K

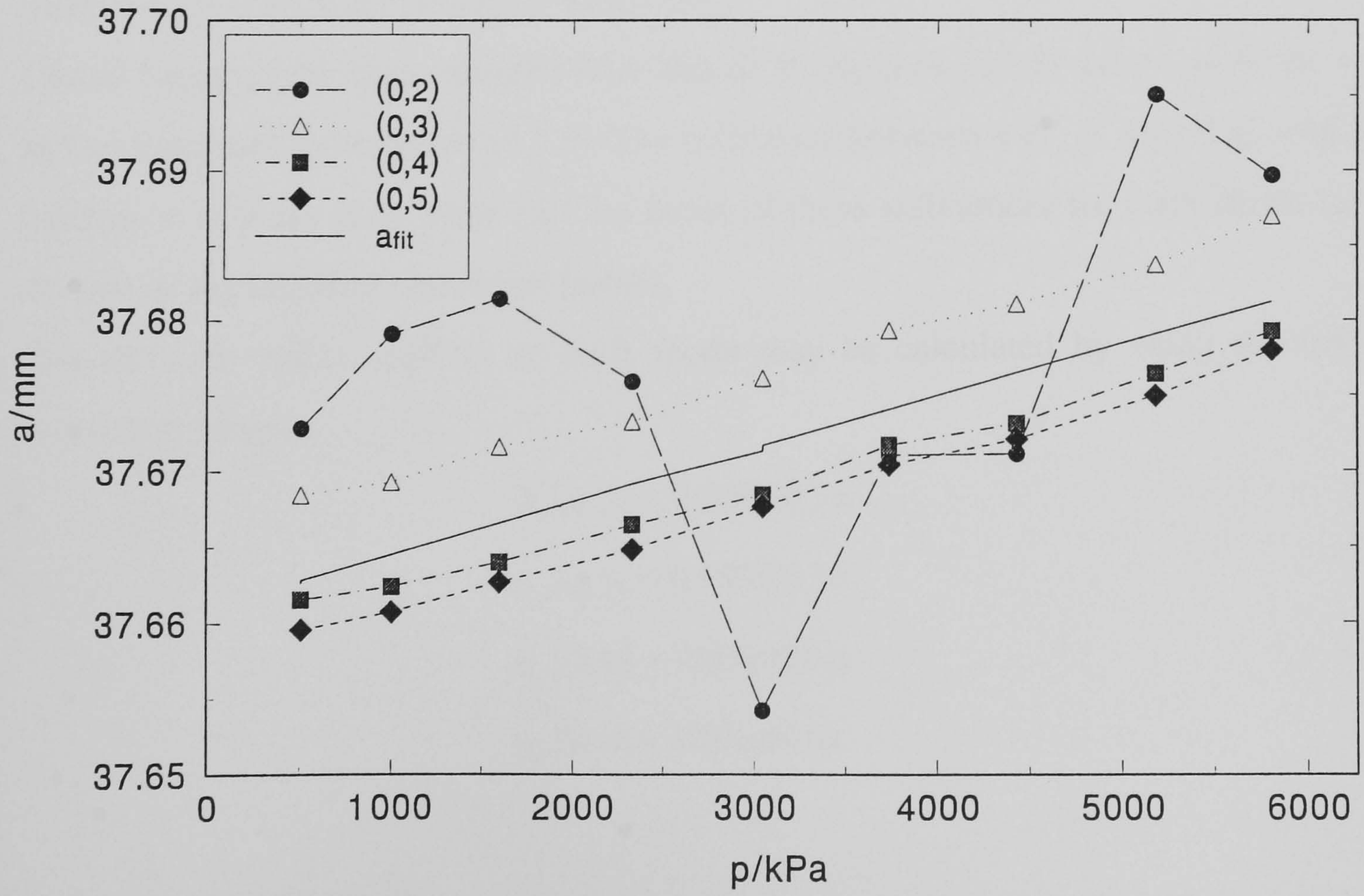

A five term fit was found to describe the data best

$$a_{\text{fit}}(T,p)/\text{mm} = (37.37 \pm 0.02) + (0.25 \pm 0.01)\left(\frac{T}{300\ \text{K}}\right) + (0.24 \pm 0.04)\times 10^{-3}(p/\text{kPa}) - (0.45 \pm 0.08)\times 10^{-3}\left(\frac{T}{300\ \text{K}}\right)(p/\text{kPa}) + (0.21 \pm 0.04)\times 10^{-3}\left(\frac{T}{300\ \text{K}}\right)^2(p/\text{kPa}) \quad (7.7.1)$$

with a standard deviation of 4.0×10^{-3} which corresponds to about 107 ppm in a. It is this fit which is illustrated in figures (7.7.1 to 7.7.6). The mode separation has not yet been solved, however, and it was this problem that was next tackled.

(7.8) Calculation of Effective Radii of Modes

As the modes exhibit the same temperature and pressure dependence but have a significant separation in the expected values of a, it was necessary to calculate a separation constant for each mode which may be based on either an effective radius or an empirical eigenvalue. The correction factors are thought to arise as a result of shell resonance effects leading to mode-dependent terms which contribute only to the real losses (and are therefore not seen in the measured halfwidth).

Global fitting of the data obtained from the (0,3), (0,4) and (0,5) modes gave the best fit as that described by equation (7.7.1). The difference between a (T, p, n) and a_{fit} was then calculated at every state point and the mean of these differences for each mode taken to determine the required correction factors.

The effective radius, $a_e(0,n)$, of each mode may be calculated by using the following correction factors,

$$a_e(0,2) = 0.999683\,a \quad (7.8.1)$$

$$a_e(0,3) = 0.999853\,a \quad (7.8.2)$$

$$a_e(0,4) = 1.000058\,a \quad (7.8.3)$$

$$a_e(0,5) = 1.000091\,a \quad (7.8.4)$$

Assignment of an effective radius allows the speed of sound calculated from each mode to be identical or within the acceptable limits of accuracy. New values of (u/a_e) were calculated using the effective radii given in equations (7.8.1) to (7.8.4). The fractional deviations of each mode given by

$$\delta\left(\frac{u}{a_e}\right)=\frac{\left\langle u/a_e\right\rangle-\left(u/a_e\right)}{\left\langle u/a_e\right\rangle}\times 10^6 \qquad (7.8.5)$$

are illustrated in figures (7.8.1 and 7.8.2), where $\langle u/a_e\rangle$ is the mean value of (u/a_e) derived from the (0,3), (0,4) and (0,5) modes

As it can be seen there is now random deviation of u/a_e with respect to pressure for the (0,3), (0,4) and (0,5) modes (figure 7.8.1) and the agreement is generally within 20 ppm. The fractional deviation of (u/a_e) for the (0,2) mode (figure 7.8.2) has notable features in common with the excess halfwidths illustrated in figure (7.3.1). The fractional deviation of $(u/a)_{0,2}$ from the mean, $\langle u/a_e\rangle$, shows a minimum value (most negative) for the four highest temperatures which occur at approximately 3000 kPa, 4000 kPa, 5500 kPa and 6800 kPa; these are the pressures at which the corresponding excess halfwidths have their maximum value. The implication of this observation is that, near the shell resonance, the observed halfwidth is not a reasonable measure of the real losses that are occurring and that the shell resonance must contribute primarily to the imaginary term of the complex frequency.

When the fractional excess halfwidth is at a minimum, the deviation in (u/a) approaches zero, as expected and in this regime, when we are not actually *at* shell resonance, the model used (equation (7.3.3)) seems to work satisfactorily even for the (0,2) mode.

Once the separation between modes and hence the effective radius of each mode had been solved non-linear regression analysis was performed on all the values of the effective radii, a_e , using the procedure outlined previously.

Several functional forms described the data equally well in terms of the standard deviation of the fit, however some implied anomalous temperature dependency and so the fit considered most sensible and which best described the data was given by the five-term fit,

Figure (7.8.1): The fractional deviation (u/a) of the (0,3), (0,4) and (0,5) modes from the mean $\langle u/a \rangle$ calculated from the (0,3), (0,4) and (0,5) modes

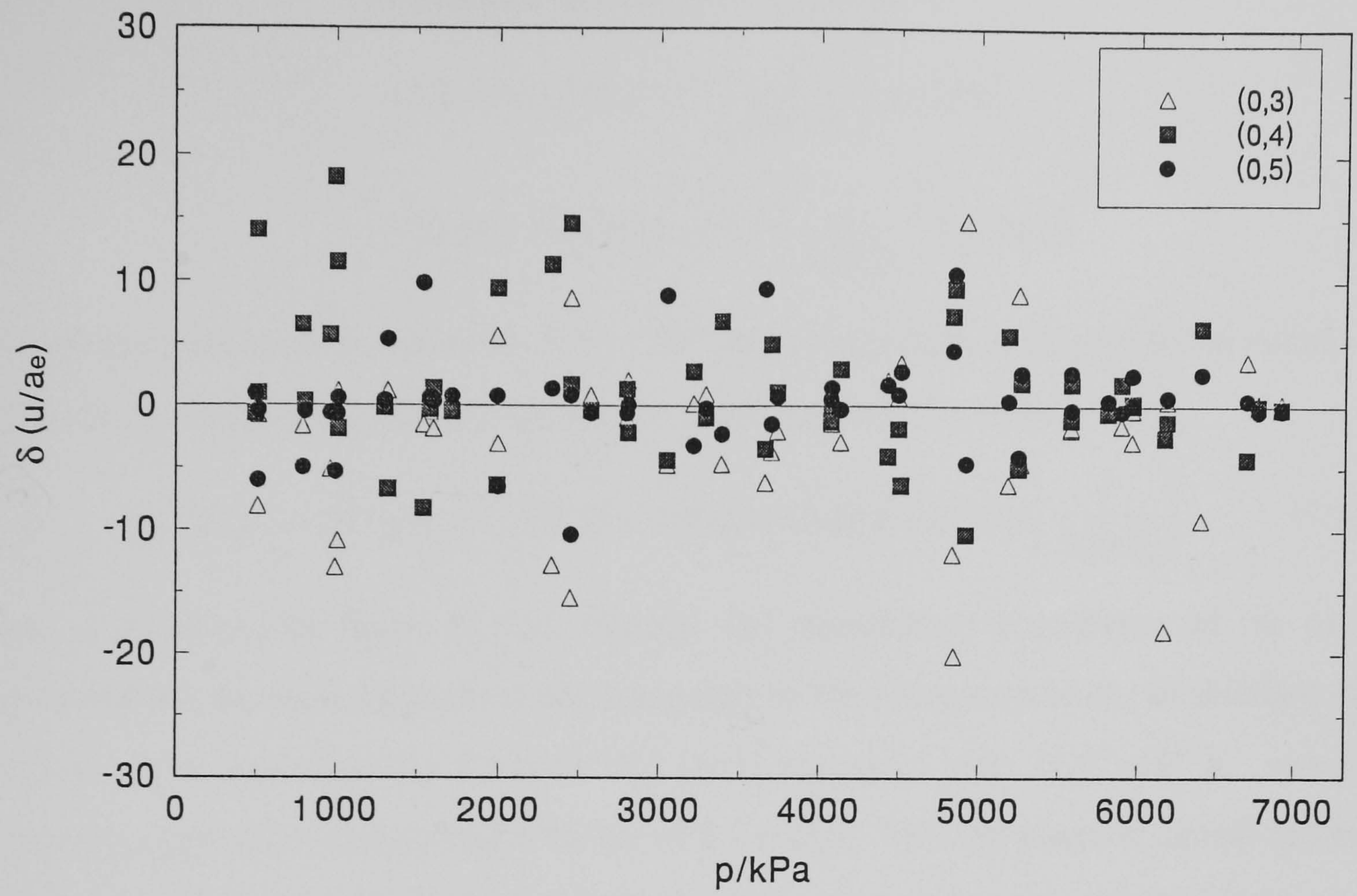

Figure (7.8.2): The fractional deviation (u/a) of the (0,2) mode from the mean $\langle u/a \rangle$ calculated from the (0,3), (0,4) and (0,5) modes

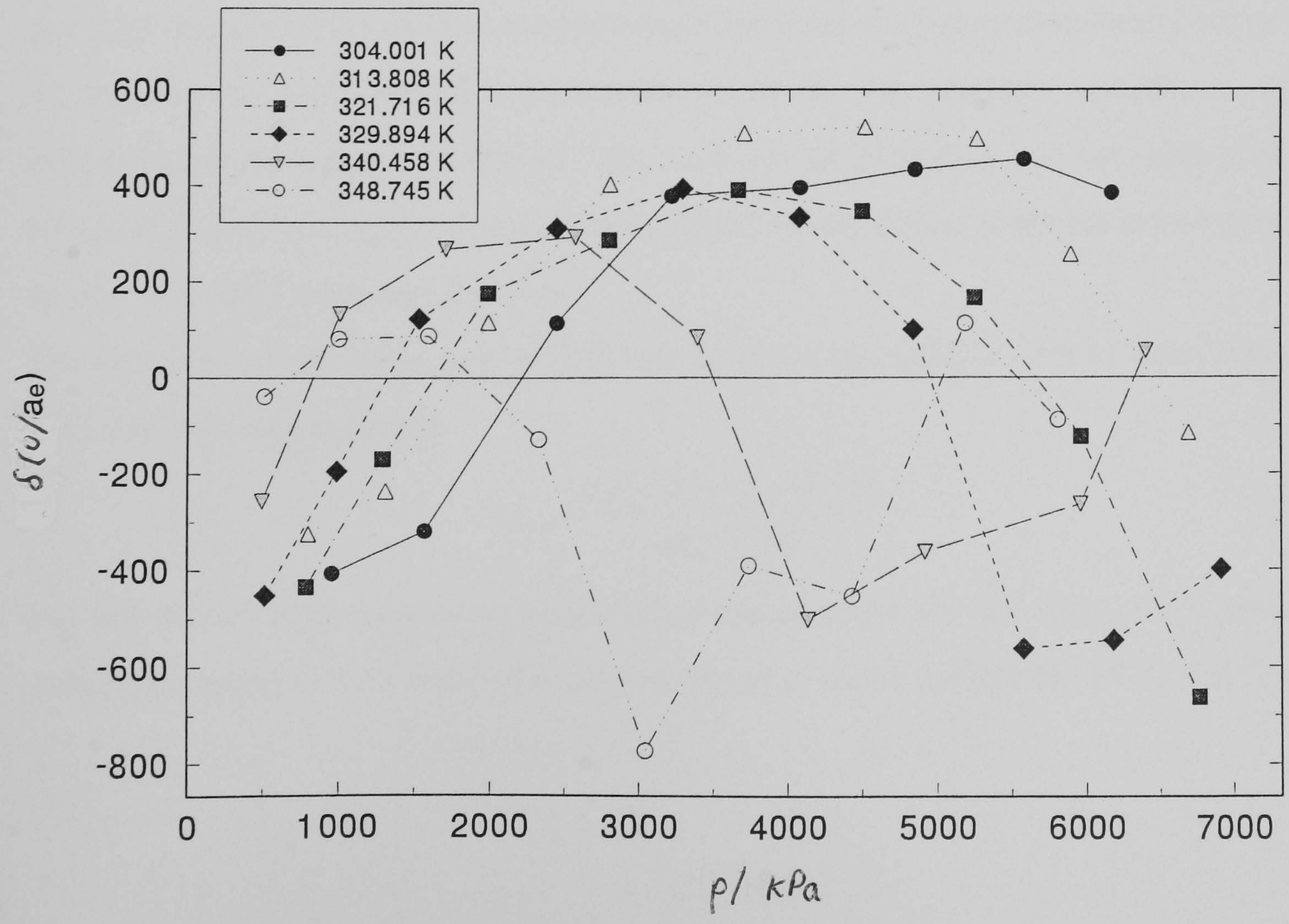

$$a_{\text{fit}}(T,p)/\text{mm} = (37.373 \pm 0.003) + (0.248 \pm 0.002)\left(\frac{T}{300\ \text{K}}\right) + (0.238 \pm 0.008)\times 10^{-3}(p/\text{kPa}) - (0.45 \pm 0.01)\times 10^{-3}\left(\frac{T}{300\ \text{K}}\right)(p/\text{kPa}) + (0.214 \pm 0.007)\times 10^{-3}\left(\frac{T}{300\ \text{K}}\right)^2(p/\text{kPa}) \quad (7.8.6)$$

which has a standard deviation of 7.27×10^{-4} and corresponds to 20 ppm in the radius. The zero-pressure temperature dependence of the radius is therefore given by

$$a_{\text{fit}}(T, p \to 0)/\text{mm} = (37.373 \pm 0.003) + (0.248 \pm 0.002)\left(\frac{T}{300\ \text{K}}\right) \quad (7.8.7)$$

and is illustrated by figure (7.8.3). Clearly, the temperature dependence of the radius derived from the measurements is not due purely to the linear expansivity of stainless steel 321 which is approximately $9.59\times10^{-6}\ \text{K}^{-1}$ [103] compared with $21.97\times10^{-6}\ \text{K}^{-1}$ obtained from the regression analysis and a factor of 2.2 higher. This difference is almost certainly due to the effects of shell motion whereby the walls of the cavity are stretched by resonant frequencies of the shell, in a way that is temperature dependent.

The behaviour of the radius to internal pressure as a function of temperature is shown by figure (7.8.4). The theoretically predicted form of the compliance for a perfect sphere is given by equation (9.2) and this has previously held well for practical spherical resonators. At the highest experimental temperature of 349 K the effective compliance of the hemispherical resonator is $10.93\times10^{-11}\ \text{Pa}^{-1}$, a factor of 22 higher than the value predicted by equation (9.2) and again almost certainly due to coincidence of the resonance modes of the gas with shell resonance features.

The deviation of individual points from the fit given by equation (7.8.6) were calculated from the following equation

$$\delta a_{\text{e}} = \frac{a_{\text{e}}(T,p) - a_{\text{fit}}(T,p)}{a_{\text{fit}}(T,p)} \quad (7.8.8)$$

and are shown with respect to temperature and pressure for the (0,3), (0,4) and (0,5) modes by figures (7.8.5) and (7.8.6) and for the (0,2) mode by figures (7.8.7) and (7.8.8).

Figures (7.8.3): Temperature dependence of zero-pressure radius

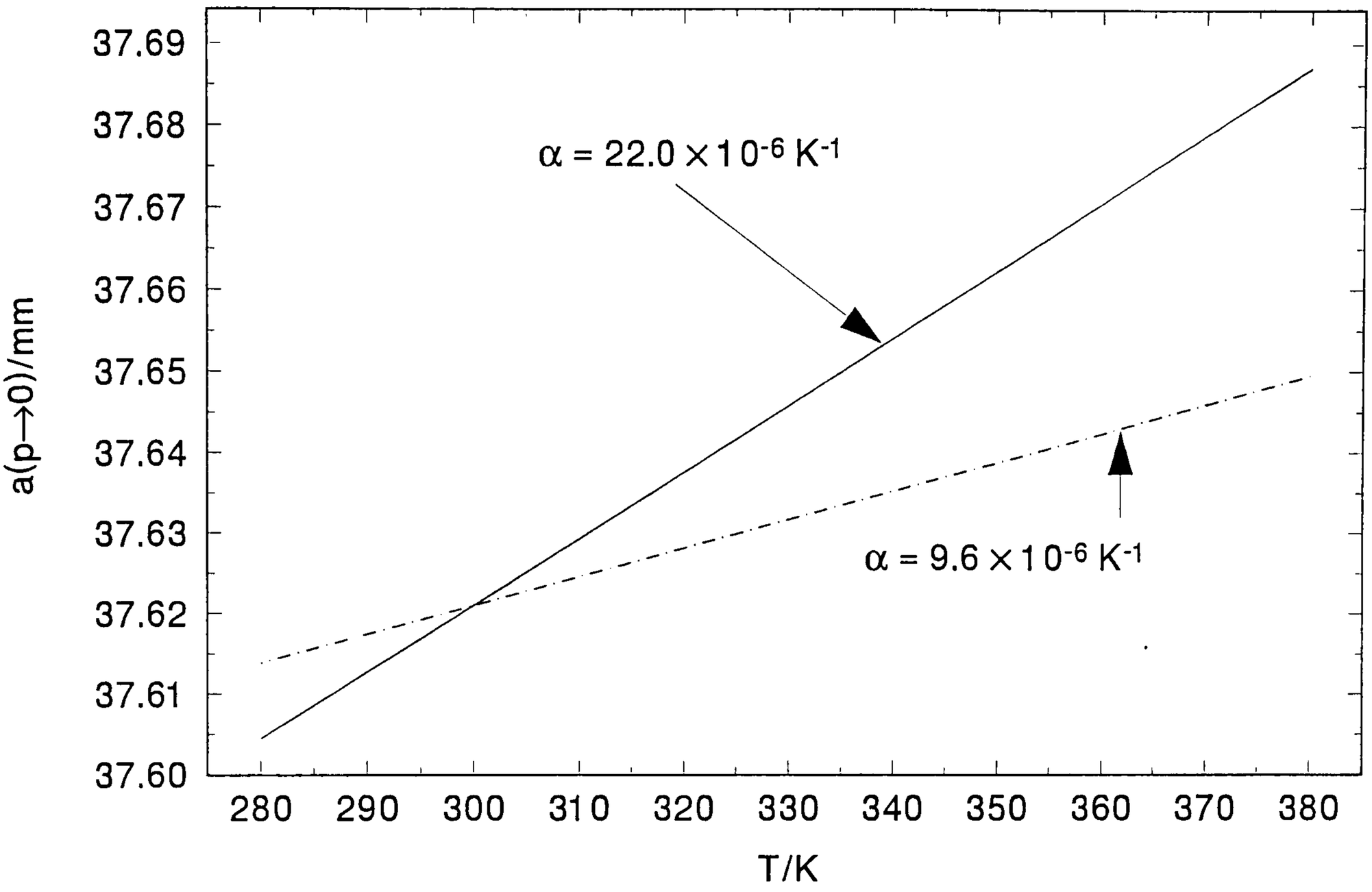

Figures (7.8.4): Temperature dependence of effective compliance of resonator's radius

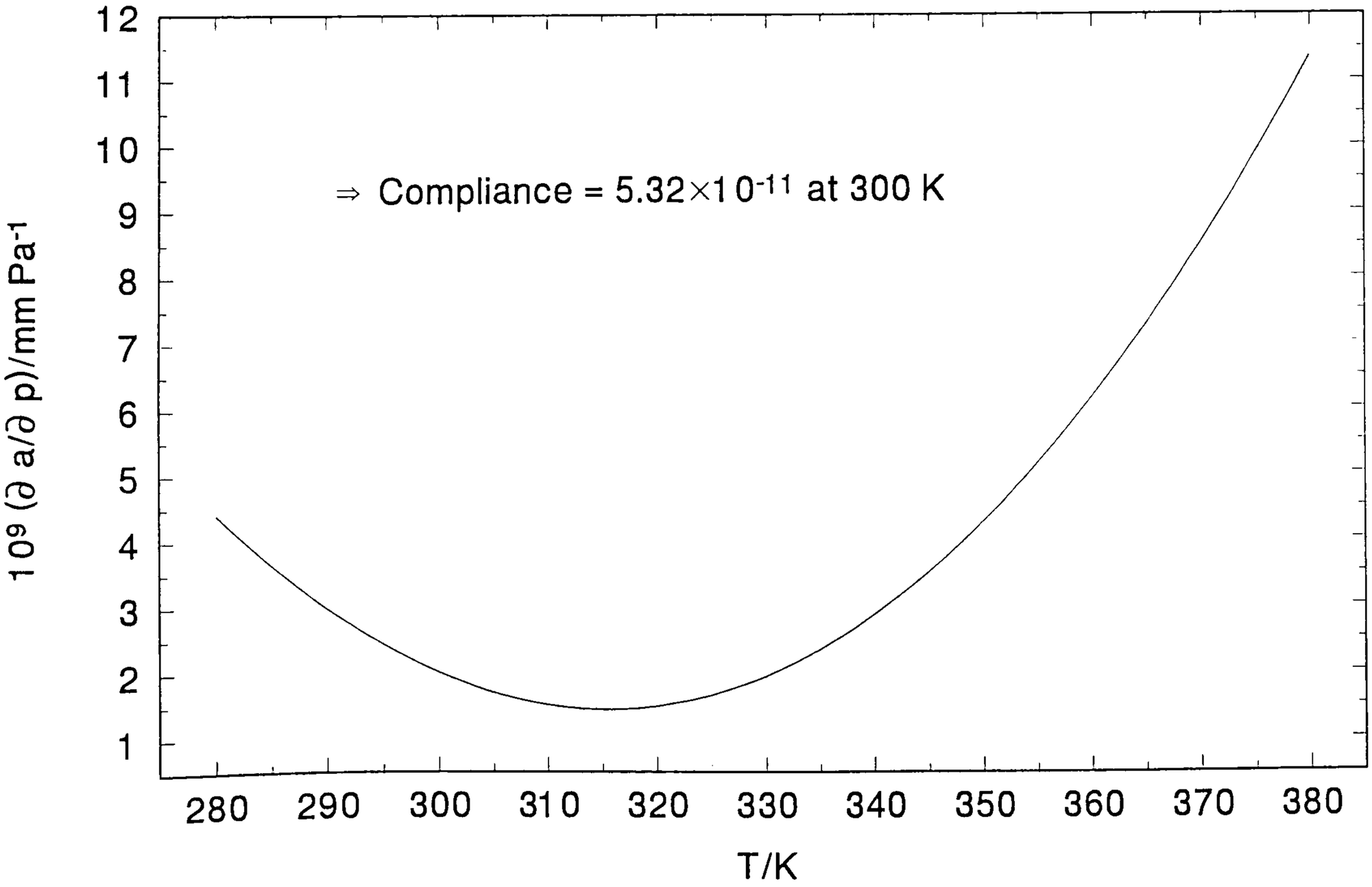

The adopted fit is within the acceptable limits of accuracy and is comparable to the accuracy achieved in the determination of the radius of a spherical resonator. For example the value quoted by Boyes in reference [59] has a standard deviation of 0.8 μm in 45 mm which would correspond to about 21 ppm in a sphere with a 37.5 mm radius. Considering the data from reference [59] consisted of fitting seven values of the radius $a\,(T, p\rightarrow 0)$ compared with fitting 200 points of $a\,(T,p,n)$ for the hemisphere and that a sphere is twice the volume of a hemisphere it gives confidence in the level of accuracy achieved in the calibration for the radius of the hemispherical cavity.

Figure (7.8.5): Deviations δa_e of the (0,3), (0,4) and (0,5) modes from the fit given by equation (7.8.6) as a function of temperature

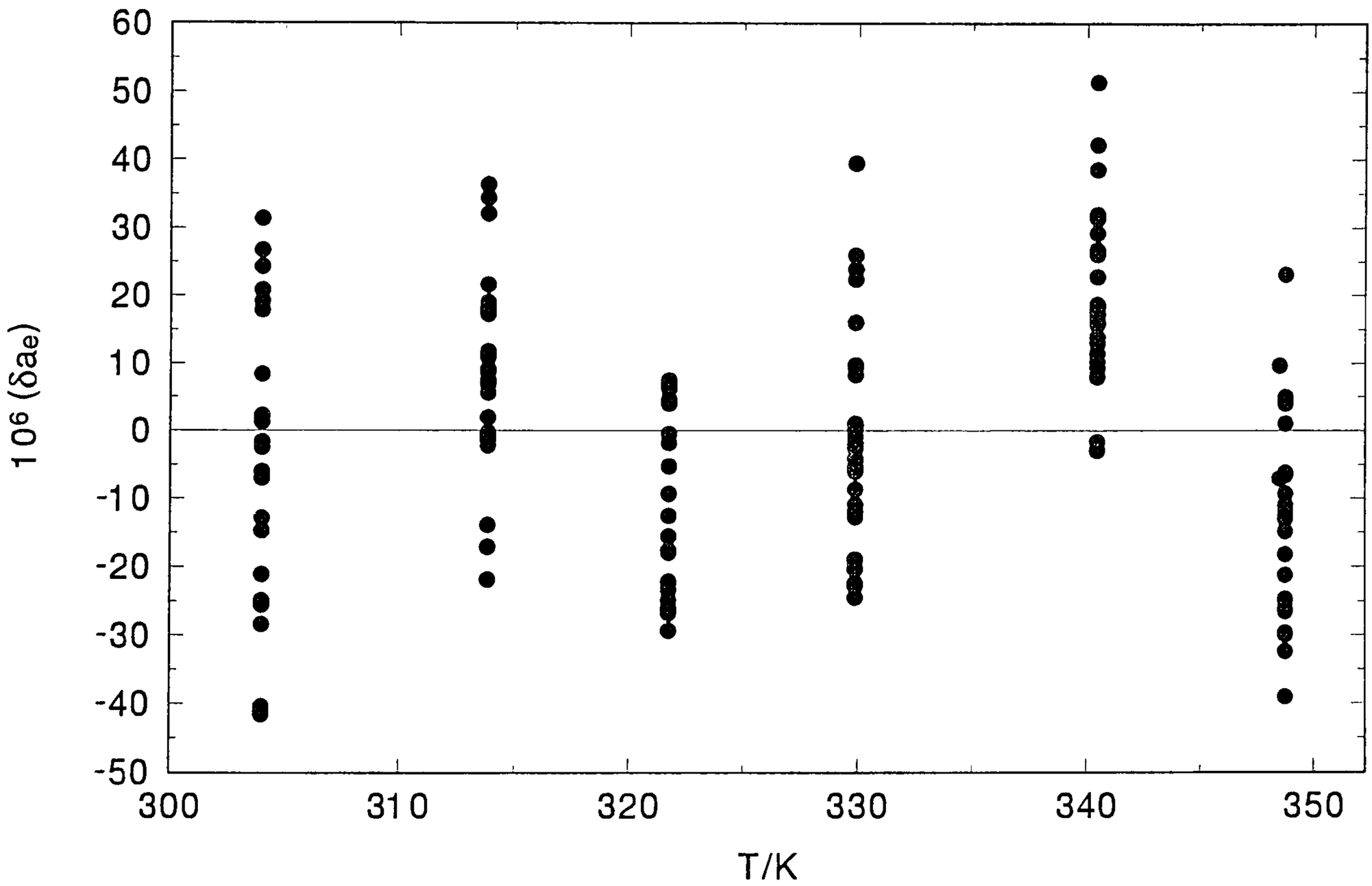

Figure (7.8.6): Deviations δa_e of the (0,3), (0,4) and (0,5) modes from the fit given by equation (7.8.6) as a function of pressure

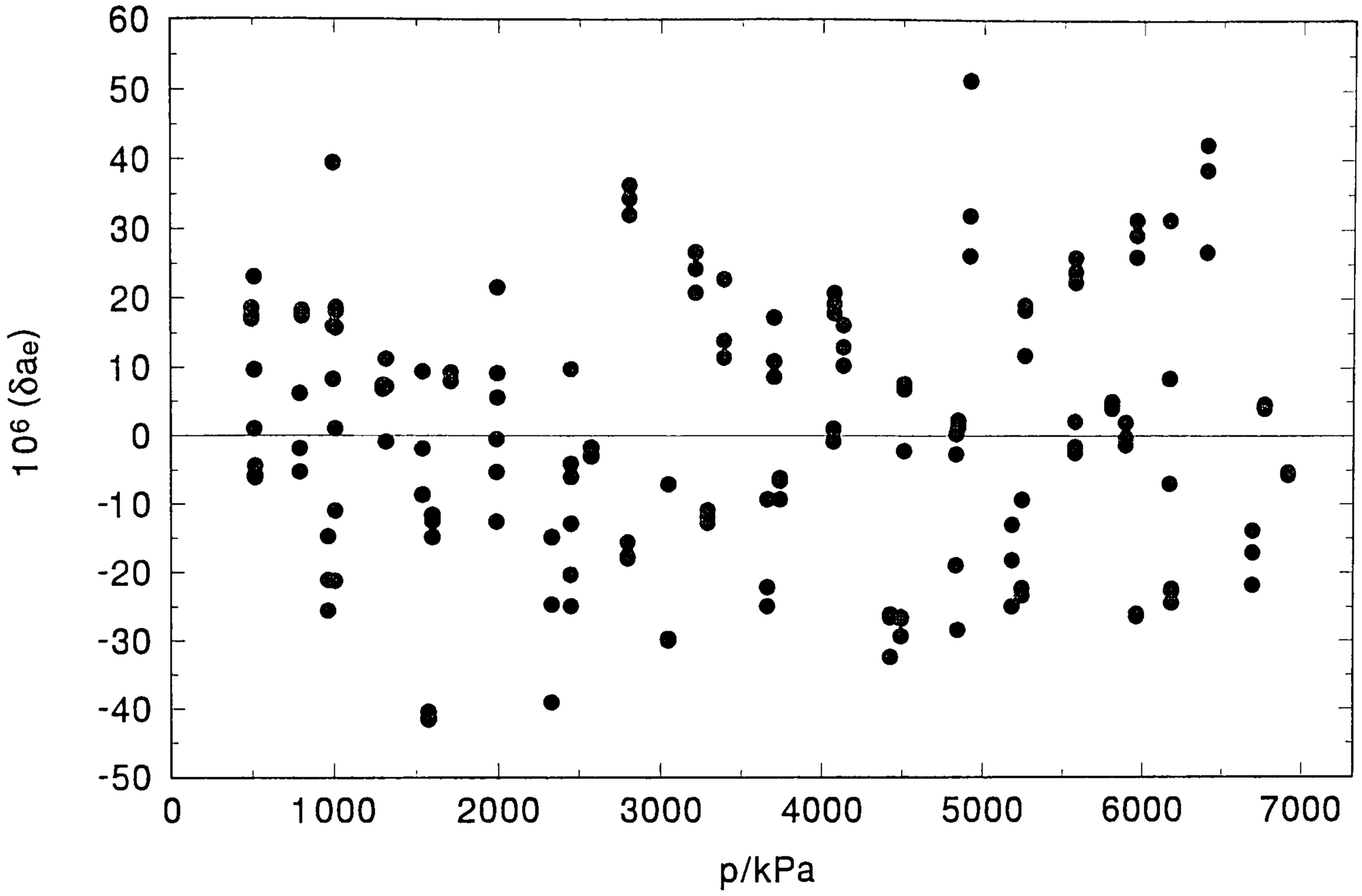

Figure (7.8.7): Deviations δa_e of the (0,2) mode from the fit given by equation (7.8.6) as a function of temperature

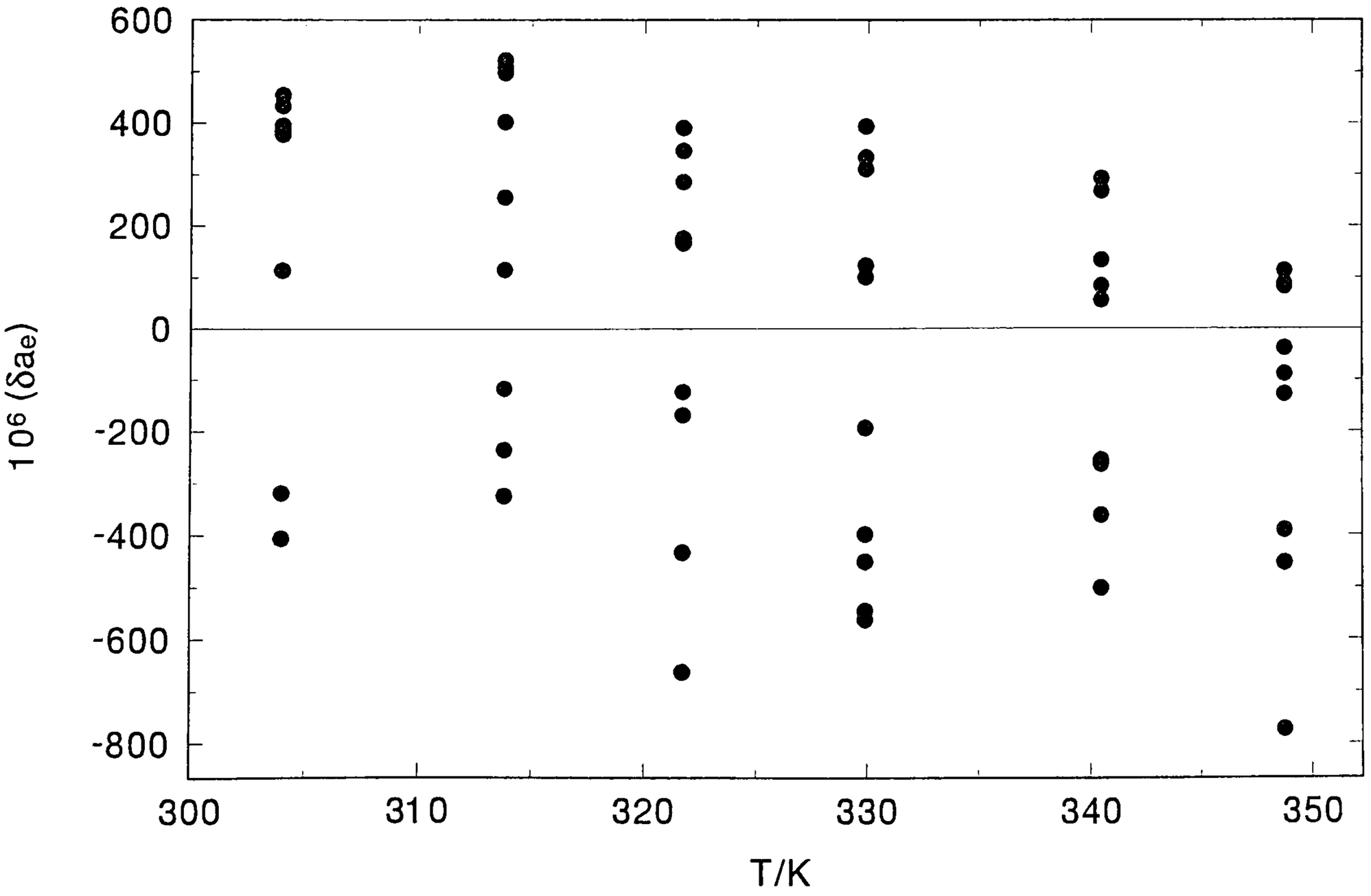

Figure (7.8.8): Deviations δa_e of the (0,2) mode from the fit given by equation (7.8.6) as a function of pressure

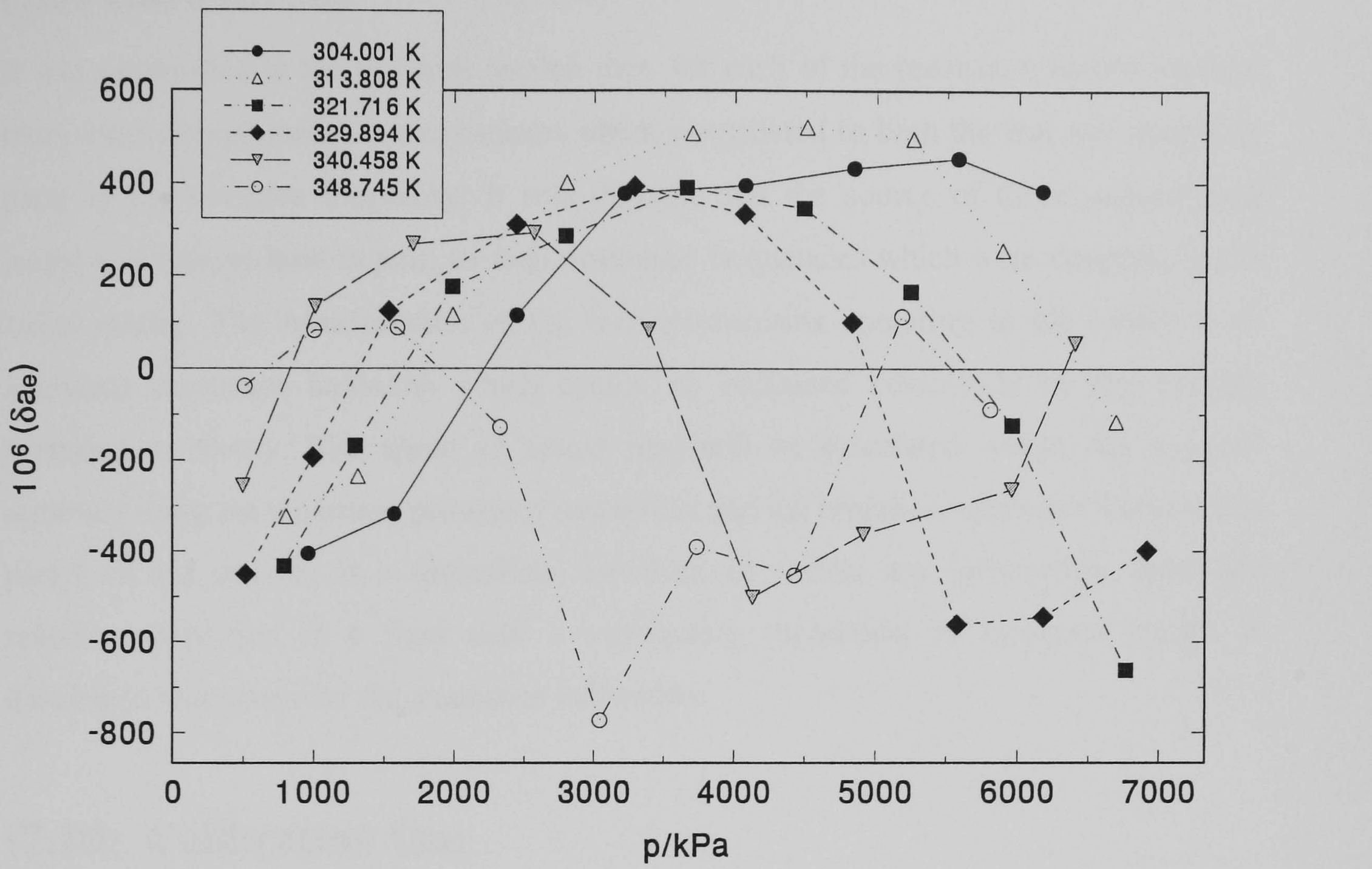

PART II Halfwidth Analysis

(7.9) Introduction

It was established in the previous section that, for each of the resonance modes studied, there were unexplained loss mechanisms which contributed to both the real and imaginary parts of the complex frequency. It was thought that the source of these unaccounted losses was due, at least in part, to shell resonance frequencies which were coupling to the radial modes. The manifestation of the loss mechanisms operating in the cavity is an increased resonance halfwidth which cannot be explained completely by the existing perturbation theory. The speed of sound may still be calculated within the required accuracy using the measured resonance halfwidths and the empirical approach discussed in part I of this chapter. It is impossible, however, to extract any information about the relaxing properties of a fluid until a satisfactory theoretical or empirical model is developed to account for the resonance halfwidths.

(7.10) Calibration Gas

In order to effectively calibrate the resonance halfwidths observed in the hemispherical cavity, measurements were performed on propene. The reason for this choice of gas was that the resonance linewidths are extremely narrow due to the relatively small transport coefficients of propene and as a consequence the quality factors were high. A full set of results, covering the whole of the experimental temperature and pressure range was also available, obtained previously by Buxton and Bailey [132] using a 40 mm radius spherical resonator.

(7.11) Measurements on Propene

Measurements of the resonance frequencies and halfwidths of the first five radial modes was made along three isotherms. The isotherms were performed at temperatures close to 300 K, 332 K and 354 K. The initial pressure p_1 was limited to the highest pressure

obtainable from the cylinder or 0.6 of the vapour pressure, whichever was the lowest. The limitation imposed on the initial pressure was to avoid the effects of precondensation [67]. The measured frequencies and halfwidths are represented by the equation

$$f_N + ig_N = \left(\frac{u}{2\pi}\right)k_N + \sum_j \left(\Delta f + ig\right)_j \qquad (7.11.1)$$

where the various loss mechanisms, given by the sum, are described in greater detail in chapter 3. If all the mechanisms were accounted for then the excess halfwidth, for a radial mode, given by

$$\Delta g = \left(g_{0,n} - g_{\mathrm{h}} - g_{\mathrm{v}} - g_{\mathrm{t}} - g_{\mathrm{b}}\right) \qquad (7.11.2)$$

would be exactly zero. If the theoretical halfwidth is well known, as it is for propene, any residual Δg corresponds to unknown loss mechanisms might then be modelled.

The propene was supplied by BOC gases and was 'N2.0 (pure)' grade with a stated mole fraction purity of 0.995. An identical grade of propene was also used for the reference measurements on which the calibration was based [132], thereby reducing the limitations on accuracy imposed by gas purity.

(7.12) Transport Properties

The largest of the known correction terms for measurements in propene are due to the thermal and viscous boundary layers. In order to calculate the magnitude of such effects, *a priori*, the thermal conductivity and viscosity must be known.

The thermal conductivity κ and viscosity η of propene as $p \rightarrow 0$ and the density dependencies of both coefficients were obtained from values given in reference [133] at pressures of 1.0 MPa and 0.1 MPa. Non linear regression analysis was used by Buxton [132] to obtain equations for κ and η at the two pressures and the results are given below.

<u>At p = 0.1 MPa:</u>

$$\kappa / \mathrm{mW \cdot m^{-1} \cdot K^{-1}} = 2.10342 + 163.03t^2 + 128.1t^4 - 379t^6 \qquad (7.12.1)$$

$$\eta / \mu\mathrm{Pa \cdot s} = 27.774t + 7.313t^2 - 12.3t^3 \qquad (7.12.2)$$

<u>and at p = 1.0 MPa:</u>

$$\kappa / \mathrm{mW \cdot m^{-1} \cdot K^{-1}} = 21.5193 - 136.90t + 528.7t^2 - 318t^3 \qquad (7.12.3)$$

$$\eta/\mu\text{Pa}\cdot\text{s} = 23.919t + 39.08t^2 - 58.9t^3 \tag{7.12.4}$$

where $t = 0.001(\text{T/K})$.

Linear extrapolation to $p \rightarrow 0$ was then possible using

$$\kappa(p \rightarrow 0) = \kappa(p = 0.1\,\text{MPa}) - \tfrac{1}{9}\{\kappa(p = 1.0\ \text{MPa}) - \kappa(p = 0.1\,\text{MPa})\} \tag{7.12.5}$$

and

$$\eta(p \rightarrow 0) = \eta(p = 0.1\,\text{MPa}) - \tfrac{1}{9}\{\eta(p = 1.0\ \text{MPa}) - \eta(p = 0.1\,\text{MPa})\} \tag{7.12.6}$$

The density dependence was calculated using

$$\frac{\partial\kappa}{\partial\rho} = \{\kappa(p = 1.0\,\text{MPa}) - \kappa(p \rightarrow 0)\}\frac{RT}{10^6\,M} \tag{7.12.7}$$

and

$$\frac{\partial\eta}{\partial\rho} = \{\eta(p = 1.0\,\text{MPa}) - \eta(p \rightarrow 0)\}\frac{RT}{10^6\,M} \tag{7.12.8}$$

The vibrational relaxation time $\tau\rho$ and its density dependence $\partial(\tau\rho)/\partial\rho$ were obtained from reference [132]. The bulk viscosity η_b, the second virial coefficient B, the second acoustic virial coefficient β_a and the heat capacity $C_{p,m}^{pg}$ were also estimated from reference [132].

(7.13) Fractional Excess Halfwidths in Propene

The fractional excess halfwidths after correction for known contributions for the first five radial modes are given for propene in figures (7.13.1) to (7.13.5). Initial examination of the fractional excess halfwidths revealed non-negligible losses which had not been adequately accounted for by the existing model.

The (0,2) mode was the most severely affected with fractional excess halfwidths on the order of 300 to 1000 ppm. As with nitrogen, the (0,2) mode in propene is obviously affected by coincidence of its resonance frequency with shell resonances of the cavity. At the lowest temperature of 300 K there are two clear maxima occurring at pressures of approximately 600 kPa and 120 kPa. At higher temperatures these maxima are shifted to lower pressures (higher frequencies) and at the highest experimental temperature of 354 K the two peaks appear to coalesce.

Figures (7.13.1): Fractional excess halfwidths of the (0,2) mode as a function of pressure in propene

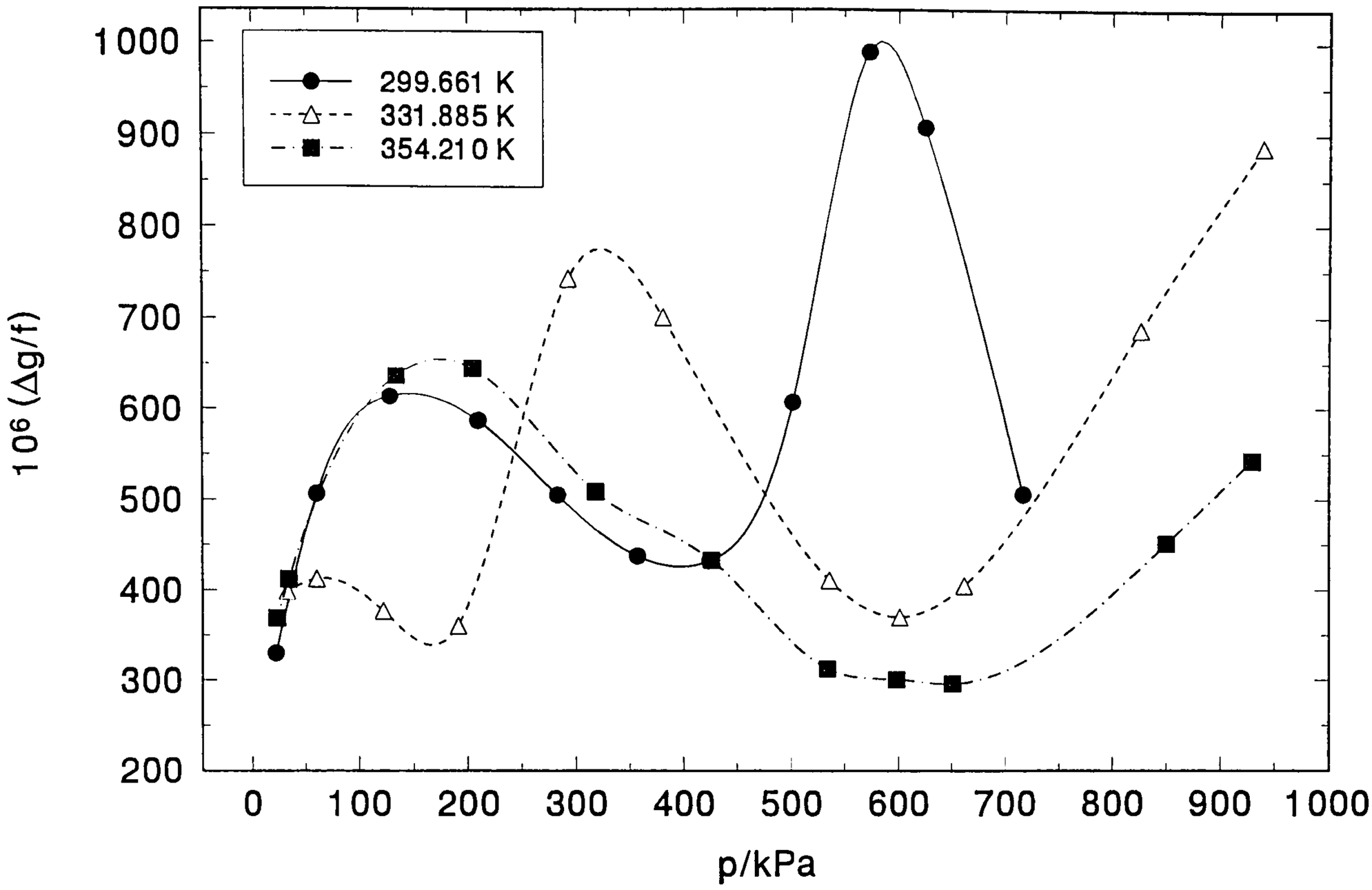

Figures (7.13.2): Fractional excess halfwidths of the (0,3) mode as a function of pressure in propene

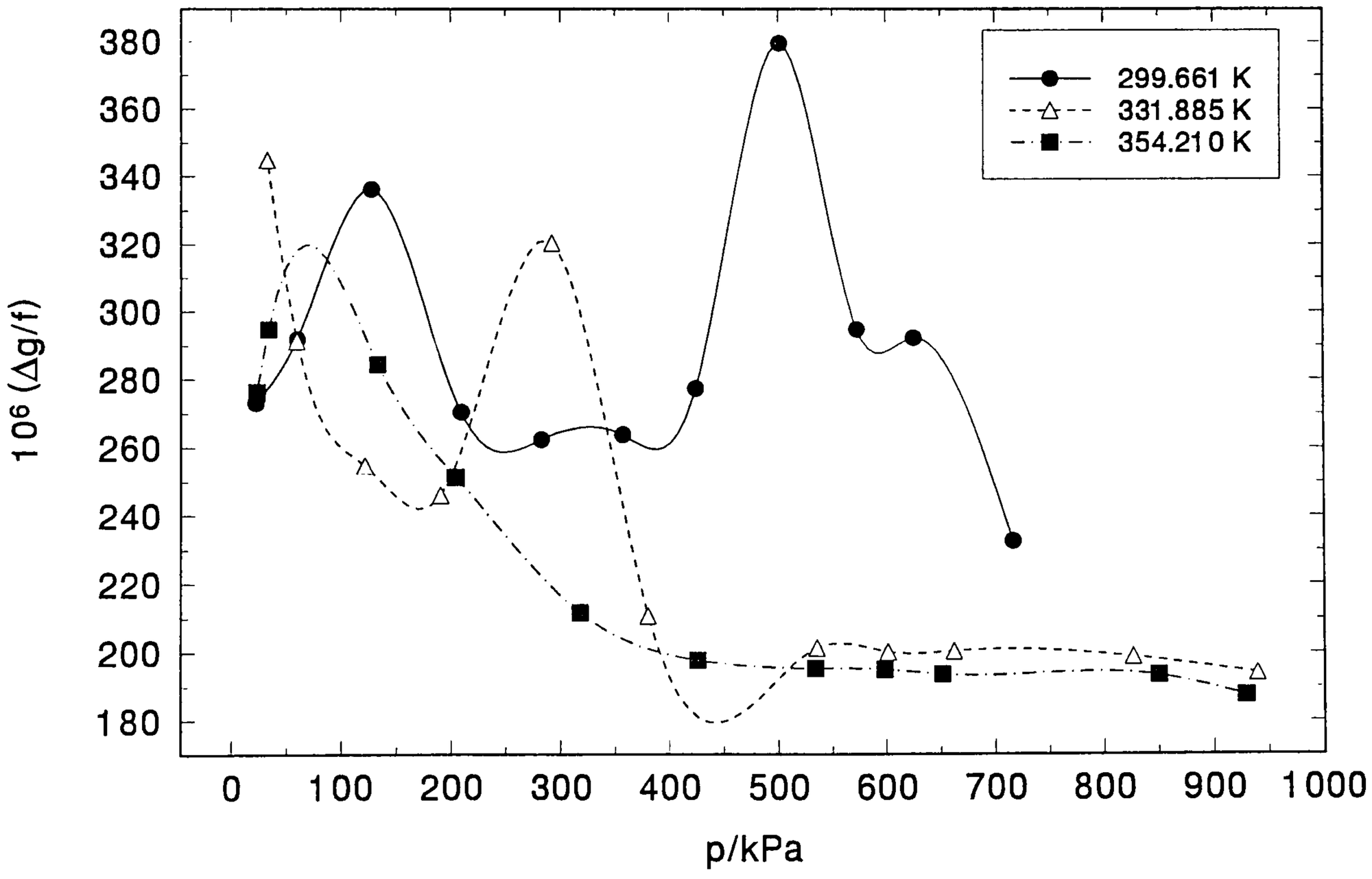

Figures (7.13.3): Fractional excess halfwidths of the (0,4) mode as a function of pressure in propene

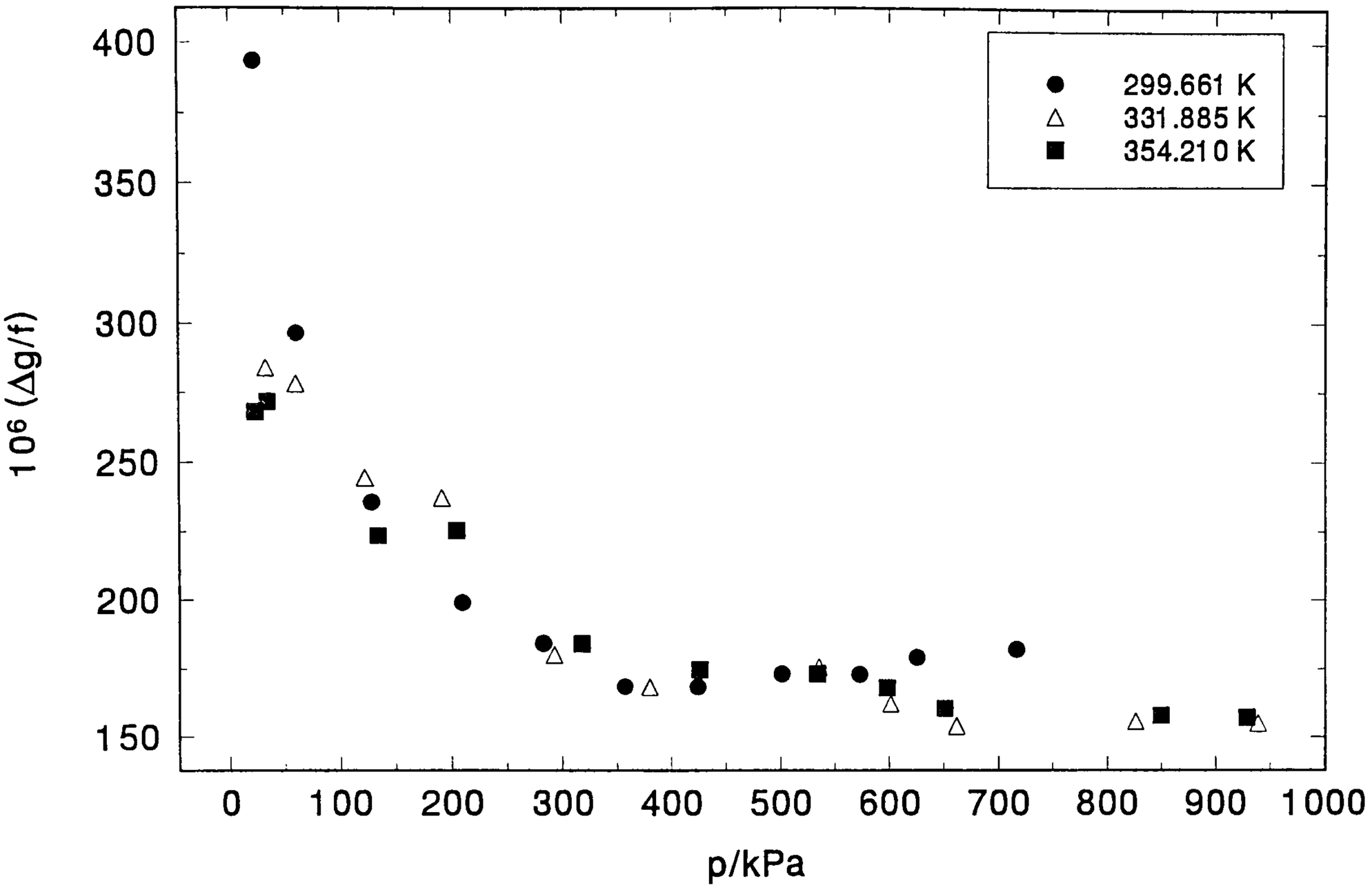

Figures (7.13.4): Fractional excess halfwidths of the (0,5) mode as a function of pressure in propene

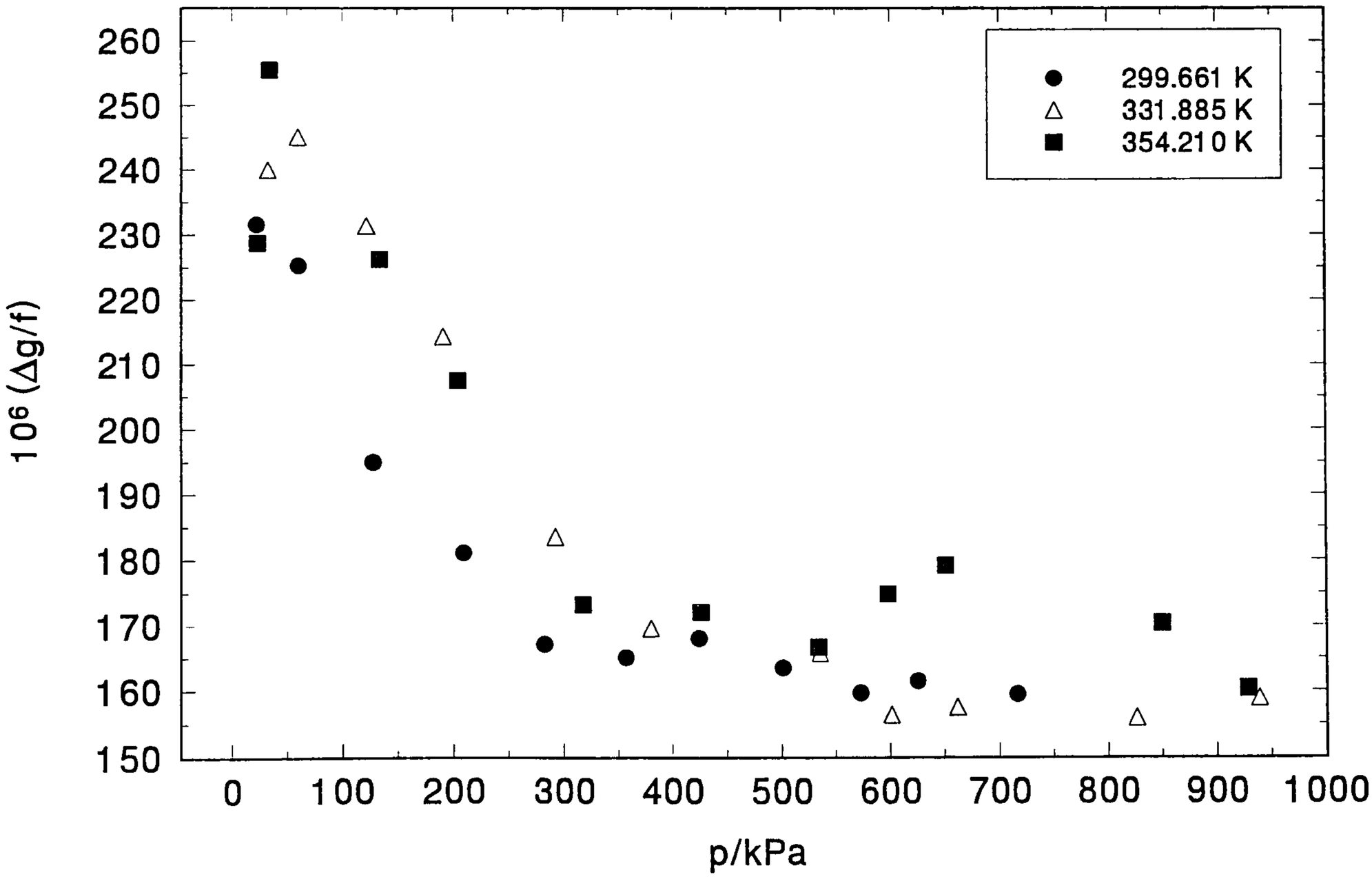

Figures (7.13.5): Fractional excess halfwidths of the (0,6) mode as a function of pressure in propene

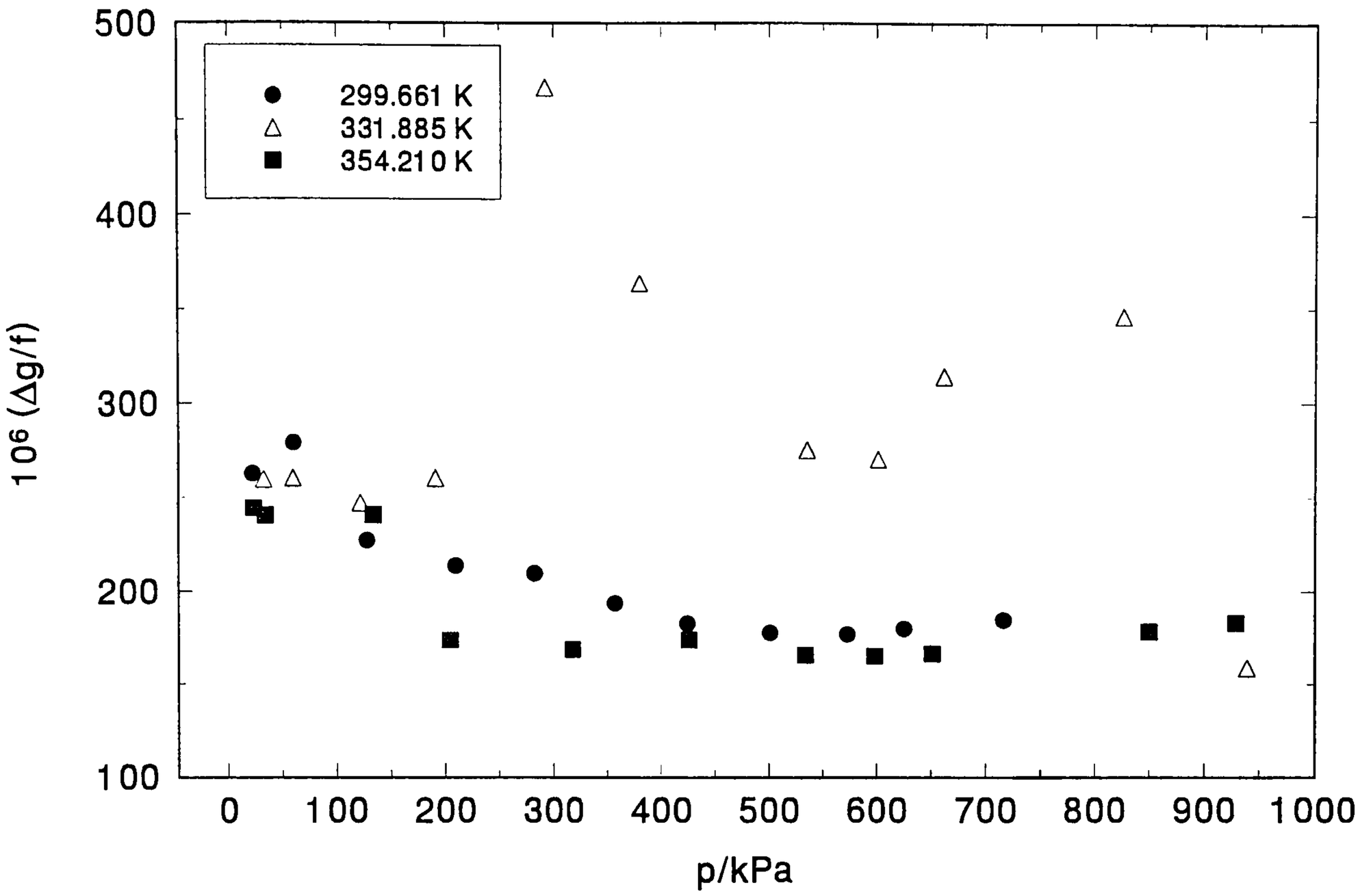

The fractional excess halfwidths of the (0,3) mode were also unacceptably high (between 190 to 380 ppm) and the behaviour was unpredictable. At the lowest experimental temperature of 300 K two maxima are observed at pressures of approximately 500 kPa and 130 kPa. At 332 K there is a maximum in Δg at a pressure of approximately 300 kPa but at the highest experimental temperature of 354 K, no sharp maxima were observed. This observation is almost certainly a knock-on effect from the behaviour of the (0,2) mode; the pressure at which the maxima in Δg occur for the (0,2) mode coincide almost exactly with those seen for the (0,3) mode. However, only the most intense features are reproduced by the (0,3) mode and they are then shifted to lower pressures which explains why no maxima are seen at the highest experimental temperatures (*i.e.* at 354 K the highest intensity feature for the (0,2) mode occurs at a pressure of about 150 kPa, if this is shifted to a lower pressure for the (0,3) mode it may not appear over the pressure range of the experiment). The behaviour of the excess halfwidth for the (0,4), (0,5) and (0,6)

modes is more predictable and much more like that seen for the (0,3), (0,4) and (0,5) modes of nitrogen. With the exception of the (0,6) mode for the isotherm performed at 332 K, there is a baseline of about 150 ppm in ($\Delta g/f$) at all pressures of about 200 kPa and higher, this then rises sharply to about 300 to 400 ppm as the pressure is reduced. The (0,6) mode exhibits maxima in ($\Delta g/f$) at pressures of approximately 800 kPa and 300 kPa in behaviour which is reminiscent of that observed for the (0,2) and (0,3) modes.

Careful examination of the excess halfwidths of both the nitrogen and propene data revealed information about the criteria upon which the remaining excess halfwidth depended and by comparison with the functional forms of known correction terms, the residual halfwidths could be attributed to the appropriate loss mechanism. The isotherms not included for this analysis were those obviously and severely affected by coincidence with shell resonance features, this is summarised in the table below.

Table 7.13.1: Summary of modes included in subsequent halfwidth analysis

Fluid	Temperature of Isotherm/K	Modes Included in Halfwidth Analysis
Nitrogen	304.001	(0,3) and (0,5)
	313.808	(0,3),(0,4) and (0,5)
	321.716	(0,3),(0,4) and (0,5)
	329.894	(0,3),(0,4) and (0,5)
	340.458	(0,3),(0,4) and (0,5)
	348.746	(0,3),(0,4) and (0,5)
Propene	299.661	(0,3), (0,4), (0,5) and (0,6)
	331.885	(0,3)*,(0,4) and (0,5)
	354.210	(0,3), (0,4), (0,5) and (0,6)
* point at p = 300 kPa not included		

The excess halfwidths of both nitrogen and propene exhibit a background contribution that is not accounted for by the existing model (equation 7.11.2) and which is not mode dependent. The magnitude of this loss is dependent on the gas; it is larger for nitrogen (about 200 ppm) than it is for propene (about 150 ppm) which suggests that the loss is, not surprisingly, dependent on the transport properties of the gas.

For a thermal boundary layer,

$$\frac{\Delta f_{\mathrm{h}} + i g_{\mathrm{h}}}{f_{0n}^{\mathrm{o}}} = \left((-1+i) \frac{(\gamma-1)}{2} \frac{\delta_{\mathrm{h}}}{a} \right) + (\gamma-1) \frac{l_{\mathrm{a}}}{a} + \left((1+i) \frac{(\gamma-1)}{2} \frac{\delta_{\mathrm{sh}}}{\alpha} \frac{\lambda_{\mathrm{g}}}{\lambda_{\mathrm{sh}}} \right) \qquad (7.13.1)$$

If the temperature of the gas and shell match then only the first term of equation (7.13.1) is important and this is proportional to $1/\sqrt{fp}$. For imperfect thermal accommodation the second term becomes important and this is proportional to $1/p$ (the importance of this term dramatically increases at low pressures, below 100 kPa). The third and smallest term accounts for penetration of the thermal wave into the shell and is proportional to $1/\sqrt{f}$. Plots of $(\Delta g/f)$ against $1/\sqrt{fp}$ for propene and nitrogen (figures 7.13.6 and 7.13.7) reveal linear relationships indicative of a first-order boundary layer effect.

Figure (7.13.6): Fractional excess halfwidths of the (0,3), (0,4), (0,5) and (0,6) modes in propene as a function of $1/\sqrt{fp}$

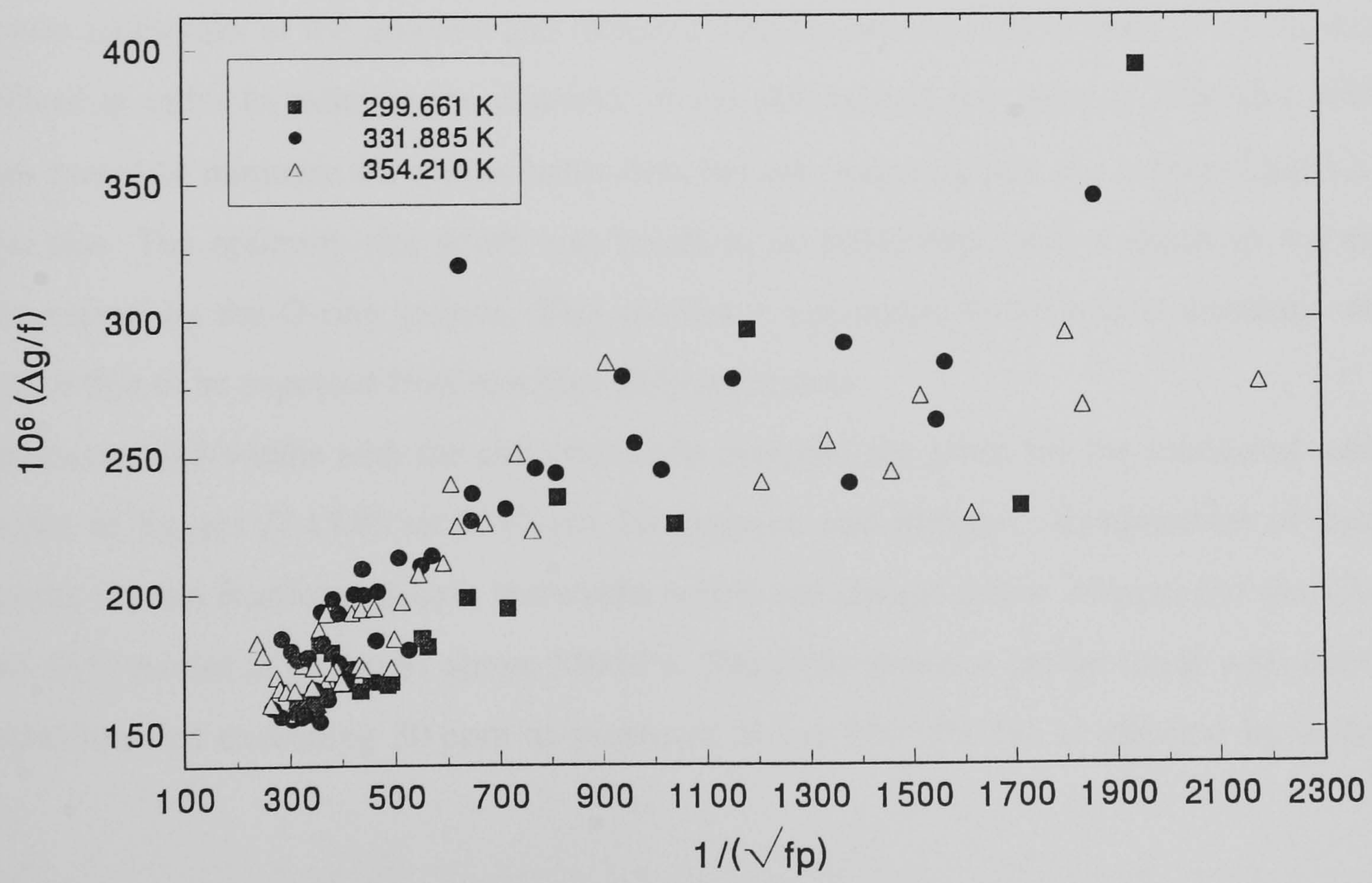

Figure (7.13.7): Fractional excess halfwidths of the (0,3), (0,4), (0,5) and (0,6) modes in nitrogen as a function of $1/\sqrt{fp}$

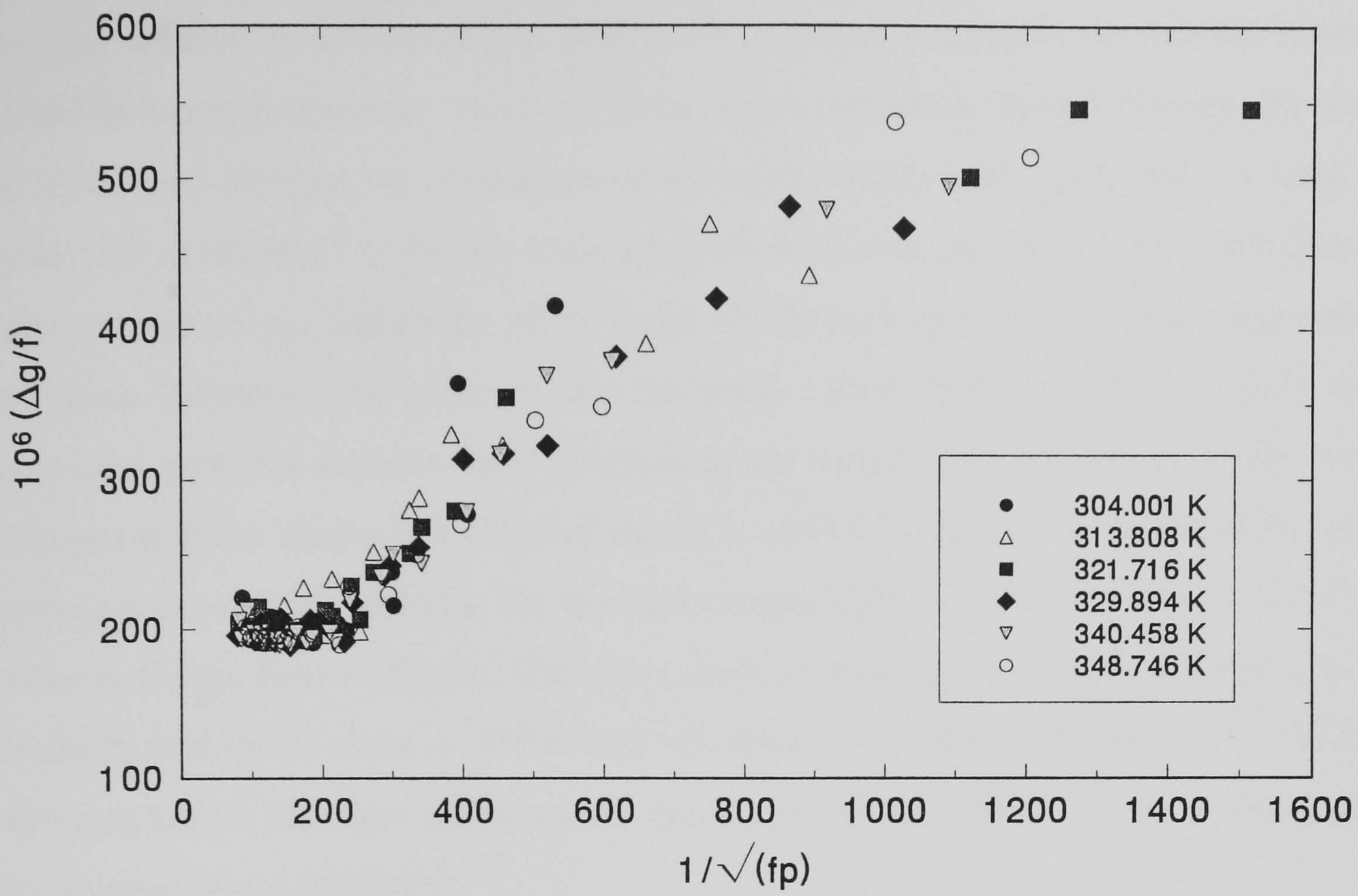

A slot around the join between the hemispherical and equatorial parts of the resonator could cause losses which would contribute substantially to the halfwidths. The fractional excess halfwidths of the propene and nitrogen data, as summarised in table (7.13.1), were utilised in order to estimate the diameter of the slot around the equator. The slot width was varied to minimise the excess halfwidths but also ensuring that the criteria $(\Delta g/f) \geq 0$ was met. The optimum slot width was found to be 0.045 mm, with a depth of 4.0 mm determined by the O-ring groove. This seemed a reasonable width and is certainly well within that to be expected from machine shop tolerances.

The excess halfwidths with the slot correction included are given for the measured radial modes in figures (7.13.8) to (7.13.16) for propene and nitrogen. Examination of these figures reveals fractional excess halfwidths which are always below 30 ppm for the (0,4) and (0,5) modes at pressures above 250 kPa. The (0,6) shows a similar trend with excess halfwidths not exceeding 30 ppm at pressures above 250 kPa but is affected by a shell

resonance feature for the isotherm at 332 K where the excess halfwidths rise to between 100 to 300 ppm. The situation is more complex for the (0,2) mode which is obviously severely affected by shell resonance effects. As observed in nitrogen, the maxima in excess halfwidth occur at pressures which are linear with temperature. The (0,3) mode also seems to have been affected by resonances of the shell, which most likely follows from the behaviour of the (0,2) mode; the isotherm performed close to 300 K is the most severely affected with excess halfwidths of the order of 120 ppm, with a maximum being reached of about 230 ppm. The peak of the fractional excess halfwidth for the (0,3) mode correlates with that seen for the (0,2) mode at this temperature. Similar trends are seen in nitrogen with the excess halfwidths of the (0,3) and (0,5) modes always below 30 ppm at pressures exceeding 1000 kPa; for the (0,5) mode, with the exception of one point, this value is always below 15 ppm. The (0,4) mode is affected by a shell resonance for the isotherm performed close to 304 K and this results in excess halfwidths rising to about 450 ppm but for the other isotherms this mode exhibits Δg's which do not exceed 45 ppm at pressures above 1000 kPa.

To summarise it appears that although the slot correction accounts adequately for the background contribution to the excess halfwidths seen for both nitrogen and propene the model fails at pressures below about 250 kPa in propene and 1000 kPa in nitrogen. This is not surprising since in the low pressure (and low density) regime the boundary layer corrections become more important and are therefore more difficult to model (*i.e.* surface roughness and regions of the cavity where the geometry may deviate from ideality (*e.g.* slots) are not adequately characterised).

Furthermore, there are still losses unaccounted for which are almost certainly the result of strong coupling between the (0,2) mode and resonances of the shell. The fractional excess halfwidths of the higher order modes are also affected by shell resonance mechanisms but in a less predictable way than the (0,2) mode. Analysis of the sound speeds reveals that even when the excess halfwidths of the modes measured exceed reasonable limits, it is only the (0,2) mode which also suffers severe shifts in the frequency which cannot be accounted for by the corresponding increase in halfwidth.

Figure (7.13.8): Fractional excess halfwidths in nitrogen of the (0,2) mode after correction for a slot

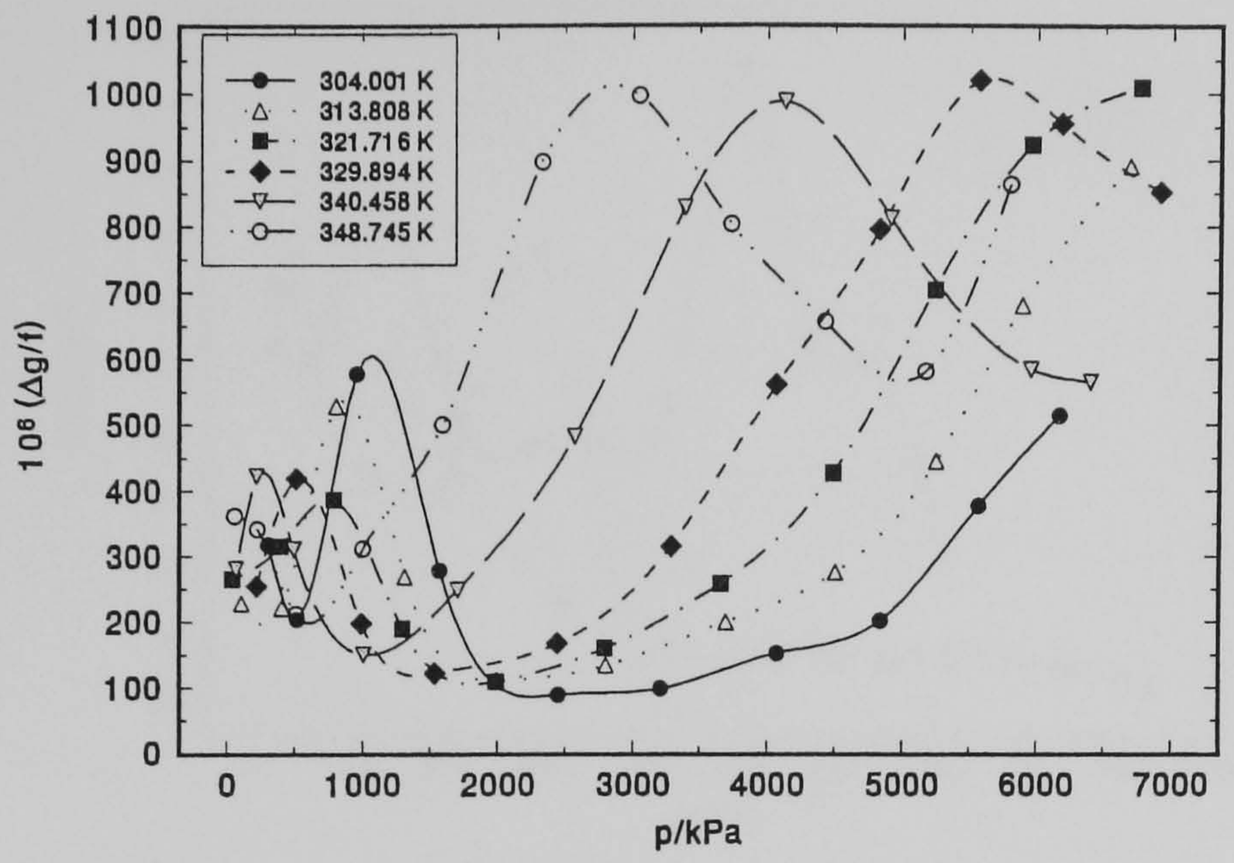

Figure (7.13.9): Fractional excess halfwidths in propene of the (0,2) mode after correction for a slot

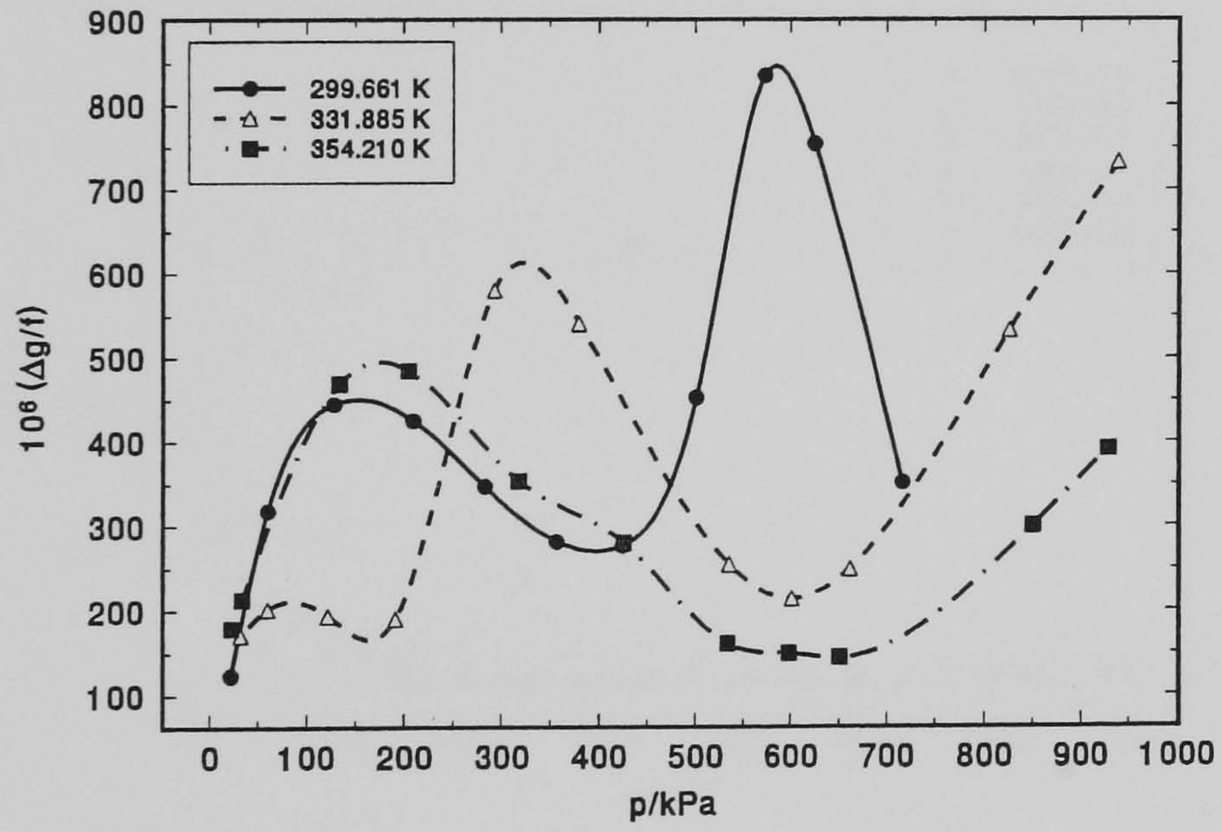

Figure (7.13.10): Fractional excess halfwidths in nitrogen of the (0,3) mode after correction for a slot

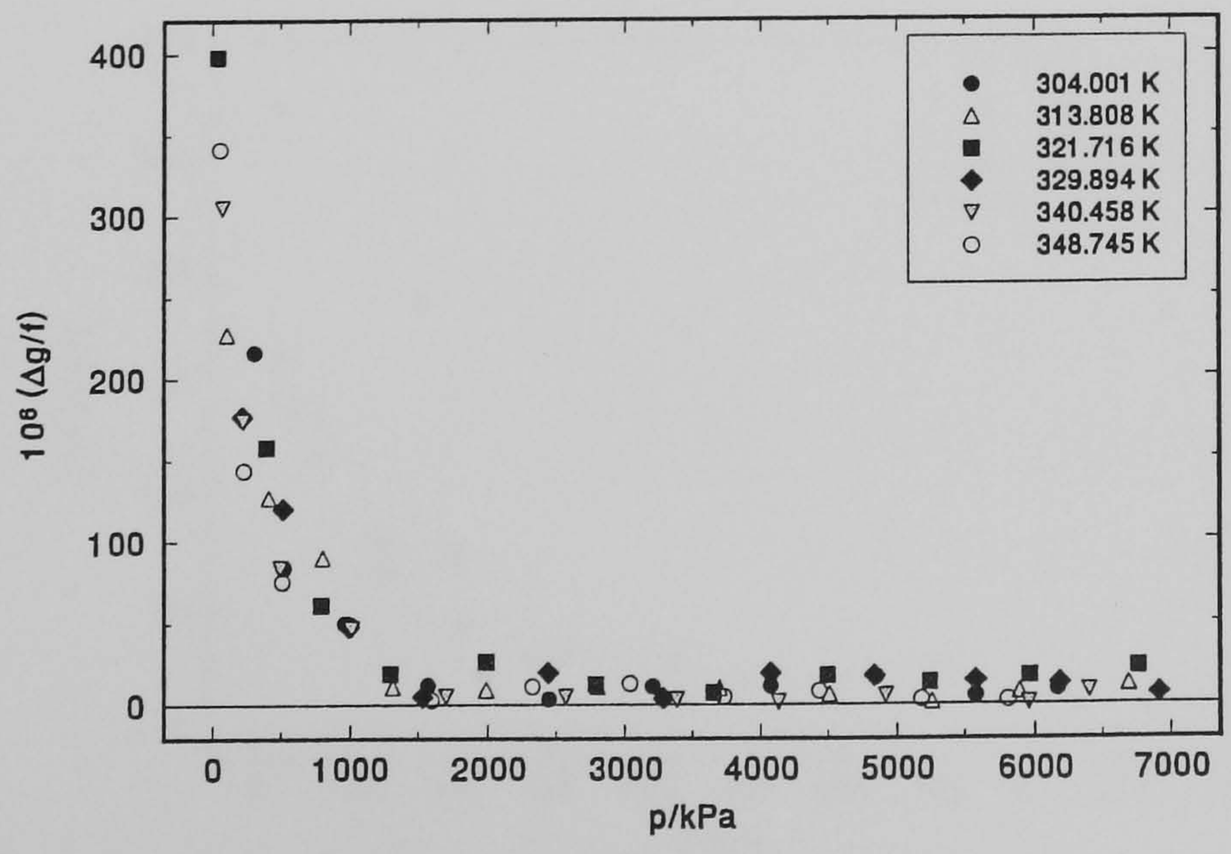

Figure (7.13.11): Fractional excess halfwidths in propene of the (0,3) mode after correction for a slot

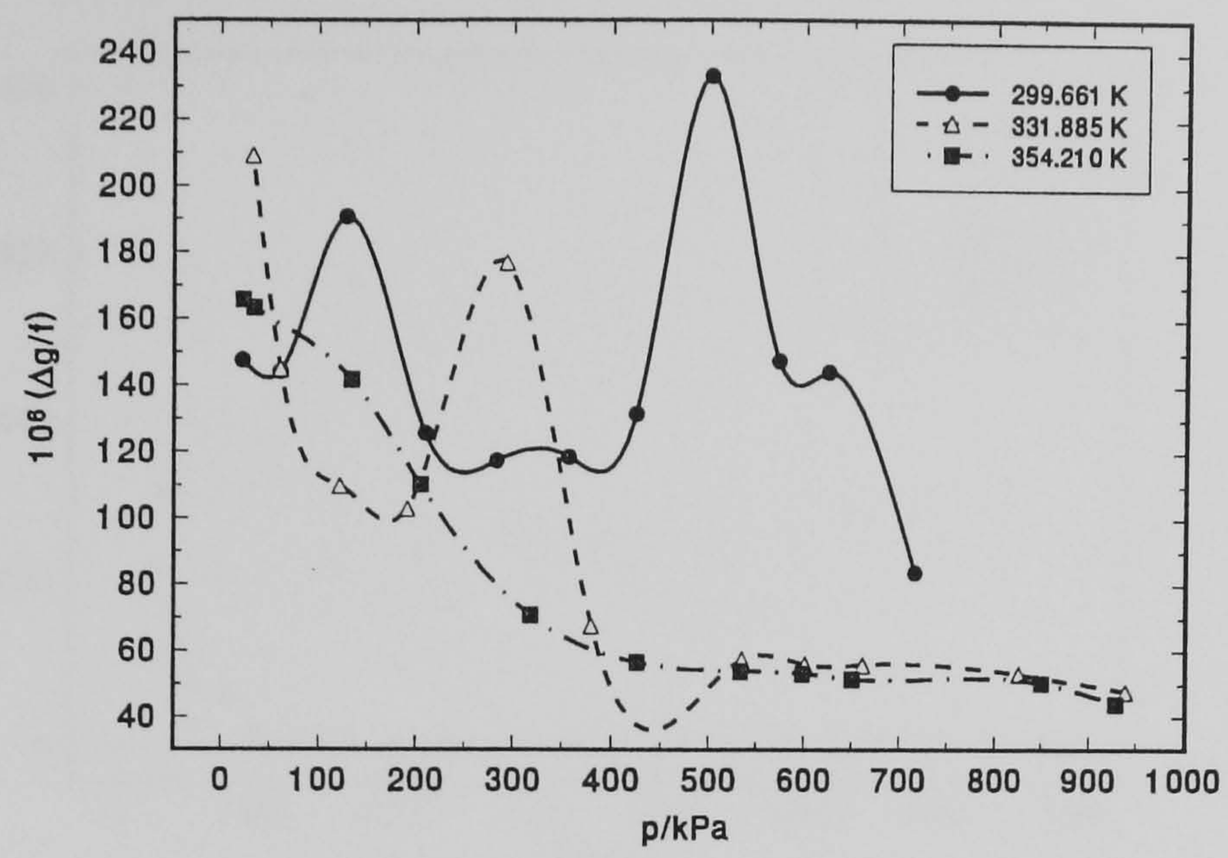

Figure (7.13.12): Fractional excess halfwidths in nitrogen of the (0,4) mode after correction for a slot

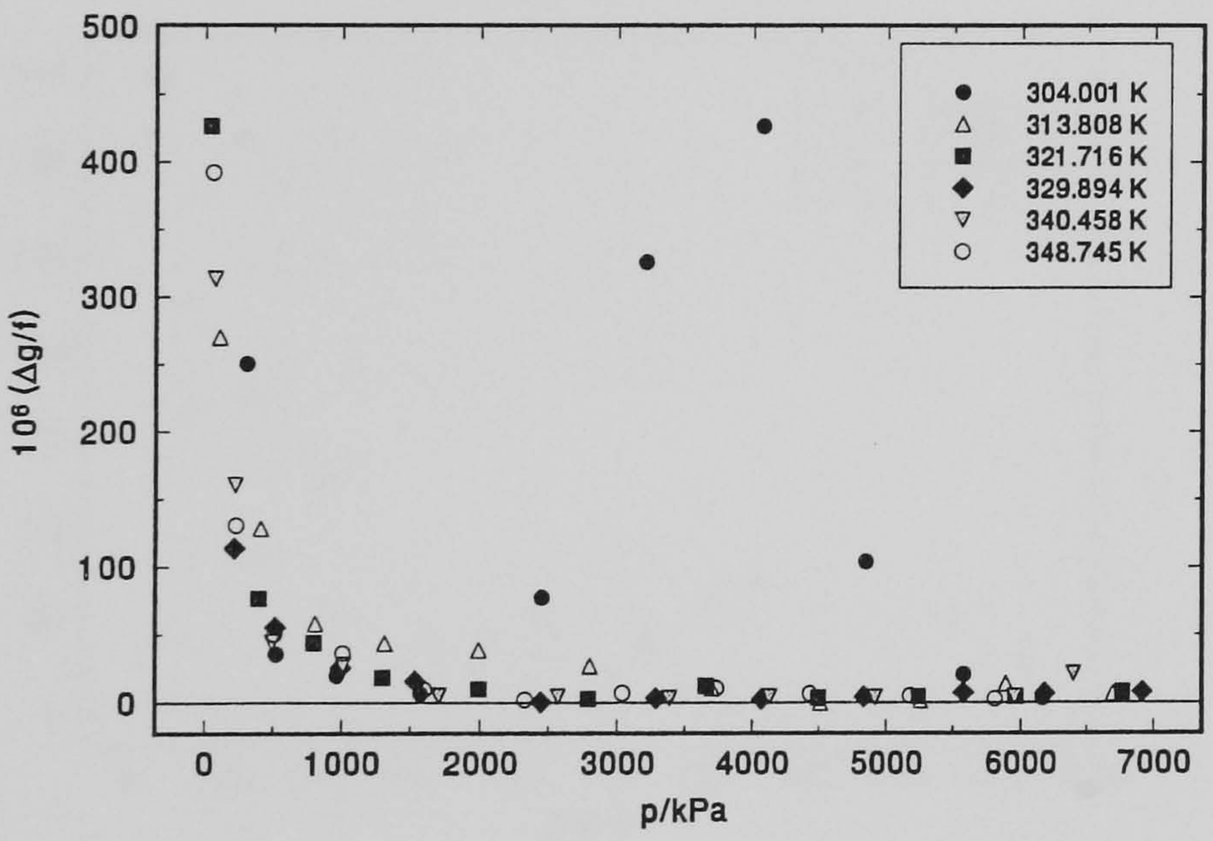

Figure (7.13.13): Fractional excess halfwidths in propene of the (0,4) mode after correction for a slot

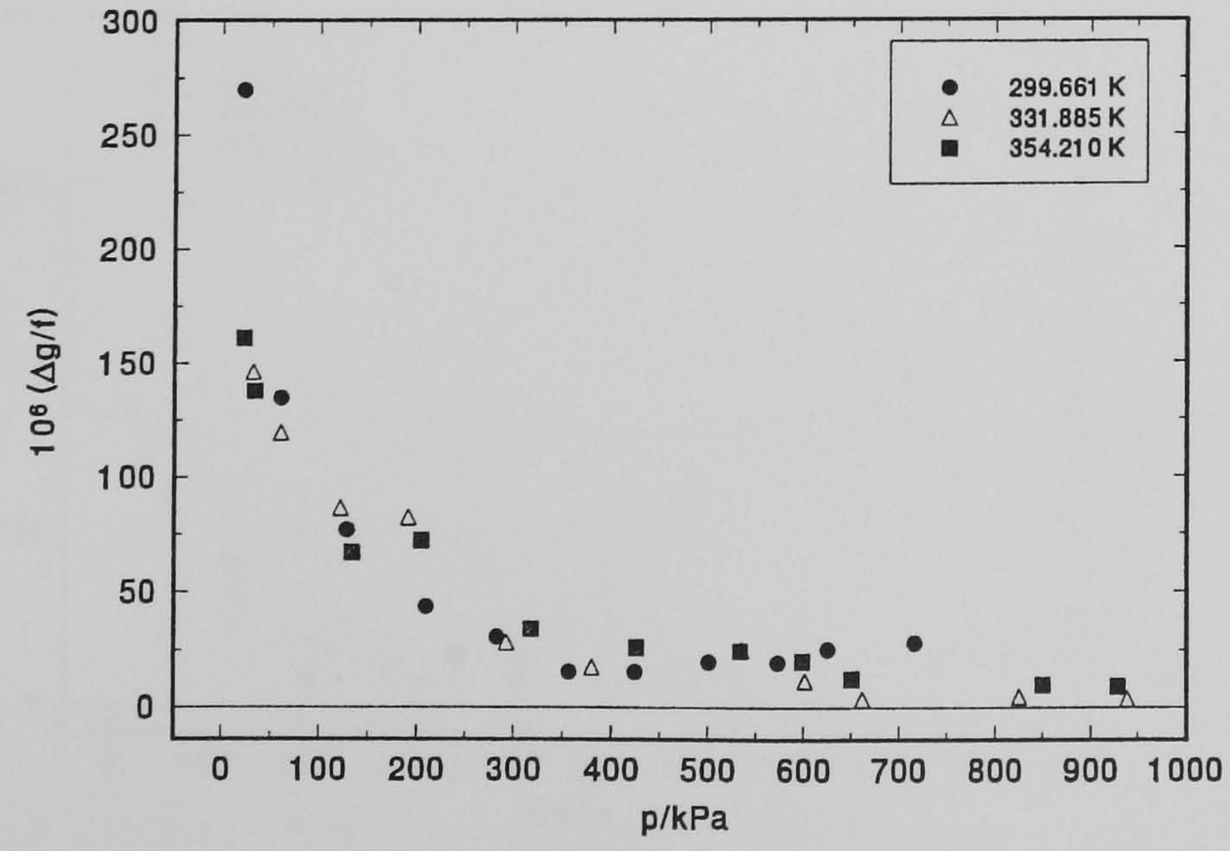

Figure (7.13.14): Fractional excess halfwidths in nitrogen of the (0,5) mode after correction for a slot

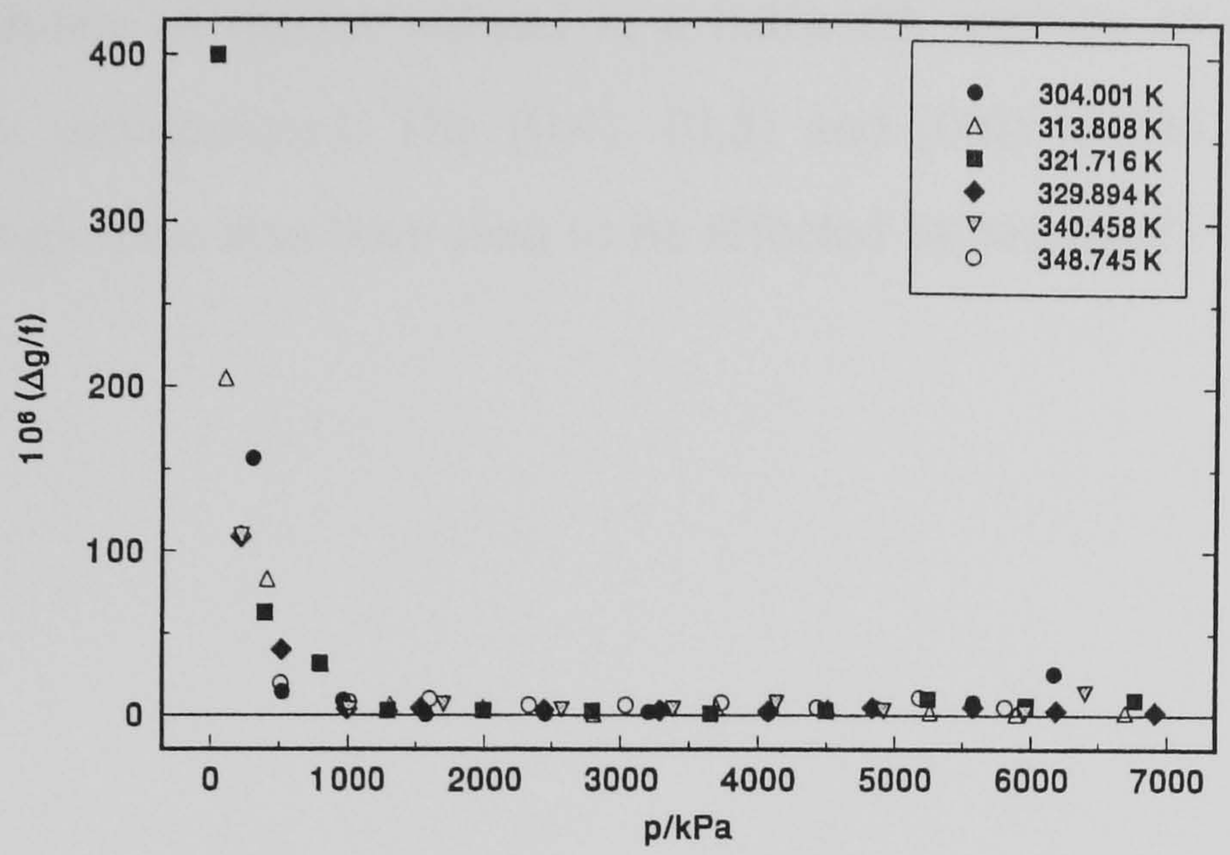

Figure (7.13.15): Fractional excess halfwidths in propene of the (0,5) mode after correction for a slot

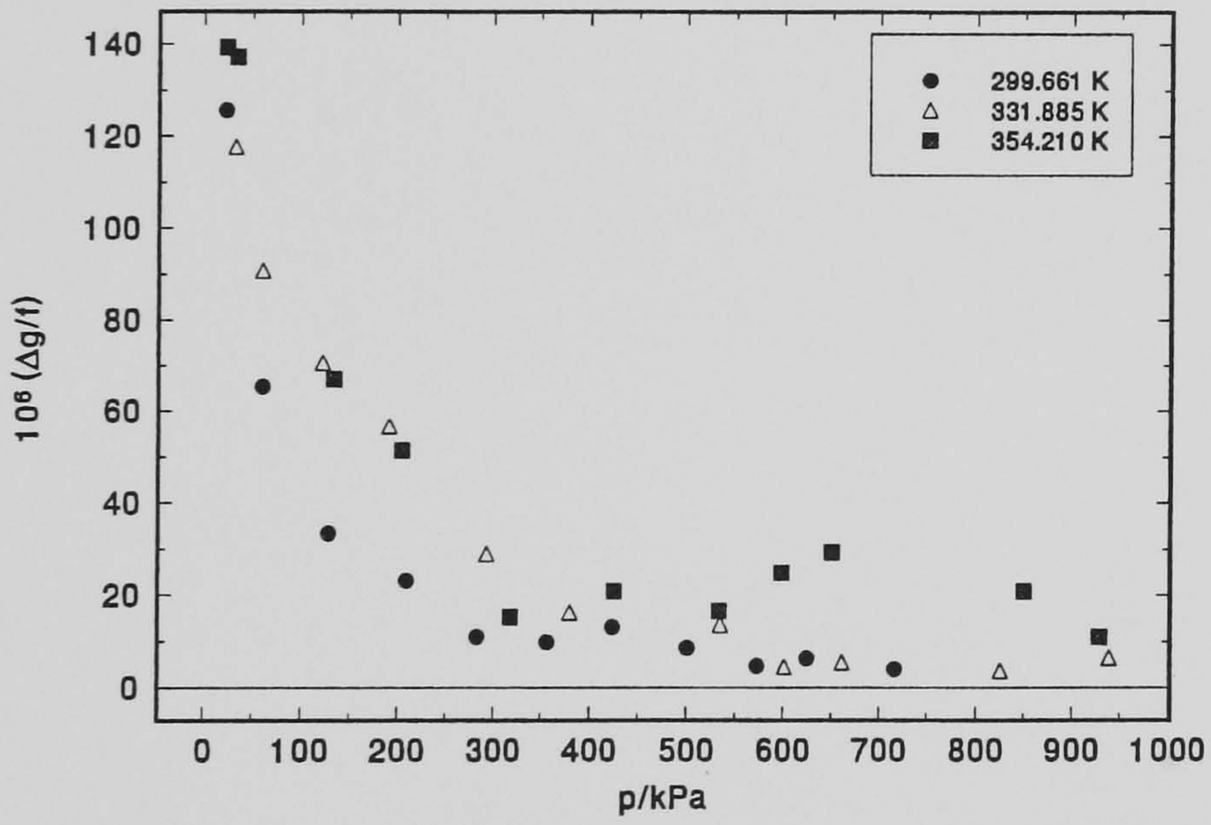

Figure (7.13.16): Fractional excess halfwidths in propene of the (0,6) mode after correction for a slot

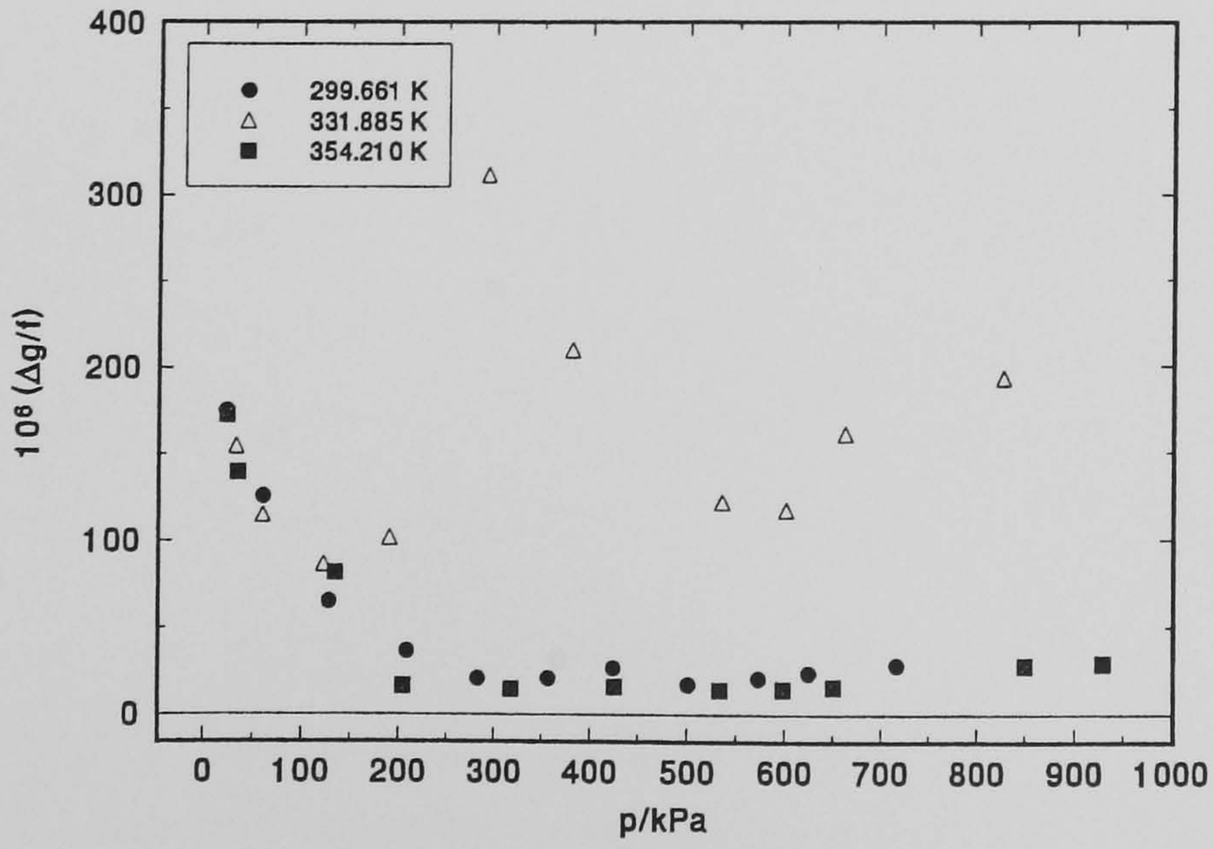

On the whole the loss mechanisms may be accounted for on the order of 20 to 30 ppm, at pressures above those affected by severe boundary layer effects, although care should be taken in the choice of modes utilised in a halfwidth analysis to ensure shell resonance effects are not incorporated. The (0,4), (0,5) and (0,6) modes appear to be the best behaved although have also been seen to be affected by seemingly random shell resonance effects.

CHAPTER 8 Experimental Results

PART I Results in Argon

(8.1) Introduction

Argon is a spherically symmetric monatomic gas which very closely behaves as an ideal gas. Consequently, the (p, V, T) behaviour of argon and its thermophysical properties are known to a high degree of accuracy.

Conventionally, argon is used as the calibration gas for acoustic resonators and it allows absolute measurements of the geometry and its temperature and pressure dependence to be determined. Although for the measurements reported in chapter 7, nitrogen was used as the calibration gas, a useful comparison and test of the model developed previously was provided by the argon measurements reported here.

(8.2) Test of Model

The proposed temperature and pressure dependency of the hemispherical geometry was verified by comparing the model developed in the previous chapter with measurements made in argon. In particular, verification of the effective eigenvalues of the radial modes in the hemispherical cavity was sought as well as agreement with the fit given by equation (7.8.6). Furthermore the model describing the loss mechanisms contributing to the excess halfwidths was tested by an analysis of the halfwidths.

Measurements in argon were obtained simultaneously using the hemispherical resonator and the spherical resonator described in chapter (4). The two systems were unified as shown in figure (8.2.1). The spherical and hemispherical resonators were connected to common vacuum and pressure lines enabling any effects from gas impurities to be nullified. Deviations arising from random fluctuations in the pressure measurement were

also negated using this set-up. The arrangement allowed direct comparison to be made between the data obtained from the hemispherical resonator and that obtained from the spherical resonator and therefore the validity of the calibration measurements could be assessed.

Figure (8.2.1): The experimental arrangement of the spherical and hemispherical systems

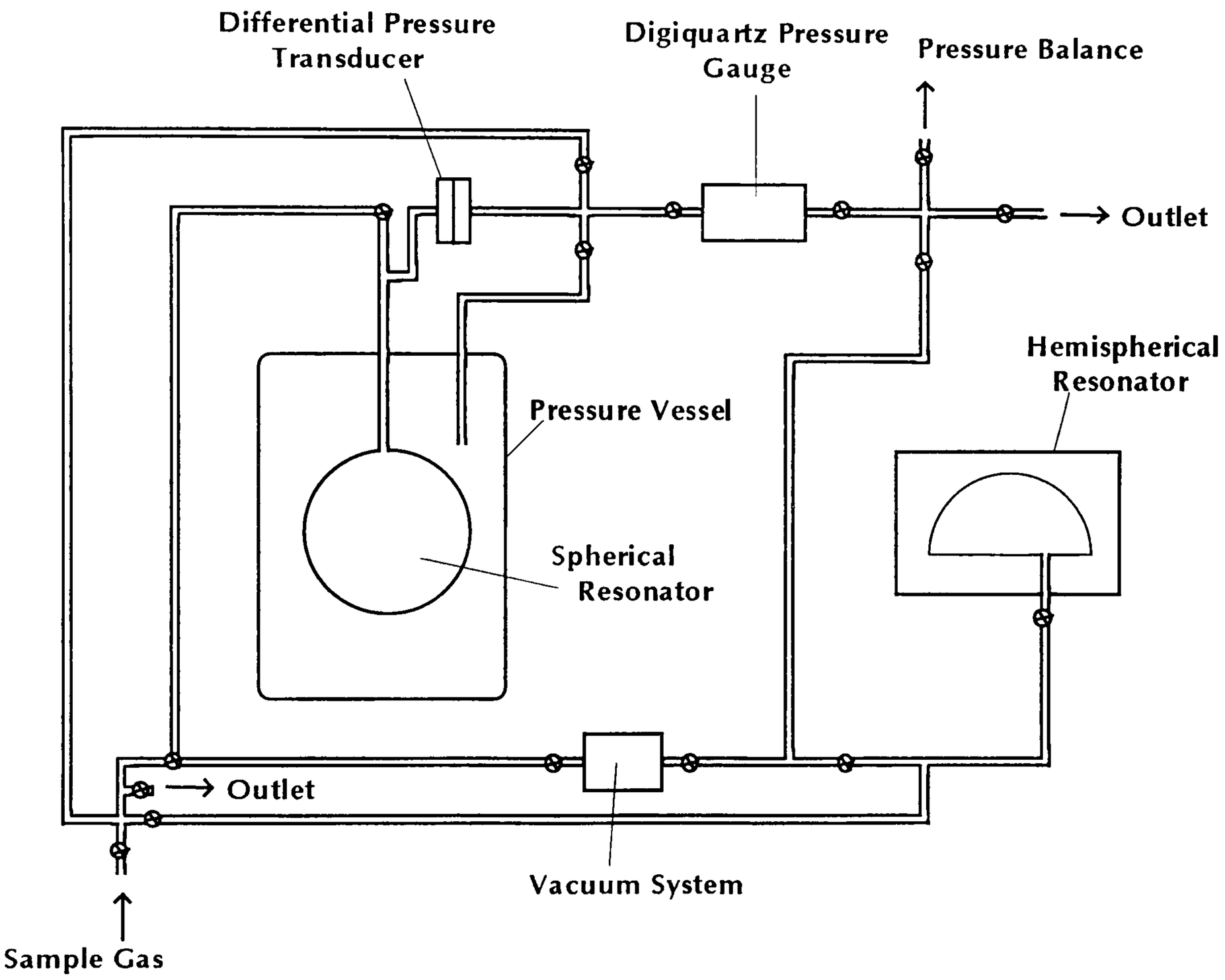

(8.3) Reference Data – Measurements in the Sphere

The reference data was obtained from measurements made in the stainless steel resonator described in chapter (4). Data was obtained along two isotherms at temperatures close to 306 K and 323 K at approximately eleven points using the procedure set out in section (6.2). For the isotherm performed at 306 K the argon used was research grade with a stated mole fraction purity of 0.999995. However, the maximum pressure obtainable from the cylinder was less than 4 MPa and since this did not cover the range over which the calibration measurements were made, the cylinder was exchanged prior to the isotherm at 323 K. The argon utilised for the isotherm performed at 323 K was 'pureshield' supplied by BOC Ltd. and has a stated mole fraction purity of 0.9995. No attempt at purification was made since the data was to be used for comparative purposes and the same sample gas filled both resonators.

(8.4) Excess Halfwidths

The halfwidths of the resonance provide a measure of the loss mechanisms occurring in the resonator. When the losses are known exactly, the difference between the calculated and measured halfwidths is zero and it is this quantity, the excess halfwidth, which provides an indication of how well the model describes the system.

The fractional excess halfwidths of radial modes in the spherical resonator are given by

$$\frac{\Delta g_{0,n}}{f_{0,n}} = \frac{g_{0,n} - g_{\mathrm{h}} - g_{\mathrm{t}} - g_{\mathrm{b}}}{f_{0,n}} \tag{8.4.1}$$

The excess halfwidths of the radial modes studied for both the isotherms was generally below about 30 ppm as illustrated by figures (8.4.1) and (8.4.2). For the isotherm at 306 K the (0,2) mode exhibited excess halfwidths much higher than expected and on the order of 60 to 70 ppm. The reason for the unexpectedly high excess halfwidths could have been due to tube effects that have been unaccounted for; one possibility was the microphone transducer which had been replaced by a commercially available insert and which introduced a small waveguide at the wall of the resonator. All the modes show excess halfwidths which are slightly pressure dependent, this behaviour was explained by Boyes [59] to be a result of shell motion: that in the region of increase (in excess halfwidth) the

Figure (8.4.1): Fractional excess halfwidths of the first five radial modes measured in argon at 305.510 K using the spherical resonator

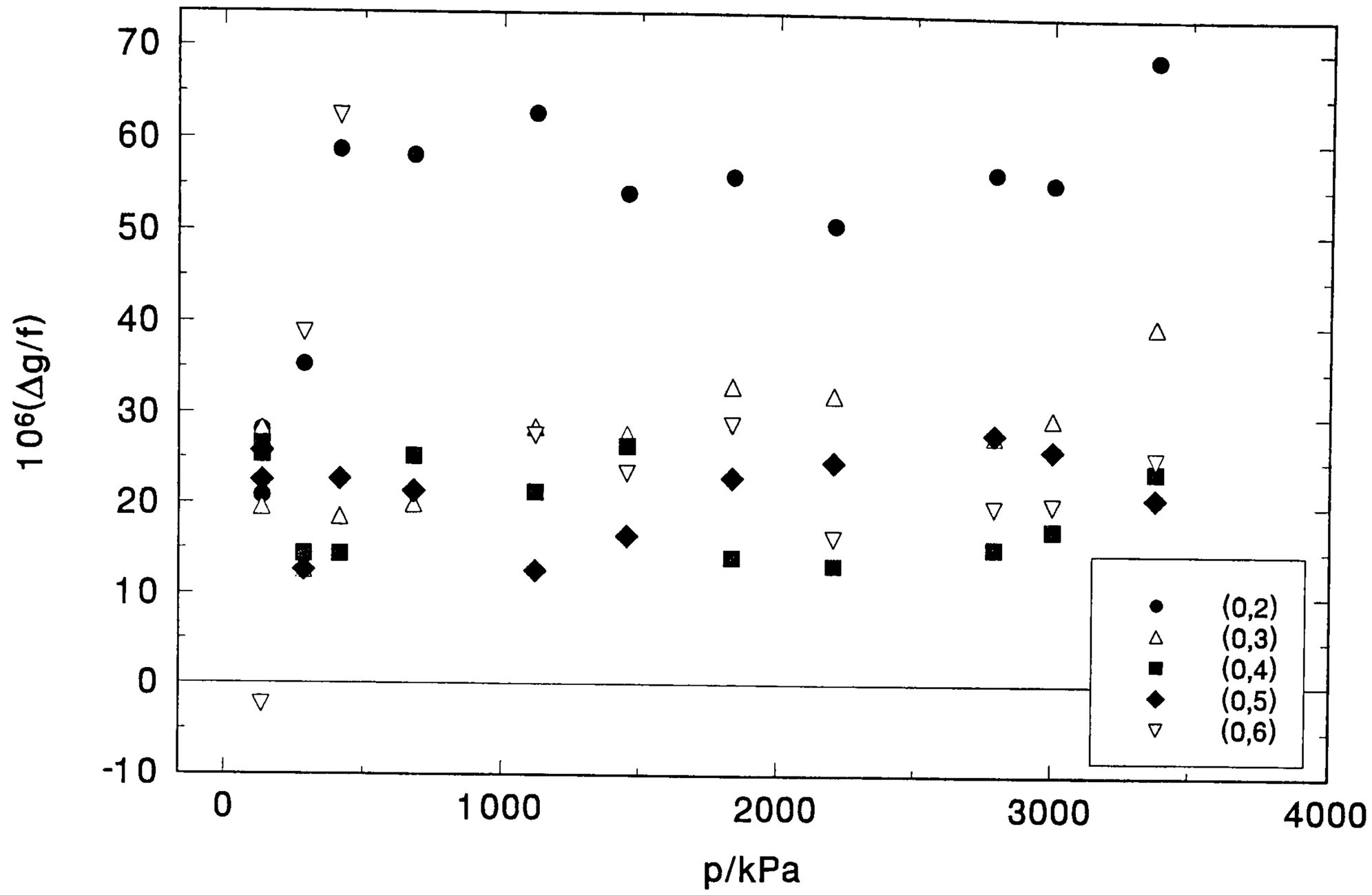

Figure (8.4.2): Fractional excess halfwidths of the first four radial modes measured in argon at 322.891 K using the spherical resonator

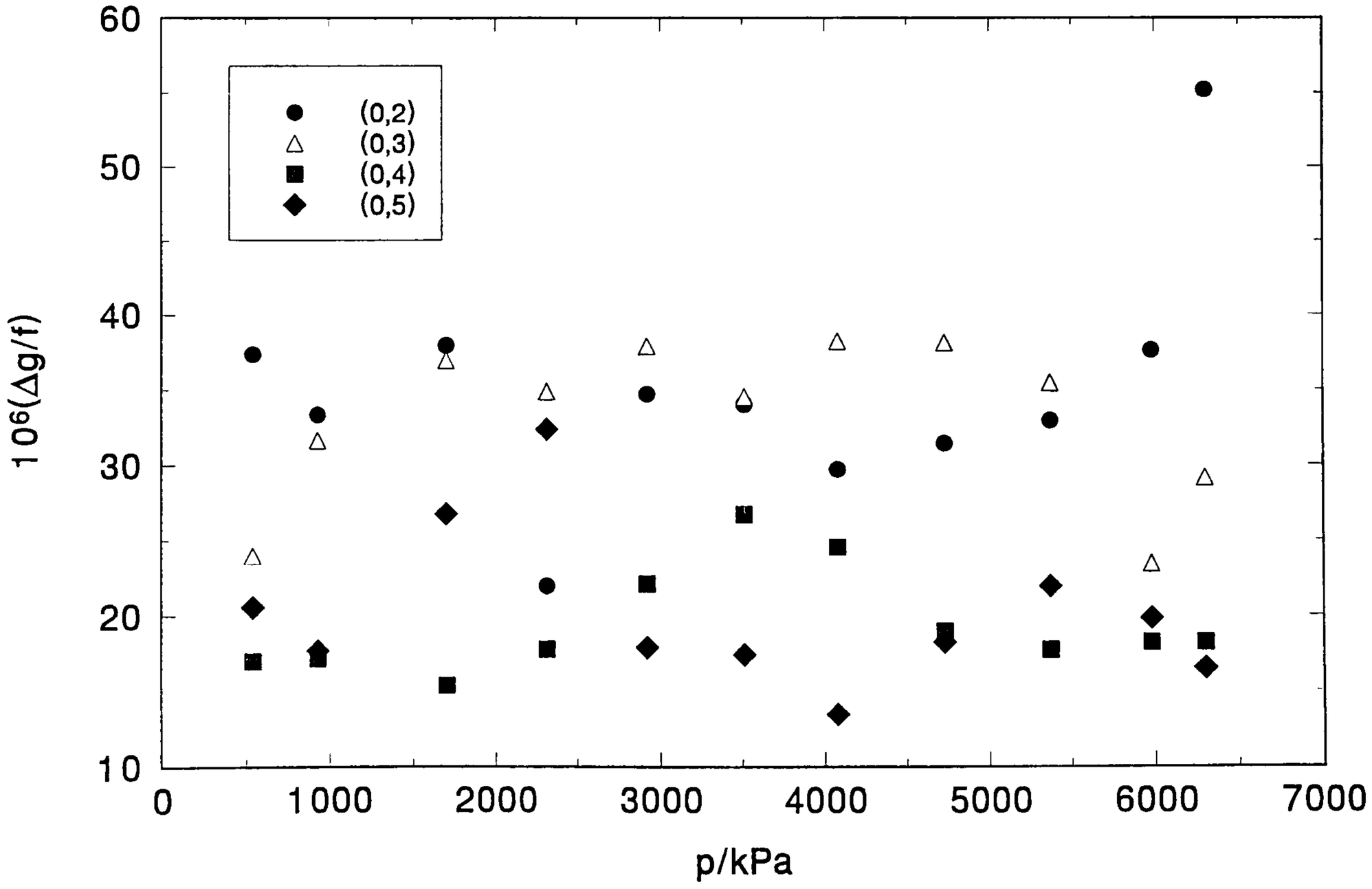

corrections are dominated by shell motion and because an exact expression of classical elasticity is used it does not hold exactly for a real non-isotropic resonator. The behaviour observed for the excess halfwidths was therefore not unexpected and the results suggested that the model used to determine the losses in the sphere was adequate and provided a suitable comparison for the model developed for the hemisphere.

(8.5) Speed of Sound

The speed of sound was extracted from the measurements of the resonance frequencies and halfwidths of the first five radial modes for the isotherm performed at 306 K and from the first four radial modes of the isotherm conducted at 323 K by utilising the equation

$$u = 2\pi a \left[\frac{f_{0,n} - f_{\mathrm{h}} - f_{\mathrm{t}} - f_{\mathrm{sh}}}{\nu_{0,n}} \right] \qquad (8.5.1)$$

where the correction terms given by Δf_{h} , Δf_{t} and Δf_{sh} and discussed fully in chapter 3 are due to the thermal boundary layer, tube effects and the effects of shell motion respectively. The radius of the sphere was calculated at the temperatures of the isotherms from equation (7.4.2). Small corrections were applied at each state point to reduce the temperature to the stated temperature of the isotherm. The estimated standard deviation of a measured resonance frequency was δf and the speed of sound was weighted by the lesser of $(2\times10^{-6} f / \delta f)$ and unity.

The fractional deviations of (u/a) obtained from each mode from the average $\langle u/a \rangle$ obtained from all the modes, or a selection of modes are depicted in figures (8.5.1) and (8.5.2) for the two isotherms.

For the isotherm performed at 305.510 K the (0,6) mode was removed from the analysis at the lowest four pressures where the agreement between the mean $\langle u/a \rangle$ of the remaining modes was on the order of a few per cent. The (0,5) mode was also removed from the analysis at the 132 kPa state point. The agreement over the whole range (after removal of the modes mentioned above) was generally less than 10 ppm and always better than 20 ppm. The best agreement was obtained at pressures of around 2 MPa, presumably

Figure (8.5.1): The fractional deviations of (*u/a*) from each mode from the average <*u/a*> calculated from selected modes in argon at 305.510 K

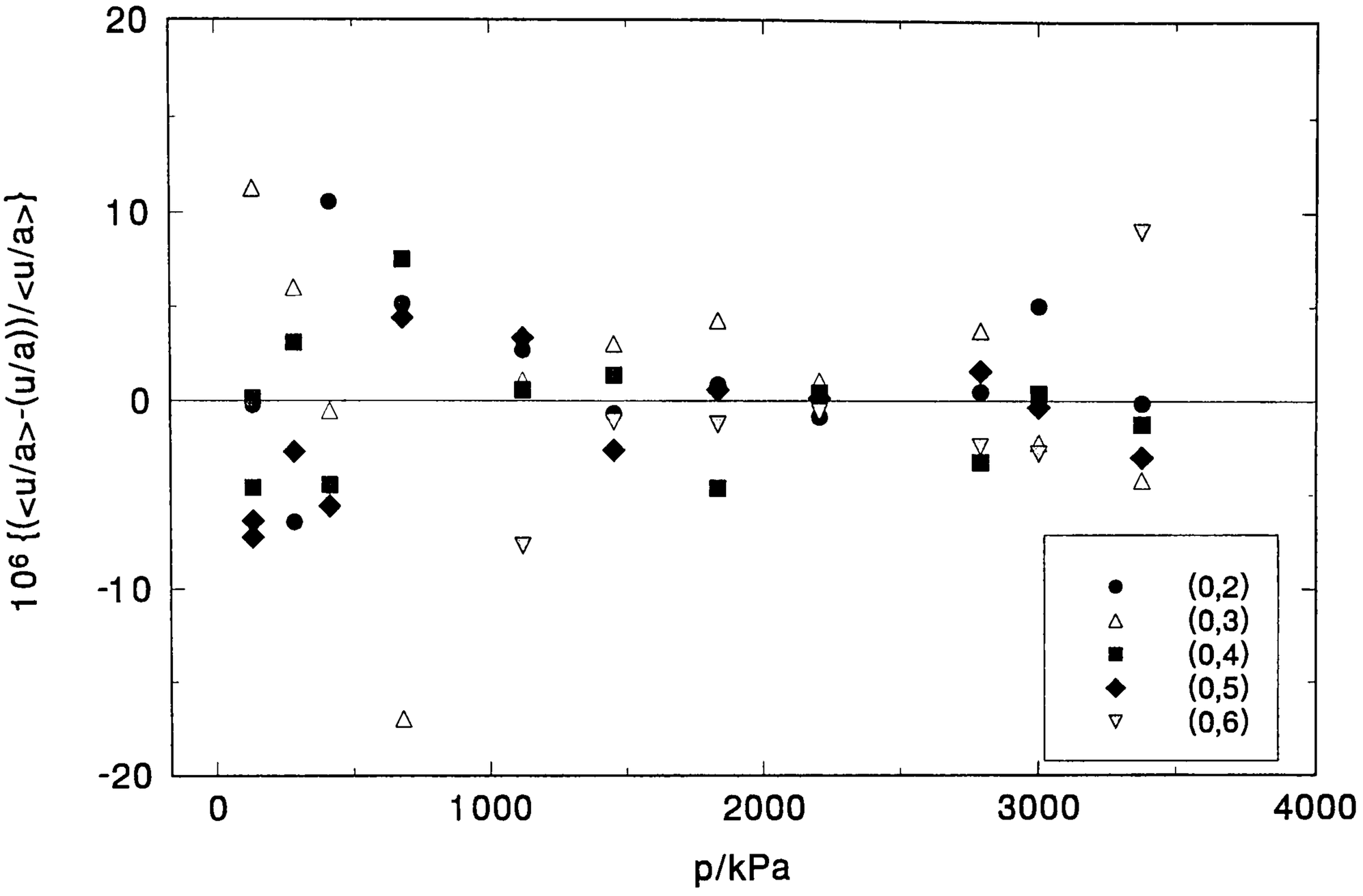

Figure (8.5.2): The fractional deviations of (*u/a*) from each mode from the average <*u/a*> calculated from selected modes in argon at 322.891 K

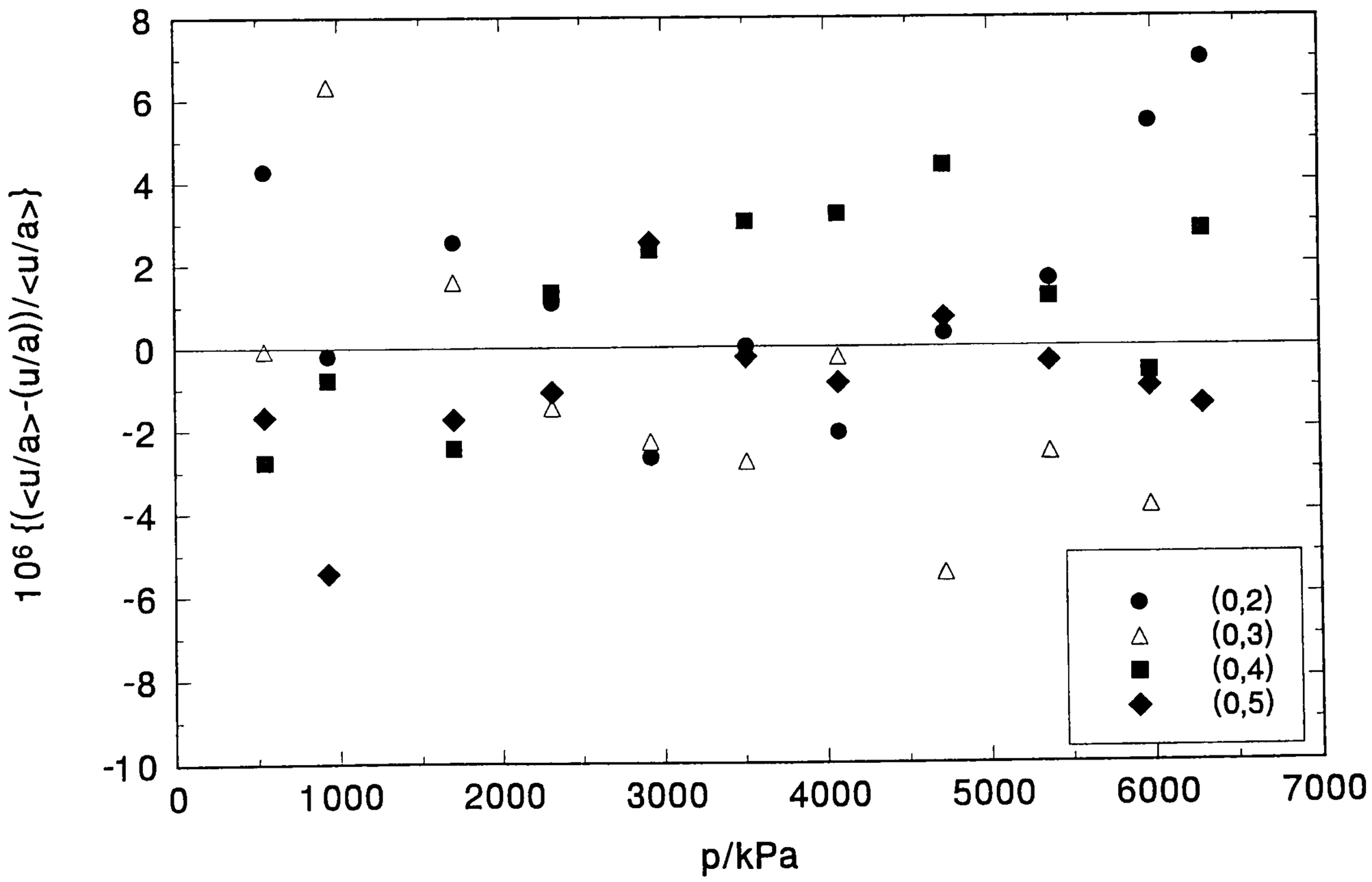

in the region where the boundary layer effects were relatively small and the resonator was experiencing very little dilation.

For the isotherm performed at 322.891 K fairly similar trends were seen as with the isotherm at 305.5 K. Again the best agreement between the modes was around the 2 MPa region, with the effects of dilation of the resonator causing an upward trend with pressure in the observed excess halfwidths. The agreement generally, however, over the entire range is very good and is always better than 10 ppm, with the inclusion of all the modes for which measurements were possible (the signal-noise ratio of the (0,6) mode was too weak to allow its measurement at this temperature).

Tables (8.5.1) and (8.5.2) summarise the results obtained from the isotherms together with the number of modes N used to determine the mean $\langle u \rangle$, the standard deviations σ from the mean and the deviations δ of u from the adopted fit.

Table (8.5.1):Mean values of u/a and u with standard deviations σ from N modes and deviations δ from the adopted pressure series at a temperature of 305.510 K

p/kPa	$\langle u/a \rangle$/Hz	$\langle u \rangle$/ms^{-1}	10^6 ($\sigma(u)/u$)	10^6 ($\delta(u)/u$)	N
3376.764	7313.3507	329.0331	5.2	6.6	5
3003.124	7302.6395	328.5512	3.1	-27.8	5
2790.637	7297.3363	328.3126	2.9	26.1	5
2206.268	7282.3077	327.6365	0.8	-7.3	5
1835.166	7273.5433	327.2422	3.3	-7.4	5
1454.566	7265.2489	326.8690	2.2	24.5	5
1120.505	7257.8312	326.5353	4.4	-15.4	5
† 669.028	7247.1201	326.0534	11.4	-230.4	4
412.859	7243.7341	325.9010	2.7	-12.1	4
282.425	7241.4335	325.7975	5.6	11.7	4
† 132.405	7239.2947	325.7013	0.1	102.8	3
132.386	7238.5324	325.6670	3.0	-2.5	4

† Pressure not included for final fit

Table (8.5.2):Mean values of u/a and u with standard deviations σ from N modes and deviations δ from the adopted pressure series at a temperature of 322.891 K

p/kPa	$\langle u/a \rangle$/Hz	$\langle u \rangle$/ms^{-1}	10^6 ($\sigma(u)/u$)	10^6 ($\delta(u)/u$)	N
† 6299.657	7641.0983	343.9015	6.6	92.1	4
5979.128	7627.1993	343.2760	3.9	-6.0	4
5369.223	7603.0144	342.1875	1.9	-2.8	4
4727.548	7578.8014	341.0977	4.1	10.3	4
4077.227	7555.4303	340.0459	2.3	16.3	4
3511.373	7535.8850	339.1662	2.4	-7.6	4
† 2920.030	7515.6128	338.2538	2.8	-147.1	4
2314.297	7497.9242	337.4577	1.4	-24.7	4
† 704.252	7479.8002	336.6420	2.4	-91.1	4
930.359	7459.9673	335.7494	4.9	30.1	4
540.611	7449.8729	335.2951	3.1	-15.6	4

† Pressure not included for final fit

Individual modes were rejected on the basis of a statistically significant reduction in the standard deviation of the mean at a given state and state points (denoted by †) were rejected on the basis of a significant reduction in the standard deviation for the isotherm. The speed of sound calculated at 306 K and 323 K using the spherical resonator is illustrated in figure (8.5.3) together with the estimated standard deviation $\sigma(u^2)/u^2$. A four-term fit was necessary to accommodate the data obtained at 306 K, whilst for the data obtained at 323 K a three-term fit was adequate. The coefficients of equation (1.1.3) which represent the argon data are given in table (8.5.3).

Figure (8.5.3): The speed of sound in argon derived at 305.510 K and 322.891 K in the spherical resonator

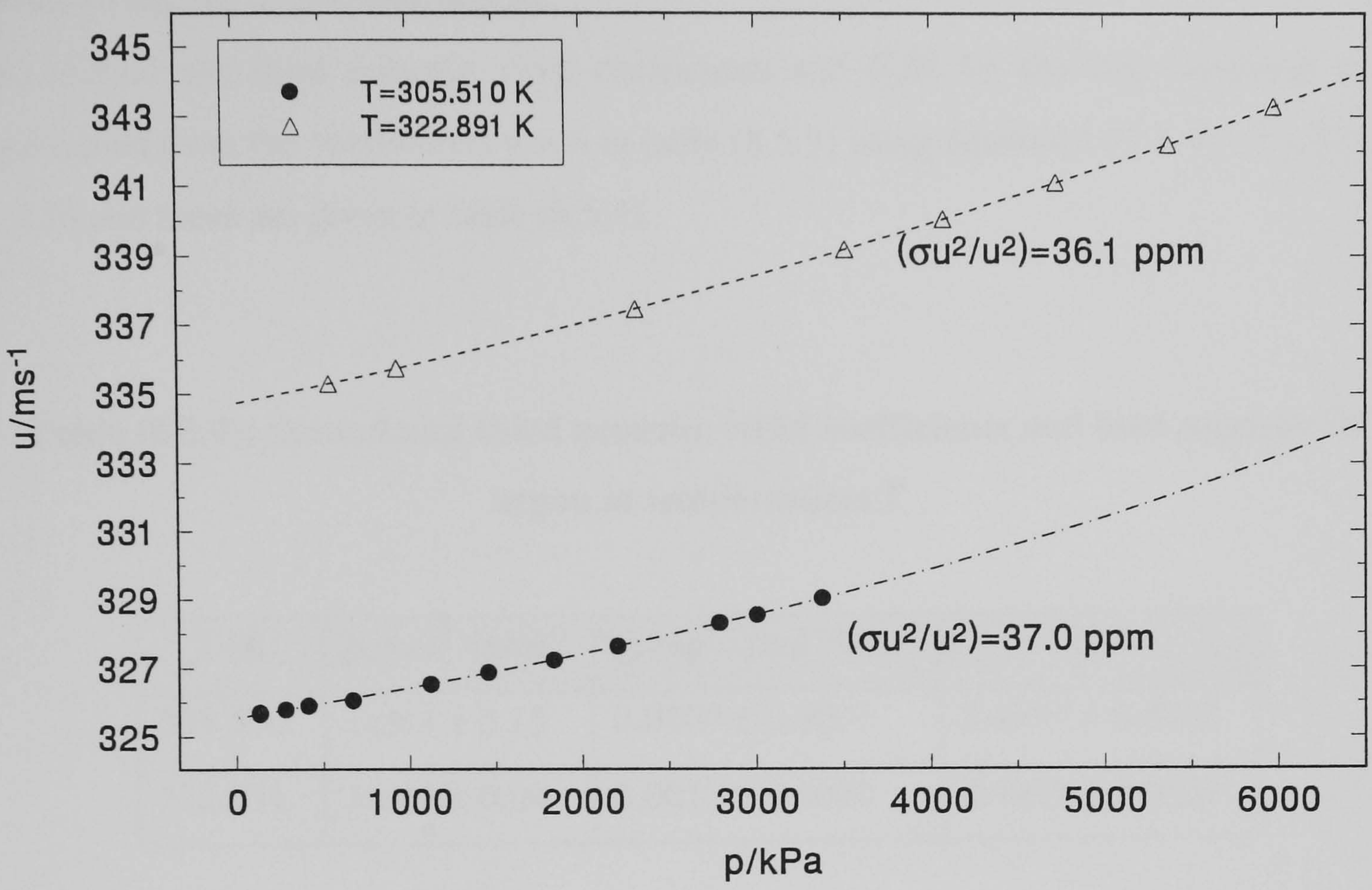

Table (8.5.3): Coefficients of equation (1.1.3) used to represent the data from measurements of (u/a) in argon

T / K	i	$\{A_i/a^2\}$/s^{-2}·Pa^{-i}	$10^6\sigma(u^2)/u^2$
305.510	0	$(52.360930 \pm 0.000997) \cdot 10^6$	37.0
	1	(0.26440 ± 0.00291)	
	2	$(0.143 \pm 0.020) \cdot 10^{-7}$	
	3	$(0.174 \pm 0.038) \cdot 10^{-14}$	
322.891	0	$(55.312417 \pm 0.001096) \cdot 10^6$	36.1
	1	(0.33865 ± 0.000823)	
	2	$(0.23430 \pm 0.00126) \cdot 10^{-7}$	

All coefficients were statistically significant at a probability of 0.999. The deviations of the selected mean speeds of sound at a given state from the adopted smoothing equation are shown in figures (8.5.4) and (8.5.5).

The second and third acoustic virial coefficients and C_p/R for the two isotherms were determined from the coefficients given in table (8.5.3) using equations (1.1.4), (1.1.5) and (1.1.6) and these are given in table (8.5.4).

Table (8.5.4): Second and third acoustic virial coefficients and heat capacity of argon at temperatures *T*

T /K	β_a/cm^3 · mol^{-1}	γ_a/cm^3 · mol^{-1} kPa^{-1}	C_p /R
305.510	12.83 ± 0.15	0.0007 ± 0.0001	2.4997 ± 0.0002
322.891	16.44 ± 0.04	0.0011 ± 0.0000	2.4989 ± 0.0001

The accuracy with which u^2 was obtained for both isotherms does not compare favourably with previous measurements performed using this resonator and, for a well-characterised gas such as argon the fractional deviation of u^2 could be expected to be a few ppm [3]. Due to the comparatively imprecise results obtained using the spherical resonator, the data was deemed unsuitable for calibration purposes and nitrogen data was used instead for this purpose as discussed in the previous chapter. The results did, however, provide a useful source of comparison for the results obtained using the hemispherical resonator.

Figure (8.5.4): Fractional deviations from the adopted 4-term fit for the speed of sound in argon at 305.510 K

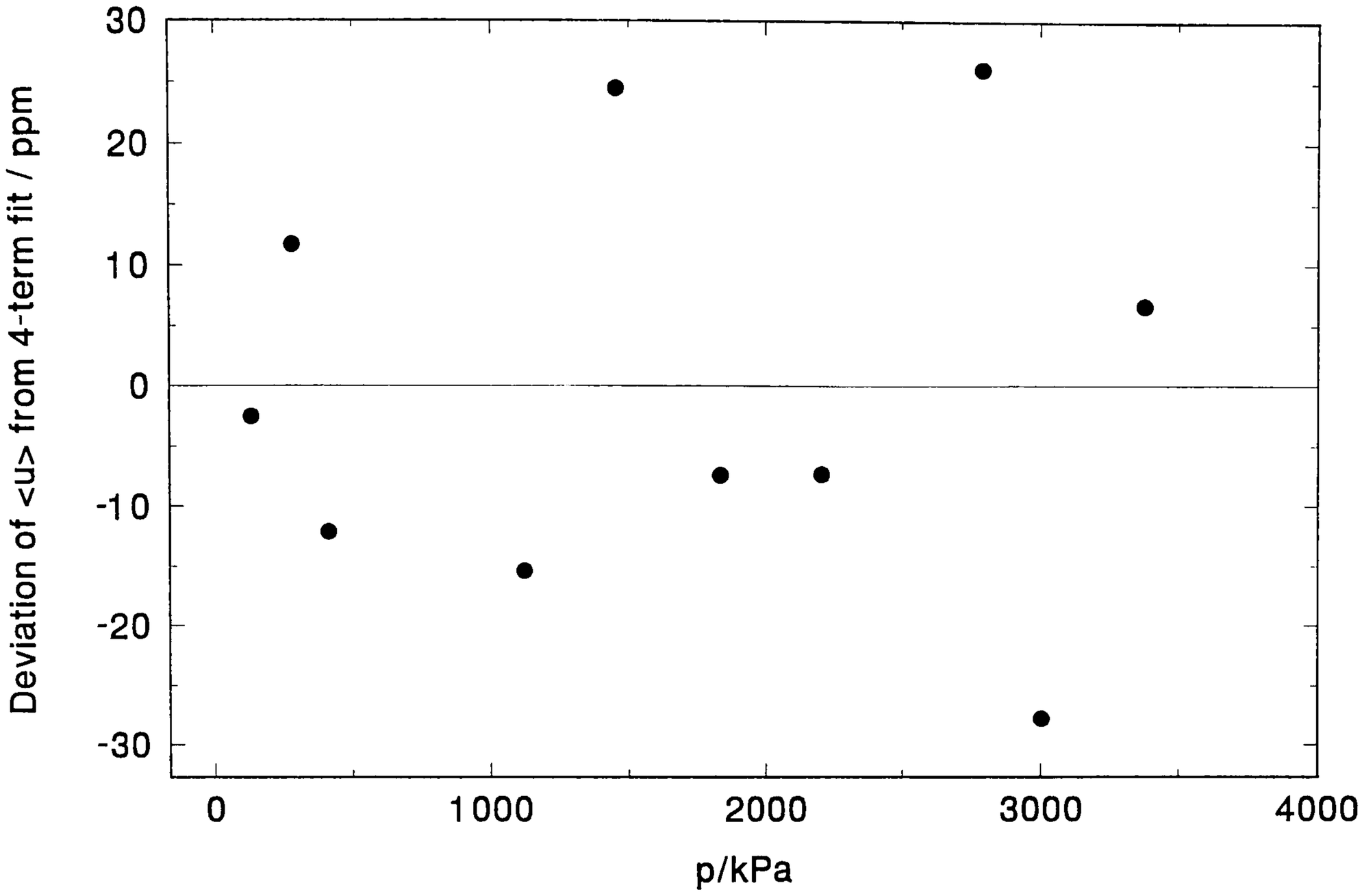

Figure (8.5.5): Fractional deviations from the adopted 3-term fit for the speed of sound in argon at 322.891 K

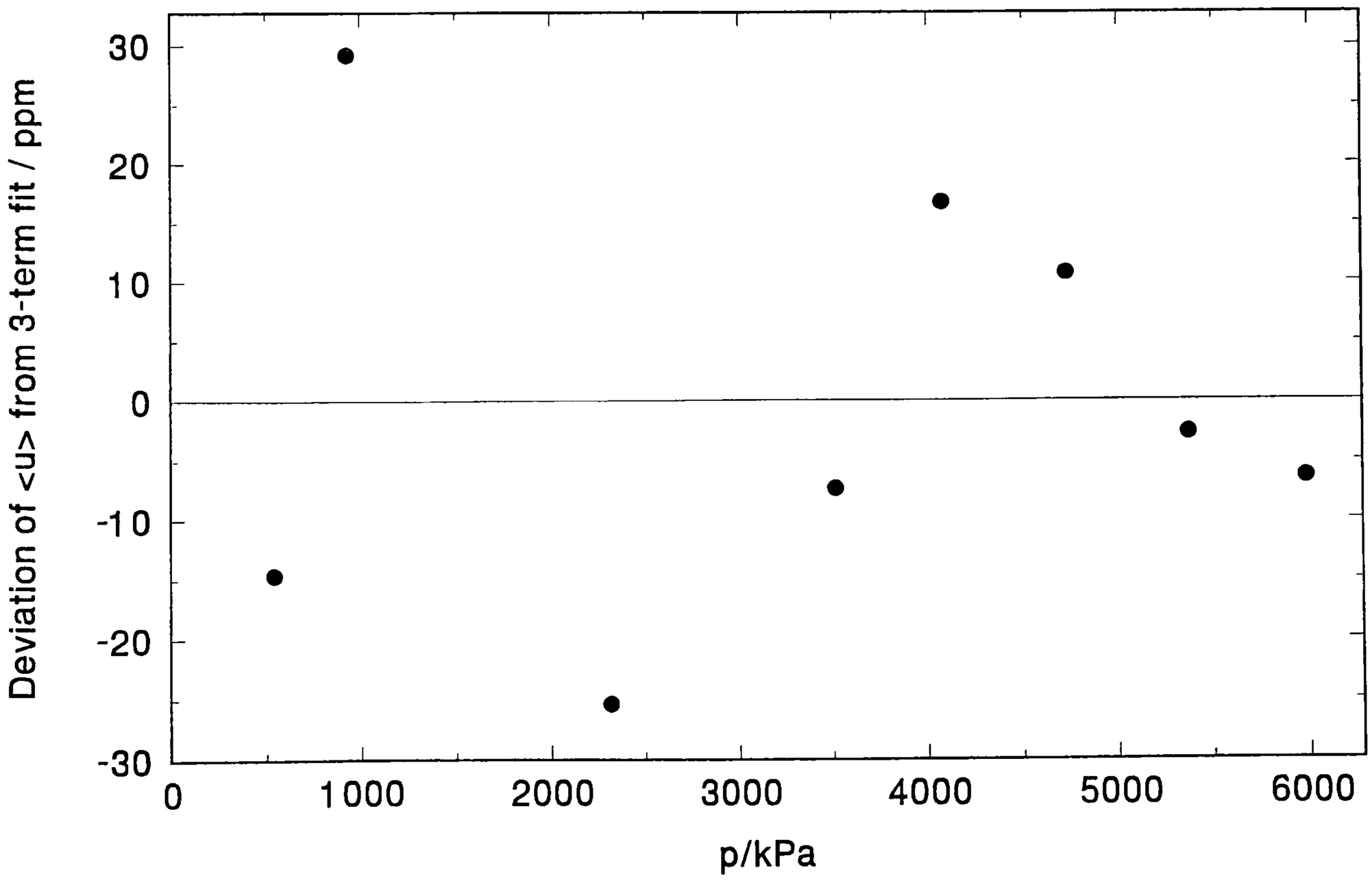

(8.6) Sample Data – Measurements in the Hemisphere

The resonance frequencies and halfwidths of the first four radial modes were measured either just before or just after the same measurements were made in the sphere. Before commencing an isotherm, the temperatures of the two resonators were set to be approximately equal and once the temperature of the spherical resonator was stable, minor adjustments were then made to the input powers of the hemispherical resonator until the temperature indicated by the long-stem PRT of the hemisphere agreed with that of the spherical resonator to 0.005 K. The stated temperature of the isotherm is the mean temperature of those indicated by the sphere's PRT and those of the hemisphere's PRT.

(8.7) Analysis

The speed of sound was extracted from the measurements of the resonance frequencies and halfwidths of the first five radial modes for the isotherm performed at 306 K and from the first four radial modes of the isotherm conducted at 323 K by using the equation

$$u = 2\pi a \left[\frac{f_{0,n} - \Delta f_{\mathrm{h}} - \Delta f_{\mathrm{v}} - \Delta f_{\mathrm{t}} - \Delta f_{\mathrm{sh}} - \Delta f_{\mathrm{slot}}}{\nu_{0,n}} \right] \tag{8.7.1}$$

where the correction terms given by Δf_{h} , Δf_{v} , Δf_{t} , Δf_{sh} and Δf_{slot} are discussed fully in the previous chapters and are due to the thermal and viscous boundary layers, tube effects, the effects of shell motion and corrections due to the slot between the hemisphere and its equator. The radius of the hemisphere was calculated at the temperatures of the isotherms from equation (7.8.7). Corrections were made to the eigenvalues by the use of the empirical eigenvalues reported in section (7.8) and the dependence of the radius on internal pressure was corrected according to equation (7.8.6). Small corrections were applied at each state point to adjust the temperature to the stated temperature of the isotherm. The estimated standard deviation of a measured resonance frequency was δf and the speed of sound was weighted by the lesser of $(2\times10^{-6} f/\delta f)$ and unity.

(8.8) Excess halfwidths

As mentioned previously if all the corrections are known exactly then the excess halfwidth will be zero. Initial estimates of the thermophysical properties used for the analysis of the loss mechanisms occurring in the sphere were obtained from reference [134 - 136]. The zero-density thermal conductivity was modified slightly as a result of the halfwidth analysis in order to obtain a more realistic value of the thermal conductivity which included the effect of gas impurities. The final modified value (from the sphere) was then used for the halfwidth analysis of the radial modes of the hemisphere.

The excess halfwidths of all the modes measured for the two isotherms are illustrated in figures (8.8.1), (8.8.2), (8.8.3) and (8.8.4). For the isotherm performed close to 306 K the excess halfwidths of the (0,3), (0,4) and (0,5) modes are all less than 15 ppm at pressures exceeding 500 kPa. Below this pressure the excess halfwidths of the (0,3), (0,4), (0,5) and (0,6) modes rises sharply to excess halfwidths of about 100 ppm at the lowest pressure of 130 kPa. The excess halfwidths could not be accommodated by adjusting the transport properties which contribute to the boundary layers (*i.e.* the thermal conductivity and the viscosity) without causing all the excess halfwidths of the points above 500 kPa to become negative. The (0,2) and (0,6) mode were obviously affected by their proximity to shell resonances. Not unexpectedly, the (0,2) mode was the most severely affected, with a maximum around 750 kPa and rising towards a second above 3500 kPa. The (0,6) mode also exhibited a broad maximum at around 1,900 kPa and spanned approximately 2,000 kPa before the excess halfwidths fell towards their expected values of a few ppm. The excess halfwidths of the (0,2) mode varied from 170 ppm to 540 ppm at the maxima and did not approach the theoretically predicted values at all.

For the isotherm performed close to 323 K the excess halfwidths of the (0,4) and (0,5) modes were below 16 ppm over the entire pressure range and generally below 10 ppm. The (0,3) mode, however, appeared to be affected by a minor shell resonance and exhibited a maximum at about 3,000 kPa, but even here the greatest excess halfwidths were less than 30 ppm. The (0,2) mode again exhibits maxima indicative of shell resonances. The excess halfwidths rose sharply from around 100 ppm to about 1,000 ppm

at the maximum which occurs at a pressure of approximately 5,300 kPa. The second maximum at a pressure of about 500 kPa was outside the range of these results.

Figure (8.8.1): Fractional excess halfwidths of the (0,3), (0,4) and (0,5) modes in argon at 305.510 K obtained using the hemispherical resonator

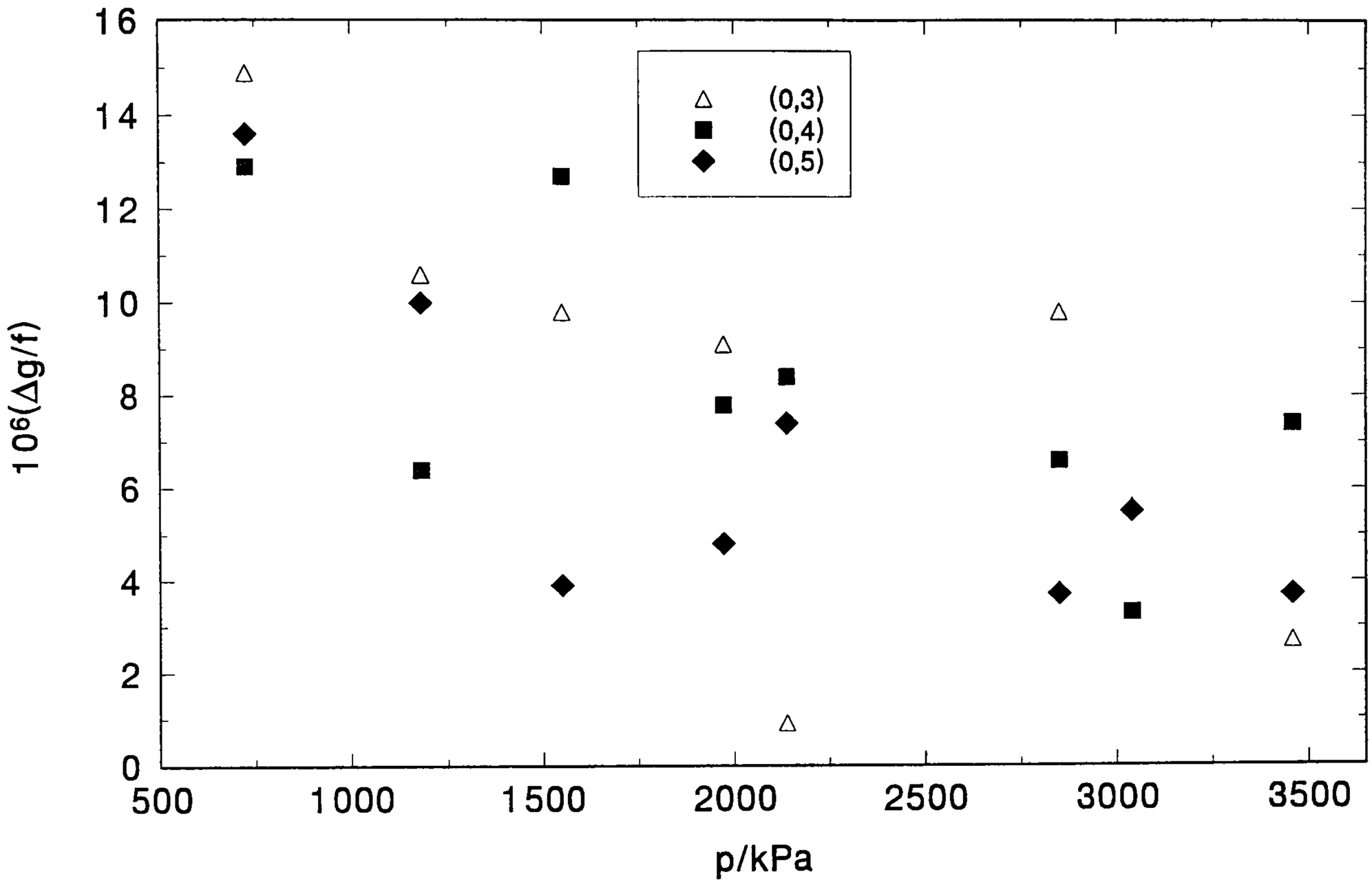

Figure (8.8.2): Fractional excess halfwidths of the (0,2) and (0,6) modes in argon at 305.510 K obtained using the hemispherical resonator

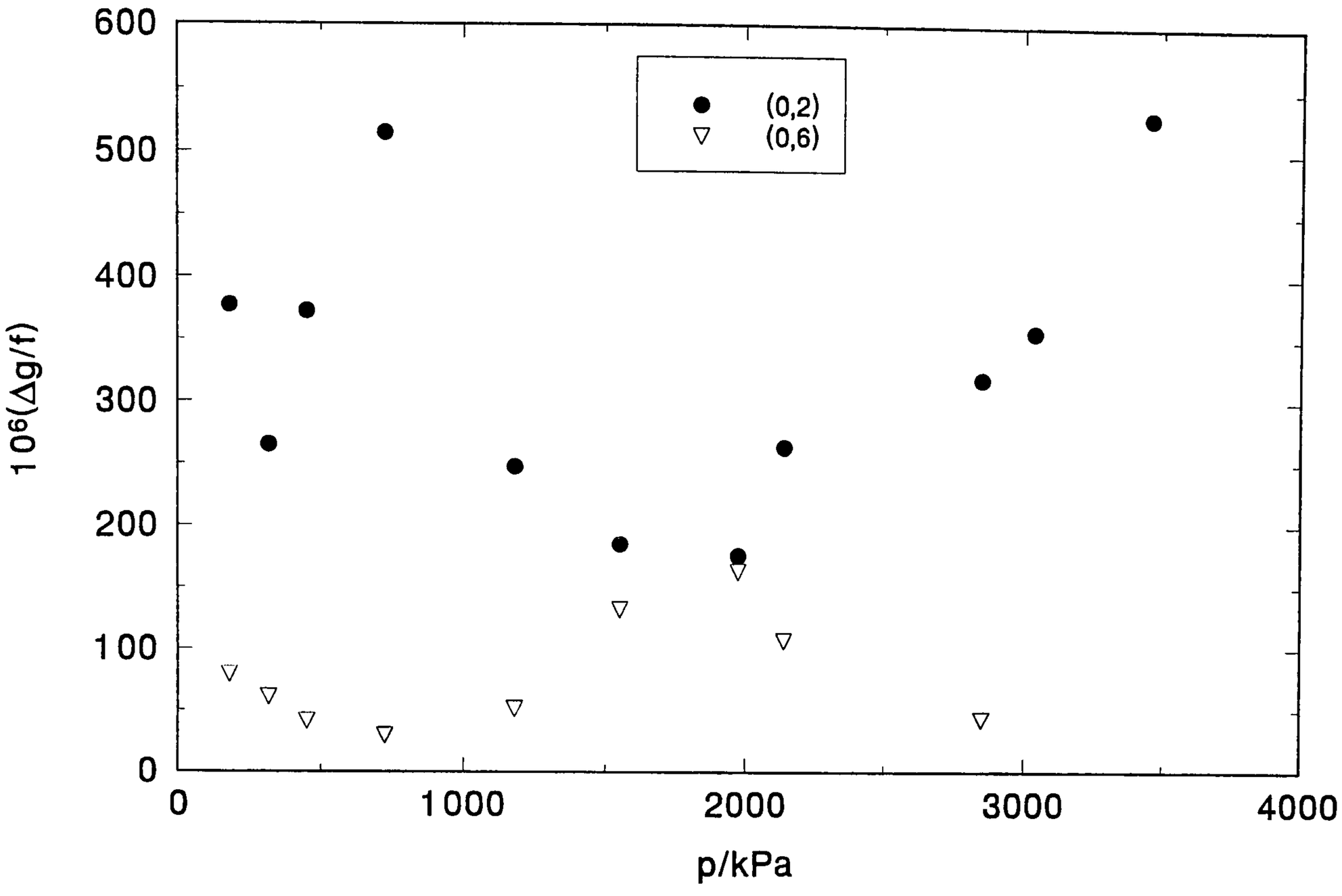

Figure (8.8.3): Fractional excess halfwidths of the (0,3), (0,4) and (0,5) modes in argon at 322.891 K obtained using the hemispherical resonator

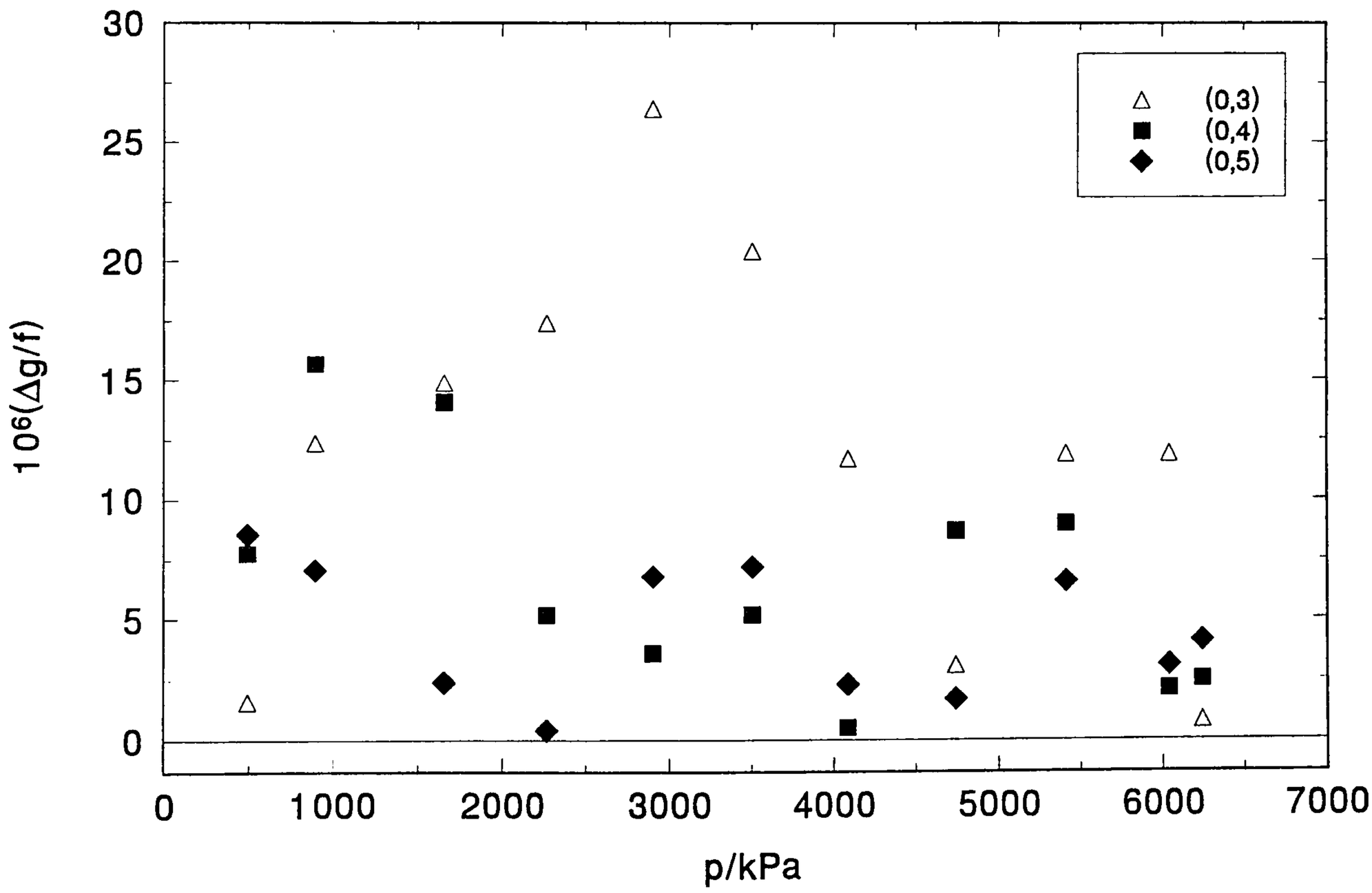

Figure (8.8.4): Fractional excess halfwidths of the (0,2) mode in argon at 322.891 K obtained using the hemispherical resonator

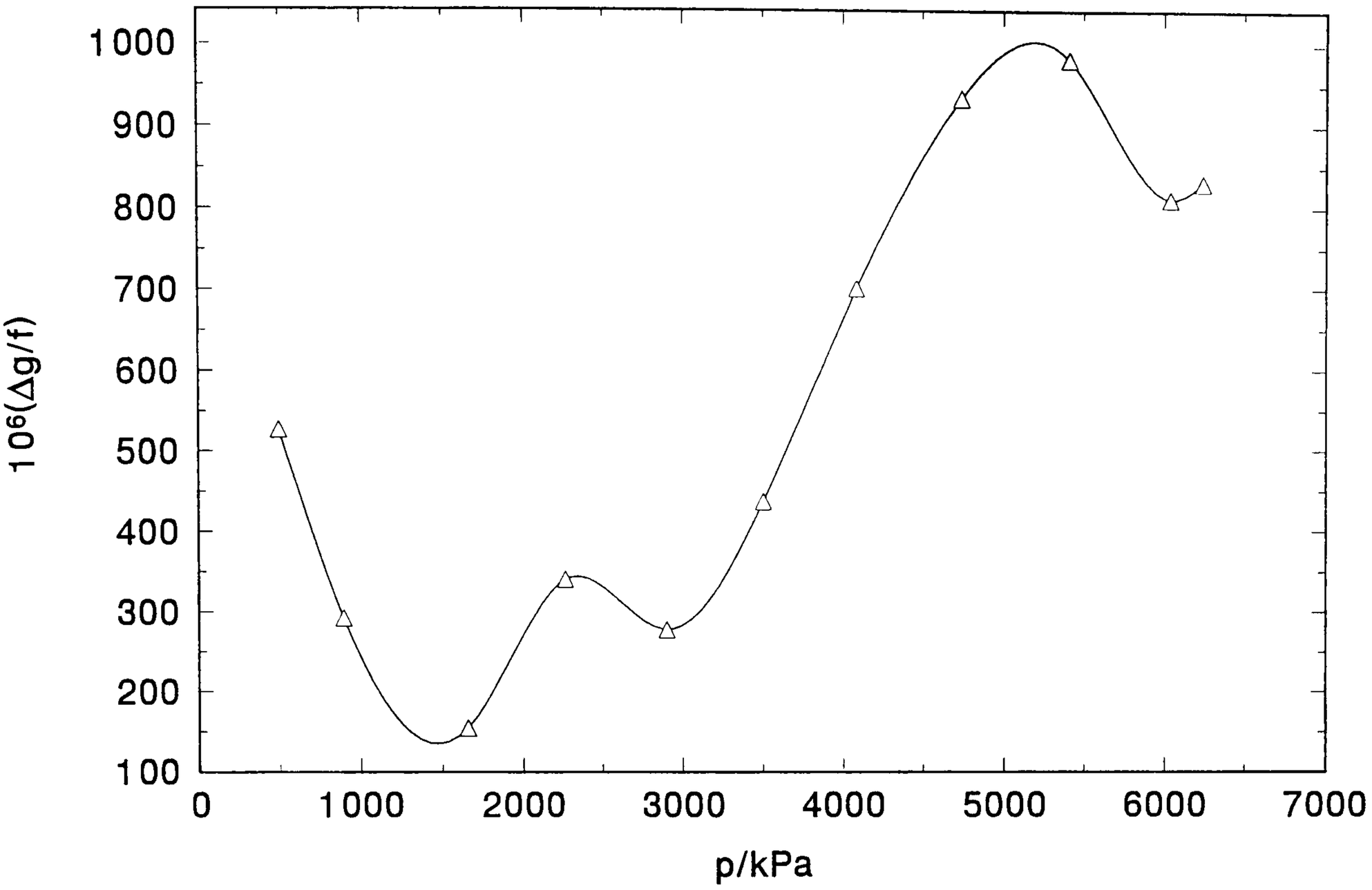

(8.9) Speed of sound

Figures (8.9.1), (8.9.2), (8.9.3) and (8.9.4) show the fractional deviations of *u/a* calculated from the individual modes from the average <*u/a*>calculated from *N* modes (see tables for the value of *N* at each state point). For the lower-temperature isotherm the agreement between the (0,3), (0,4) and (0,5) modes is about 10 ppm over most of the pressure range. At the lowest pressure for this isotherm the agreement falls to around 20 ppm but is still surprisingly good. A similar level of agreement is also seen for the higher-temperature isotherm, where the fractional deviations of the (0,3), (0,4) and (0,5) modes is below 10 ppm over the entire pressure range. The lowest pressure of this isotherm is around

Figure (8.9.1): The fractional deviations of the calculated values of *u/a* for the (0,3), (0,4) and (0,5) modes from the average <*u/a*> calculated from *N* modes for the isotherm in argon at a temperature of 305.510 K

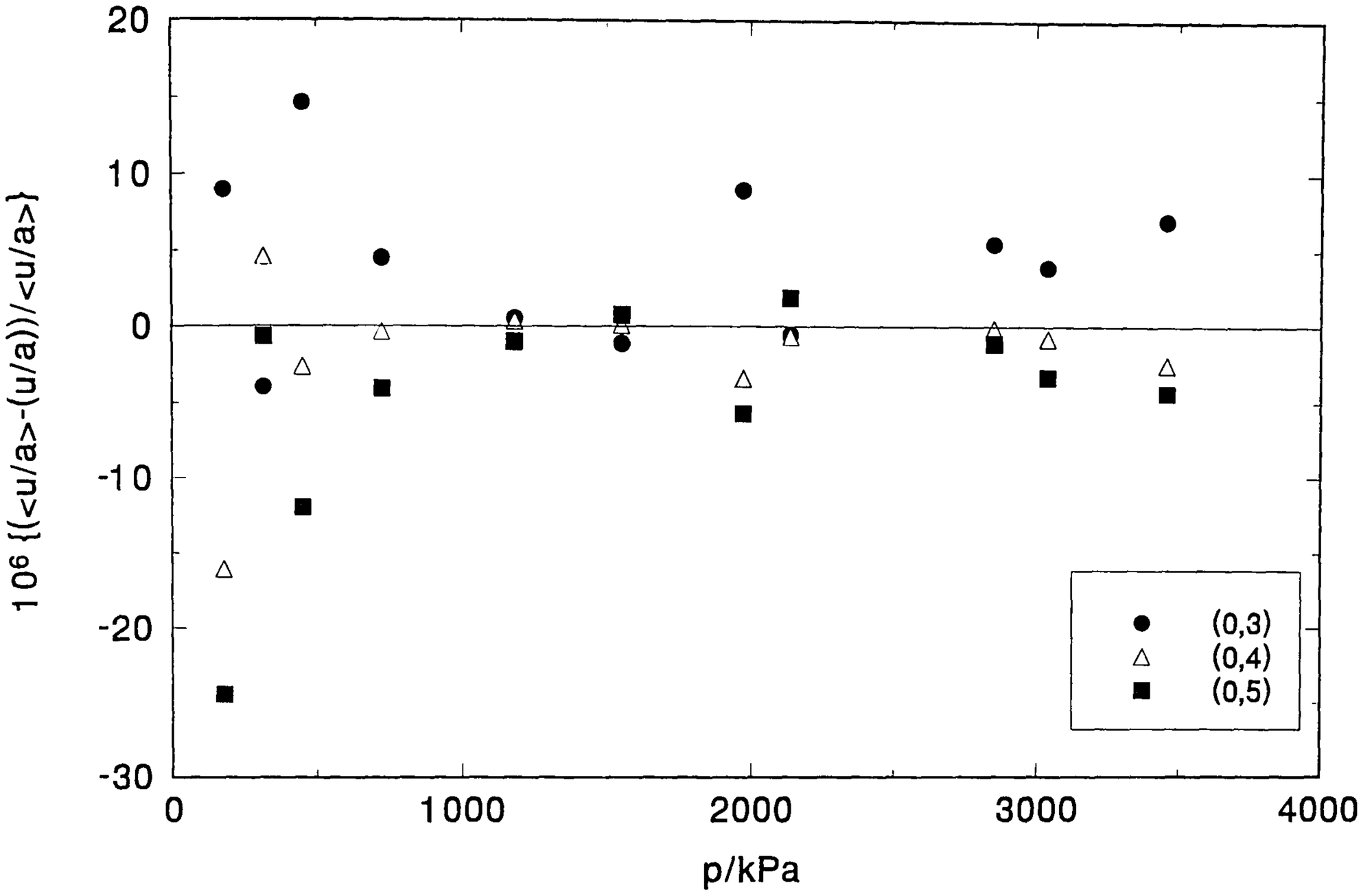

Figure (8.9.2): The fractional deviations of the calculated values of *u/a* for the (0,2) and (0,6) modes from the average <*u/a*> calculated from *N* modes for the isotherm in argon at a temperature of 305.510 K

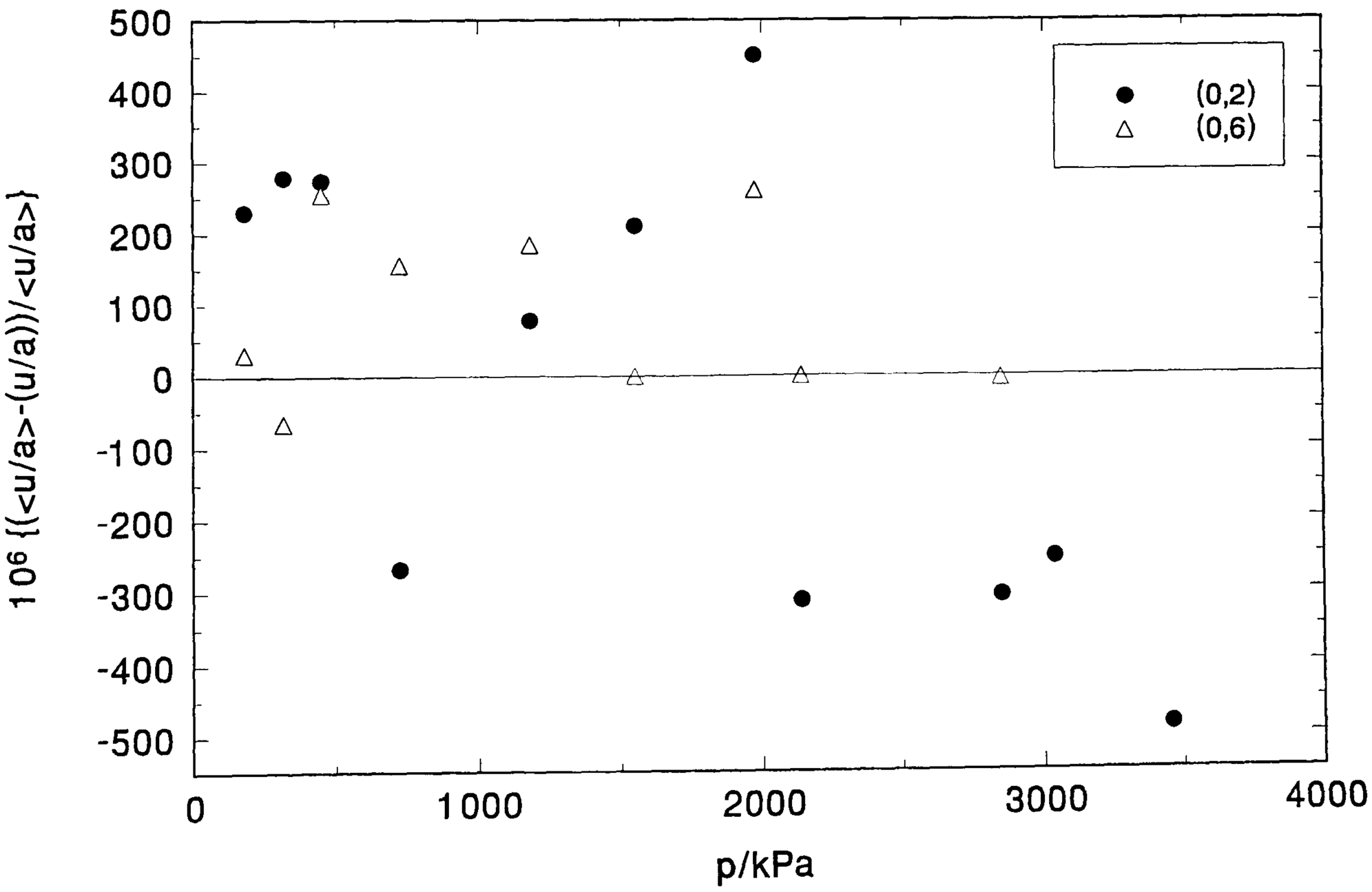

Figure (8.9.3): The fractional deviations of the calculated values of *u/a* for the (0,3), (0,4) and (0,5) modes from the average <*u/a*> calculated from *N* modes for the isotherm in argon at a temperature of 322.891 K

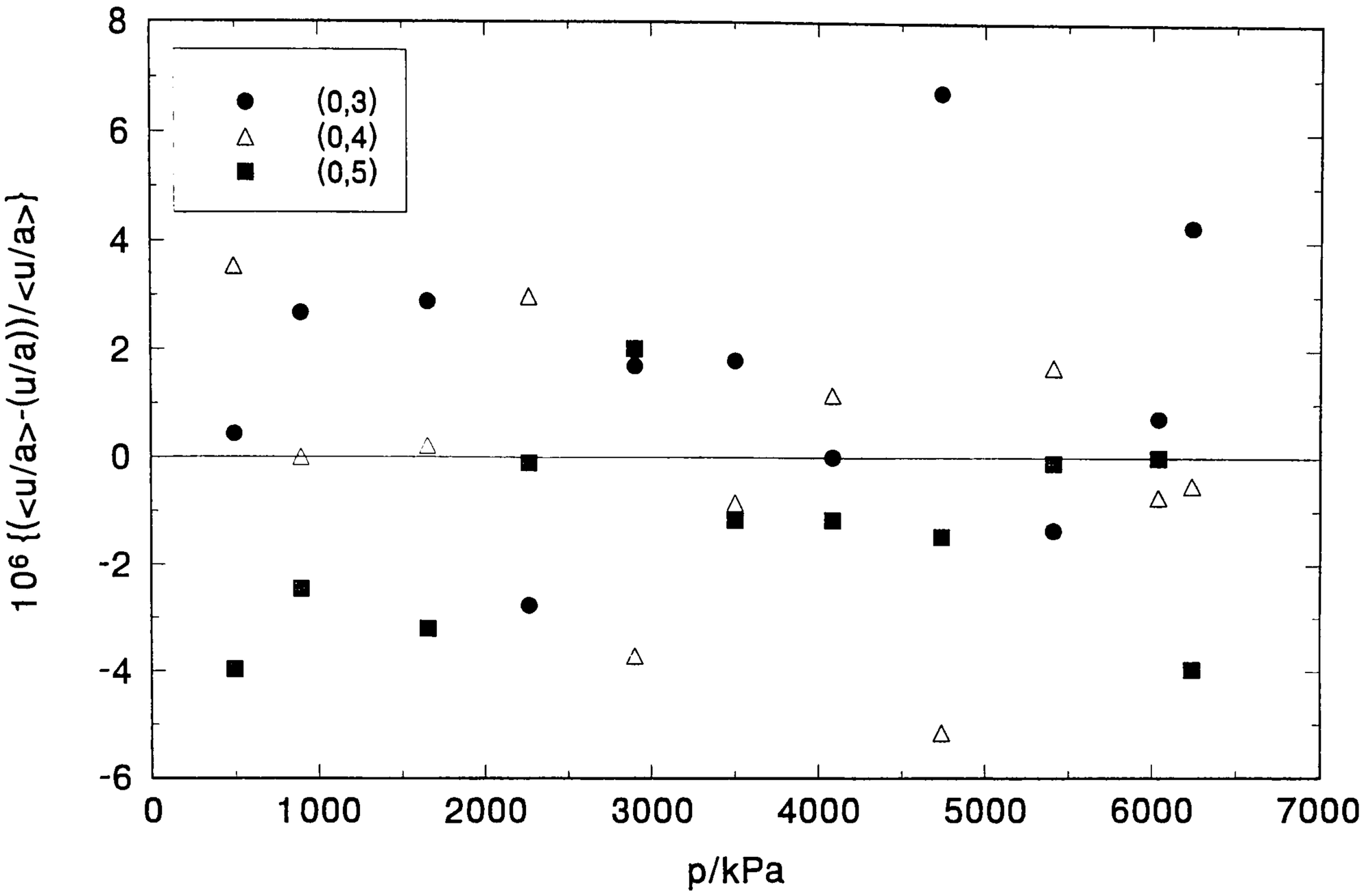

Figure (8.9.4): The fractional deviations of the calculated values of *u/a* for the (0,2) mode from the average <*u/a*> calculated from *N* modes for the isotherm in argon at a temperature of 322.891 K

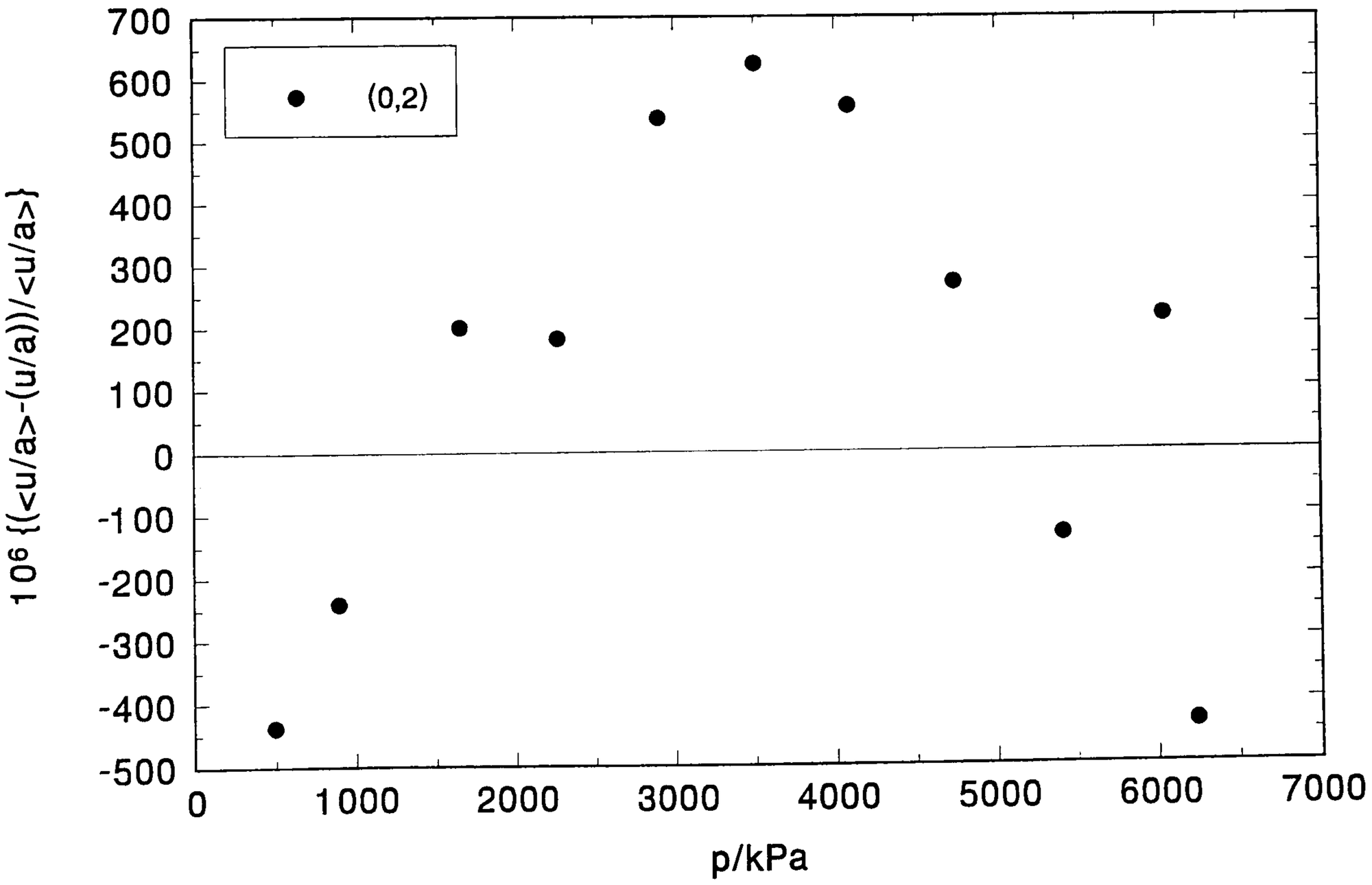

450 kPa and so no sharp deviations are expected as the pressure range does not extend sufficiently low. The (0,2) and (0,6) modes of the isotherm at 305.5 K deviate from the mean *u/a* in a manner consistent with shell resonance effects as implied by the excess halfwidths. The (0,2) mode shows two peaks at which (*u/a*) calculated from the (0,2) mode deviates most strongly. The first of these peaks coincides with a maximum in $\Delta g/f$ also observed for this mode. The second corresponds to the maximum in $\Delta g/f$ observed for the (0,6) mode and suggests there is coupling between these modes and the same shell resonance feature. The value of *u/a* calculated from the (0,6) mode also shows a maximum in deviation from the mean *u/a* over a range which encompasses the maximum $\Delta g/f$ observed for the (0,6) mode and the higher frequency (low pressure) maximum observe for the (0,2) mode. The deviations of the (0,2) mode of the isotherm at 322.9 K exhibit a broad peak, but the maximum does not correspond with the maximum in $\Delta g/f$ observed for this mode which is also extremely broad and therefore, the absence of coincidence, is not too surprising.

Table (8.9.1): Mean values of *u/a* and *u* with standard deviations σ from *N* modes and deviations δ from the adopted pressure series at a temperature of 305.510 K

p/kPa	<*u*/*a*>/Hz	<*u*>/ms^{-1}	10^6 ($\sigma(u)/u$)	10^6 ($\delta(u)/u$)	*N*
3458.339	8742.6217	328.9460	6.1	5.9	3
3038.906 †	8730.3187	328.4831	3.7	-10.3	3
2849.280	8724.7843	328.2749	4.1	-28.3	4
2137.488	8705.4559	327.5476	1.3	-7.9	4
1972.630	8701.3090	327.3916	7.9	17.2	3
1550.604	8690.2743	326.9764	0.8	2.9	4
1180.337 †	8681.2322	326.6362	0.8	28.0	3
725.040	8669.9822	326.2129	4.3	-2.6	3
450.886	8663.5223	325.9698	13.5	-9.5	3
316.385	8660.4258	325.8533	4.3	-11.4	3
178.959	8657.5288	325.7443	25.3	12.9	4

Table (8.9.2):Mean values of *u/a* and *u* with standard deviations σ from *N* modes and deviations δ from the adopted pressure series at a temperature of 322.891 K

p/kPa	<*u*/*a*>/Hz	<*u*>/ms^{-1}	10^6 (σ(*u*)/*u*)	10^6 (δ(*u*)/*u*)	*N*
6240.370	9134.0025	343.8031	4.1	7.8	3
6037.828	9123.9220	343.4237	0.8	-4.1	3
5408.223	9093.8598	342.2922	1.5	-0.3	3
4738.048	9063.3193	341.1426	6.0	-1.7	3
4085.227	9035.0286	340.0778	1.1	-8.6	3
3501.873	9011.1349	339.1784	1.6	-2.0	3
2899.930	8987.7013	338.2964	3.2	-0.5	3
2264.897	8964.4210	337.4201	2.9	4.8	3
1654.252	8943.4584	336.6311	3.1	15.5	3
893.059	8918.9265	335.7077	2.6	-4.9	3
493.011	8906.9708	335.2577	3.8	-6.0	3

† State points not included in the analysis

Tables (8.9.1) and (8.9.2) summarise the results obtained from the isotherms together with the number of modes *N* used to determine the mean <*u*>, the standard deviations σ from the mean and the deviations δ of *u* from the adopted fit.

Initial estimates of the second acoustic virial coefficient β_a and the second virial coefficient *B* were obtained from the analysis of the speed of sound in the sphere. The calculated acoustic virial coefficients were then used to update the initial estimates until internal self-consistency was achieved. The results of the regression analyses of the calculated values of <*u*/*a*> from the two isotherms using the pressure-explicit series given by equation (1.1.3) are given in table (8.9.3).

Table (8.9.3): Coefficients of equation (1.1.3) used to represent the data from measurements of (u/a) in argon.

T / K	i	$\{A_i/a^2\}$/s^{-2}·Pa^{-i}	$10^6\sigma(u^2)/u^2$
305.510	0	$(74.882316 \pm 0.000948) \cdot 10^6$	28.8
	1	(0.38162 ± 0.00136)	
	2	$(0.1927 \pm 0.0038) \cdot 10^{-7}$	
322.891	0	$(79.087465 \pm 0.000696) \cdot 10^6$	15.2
	1	(0.48566 ± 0.000478)	
	2	$(0.33653 \pm 0.00068) \cdot 10^{-7}$	

All coefficients were statistically significant at a probability of 0.999. The deviations of the mean speeds of sound at a given state from the adopted smoothing equation are shown in figures (8.9.5) and (8.9.6) where points not included in the fit are indicated.

The coefficients are related to the second and third virial coefficients through

$$\beta_a = \frac{RTA_1}{A_0} \tag{8.9.1}$$

and

$$\gamma_a = \frac{RTA_2}{A_1} \tag{8.9.2}$$

and the heat capacity C_p is related to A_0 through

$$A_0 = \frac{RT\gamma^{pg}}{M} \tag{8.9.3}$$

where γ^{pg} is the ratio of the perfect gas heat capacities and is related to C_p/R by

$$\gamma^{pg} = \frac{1}{\left(1 - R/C_{p,m}^{pg}\right)} \tag{8.9.4}$$

The second and third acoustic virial coefficients and C_p/R for the two isotherms are given in table (8.9.4) and were determined from the coefficients given in table (8.9.3) and using equations (8.9.1) to (8.9.4).

Figure (8.9.5): Fractional deviation of the mean <*u*> in argon from the adopted smoothing equation at 305.510 K using the hemispherical resonator

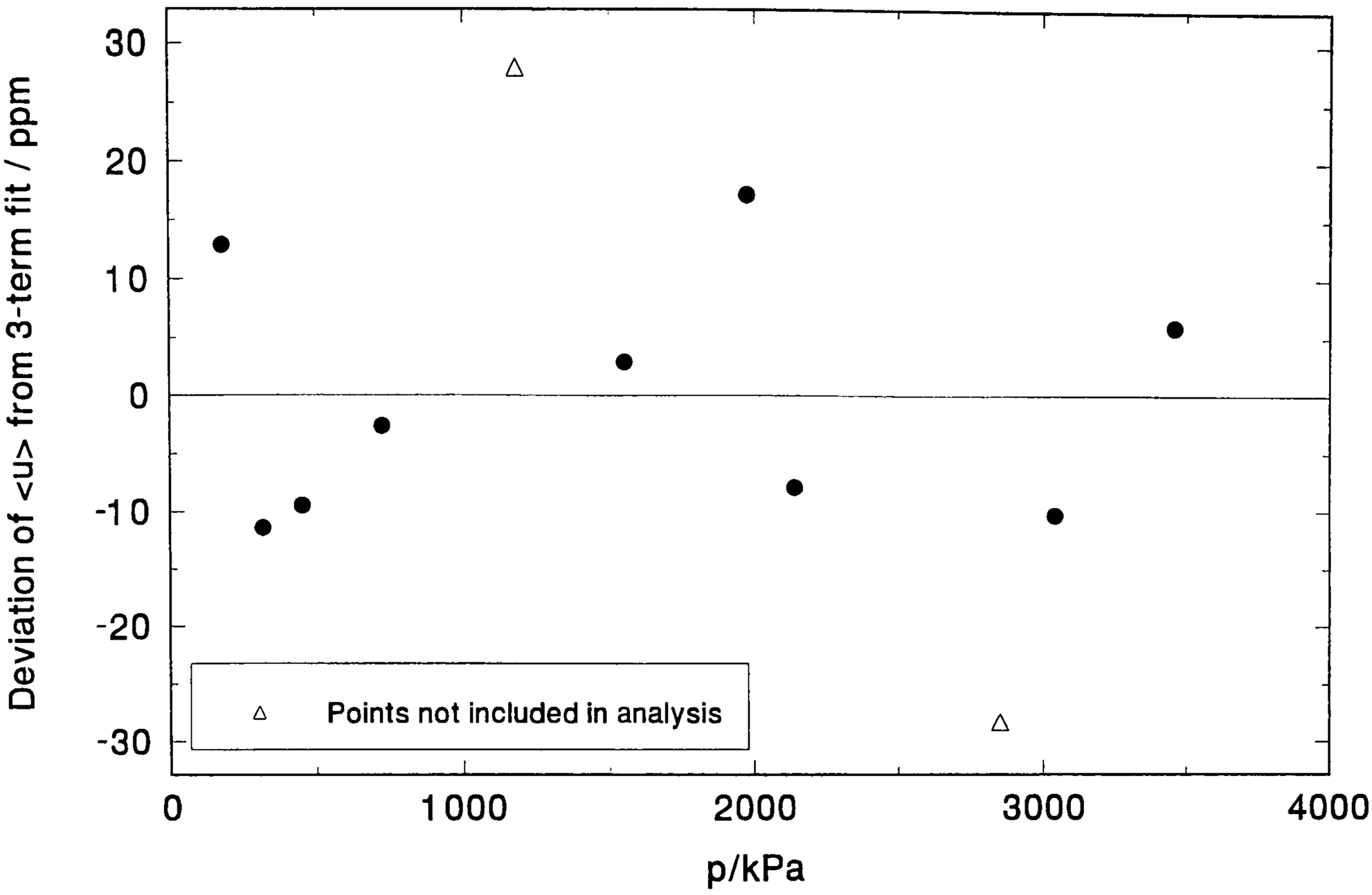

Figure (8.9.6): Fractional deviation of the mean <*u*> in argon from the adopted smoothing equation at 322.891 K using the hemispherical resonator

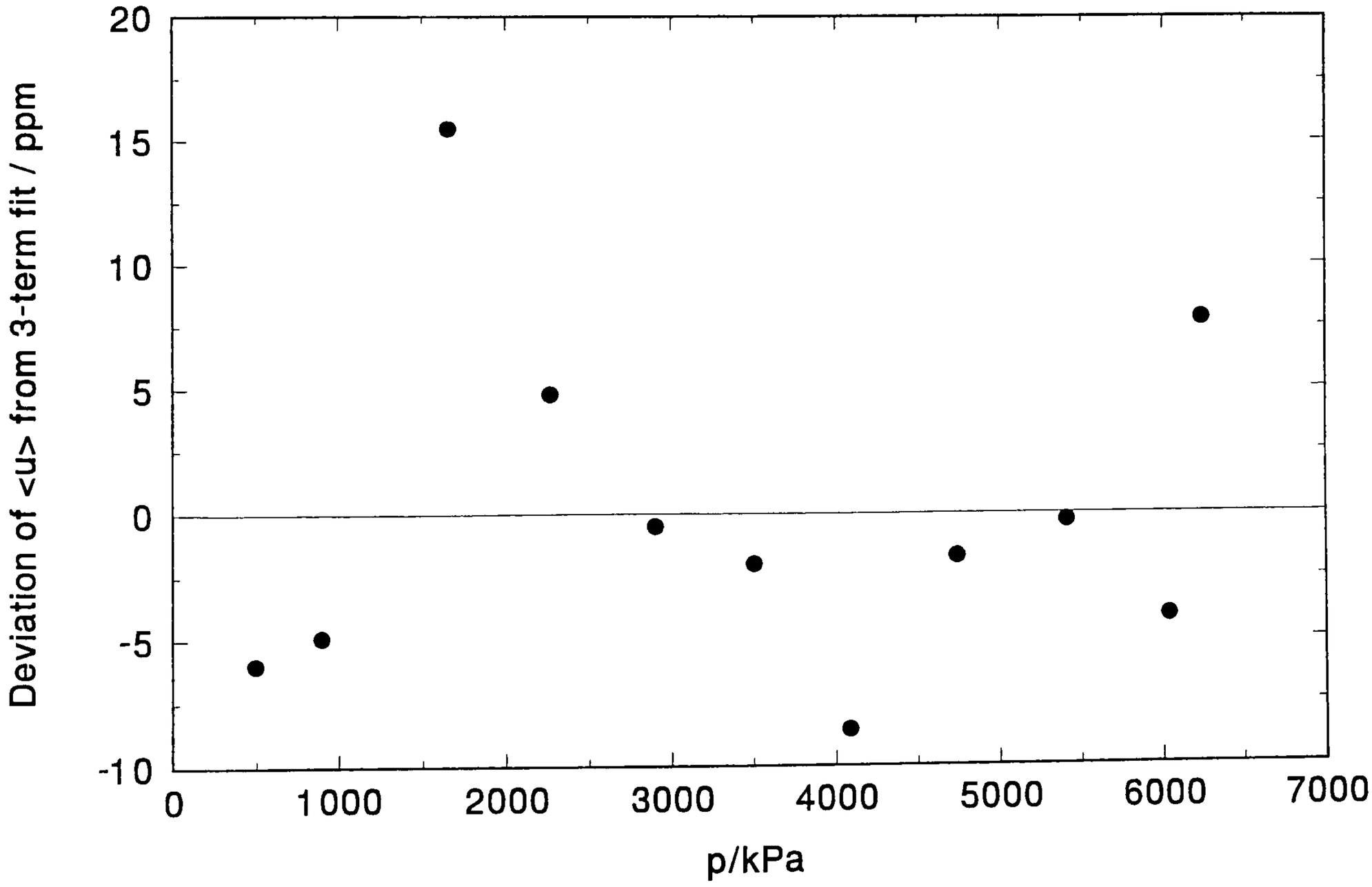

Table (8.9.4): Second and third acoustic virial coefficients and heat capacity of argon at temperatures *T*

T /K	β_a/cm^3 · mol^{-1}	γ_a/cm^3 · mol^{-1} kPa^{-1}	C_p /R
305.510	12.96 ± 0.05	0.0007 ± 0.0000	2.4989 ± 0.0001
322.891	16.49 ± 0.02	0.0011 ± 0.0000	2.4986 ± 0.0001

(8.10) Comparison of the Speed of Sound from Spherical and Hemispherical Resonators

The speeds of sound predicted using equation (1.1.3) with the coefficients from table (8.5.3) for the sphere and table (8.9.3) for the hemisphere are illustrated in figure (8.10.1) for the isotherm at 305.510 K and in figure (8.10.3) for the isotherm at 322.891 K. The agreement between the predicted speeds of sound for the lower temperature isotherm are fairly reasonable at pressures up to about 2,300 kPa and do not exceed about 100 ppm. However, at pressures above 2,300 kPa the deviation increases sharply and at the highest experimental pressure is about 500 ppm.

It can be seen by the plot of u against p that for the higher-temperature isotherm the agreement is very good over the range studied and if extended to higher pressures the agreement between the adopted fits is still valid. The fractional deviation of the fit predicted by the hemisphere from that predicted by the sphere is plotted in figure (8.10.4) and shows the deviation is about 25 ppm as the pressure is reduced but increases to about 100 ppm at the highest pressures of 6200 kPa. However within the standard deviations of the fits there is complete agreement at pressures exceeding 3,000 kPa and below this pressure the disagreement is at worst 50 ppm.

Figure (8.10.1): Comparison of the speed of sound *u* calculated from the adopted fits obtained using the hemisphere and the sphere at 305.510 K

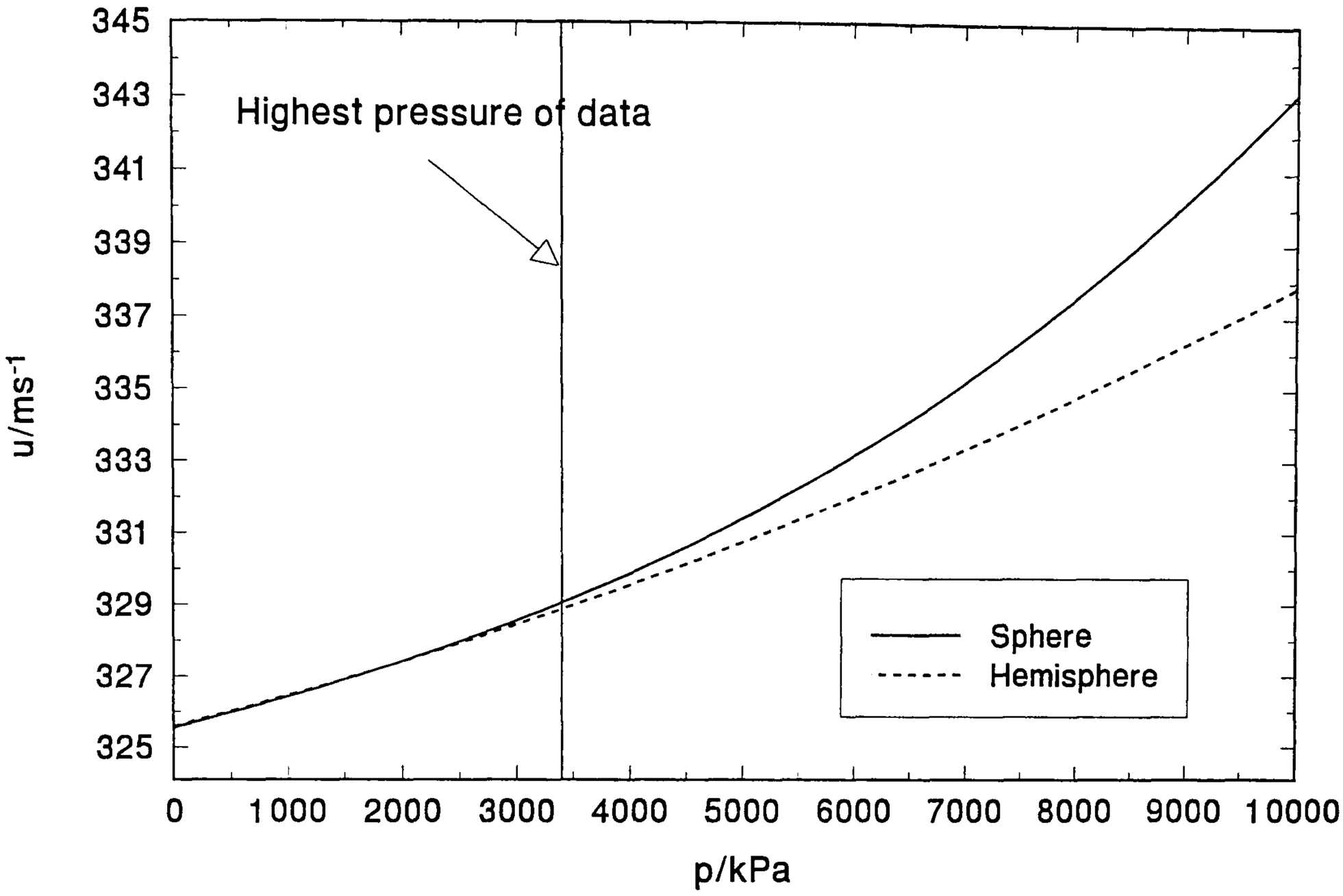

Figure (8.10.2): Fractional deviation of the speed of sound calculated from the adopted smoothing equation of the sphere with that of the hemisphere at 305.510 K

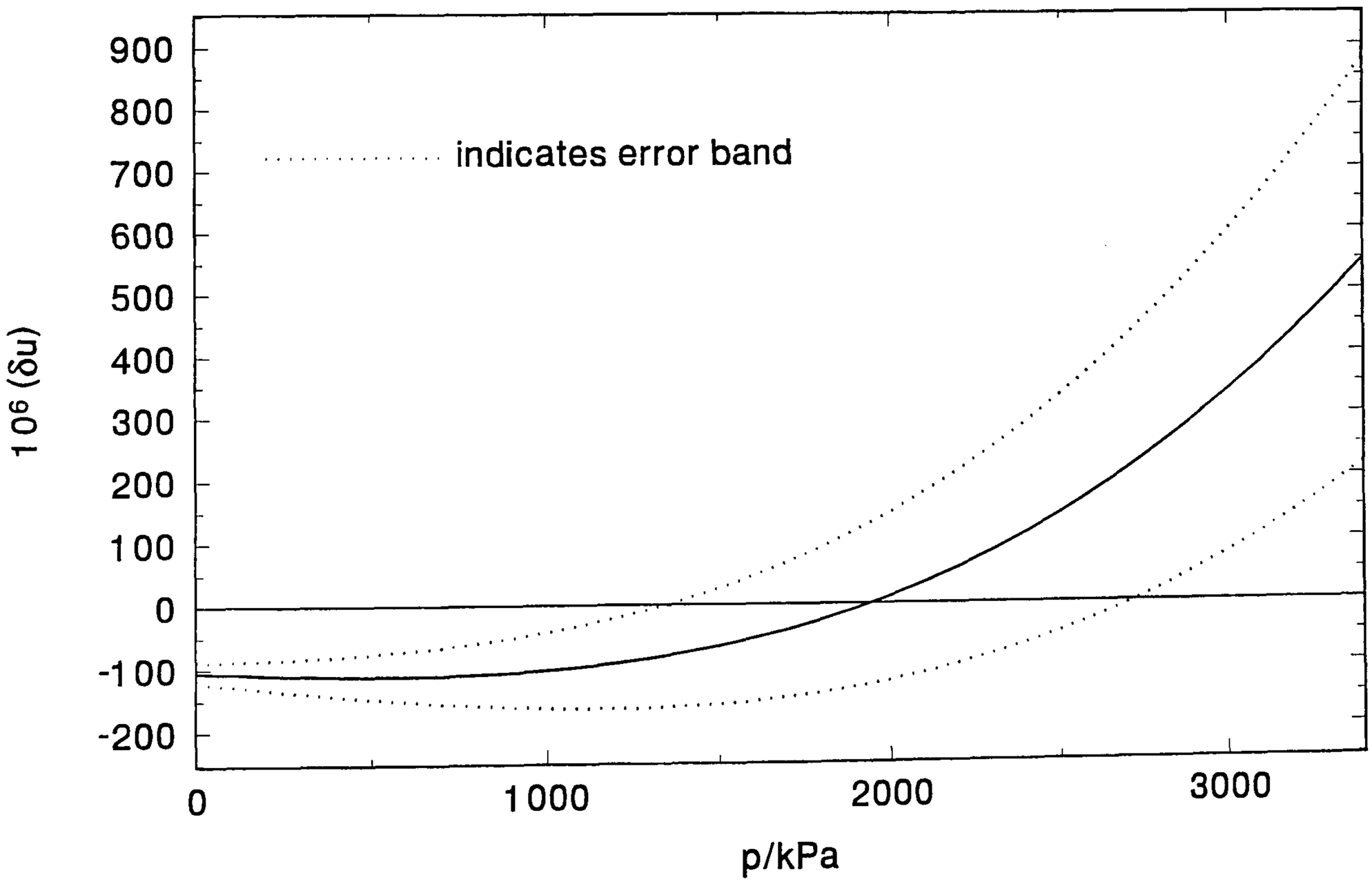

Figure (8.10.3): Comparison of the speed of sound *u* calculated from the adopted fits obtained using the hemisphere and the sphere at 322.891 K

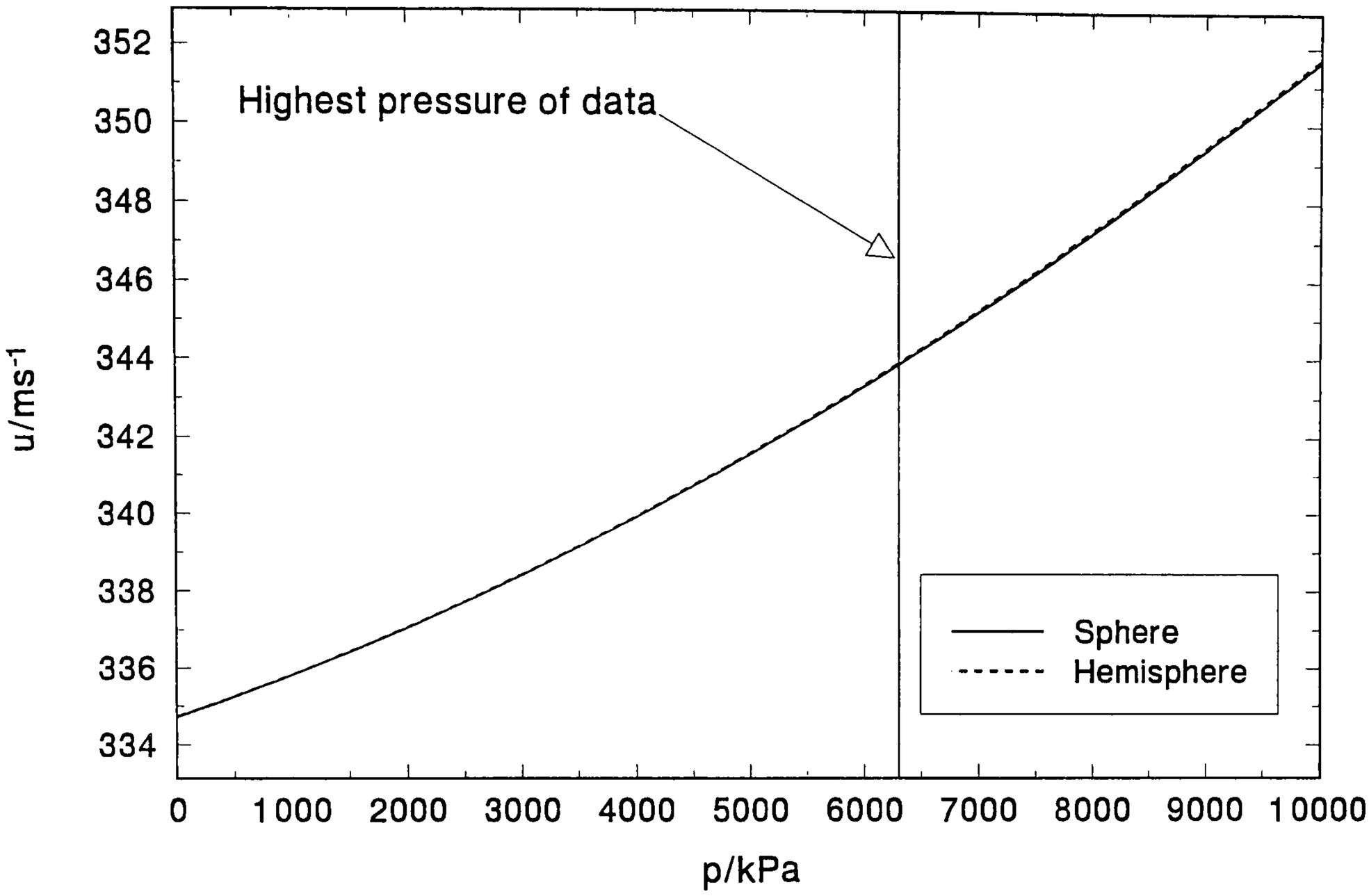

Figure (8.10.4): Fractional deviation of the speed of sound calculated from the adopted smoothing equation of the sphere with that of the hemisphere at 322.891 K

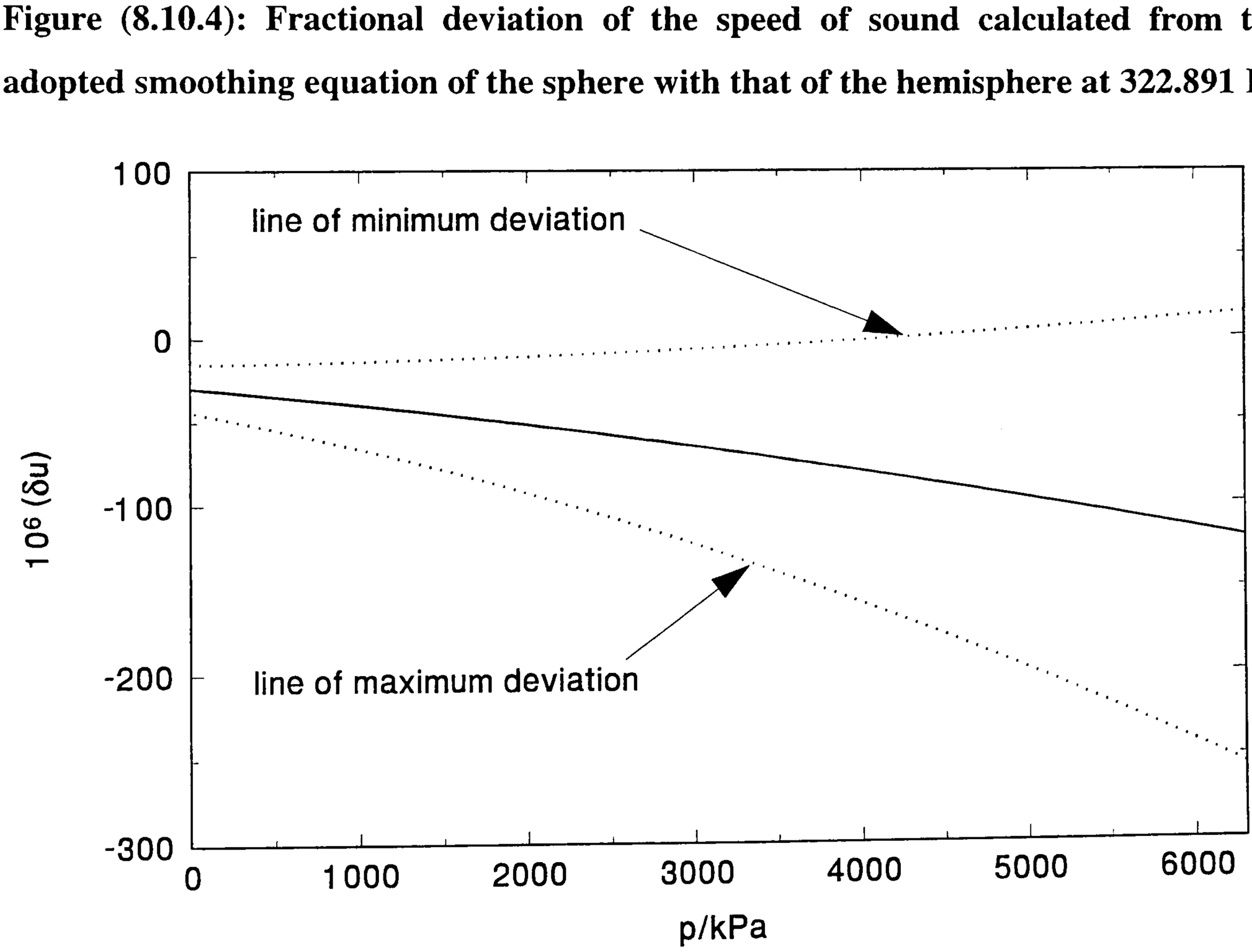

PART II Results in Tetrafluoromethane

(8.11) Introduction

Tetrafluoromethane is a comparatively simple molecule with a quasi-spherical symmetry. The normal boiling temperature is 145 K, the critical temperature is 228 K and the Boyle temperature is 518 K. Its structural simplicity and high thermal stability make it a compound of much interest and it has been the subject of a number of other studies [18, 137 - 140]. For pressures below 50 atm., MacCormack and Schneider measured the thermal compressibilities of the gas [142]. Precise measurements of B were reported by Douslin, Harrison, Moore and McCullough at temperatures from 0 to 350 °C and pressures up to 394 atm. [140]. The speed and absorption of sound in CF_4 has been measured by Ewing and Trusler [18] in the temperature range 175 to 300 K and at pressures in the range 0.08 to 1.0 MPa: these measurements were extended by Boyes to cover the range up to 375 K [59]. The vibrational relaxation time of CF_4 has been measured by numerous workers [18, 59, 137, 138] and a comparison is made of these values with the results obtained in this work.

The relatively large relaxation times of the CF_4 molecule often means that very low pressure measurements are difficult to access with the acoustic technique as the modes become broad due to relaxation absorption and may suffer overlap from neighbouring non-radial modes. The signal to noise ratio becomes so low at frequencies which are comparable to the inverse of the relaxation time that it becomes impossible to determine precisely the resonance frequencies. The hemispherical geometry offers an advantage in that, because of the positioning of the transducers, the non-radial modes are not excited with sufficient amplitude to be detected and possible overlap with the radial modes is therefore effectively eliminated. Furthermore, the signal strength of the modes is so great that their observation even at greatly reduced pressures is comparatively easy. The disadvantage of the geometry, as discussed previously, is that the radial modes in a hemispherical cavity also suffer viscous losses which add to the linewidths of the resonance modes: a problem overcome by adequate modelling of the loss mechanisms.

Since the speed of sound in CF_4 is substantially lower than any of the previous gases studied it was of further interest to observe the effects of coupling of gas and shell motion, particularly the effect of shell resonance on the (0,2) mode which has a significantly lower resonance frequency in tetrafluoromethane.

(8.12) Measurements

The tetrafluoromethane was electronics grade material with a specified mole fraction purity of 0.9999. Information provided by the manufacturer indicated that air and water were the main impurities. Before use, a sample was transferred under vacuum to a small stainless steel cylinder where it was degassed by repeated cycles of freezing, evacuation and melting.

Measurements were made along four isotherms at temperatures close to 300 K, 315 K, 332 K and 352 K. The maximum pressure employed was 6.4 MPa which was the maximum obtainable from the cylinder. The resonance frequencies and halfwidths of the first four radial modes were measured for all four isotherms, although at the lowest pressures it was not always possible to measure the (0,5) mode. For the isotherm at 332 K, measurements were also made of the (0,6) mode but this was not possible with the other isotherms. The resonance frequencies $f_{0,n}$ and halfwidths $g_{0,n}$ of the radial modes were obtained from the measurements of the amplitude and phase of the transmitted and received signals of frequencies near the resonance, as described in section (6.2). For the isotherms at 300 K, 315 K and 352 K measurements were made at 12 pressures whilst, for the isotherm at 332 K, measurements were made at only 10 pressures in the range studied.

(8.13) Analysis

Measurements of the speed of sound u were obtained from the values of u/a obtained directly from an isotherm. The measurements made on nitrogen, discussed in chapter 7, were used to determine the radius of the resonator at zero pressure as a function of temperature (equation 7.8.7). The compliance $(1/a)\,(\partial a/\partial p)$ of the resonator under the conditions of the experiment was calculated from equation (7.8.6). Values of the compliance, which is temperature dependent, leads to corrections of the resonance frequency due to the elastic response of the shell to the sound field. The breathing

resonance of the shell was also calculated and the appropriate corrections made according to equation (3.19.2).

The thermal boundary layer correction requires values of the thermal conductivity κ and the correlation used was that given by Ewing *et al.* as

$$\kappa/\left(\mathrm{mWm^{-1}K^{-1}}\right) = -3.0 + 24.50\left(T/350\ \mathrm{K}\right) \qquad (8.13.1)$$

which is based on a linear extrapolation of the results of Choy and Raw [143]. The viscous boundary layer corrections require values of the viscosity which were calculated from the values reported by Gough et. al. [136]; their smoothed values were obtained using a capillary flow viscometer at 10 temperatures between 150 K and 320 K and were fitted to give the following correlation

$$\eta/\left(10^{-7}\ \mathrm{kg\,m^{-1}s^{-1}}\right) = 11.6 + 81.4\left(T/150\ \mathrm{K}\right) \qquad (8.13.2)$$

According to the authors their values are accurate to ±1% at room temperature and where measurements were taken (for different gases) at 120 K, the accuracy was estimated at ±1.7%.

Corrections for imperfect thermal and viscous accommodation between the gas and the wall of the resonator were not important under the conditions of the measurements and accordingly the thermal and momentum accommodation lengths were taken as unity. Corrections to the resonance frequencies and halfwidths due to the effects of the inlet tube and transducers were calculated using the equations given in section (3.21). The slot between the hemispherical cavity and its equatorial plate was corrected for using the dimensions of the slot obtained from the analysis of propene and nitrogen reported in the previous chapter and the equations given in section (3.22).

(8.14) Vibrational relaxation

Under the conditions of the measurements, in particular the low pressure regime, vibrational relaxation becomes an important loss mechanism. The major influence is on the resonance halfwidths, since the frequencies used are always small compared with the inverse of the vibrational relaxation time τ ($\omega\tau < 0.18$ under all conditions). An analysis of the halfwidths, after allowance for the other loss mechanisms contributing to $g_{0,n}$, allowed determination of the vibrational relaxation time. This was then used to

correct the resonance frequencies for the very small dispersion that occurs at audio frequencies.

The results of Byers [137] who measured the entire dispersion curves of CF_4 at 295.15 K supports the assumption that the entire vibrational heat capacity relaxes with a single time constant τ. The effective ratio of heat capacities $\gamma(\omega)$ at angular frequency ω is then

$$\frac{\gamma(\omega)}{\gamma} = 1 + \frac{\omega\tau(\gamma-1)\Delta\{\omega\tau(1-\gamma\Delta)-i\}}{\left[1+\{\omega\tau(1-\gamma\Delta)\}^2\right]} \tag{8.14.1}$$

where $\Delta = C_{vib}/C_p$ and C_{vib} is the vibrational contribution to the heat capacity. The relaxing heat capacity can be calculated extremely accurately using statistical mechanics. A series expansion of equation (8.14.1) in powers of $\omega\tau$ leads to

$$\left\{\frac{\gamma(\omega)}{\gamma}\right\}^{\frac{1}{2}} = 1-(i/2)(\gamma-1)\Delta\omega\tau+\tfrac{1}{2}(\gamma-1)\Delta(\omega\tau)^2 \times\{1-\tfrac{1}{4}\Delta(1+3\gamma)\}+O(\omega^3\tau^3). \tag{8.14.2}$$

This gives the contribution of vibrational relaxation to the coefficient of absorption as

$$\alpha_{rel} = \frac{(\omega/u)}{\mathcal{F}m\left[\{\gamma(\omega)/\gamma\}^{\frac{1}{2}}\right]} = \frac{(\gamma-1)\Delta\omega^2\tau}{2u}+O(\omega^3\tau^3) \tag{8.14.3}$$

and the sound speed at angular frequency ω is

$$\begin{aligned} \boldsymbol{u}_\omega &= \boldsymbol{u}\cdot\mathcal{R}e\left\{\frac{\gamma(\omega)}{\gamma}\right\}^{\frac{1}{2}} \\ &= u\left[1+\tfrac{1}{2}(\gamma-1)\Delta(\omega\tau)^2\{1-\tfrac{1}{4}\Delta(1+3\gamma)\}\right]+O(\omega^3\tau^3), \end{aligned} \tag{8.14.4}$$

where u is the zero-frequency speed of sound. The contribution that vibrational relaxation makes to the halfwidths g_{rel} is given by

$$\frac{g_{rel}}{f} = \left(\frac{u}{2\pi}\right)\alpha_{rel} \approx (\gamma-1)\Delta\pi f\tau \tag{8.14.5}$$

The product $\tau\rho$ is expected to be almost independent of the density along an isotherm and so $\tau\rho$ is obtained by analysis of the halfwidths in terms of the equation

$$\{g_{0,n}-g_h-g_v-g_t-g_{slot}-g_{cl}\} = \left\{\frac{(\gamma-1)\Delta\pi f^2}{\rho}\right\}(b_0+b_1\rho) \tag{8.14.6}$$

where $g_{cl} = (u/2\pi)\alpha_{cl}$, $b_0 = \tau\rho$ and $b_1 = \partial(\tau\rho)/\partial\rho$ is an additional term which was necessary in order to accommodate the data adequately.

Prior to correction for the vibrational relaxation the fractional excess halfwidths were on the order of 30 ppm to 1900 ppm, except the (0,2) mode which was not included in the analysis and is discussed separately. The halfwidths were fitted as described above, with minor adjustments also being made initially to the zero-density thermal conductivity. Several iterations were performed until the calculated excess halfwidths approached zero over the entire pressure range but without becoming negative. It was found that at the lowest pressures, as also observed previously (in argon, nitrogen and propene), that the excess halfwidths rise sharply at pressures below 500 kPa and this could lead potentially to artificially high values of the relaxation time. However, when low pressure points were included in the halfwidth analysis, the excess halfwidths of the modes at higher pressures were calculated to have values of $\Delta g/f$ which were less than zero. The cause of this observation is inadequate modelling of halfwidths at the lowest pressures where the thermal and viscous boundary layers are most important and effects due to small slots and surface imperfections, which are negligible at higher pressures, become apparent.

Table (8.14.1): Summary of modes included in analysis of halfwidths

T = 299.682 K			T = 315.468 K		
p/kPa	Modes included in halfwidth analysis	N	p/kPa	Modes included in halfwidth analysis	N
5580.135	(0,3) (0,4) (0,5)	3	6197.352	(0,3) (0,4) (0,5)	3
4375.576	(0,3) (0,4)	3	5389.207	(0,3) (0,4) (0,5)	3
3985.460	(0,3) (0,4) (0,5)	2	5157.846	(0,3) (0,4) (0,5)	3
3548.070	(0,3) (0,4) (0,5)	3	4417.434	(0,3) (0,4) (0,5)	3
2892.902	(0,3) (0,4) (0,5)	3	3672.441	(0,3) (0,4) (0,5)	3
2471.885	(0,3) (0,4) (0,5)	3	3004.812	(0,3) (0,4) (0,5)	3
2071.590	(0,4) (0,5)	2	2316.665	(0,3) (0,4) (0,5)	3
1333.352	(0,3) (0,4) (0,5)	3	1772.005	(0,3) (0,4) (0,5)	3
933.590	(0,3) (0,5)	2	1150.124	(0,3) (0,4) (0,5)	3
612.497	(0,3) (0,4) (0,5)	3	524.242	(0,3) (0,4) (0,5)	3
226.831	(0,3) (0,4)	2	145.799	(0,3) (0,4)	2
102.269	(0,3) (0,4) (0,5)	3	42.007	(0,3) (0,4) (0,5)	3

Table (8.14.2): Summary of modes included in analysis of halfwidths

T = 331.599 K			T = 352.022 K		
p/kPa	Modes included in halfwidth analysis	N	p/kPa	Modes included in halfwidth analysis	N
3680.143	(0,3) (0,4) (0,5) (0,6)	4	6444.041	(0,3) (0,4) (0,5)	3
3148.688	(0,3) (0,4) (0,6)	3	5967.930	(0,3) (0,4) (0,5)	3
2714.737	(0,3) (0,4) (0,5)	3	5100.583	(0,3) (0,4) (0,5)	3
2260.136	(0,3) (0,4) (0,5) (0,6)	4	4423.140	(0,3) (0,4) (0,5)	3
1783.323	(0,3) (0,4) (0,5) (0,6)	4	3841.015	(0,3) (0,4) (0,5)	3
1407.301	(0,3) (0,4) (0,5) (0,6)	4	2770.669	(0,3) (0,5)	2
803.806	(0,3) (0,4)	2	2246.396	(0,3) (0,4) (0,5)	3
415.828	(0,3) (0,4) (0,5) (0,6)	4	1521.451	(0,3) (0,4) (0,5)	3
198.610	(0,3) (0,4) (0,5)	3	951.559	(0,3) (0,4) (0,5)	3
25.904	(0,3) (0,4) (0,5)	3	384.218	(0,4) (0,5)	2
			155.939	(0,3) (0,4)	2
			20.465	(0,3) (0,4)	2

The low pressures were removed in a stepwise manner from the analysis in order to obtain internally consistent values for the vibrational relaxation times upon further iterations. Tables (8.14.1) and (8.14.2) summarise the modes and state points which were included in the analysis.

The resulting vibrational relaxation times are given in table (8.14.3) and the results are compared with those of Ewing [18], Boyes [59], Byers [137] and Corran [138] in figure (8.14.1). Agreement with the relaxation times given by other workers is extremely good, considering the number of contributions to the halfwidth arising through the various loss mechanisms described. The results do seem to be systematically higher than those reported by Boyes [59] and this is could be explained by the uncertainty of the contribution to the halfwidth from relaxation or other effects, particularly at the lowest pressures. However, the result reported by Corran [138] of 3100 ns at 1 kg m^{-3} and 293 K lies above Boyes results by 460 ns. Interpolation of our

Table (8.14.3): Vibrational relaxation times in tetrafluoromethane at a density of 1 kg m^{-3}

T /K	τρ /(ns kg m^{-3})	{∂ (τρ)/∂ρ} /ns
299.682	2681 ± 12	8.5 ± 0.8
315.468	2390 ± 177	5.3 ± 1.2
331.599	2202 ± 78	8.0 ± 1.4
352.022	2110 ± 169	5.6 ± 1.6

Figure (8.14.1): Vibrational relaxation times in tetrafluoromethane at a density of 1 kg m^{-3}, as a function of temperature.

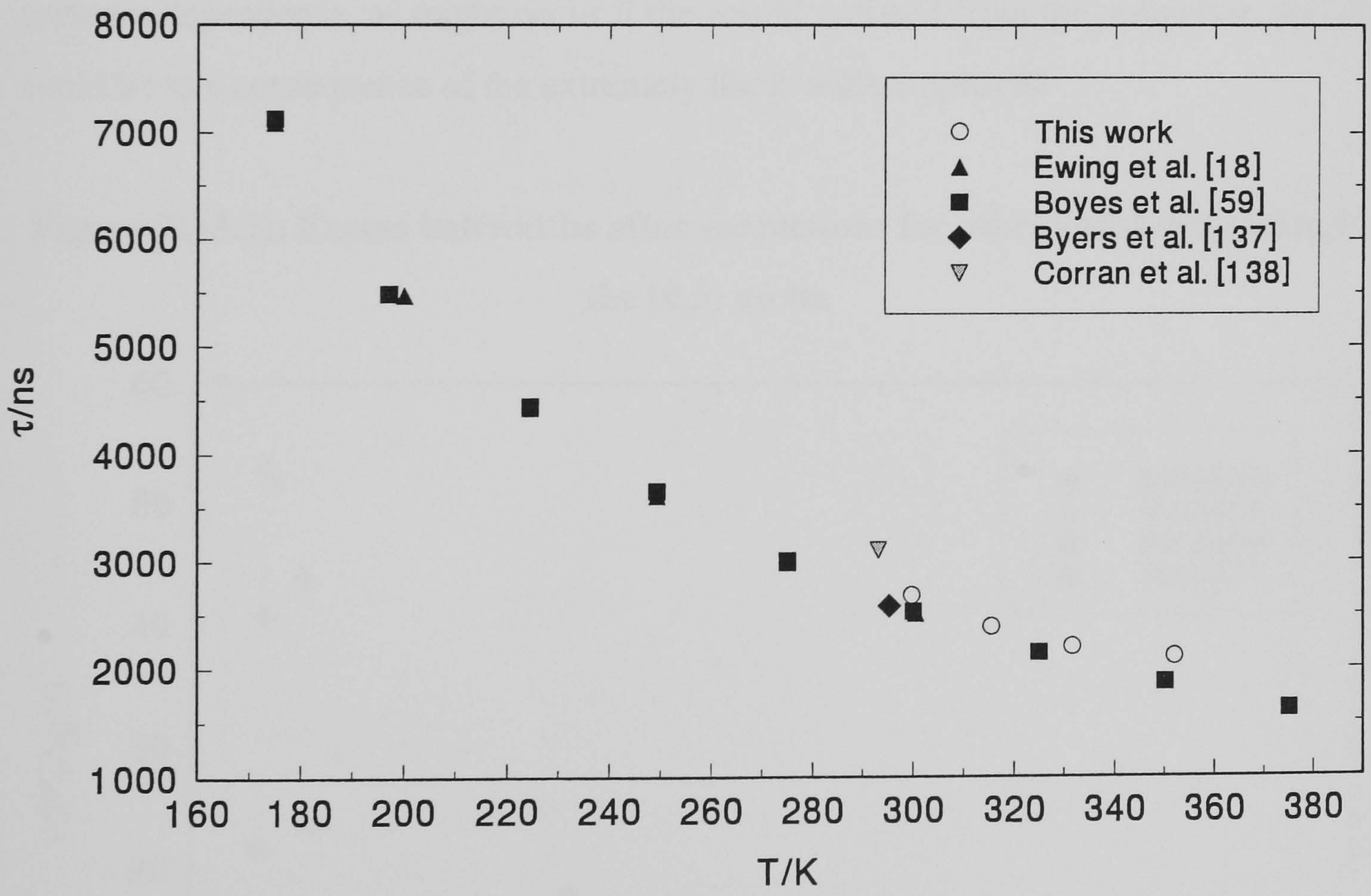

results to 300 K gives a relaxation time of approximately 2687 ns which is only 158 ns above Boyes result at 300 K. Boyes also reports a value of 1870 ns at 350 K, compared with an interpolation of our results which gives 2100 ns, a difference of 230 ns but, when the increased uncertainty in our results at this temperature is considered, the agreement is good.

(8.15) Excess halfwidths

The residual excess halfwidths for all the modes included in the halfwidth analysis after correction for relaxation absorption are shown in figures (8.15.1), (8.15.2), (8.15.3), (8.15.4) and (8.15.5). The excess halfwidths are consistently below 30 ppm over the whole range for those modes included in the analysis and at pressures in excess of 500 kPa, the fractional excess halfwidths are generally below 15 ppm as shown by figure (8.15.6). It is noteworthy that, above 1 MPa, the excess halfwidths exhibit no pressure dependence, as might occur if the sound radiated from the resonator, and this could be as a consequence of the extremely thick walls employed.

Figure (8.15.1): Excess halfwidths after corrections for vibrational relaxation for the (0,3) mode

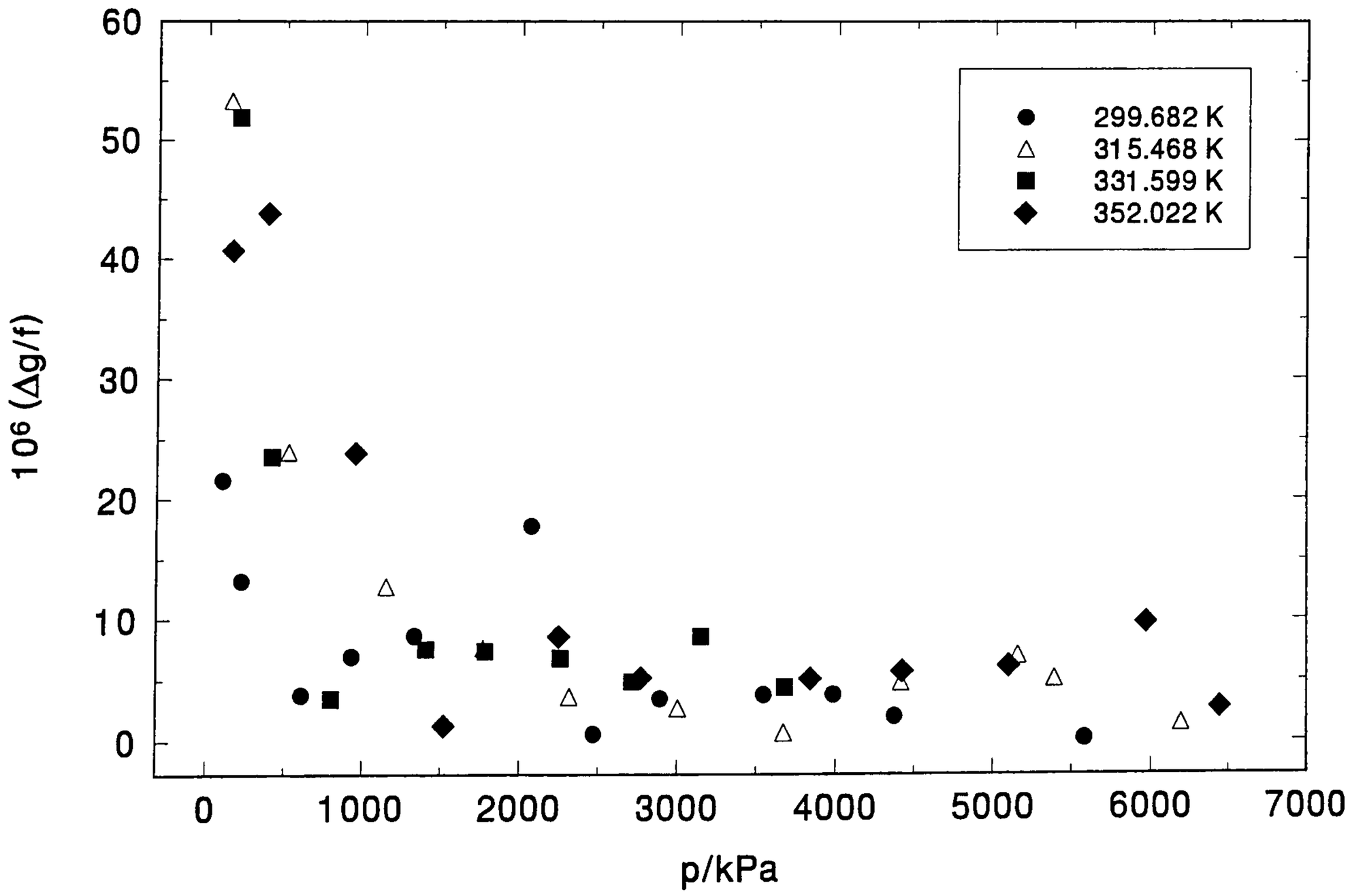

Figure (8.15.2): Excess halfwidths after corrections for vibrational relaxation for the (0,4) mode

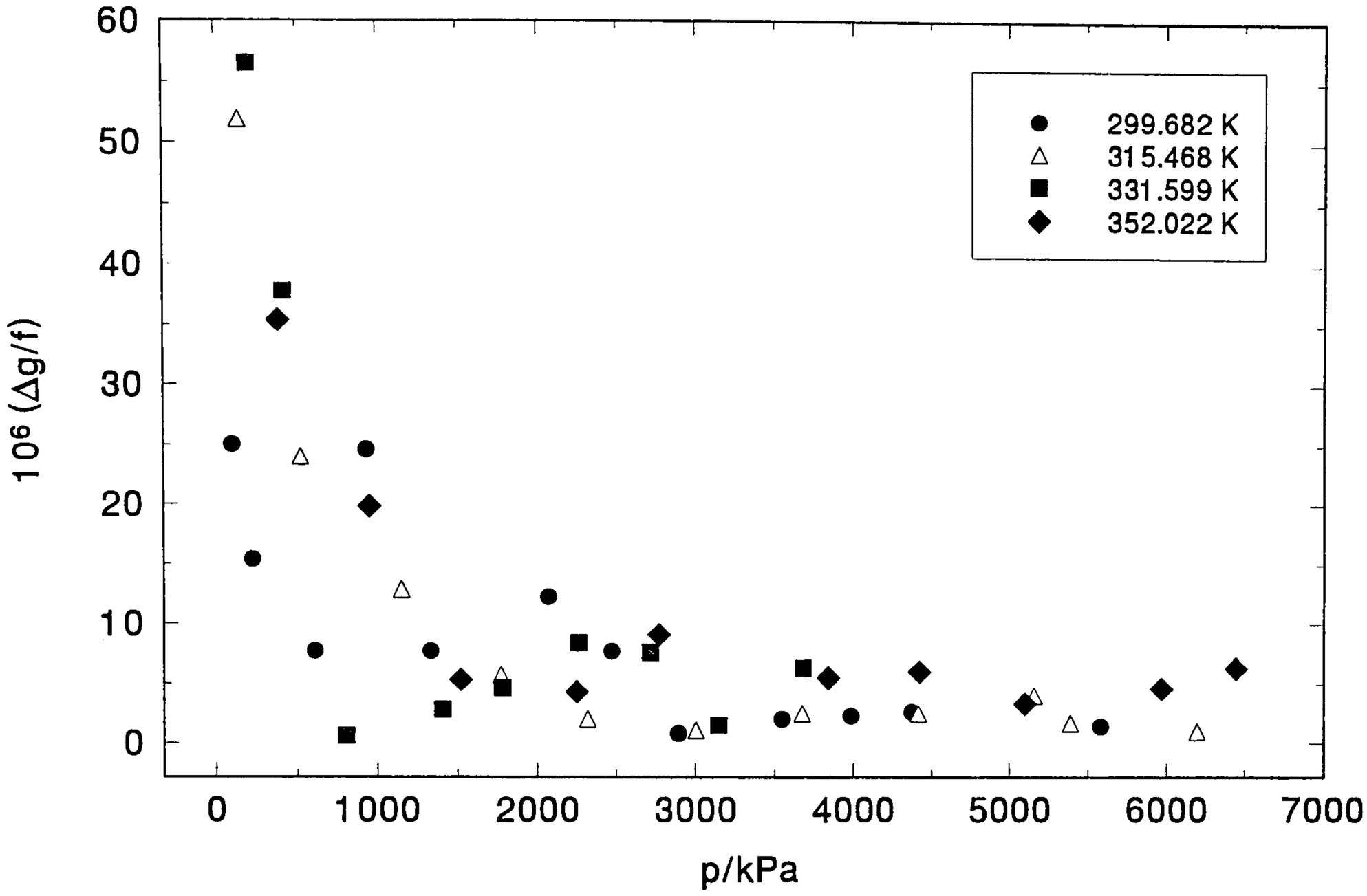

Figure (8.15.3): Excess halfwidths after corrections for vibrational relaxation for the (0,5) mode

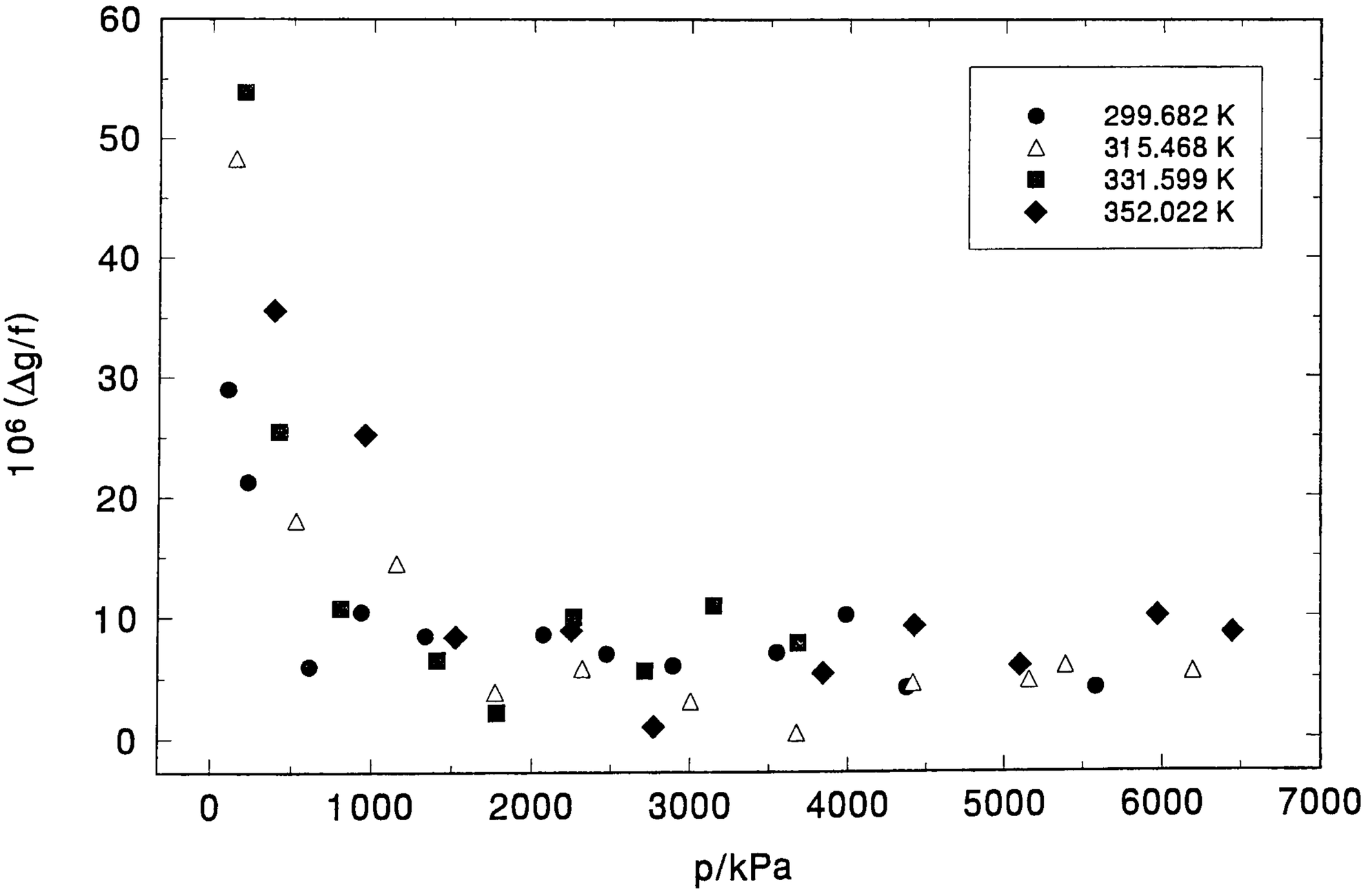

Figure (8.15.4): Excess halfwidths after corrections for vibrational relaxation for the (0,6) mode

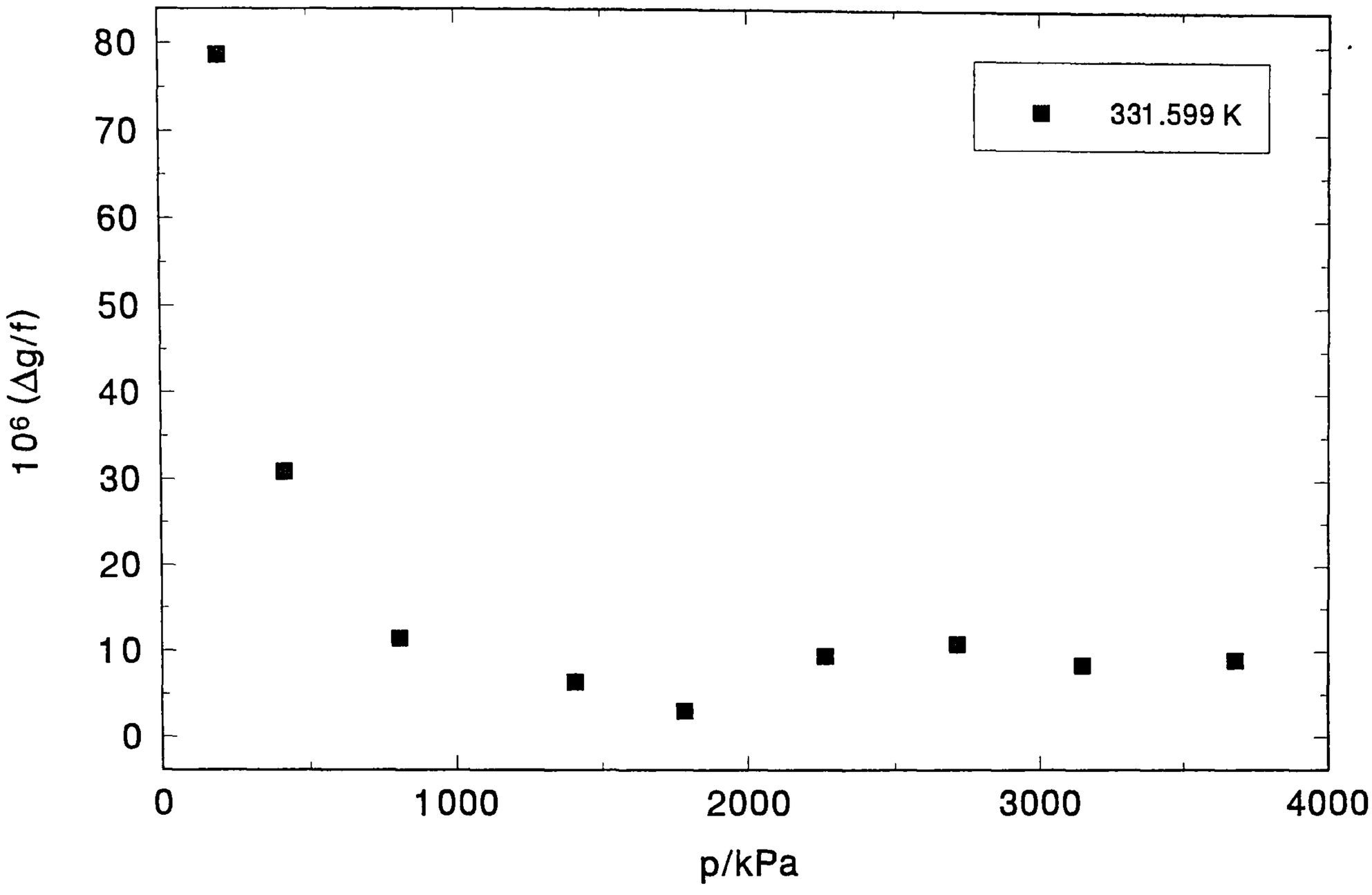

Figure (8.15.5): Excess halfwidths after corrections for vibrational relaxation for all the modes utilised in the halfwidth analysis

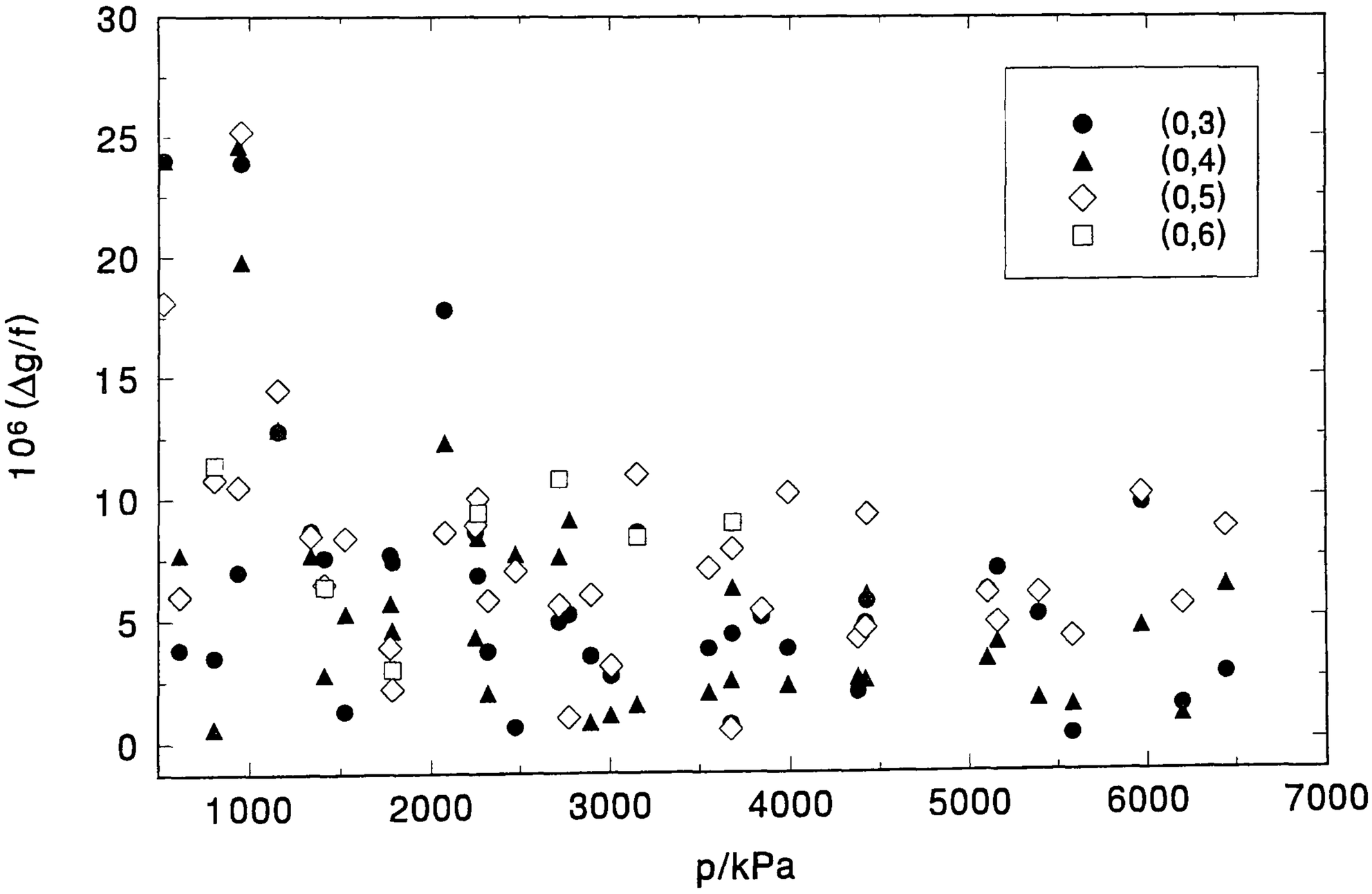

Figure (8.15.6): Excess halfwidths after corrections for vibrational relaxation for the (0,2) mode

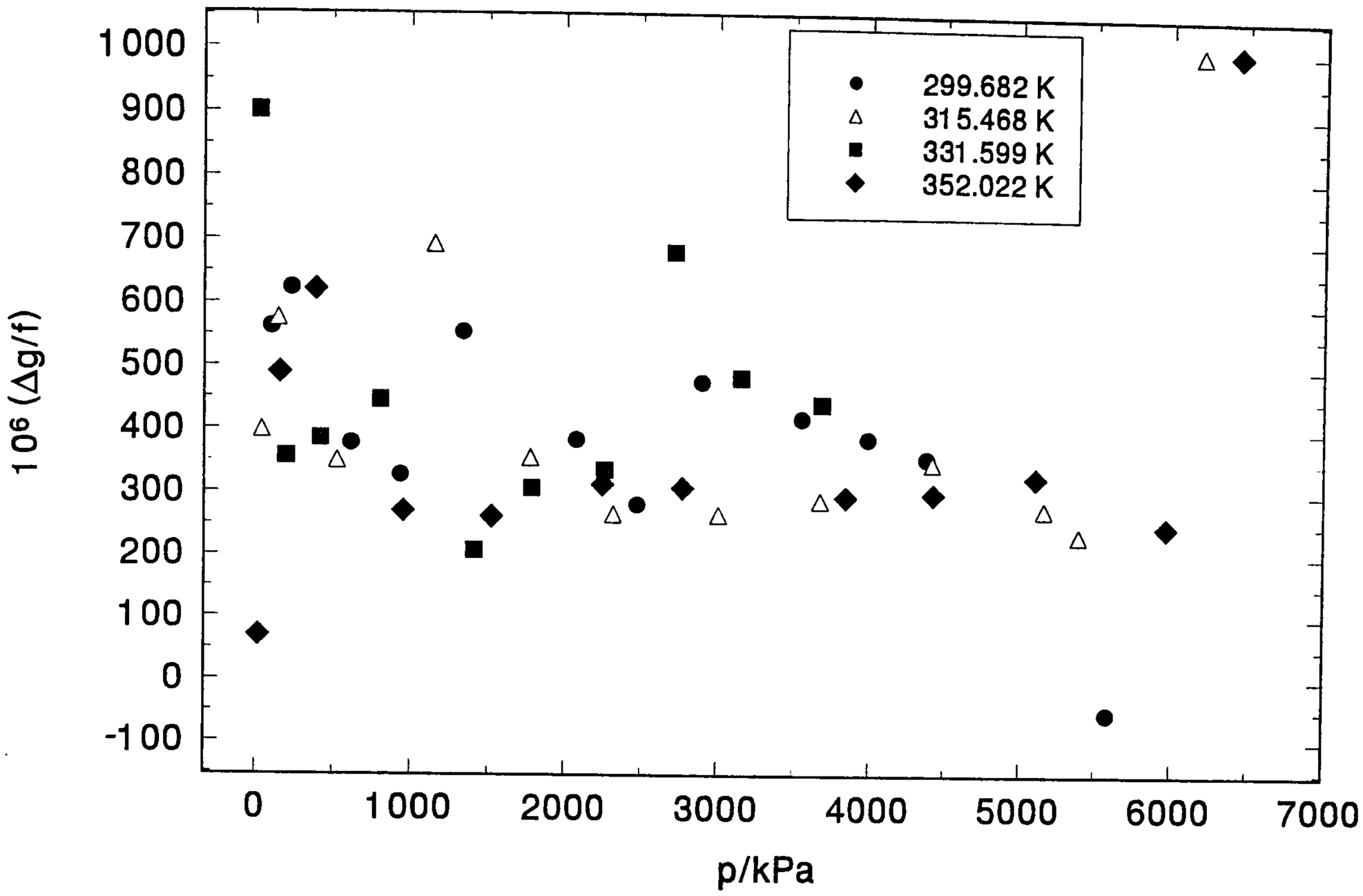

The excess halfwidths observed for the (0,2) mode exhibit very different behaviour from that of the other radial modes. Generally, the fractional excess halfwidths of the (0,2) mode are between 200 and 700 ppm over the whole experimental range. Larger deviations are also observed, however, particularly at the highest pressures where excess halfwidths are in excess of 1000 ppm. Although discrete maxima in $\Delta g/f$ are not seen (as they are for this mode at higher frequencies), there are obviously still large contributions to g_{02} which have not been accounted for and these may be the result of coupling between shell and resonance frequencies, albeit in a less definitive manner in this frequency regime.

(8.16) Speed of Sound

The zero frequency speed of sound was calculated using equation (1.1.3) and the various correction terms given by the equations in chapter 3, which include contributions from the thermal and viscous boundary layers, for the effects of tubes and slots, for the elastic response of the shell to the sound field and for the effects of relaxation. The contribution Δf_{rel} of vibrational relaxation to the resonance frequencies is given by

$$\frac{\Delta f_{rel}}{f} \approx 2(\gamma-1)\Delta(\pi f\tau)^2\left\{1-\frac{\Delta(1+3\gamma)}{4}\right\} \qquad (8.16.1)$$

This correction was greatest for the (0,5) mode at 299.7 K and 102 kPa, where the effects of dispersion accounted for 15 ppm. At the highest pressures of 6 MPa and at a temperature of 352 K the correction accounts for much less than 1 ppm for the (0,4) mode.

Small corrections were also applied to account for small differences between the measured temperature of the state point and the stated temperature of the isotherm (also the mean temperature of the isotherm). The speed of sound determined from each mode was weighted by the lesser of $(2\times10^{-6}f/\delta f)$ and unity, where δf is the estimated standard deviation of a measured resonance frequency. The fractional deviations (u/a) for each mode from the mean $\langle u/a\rangle$ calculated from selected modes are illustrated in figures (8.16.1), (8.16.2), (8.16.3), (8.16.4) and (8.16.5). The agreement, with exclusion of the (0,2) mode, is exceptionally good over the whole temperature and pressure range, with fractional deviations generally not exceeding 4 ppm. Modes were excluded from the calculation of the mean $\langle u/a\rangle$ when their inclusion lead to a significant increase in the standard deviation. The number of modes included at each state point are summarised in tables (8.16.1), (8.16.2), (8.16.3) and (8.16.4).

The (0,2) mode generally agrees within 0.03%, which is much better than that expected on the basis of the halfwidth measurements dicussed above but still well below the level of agreement required. The majority of the data used to obtain the speed of sound from the (0,2) mode was too high and probably results from the effective eigenvalue determined in section (7.8) being artificially too low as a result of shell resonance effects which made this difficult to determine accurately.

Figure (8.16.1): The fractional deviations of (u/a) determined from the (0,2) mode, from the mean <u/a> calculated from the modes summarised in tables (8.14.1) and (8.14.2)

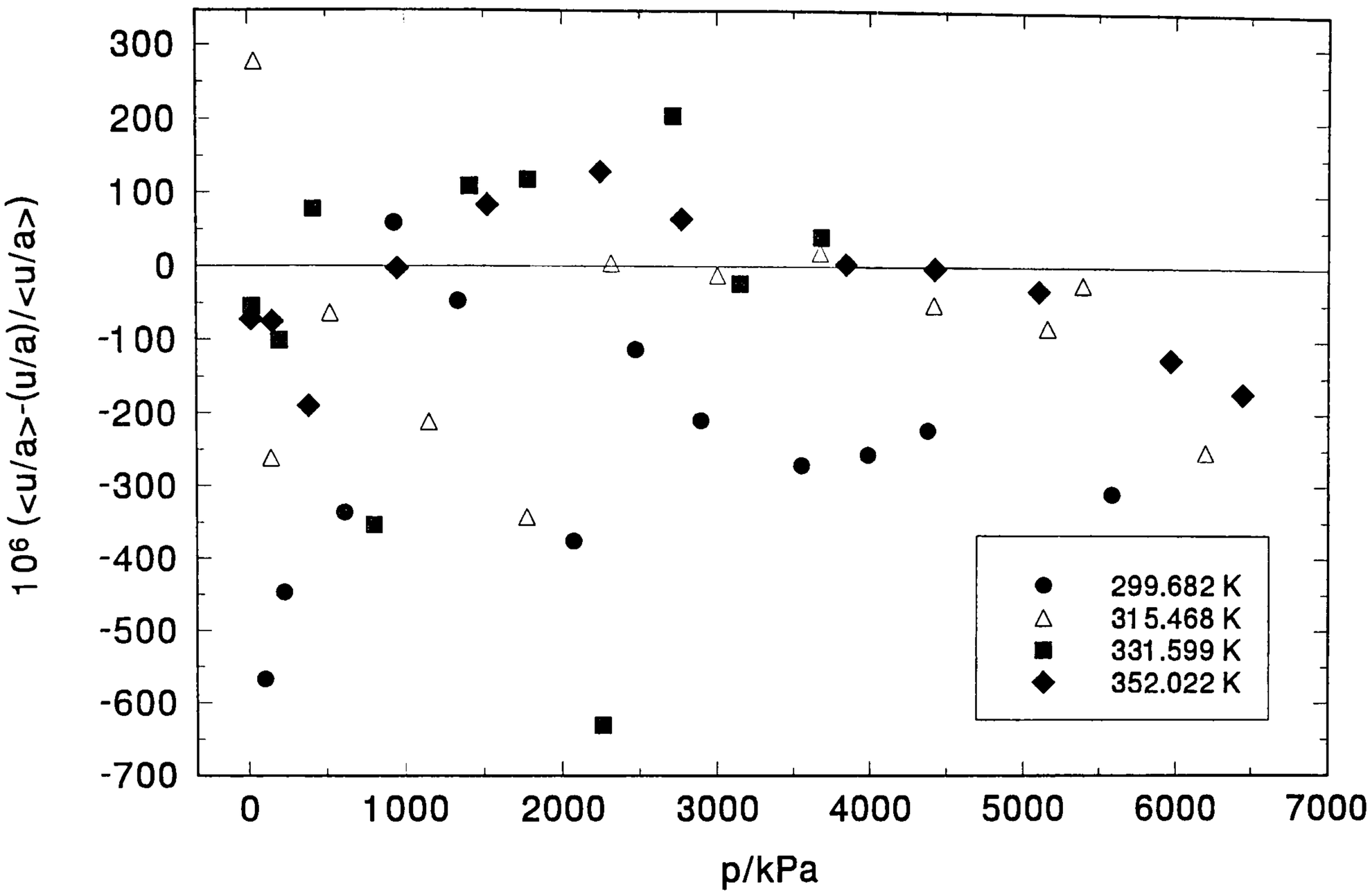

Figure (8.16.2): The fractional deviations of (u/a) determined from the (0,3) mode, from the mean <u/a> calculated from the modes summarised in tables (8.14.1) and (8.14.2)

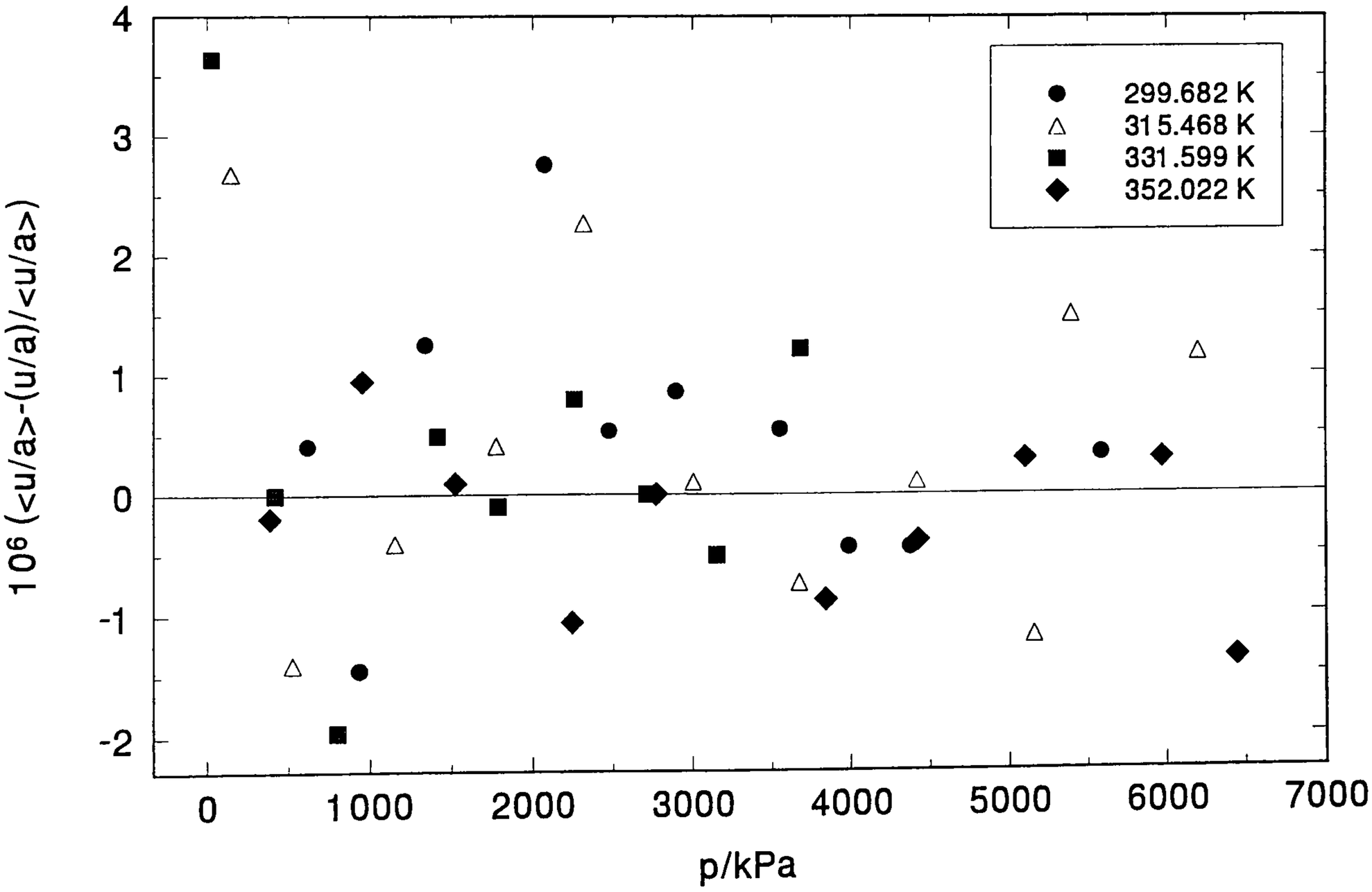

Figure (8.16.3): The fractional deviations of (*u*/*a*) determined from the (0,4) mode, from the mean <*u*/*a*> calculated from the modes summarised in tables (8.14.1) and (8.14.2)

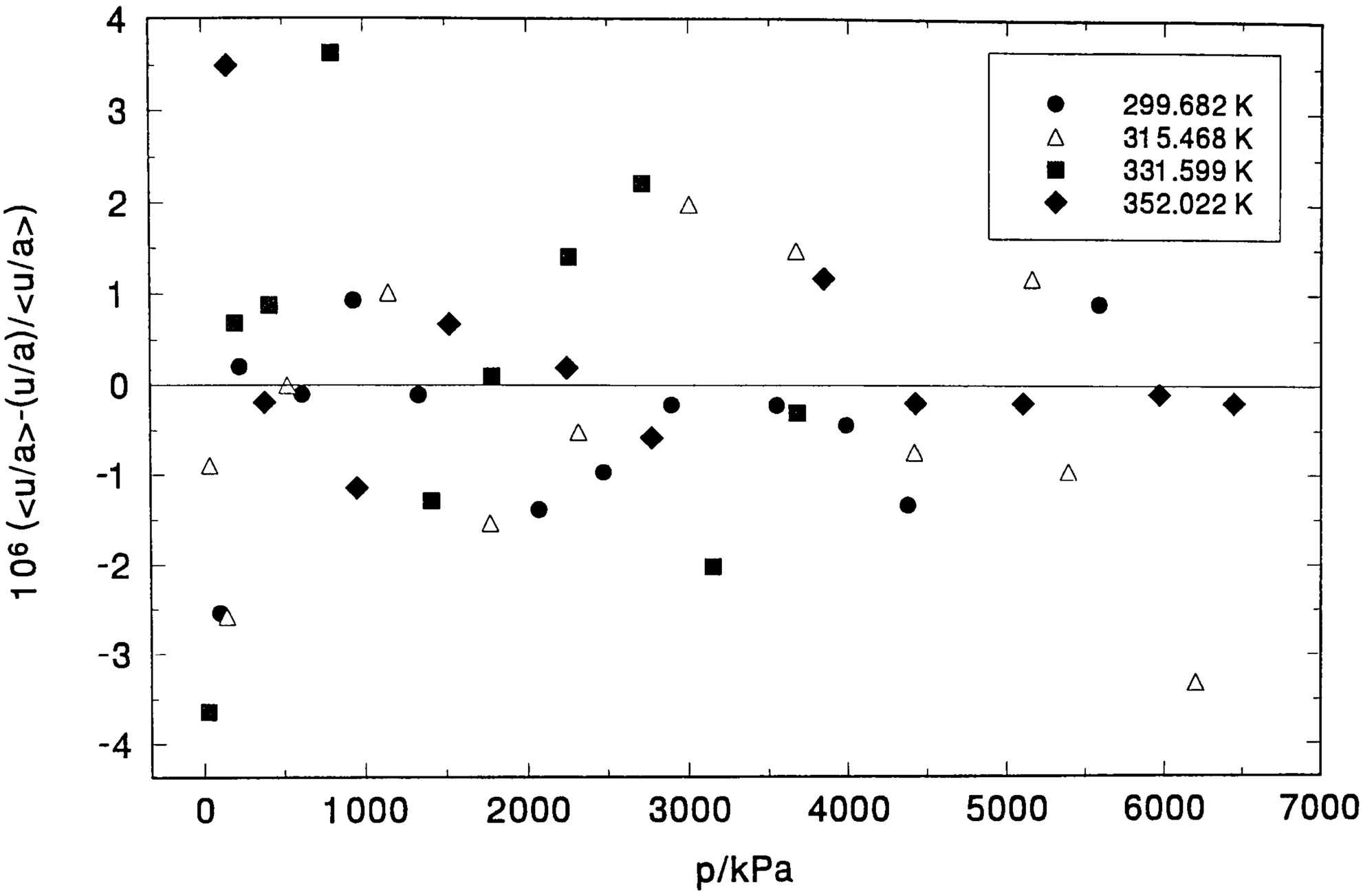

Figure (8.16.4): The fractional deviations of (*u*/*a*) determined from the (0,5) mode, from the mean <*u*/*a*> calculated from the modes summarised in tables (8.14.1) and (8.14.2)

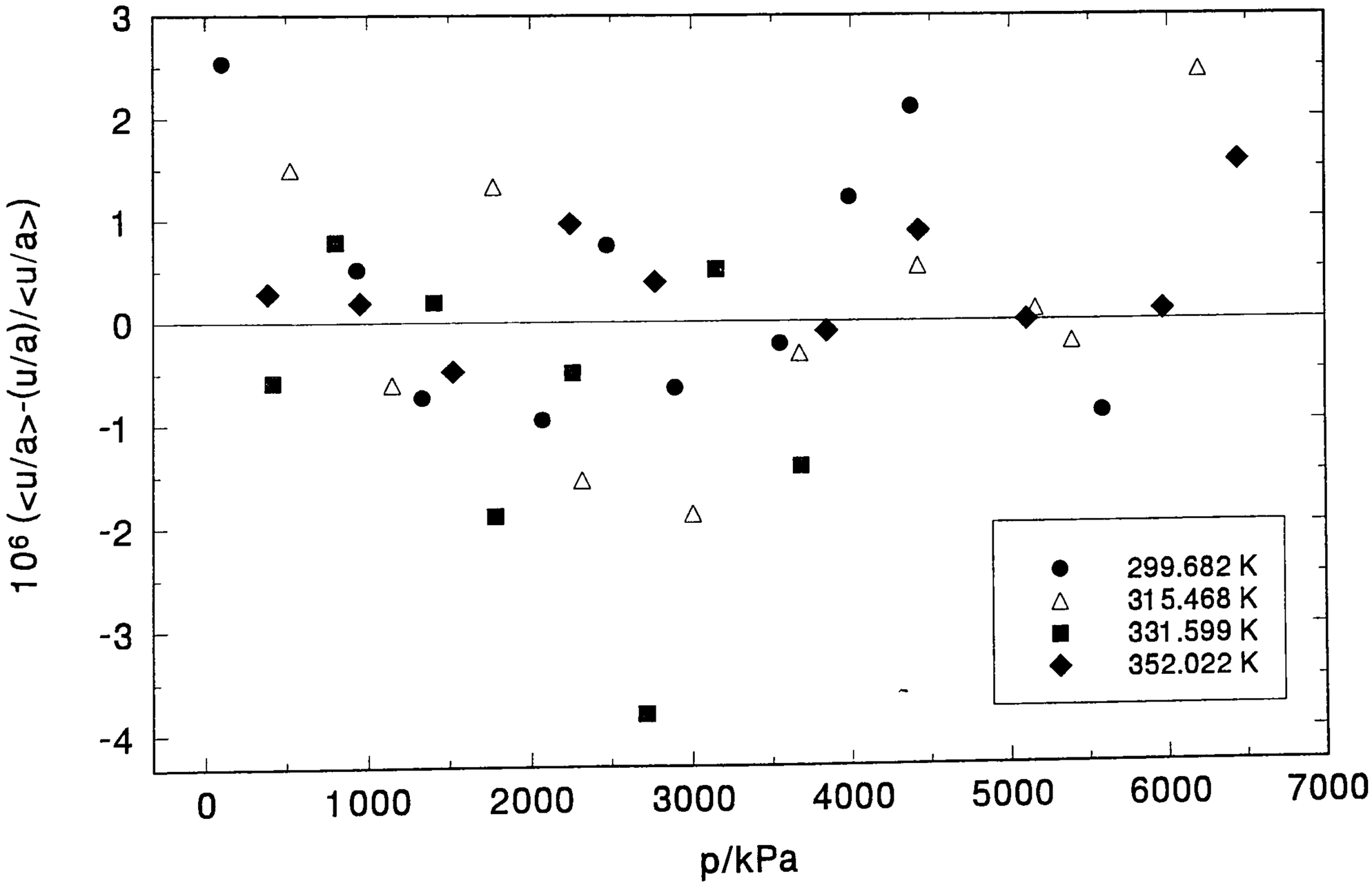

Figure (8.16.5): The fractional deviations of (u/a) determined from the (0,6) mode, from the mean $\langle u/a \rangle$ calculated from the modes summarised in tables (8.14.1) and (8.14.2)

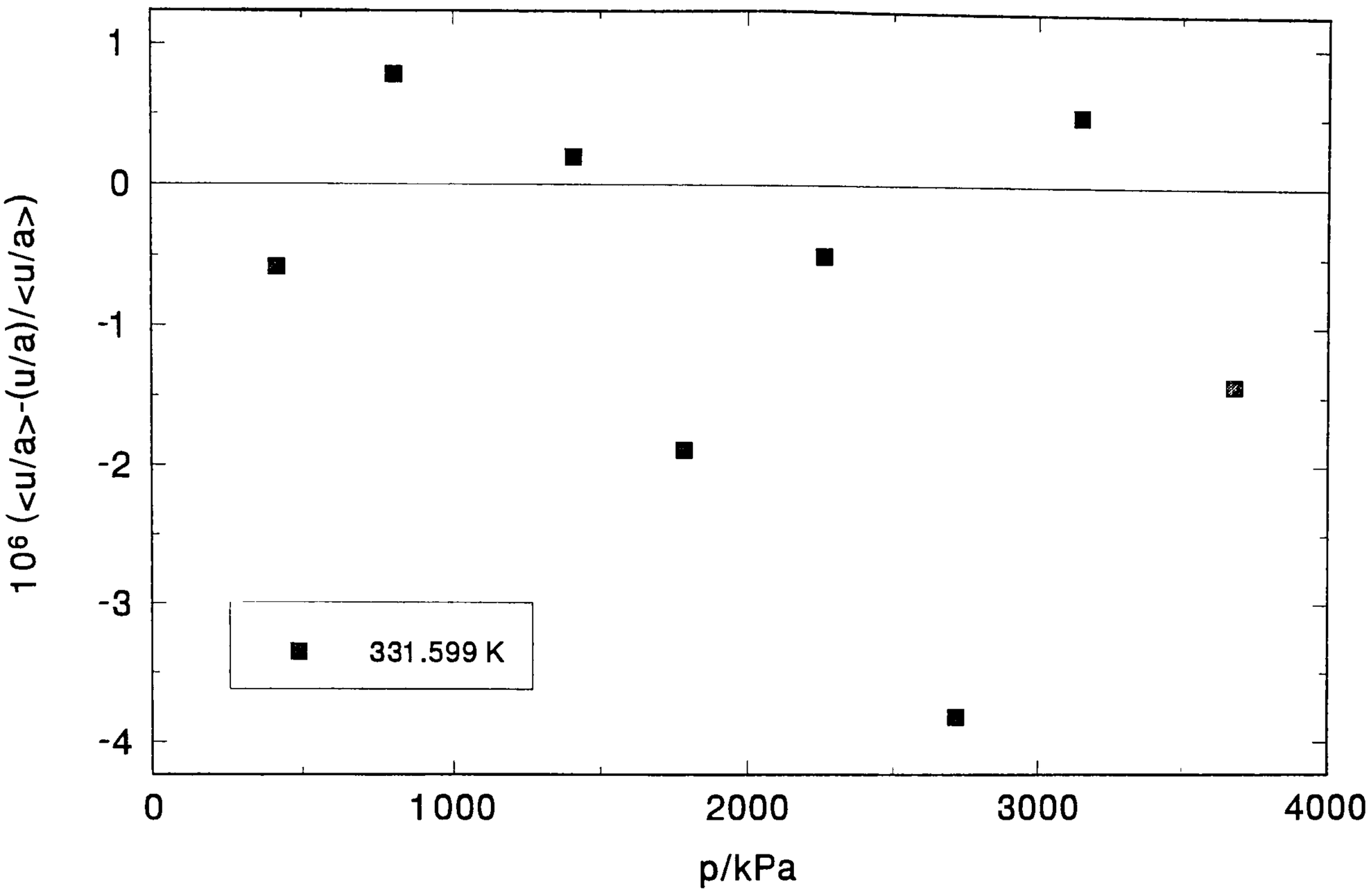

The density explicit expansion:

$$u^2(T,\rho_n) = \frac{RT\gamma^{pg}}{M}\left(1+\beta_a\rho_n+\gamma_a\rho_n^2+\cdots\right) \tag{8.16.2}$$

was utilised to express the speed of sound in terms of the temperature T and the amount of substance density ρ_n. Regression analysis with equation (8.16.2) and the corresponding pressure explicit expansion allowed the heat capacities and virial coefficients to be determined. It was found that use of the density-explicit expansion led to a more rapid convergence of the data than the pressure-explicit expansion, although results were obtained for both cases. The isotherms at 299.7 K, 315.5 K and 352.0 K required five-terms in order to fit the data adequately whereas the density series required just three terms. The isotherm at 331.6 K also required a three-term fit to describe the data adequately with the density expansion whereas four terms were required to describe the data with the pressure-explicit expansion (fewer terms were needed for this isotherm compared with the other isotherms on account of the lower pressure range investigated). Systematic errors may occur when either of these infinite

expansions are truncated, with the values of the coefficients depending on the order of the adopted fit. The reduced pressure range of the isotherm at 331.6 K, means systematic errors for this isotherm will differ from those of the other isotherms for which the product $\beta_a(T)\rho_{max}$ is approximately constant.

For each of the isotherms an iterative procedure was followed to determine the heat capacities and acoustic virial coefficients. As fairly good estimates of B were available already, these were used to estimate the density (otherwise the density is estimated assuming perfect-gas behaviour) and the data was then analysed to deduce β_a. The second virial coefficient was then calculated from β_a and the updated value of B used to obtain improved estimates of the density: the third virial coefficient was not used to calculate the densities. The procedure was repeated until internal consistency was obtained.

Tables (8.16.1) to (8.16.4) list the mean values of u and u/a at each of the 46 state points investigated, together with the fractional standard deviations $\sigma(u)/u$ and the number of modes N from which they were determined. Also in the tables are the fractional deviations $\delta(u)/u$ of u from the adopted fit for the pressure explicit and density explicit series expansions. State points not included in the fit for the pressure *or* density series are denoted by ‡; those not included in the density series only are denoted by †. The deviations from the adopted fits (for the pressure and density series) are shown in figures (8.16.6) to (8.16.13).

Table (8.16.1): Mean values of *u/a* and *u* with standard deviations σ from *N* modes and deviations δ_p and δ_ρ from the pressure and density series respectively at a temperature of 299.682 K

p/kPa	<*u*/*a*>/Hz	<*u*>/ms^{-1}	10^6 ($\sigma(u)/u$)	10^6 ($\delta_p(u)/u$)	10^6 ($\delta_\rho(u)/u$)	*N*
5580.135	4351.8507	163.7198	1.0	-0.1	-5.9	3
4375.576	4406.9070	165.7911	1.7	4.3	15.8	3
3985.460	4432.5728	166.7567	1.0	-8.8	-4.8	3
3548.070	4465.1680	167.9829	0.3	2.6	1.1	3
2892.902	4520.1240	170.0504	0.9	7.8	3.6	3
2471.885	4558.6231	171.4988	1.0	-3.4	-8.3	3
2071.590	4597.2062	172.9503	2.3	-5.6	-7.5	3
1333.352	4672.4351	175.7805	1.0	4.7	2.4	3
933.590	4714.8534	177.3763	1.2	-1.1	-0.3	3
612.497	4749.6558	178.6856	0.4	-0.7	6.0	2
‡ 226.831	4792.0901	180.2820	139.4	-15.7	7.2	3
‡ 102.269	4806.6702	180.8305	3.6	131.0	162.2	2

Table (8.16.2):Mean values of *u/a* and *u* with standard deviations σ from *N* modes and deviations δ_p and δ_ρ from the pressure and density series respectively at a temperature of 315.468 K

p/kPa	<*u*/*a*>/Hz	<*u*>/ms^{-1}	10^6 ($\sigma(u)/u$)	10^6 ($\delta(u)/u$)	10^6 ($\delta(u)/u$)	*N*
6197.352	4562.2408	171.6944	3.0	3.6	2.7	3
† 5389.207	4571.2354	172.0329	1.2	-12.6	-14.8	3
5157.846	4576.9813	172.2491	1.2	3.6	-3.8	3
4417.434	4603.2055	173.2361	0.6	4.6	-3.2	3
3672.441	4640.4332	174.6371	1.2	6.4	2.5	3
3004.812	4681.4439	176.1805	1.9	0.4	2.3	3
2316.665	4729.9733	178.0068	2.0	-8.9	-0.7	3
1772.005	4772.2056	179.5962	1.4	-3.3	1.4	3
1150.124	4823.8129	181.5383	0.8	4.2	0.6	3
524.242	4878.7821	183.6070	1.4	7.6	-1.9	3
† 145.799	4913.1978	184.9022	3.7	-8.5	-13.9	2
‡ 42.007	4928.2412	185.4684	193.4	1095.5	1093.1	3

Table (8.16.3):Mean values of *u/a* and *u* with standard deviations σ from *N* modes and deviations δ_p and δ_ρ from the pressure and density series respectively at a temperature of 331.599 K

p/kPa	<*u*/*a*>/Hz	<*u*>/ms^{-1}	10^6 ($\sigma(u)/u$)	10^6 ($\delta(u)/u$)	10^6 ($\delta(u)/u$)	*N*
3680.143	4814.7557	181.2617	1.2	0.5	-0.5	4
3148.688	4837.2091	182.1070	1.8	-1.8	1.8	4
2714.737	4858.6447	182.9140	2.9	6.7	6.0	4
2260.136	4883.6803	183.8565	1.2	-9.3	-12.5	4
1783.323	4912.8333	184.9540	1.6	10.9	8.8	4
1407.301	4937.4600	185.8812	0.9	-3.1	-2.0	4
803.806	4980.0180	187.4833	2.8	-4.3	0.4	4
415.828	5009.1199	188.5789	0.7	5.2	6.3	3
198.610	5025.8670	189.2094	23.7	-1.5	-5.9	3
‡ 25.904	5091.9591	191.6976	5.1	10472	10461	2

Table (8.16.4):Mean values of *u/a* and *u* with standard deviations σ from *N* modes and deviations δ_p and δ_ρ from the pressure and density series respectively at a temperature of 352.022 K

p/kPa	<*u*/*a*>/Hz	<*u*>/ms^{-1}	10^6 ($\sigma(u)/u$)	10^6 ($\delta(u)/u$)	10^6 ($\delta(u)/u$)	*N*
6444.041	5002.9970	188.4329	1.5	0.2	-2.8	3
5967.930	4997.4871	188.2254	0.2	-0.8	2.6	3
5100.583	4996.8065	188.1997	0.3	3.0	2.7	3
4423.140	5003.9287	188.4680	0.8	-4.8	-4.1	3
3841.015	5015.0422	188.8866	1.0	3.0	4.0	3
2770.669	5046.0571	190.0547	0.5	-0.6	-1.7	3
2246.396	5065.8036	190.7985	1.1	-1.0	-2.9	3
1521.451	5097.5313	191.9934	0.6	3.0	0.9	3
951.559	5125.7076	193.0547	1.1	-2.7	1.2	3
† 384.218	5156.4243	194.2116	0.2	0.8	19.0	3
‡ 155.939	5169.6866	194.7111	73.3	43.2	71.0	2
‡ 20.465	5180.0508	195.1015	115.9	515.4	551.0	2

Figure (8.16.6): Fractional deviations of *u* from the adopted 3-term density series at a temperature of 299.682 K

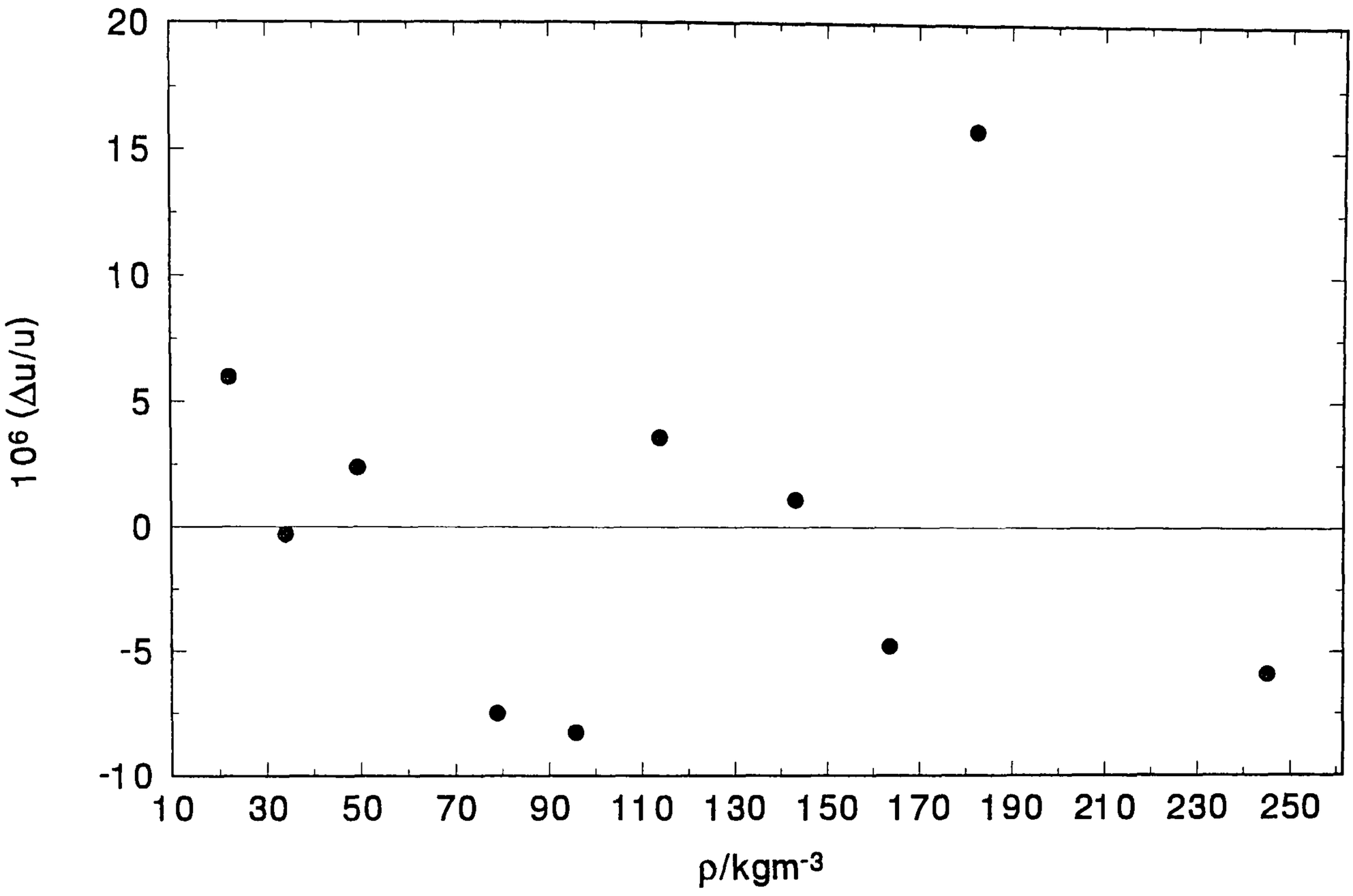

Figure (8.16.7): Fractional deviations of *u* from the adopted 5-term pressure series at a temperature of 299.682 K

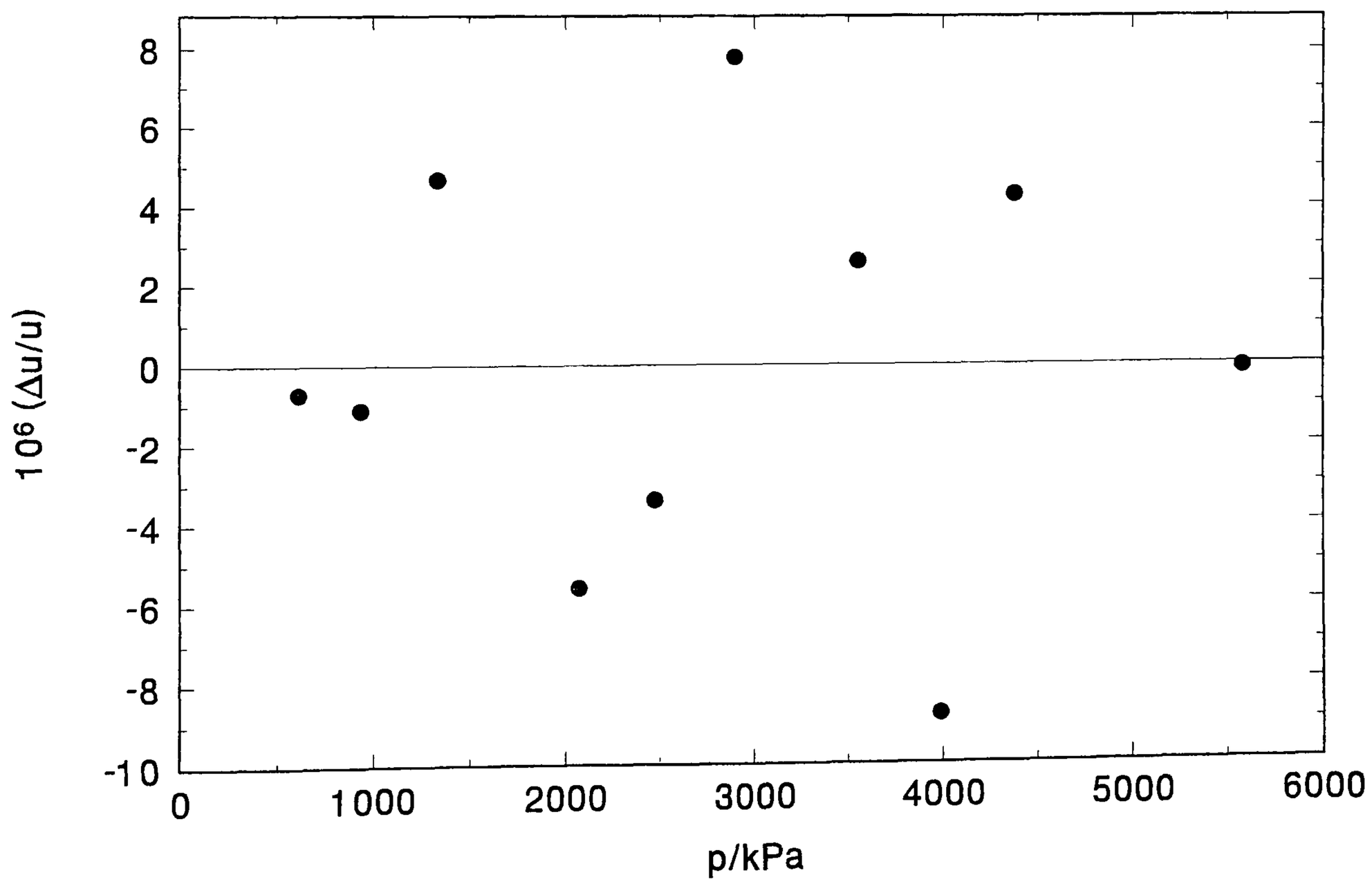

Figure (8.16.8): Fractional deviations of *u* from the adopted 3-term density series at a temperature of 315.468 K

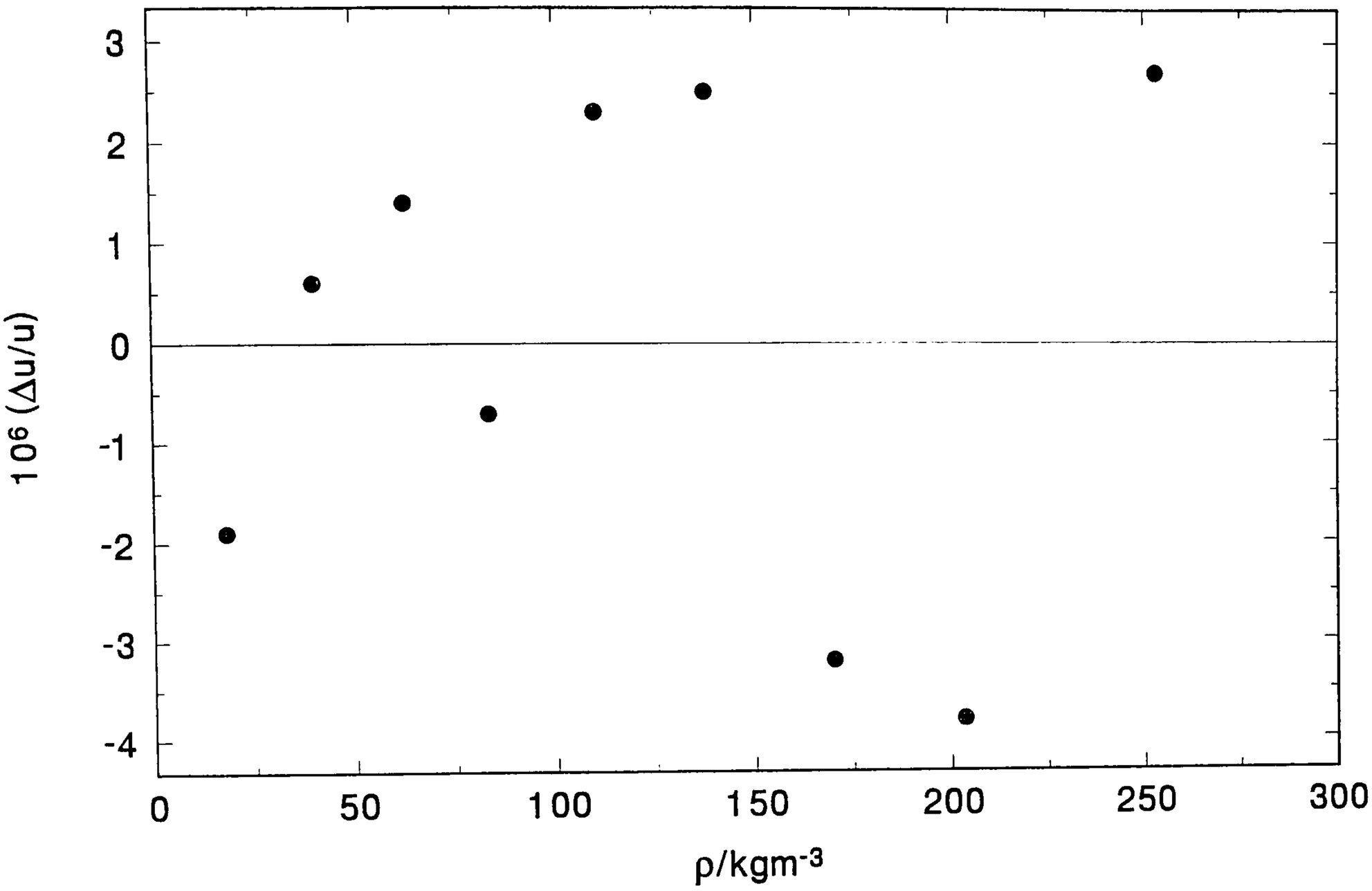

Figure (8.16.9): Fractional deviations of *u* from the adopted 5-term pressure series at a temperature of 315.468 K

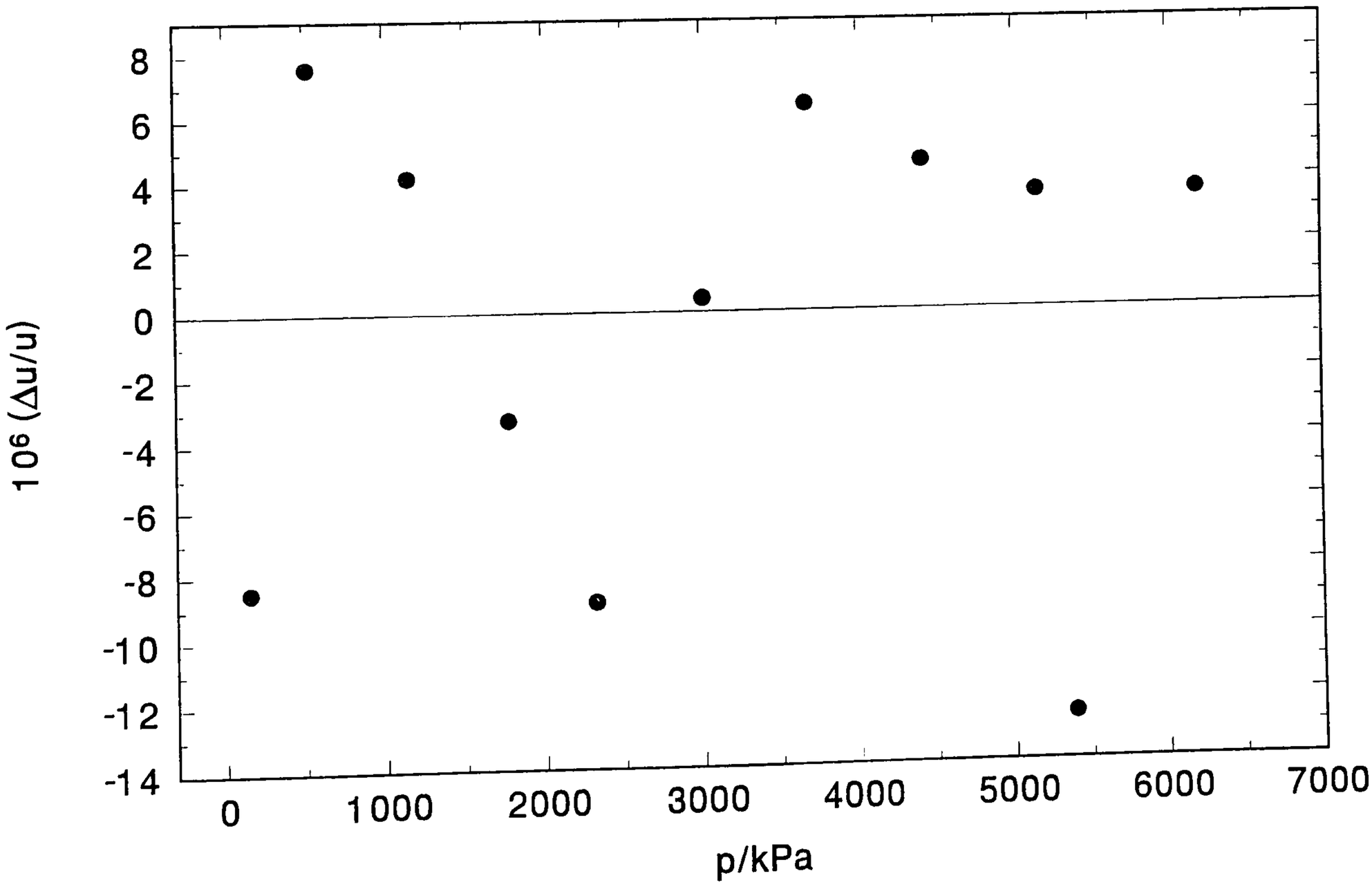

Figure (8.16.10): Fractional deviations of *u* from the adopted 3-term density series at a temperature of 331.599 K

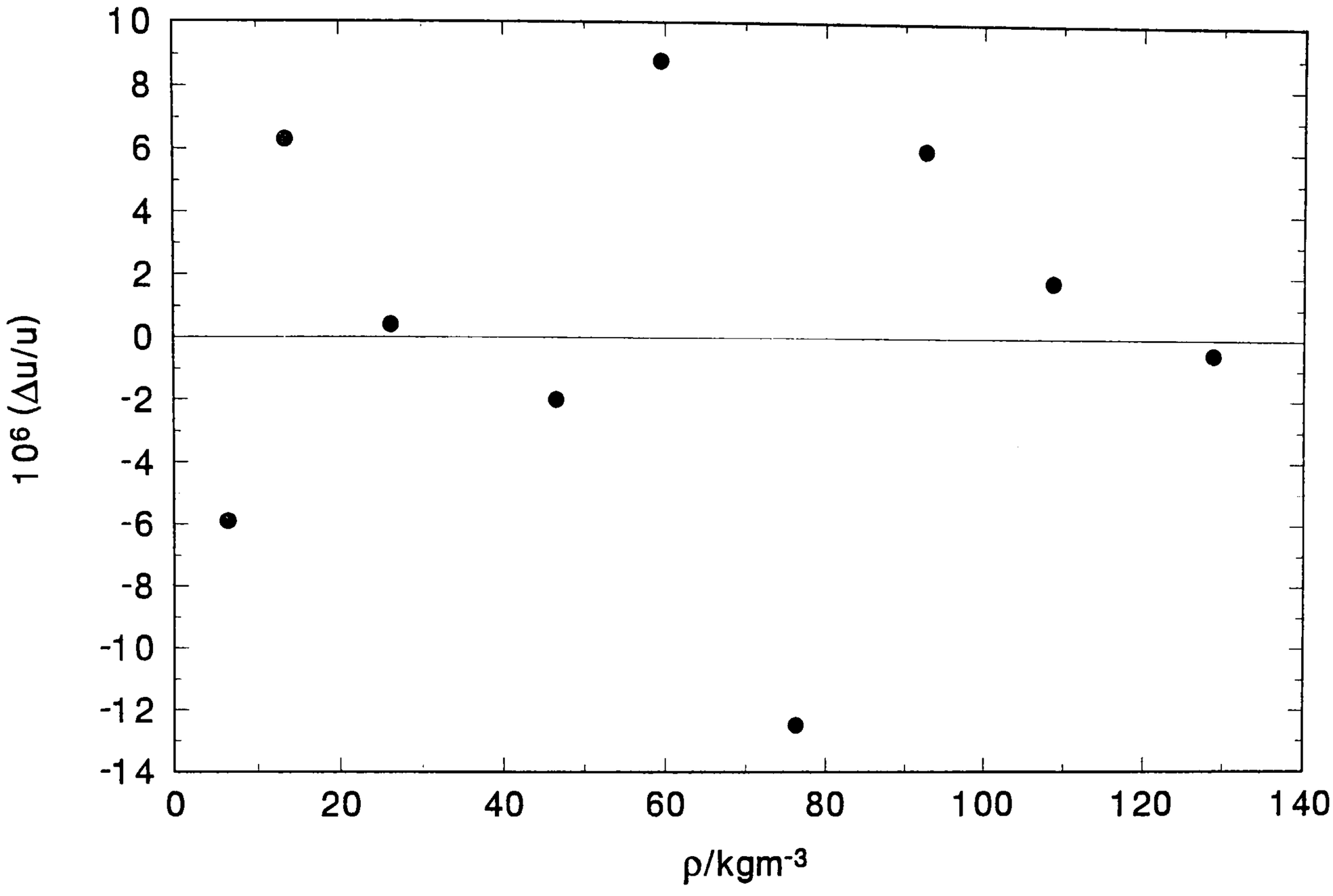

Figure (8.16.11): Fractional deviations of *u* from the adopted 4-term pressure series at a temperature of 331.599 K

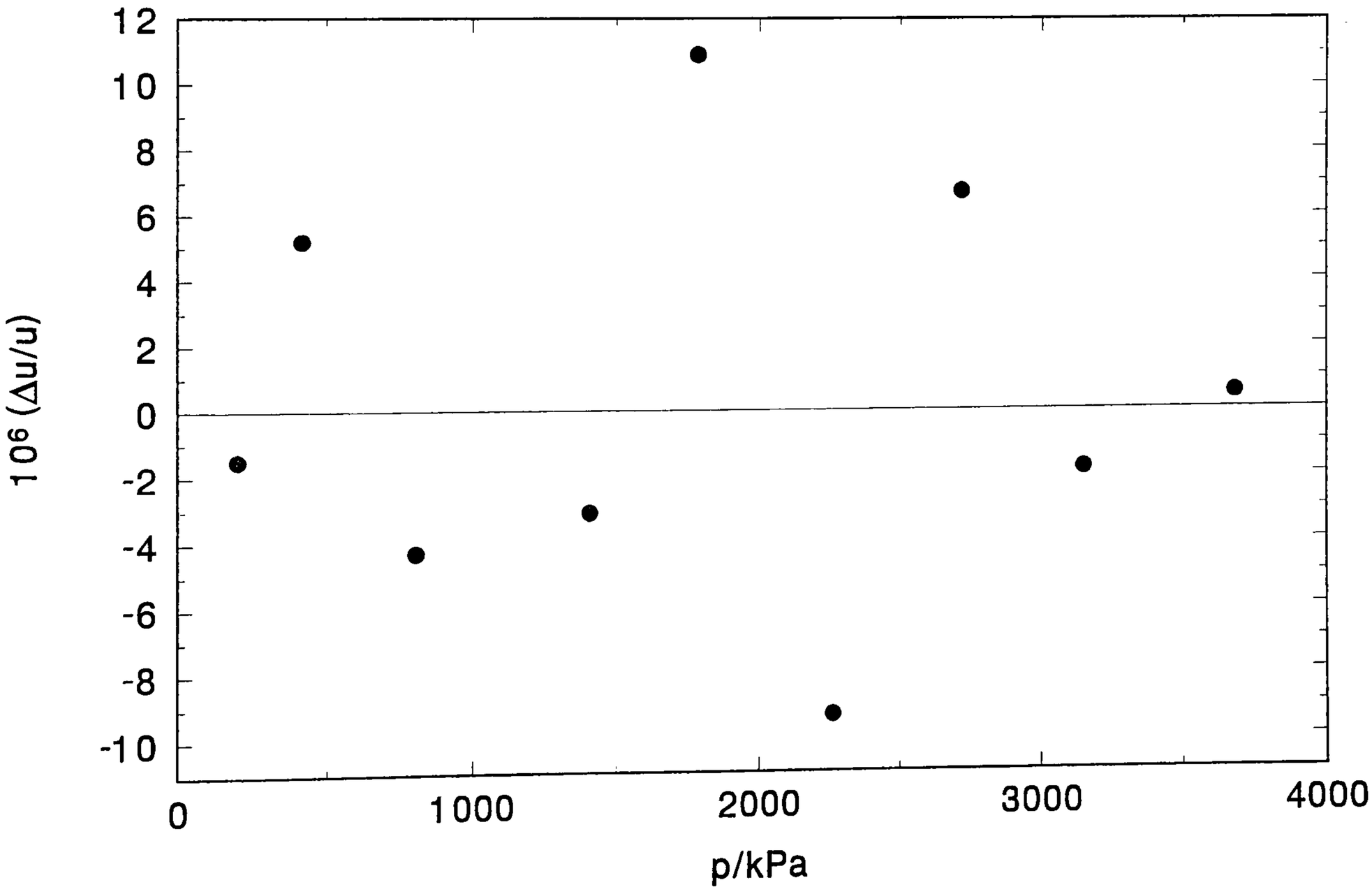

Figure (8.16.12): Fractional deviations of *u* from the adopted 3-term density series at a temperature of 352.022 K

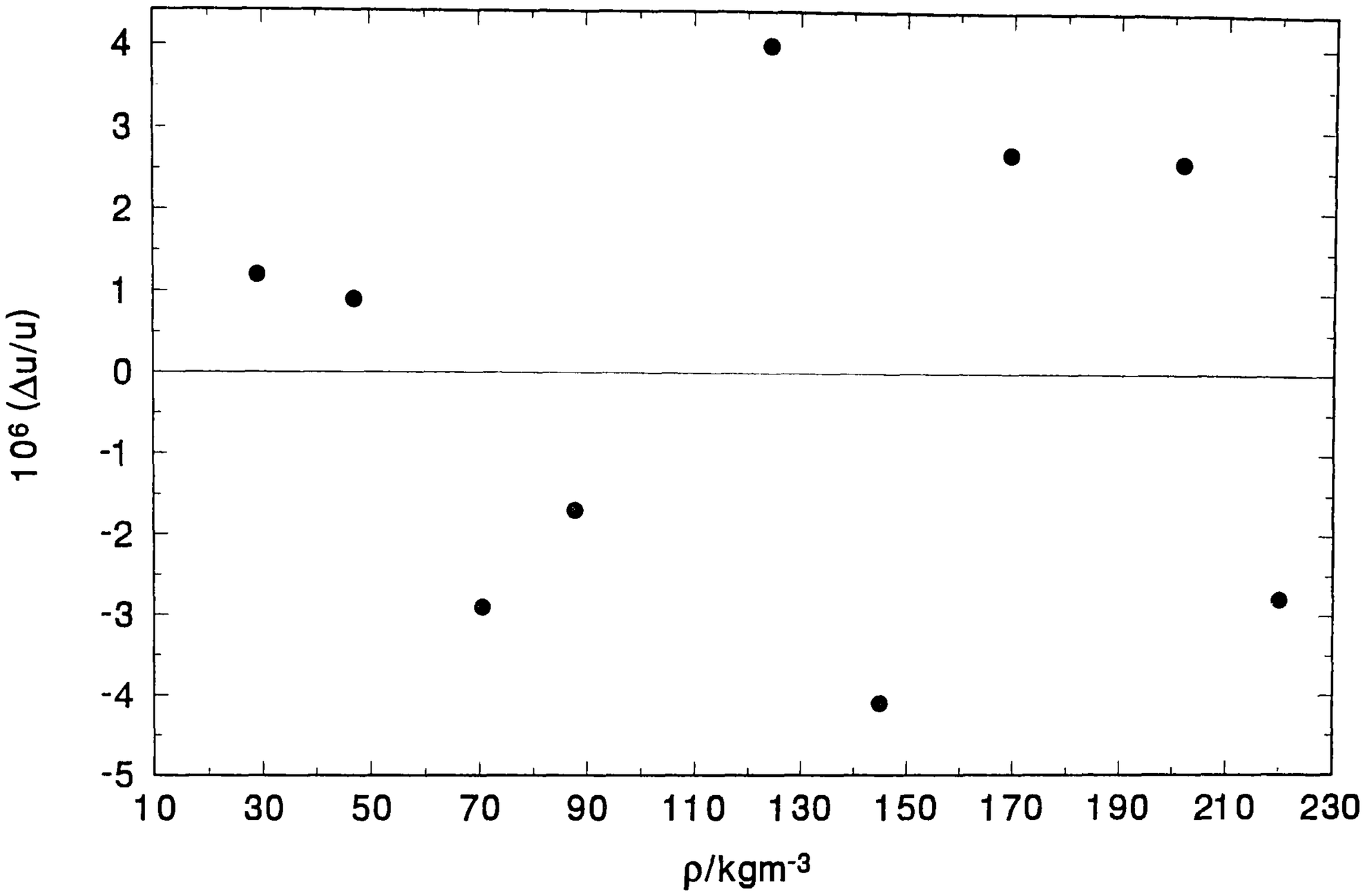

Figure (8.16.13): Fractional deviations of *u* from the adopted 5-term pressure series at a temperature of 352.022 K

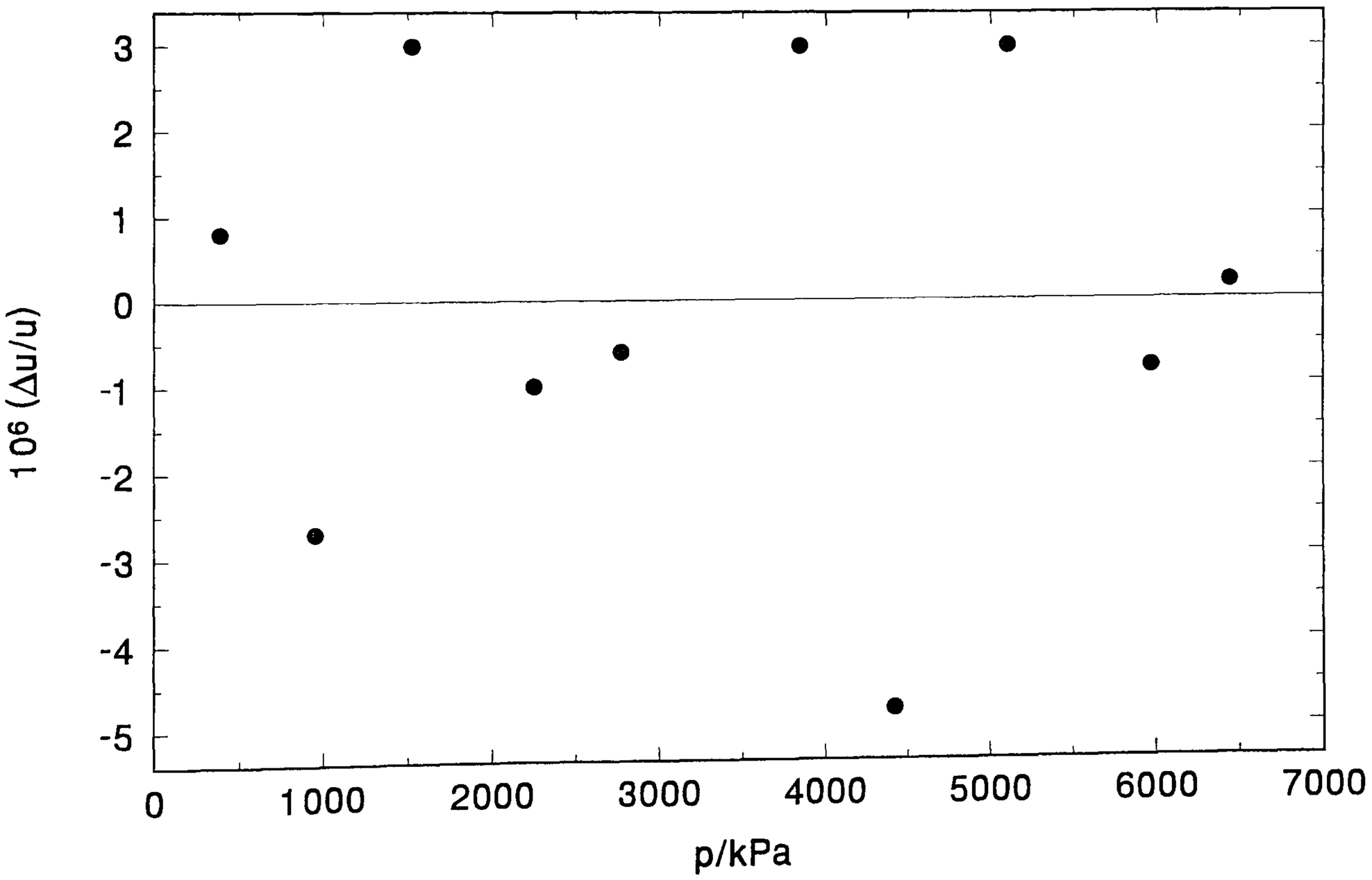

The derived values of the heat capacity and the second and third acoustic virial coefficients are given in table (8.16.5) and (8.16.6), together with their standard deviations and the fractional standard deviation of u^2 for each isotherm.

Table (8.16.5): Heat capacities and virial coefficients of tetrafluoromethane determined using a density series

T /K	$C_{p,\mathrm{m}}/R$	β_a /cm^3 mol^{-1}	γ_a /dm^6 mol^{-2}	$10^6\,\{\sigma(u^2)/u^2\}$
299.682	7.2459 ± 0.0007	-115.51 ± 0.01	0.0178 ± 0.0000	12.9
315.468	7.5143 ± 0.0003	-98.98 ± 0.00	0.0172 ± 0.0000	5.1
331.599	7.6687 ± 0.0009	-87.15 ± 0.03	0.0185 ± 0.0000	17.5
352.022	7.9513 ± 0.0005	-66.46 ± 0.01	0.0159 ± 0.0000	5.7

Table (8.16.6): Heat capacities and virial coefficients of tetrafluoromethane determined using a pressure series

T /K	$C_{p,\mathrm{m}}/R$	β_a /cm^3 mol^{-1}	γ_a /dm^6 mol^{-2}	$10^6\,\{\sigma(u^2)/u^2\}$
299.682	7.2423 ± 0.0023	-115.94 ± 0.12	0.0034 ± 0.0001	9.6
315.468	7.5144 ± 0.0011	-99.17 ± 0.07	0.0039 ± 0.0000	13.4
331.599	7.6700 ± 0.0013	-86.87 ± 0.08	0.0043 ± 0.0000	17.3
352.022	7.9472 ± 0.0007	-66.79 ± 0.04	0.0044 ± 0.0000	5.3

Figure (8.16.14) gives the values of $C_{p,\mathrm{m}}/R$ determined from the density series and also those obtained from reference [18] for comparison. The deviation $\Delta C_{p,\mathrm{m}}/R$ from the calculated values are also shown in figure (8.16.15), where

$$\Delta C_{p,\mathrm{m}}^{\mathrm{pg}} = C_{p,\mathrm{m}}^{\mathrm{pg}}(\mathrm{expt.}) - C_{p,\mathrm{m}}^{\mathrm{pg}}(\mathrm{calc.}) \qquad (8.16.3)$$

and the calculated heat capacities were calculated from the vibrational frequencies given in reference [141]. The calculated heat capacity has an uncertainty of approximately $0.007R$.

The experimental values obtained are systematically lower than the values calculated from the sum of the Plank-Einstein functions used to determine $C_{p,\mathrm{m}}^{\mathrm{pg}}$ and are clearly not as accurate as the values obtained by Ewing in reference [18]. However, although the values obtained experimentally with the hemisphere fall outside the theoretical

Figure (8.16.14): Perfect-gas heat capacities $C^{pg}_{p,m}$ of tetrafluoromethane

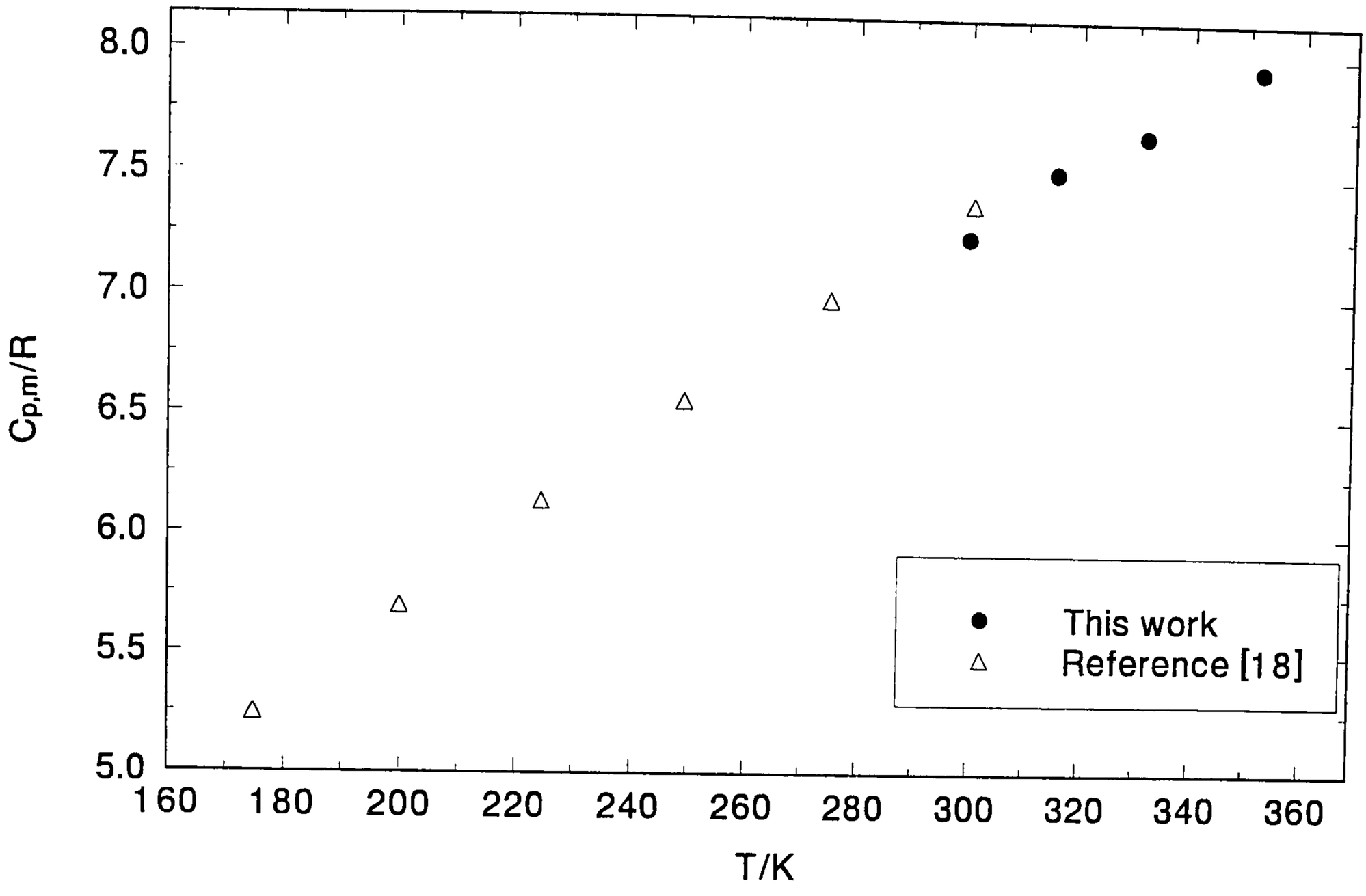

Figure (8.16.15): Deviations of experimental from calculated perfect-gas heat capacities $\Delta C^{pg}_{p,m}$ of tetrafluoromethane

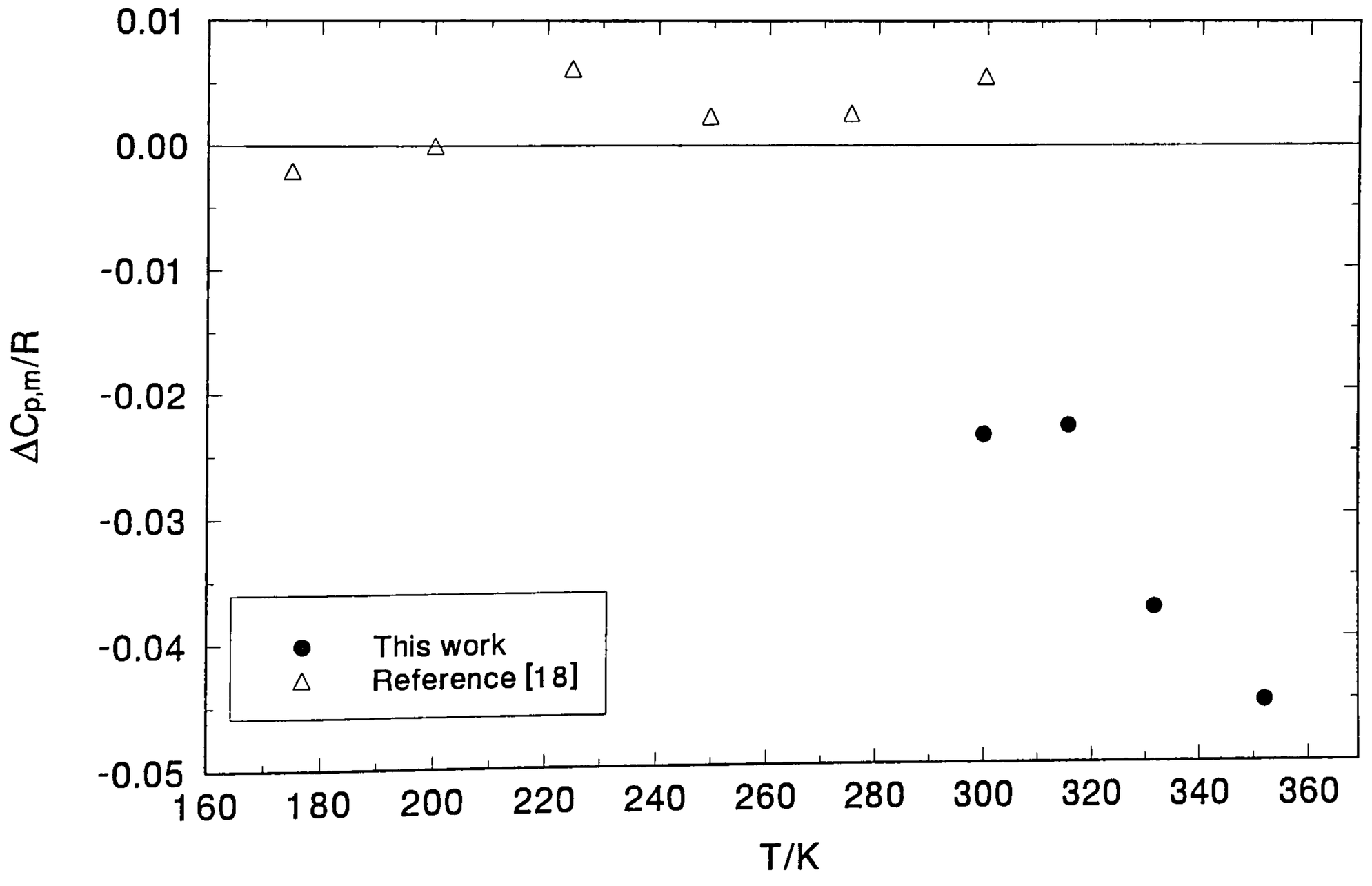

values, even when taking account of the estimated uncertainties, the heat capacity $C_{p,\mathrm{m}}^{\mathrm{pg}}$ is obtained within 0.025 and 0.05 R and with further modelling, improved estimates of $C_{p,\mathrm{m}}^{\mathrm{pg}}$ are expected.

Figure (8.16.16) gives the values of β_a determined from the density series and also those values obtained from reference [18] for comparison. The deviation $\Delta\beta_a$ from the calculated values are shown in figure (8.16.17), where

$$\Delta\beta_a = \beta_a(\text{expt.}) - \beta_a(\text{calc.}) \qquad (8.16.4)$$

The calculated second acoustic virial coefficients were determined from reference [18] using the recommended values of β_a and the expression for the second virial coefficient derived from the square well potential. For the two lowest-temperature isotherms, the deviations of β_a from the values predicted by Ewing *et al.* are comparable with the standard deviation determined at each temperature. However, for the isotherms performed at 331.6 K and 352.0 K, the deviations are much larger than the estimated standard deviations of β_a calculated at each temperature.

The third acoustic virial coefficients are compared with those of reference [18] in figure (8.16.18). The value of γ_a at 331.6 K deviates substantially from the value expected by interpolation of the other results. The different pressure range of this isotherm compared with the other three may partly account for the difference but it is higher by approximately 0.002 $\mathrm{dm^6\,mol^{-2}}$ and is therefore likely that this sample was contaminated.

Figure (8.16.6): Second acoustic virial coefficients β_a of tetrafluoromethane

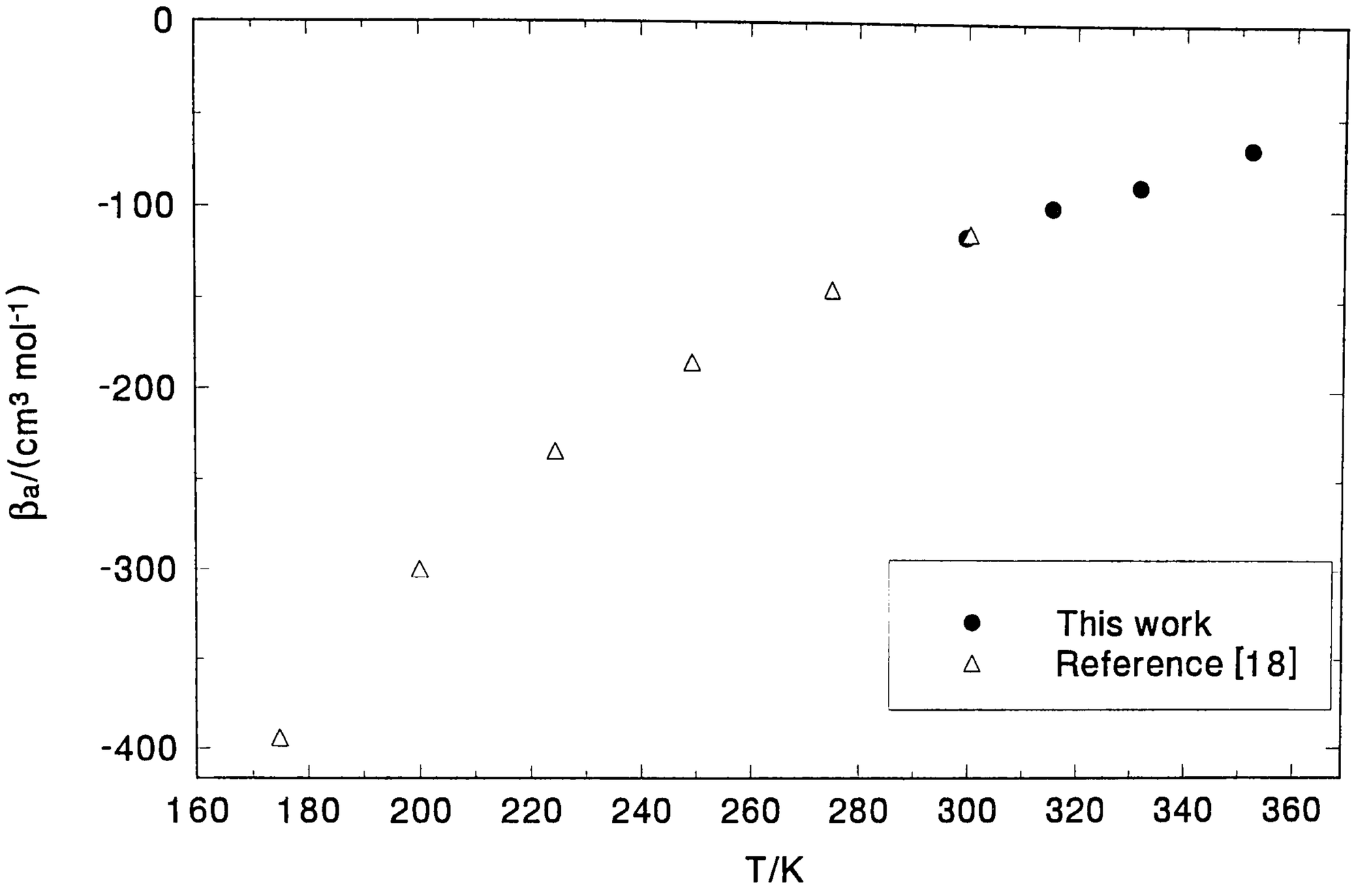

Figure (8.16.17): Deviations of experimental from calculated second acoustic virial coefficients $\Delta\beta_a$ of tetrafluoromethane

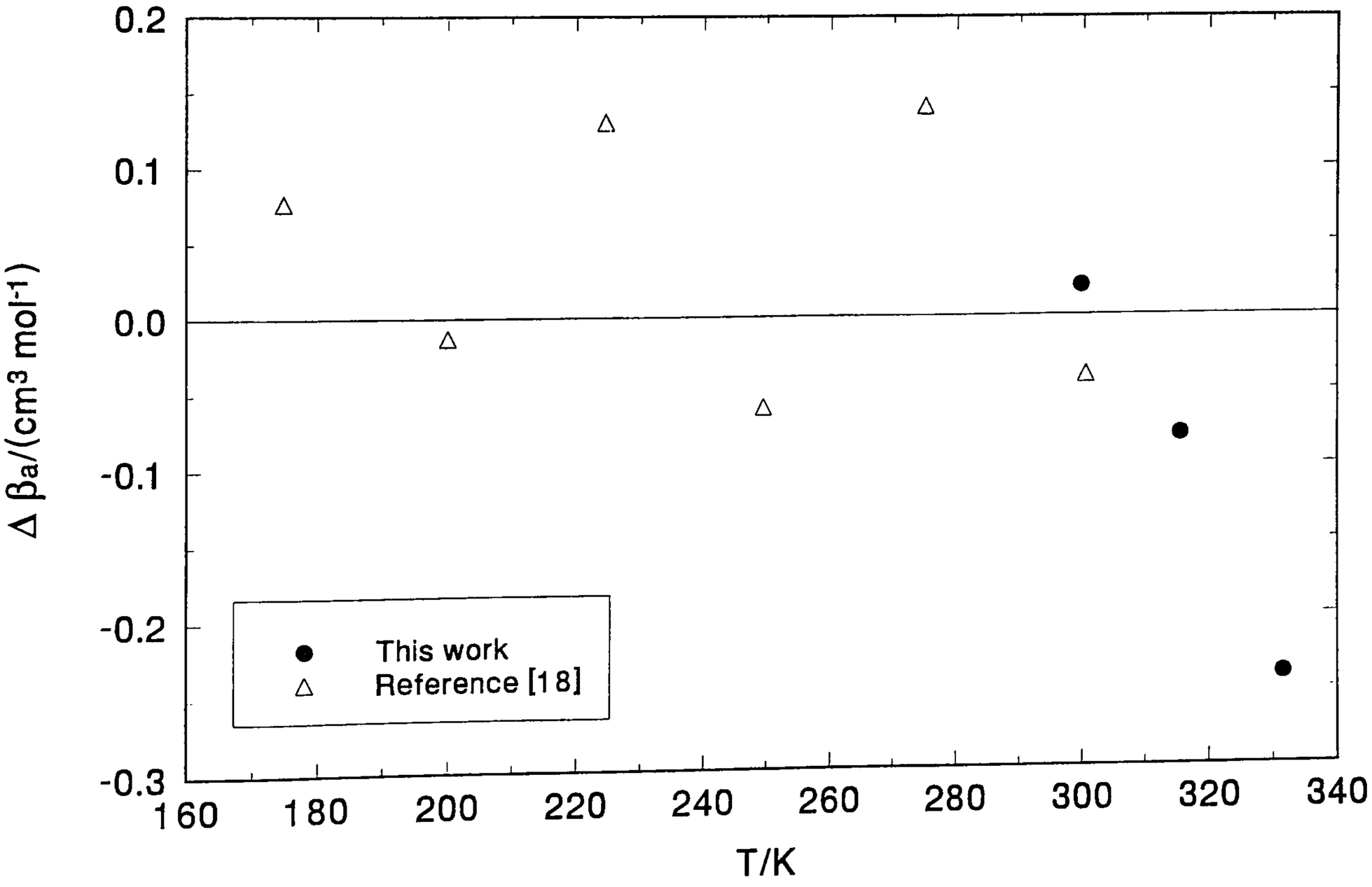

Figure (8.16.18): Third acoustic virial coefficients γ_a of tetrafluoromethane

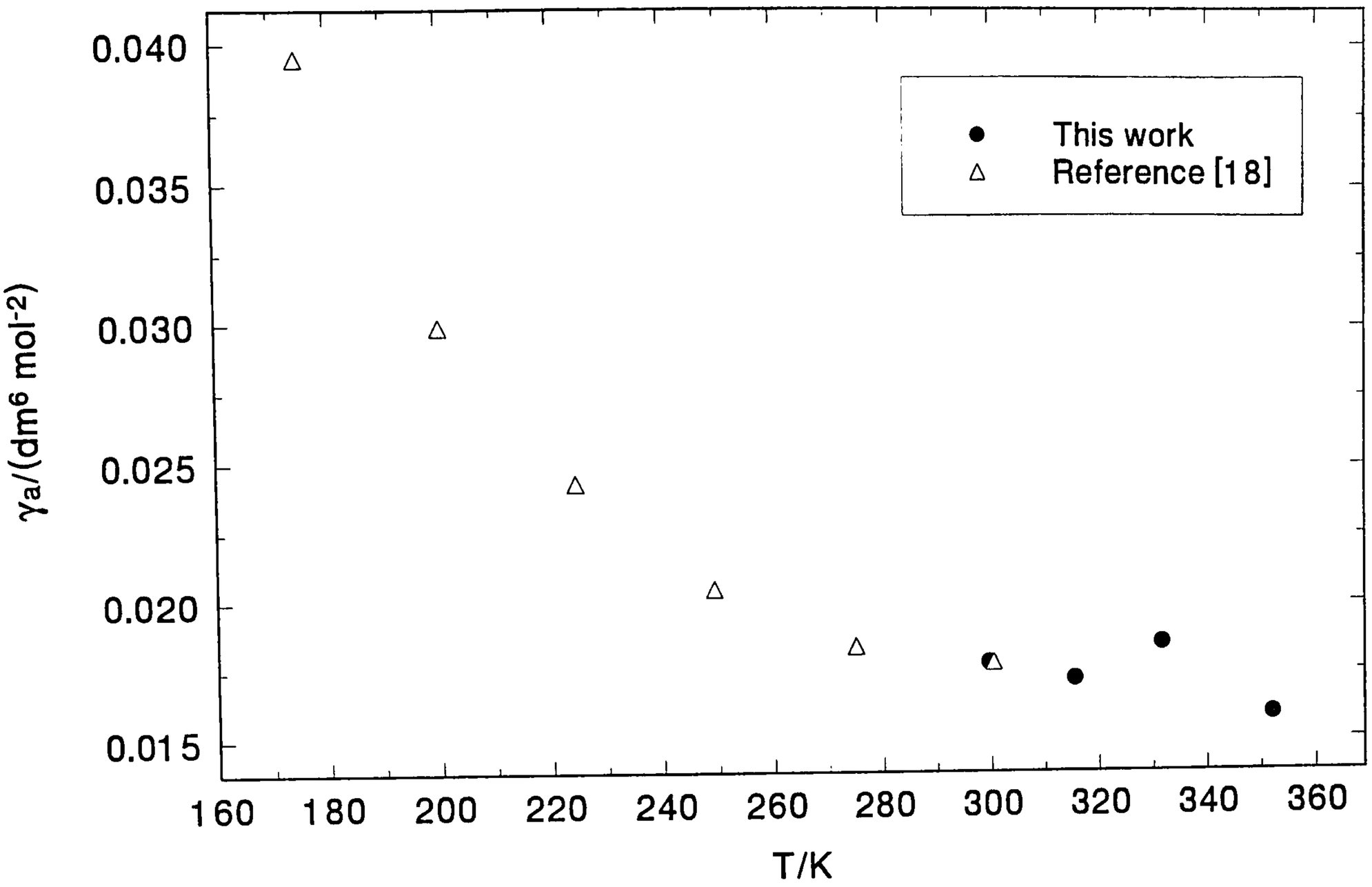

CHAPTER 9

Summary and Concluding Remarks

The hemispherical acoustic resonator was designed for measuring the speeds of sound at pressures up to 40 MPa and has several advantages, as discussed in chapter 1, over other geometries which make it suitable for this purpose.

A selection of gases was made to allow the performance of the resonator to be investigated fully for gases with very different behaviour. Nitrogen, argon and tetrafluoromethane were studied at the highest pressures of about 7 MPa, while low pressure measurements were made on propene and the tetrafluoromethane. The speed of sound in both nitrogen and argon is very high, whilst for propene and tetrafluoromethane it is substantially lower, with the latter showing marked effects from vibrational relaxation.

The acoustic model for the spherical cavity has been reported elsewhere [10, 30, 42, 76, 150, 151] and it was extended in chapter 3 to include the hemispherical geometry. The additional perturbations experienced by the resonance frequencies of the hemisphere as a result of thermal and viscous waves at the equatorial surface were derived, and the correction terms for holes in the resonator wall were modified to account for the different signal intensities experienced by holes in the equatorial surface compared with holes in the spherical wall.

Characterisation of the cavity was reported in chapter 5 and this supported the theory that the eigenvalues of the sphere and the hemisphere were identical and that the basis of the acoustic model for the hemisphere was valid. Construction of a prototype equatorial plate allowed measurements of the relative intensity of the signals as a function of r/a to be made and hence, the position of the nodes and anti-nodes of the first four radial modes to be established. The prototype plate was also used to verify the functional forms of the equations describing the perturbations to the resonance frequencies and halfwidths. In particular, changes to the area of an opening in the equatorial plate, its position with respect to r/a and the length of the waveguide at $r/a = 0$ were investigated and their effect on the measured halfwidths observed. It was

found that the experimental halfwidths were in excellent agreement with the theoretically predicted functional forms.

Conventionally, the effect of the internal pressure on the dimensions of the cavity is modelled through the compliance which expresses the dilation of the vessel with respect to pressure. The compliance χ for a perfectly cylindrical, thick-walled vessel with capped ends [86] is

$$\chi = \frac{1}{E}\left[\frac{a^2(2-\sigma)}{2(b-a)}\right] \tag{9.1}$$

and for a perfectly spherical shell with an internal radius of a and an external radius of b, the compliance is given by

$$\chi = \frac{1}{E}\left[\frac{(b^3+2a^3)(1-\sigma)}{2(b^3-a^3)}+\sigma\right] \tag{9.2}$$

where σ is Poisson's ratio and E is Young's modulus. Clearly, the hemispherical vessel does not resemble closely either geometry (it is hemispherical on the interior surface and cylindrical on the exterior surface) although it was expected to behave as some hybrid of the two equations. Modelled as a cylinder, the resonator would be expected to have a compliance of 2.8×10^{-13} Pa^{-1} and as an isotropic sphere a compliance of 4.8×10^{-12} Pa^{-1} at 300 K.

Isothermal measurements performed on nitrogen at pressures up to 7 MPa and temperatures between 300 and 355 K allowed the resonator's geometry to be characterised. Measurements of u/a from the hemisphere were compared with values of the speed of sound calculated from the virial coefficients given in reference [59], and it was found that the compliance of the cavity was temperature dependent and that the pressure dependency was quite different from that predicted by equations (9.1) or (9.2). The effective compliance of the hemisphere calculated from the experimental results at 300 K was 5.3×10^{-11} Pa^{-1}, a factor of 11 higher than the value predicted for a sphere (equation 9.2) and 190 times higher than that predicted by the cylindrical model (equation 9.1). The temperature dependency was also much higher than could be expected by any temperature dependency of Young's modulus. The expansivity of stainless steel 321 is approximately 9.6×10^{-6} K^{-1} but from the measurements this was estimated as 22.0×10^{-6} K^{-1}.

An empirical model was therefore developed which described the pressure and temperature dependency of the radius with the 5-term fit given by equation (7.8.6). The separation between the modes was then solved by introducing effective radii for each mode which reduced the standard deviation of the fit to 20 ppm. Use of equation (7.8.6) and the effective radii then allowed the speed of sound to be calculated within the desired accuracy.

Clearly, a disadvantage of the hemispherical geometry is that the theoretical compliance is not known and values of the compliance and expansivity calculated from the measurements do not reflect literature values [103]. However, by accepting a certain amount of empiricism to describe the behaviour of the cavity, the radius $a\,(T, p, n)$ was calculated with a standard deviation of 20 ppm allowing the speed of sound to be determined with a fractional standard deviation of 20 ppm or less.

It was thought that the effective compliance of the vessel was much larger than had been expected because there was coupling between resonance modes of the shell and those of the gas. This strong coupling severely perturbed the resonance frequencies and lead to values of $a\,(T, p,n)$ which were artificially high.

Further evidence for coupling between the radial modes and resonances of the shell was seen most clearly for the (0,2) mode. For all the gases, except CF_4, reported here distinct maxima were seen when the fractional excess halfwidths $\Delta g_{0,2}/f_{0,2}$ were plotted against pressure (or frequency). It was also found that the frequencies at which these maxima occurred were linearly dependent on the temperature, irrespective of the gas. The reason distinct maxima were not seen for $\Delta g_{0,2}/f_{0,2}$ for the tetrafluoromethane was due to the much lower sound speed in this gas; hence the resonance frequencies of the (0,2) mode were coupled to the shell resonances more weakly in this gas. Whilst large losses to the resonance halfwidths were still observed in CF_4, these were much less well- defined.

The empirical model describing the behaviour of the cavity to changes in temperature and pressure was verified by a direct comparison of measurements made in the hemispherical and spherical resonators using argon.

The large excess halfwidths experienced initially were modelled using the data obtained from both the nitrogen and propene isotherms. An analysis of $\Delta g_{0,n}/f_{0,n}$ for the (0,3), (0,4), (0,5) and (0,6) modes revealed large losses which could be modelled as an

annular slot at the junction between the hemispherical shell and its equatorial plate. The slot width was calculated to be 0.045 mm which is reasonable on the basis of machine-shop tolerances. It was possible to measure the resonance frequencies and halfwidths of propene only at pressures less than 1 MPa (in order to avoid the effects of precondensation), but even at these low pressures the measurements could be made with ease and the halfwidths successfully modelled. The slot correction was included in the analysis of the halfwidths for argon and lead to excess halfwidths that were generally less than 20 ppm. However, the $\Delta g/f$ were less than 10 ppm at pressures greater than 1 MPa which was the pressure regime the resonator had been designed for originally. The excess halfwidths also revealed no pressure dependency (as might occur if there were radiation of sound from the external surface) unlike the stainless steel resonator described in section (4.16).

Although this was not part of the original motivation in design, the hemispherical geometry worked well for the relaxing gases as measurements could be made relatively easily at extremely low pressures. Measurements in CF_4 were made at pressures of a few kPa and although there was broadening of the modes, the signal-noise ratio of the signals remained extremely high and the vibrational relaxation times were measured successfully and found to be in good agreement with the literature.

Although the results were not reported here, preliminary measurements on CO_2 were also made using the hemisphere at pressures of about 100 kPa to 3.2 MPa and although severe broadening was observed the measurements were significantly easier than measurements obtained using a spherical resonator [40].

For a spherical geometry, where the transducers are in the walls of the cavity, the signals are relatively weak and require substantial amplification which makes low pressure measurements extremely difficult when a relaxing gas is being studied. However, the positioning of the source transducer in the centre of the equatorial plate at $r/a = 0$ is a major advantage of the hemispherical geometry as it means that the signals remain intense at high pressures (when the loads on the transducer membranes are high and the transducers less sensitive) and the signal-noise ratio remains large even at low pressures, so measurements can still be made with relative ease; an area in which the hemispherical geometry could be exploited further for the study of relaxing gases. Furthermore, because the non-radial modes have no acoustic density at $r/a = 0$,

they are not excited with any significant amplitude and therefore no overlap between radial and non-radial modes is experienced when, for a different geometry, broadening of the modes may cause this to be a problem. For example, in a sphere the eigenvalues for the (0,2) and non-radial (3,1) modes differ by less than 0.5 per cent and overlap between these modes was a severe problem in earlier measurements on CF_4 in a spherical cavity [18].

References

1 IUPAC: Experimental Thermodynamics Volume II. W. Van Dael; Chapter 11: Thermodynamic Properties and the Velocity of Sound, Editors: B. Le Neindre, B. Vodar. Butterworths, London 1975.

2 Ewing M. B., McGlashan M.L., Trusler J. P. M., Molecular Physics, 1987, **60**, No. 3, 681-690.

3 Moldover M. R., Trusler J. P. M., Edwards T. J., Mehl J. B., Davis R. S., Journal of Research of the National Bureau of Standards, 1988, **93**, (2).

4 Moldover M. R., IEEE Transactions on Instrumentation and Measurement, Vol. 38, No. 2, April 1989.

5 Moldover M. R., Mehl J. B., Precision Measurement and Fundamental Constants II. Editors; Taylor B. N., Phillips W. D., Nat. Bur. Stand. (U.S.) Special Publication.

6 Sanchez Ochoa J. C., Ewing M. B., Acoustic thermometry using a spherical resonator NPL report 82/0427

7 Moldover M. R., Trusler J. P. M., Metrologia 1988, **25**, 165-187.

8 Moldover M. R., Waxman M., Greenspan M., High Temperatures, High Pressures 1979,**11**, 75-86.

9 Colgate S. O., Sona C. F., Reed K. R., Sivaraman A., J. Chem. Eng. Data, 1990, **35**, 1-5.

10 Mehl J. B., Moldover M. R., Proceedings of the 8th Symposium on Thermophysical Properties. Edited by Sengers J. V., Am. Soc. Mech. Eng., NY 1982.

11 Colgate S. O., Reed K. R., Sivaraman A., J. Chem. Thermo., 1990, **22**, 245-252.

12 Ewing M. B., Goodwin A. R. H., J. Chem. Thermo., 1992, **24**, 301-315.

13 van Itterbeek A., Nihoul J., Acustica, 1955, **5**, 142.

14 Sun T. F., Kortbeek P. F., Trappeniers N. J., Biswas S. N., Phys. Chem. Liq. 1987, **16**, 163.

15 Moldover M. R., Mehl J. B., Topics in Current Physics. Photoacoustic, Photothermal and Photochemical Processes in Gases, Volume 49, 1989.

16 Trusler J. P. M., Costa-Gomes M. F., J. Chem. Thermo., 1998, **30**, 527-534.

17 Ewing M. B., Trusler J. P. M., Physica A, 1992, **184**, 415-436.

18 Ewing M. B., Trusler J. P. M., J. Chem. Phys., 1989, **90**, (2) 1106.

19 Ewing M. B., Goodwin A. R. H., J. Chem. Thermo., 1992, **24**, 531-547.

20 Trusler J. P. M., J. Chem. Thermo., 1994, **26**, 751-763.

21 Greenspan M., J. Acoust. Soc. Am., 1956, **28**, (4).

22 Goodwin A. R. H., Moldover M. R., J. Chem. Phys., 1990, **93**, (4).

23 Estrada-Alexanders A. F., Trusler J. P. M., J. Chem. Thermo., 1998, **30**, 1589-1601.

24 Boyes S. J., Ewing M. B., Goodwin A. R. H., J. Chem. Thermo., 1992, **24**, 1151-1166.

25 Ewing M. B., Goodwin A. R. H., McGlashan M. L., Trusler J. P. M., J. Chem. Thermo., 1987, **19**, 721-739.

26 Greenspan M., J. Acoust. Soc. Am., 1950, **22**, (5).

27 Lestz S. S., J. Chem. Phys., 1963, **18**, (12).

28 Estrada-Alexanders A. F., Trusler J. P. M., J. Chem. Thermo., 1997, **29**, 991-1015.

29 Trusler J. P. M., Zarari M., J. Chem. Thermo., 1992, **24**, 973-991.

30 Moldover M. R., Mehl J. B., Greenspan M., J. Acoust. Soc. Am. 1986, **79**, (2), 253.

31 Mehl J. B., J. Acoust. Soc. Am., 1985, **78**, (2).

32 Colgate S. O., Sivaraman A., Dejsupa C., McGill K., J. Chem. Thermo., 1991, **23**, 647-652.

33 Colgate S. O., Sivaraman A., Dejsupa C., McGill K., Rev. Sci. Instru., 1991, **62**, (1).

34 Colgate S. O., Sivaraman A., Int. J. Thermo., 1996, **17**, (1), 15-21.

35 Assael M. J., Trusler J. P. M., Tsolakis T. F., Thermophysical Properties of Fluids: an Introduction to their Prediction. London: Imperial College Press; River Edge, NJ, 1996.

36 Editors: Eliezer S., Ricci R. A., High Pressure Equations of State: Theory & Applications, Proceedings of the International School of Physics, course CXII.

37 Costa Gomes M. F., Trusler J. P. M., J. Chem. Thermo., 1998, **30**, 1121-1129

38 Ewing M. B., Goodwin A. R. H., J. Chem. Thermo., 1993, **25**, 1503-1511.

39 Estrada-Alexanders A. F., Trusler J. P. M., J. Chem. Thermo., 1998, **30**, (12), 1589.

40 Angerstein J. L., Ewing M. B., Unpublished work 1993.

41 Ewing M. B., Goodwin A. R. H., J. Chem. Thermo., 1992, **24**, 1257-1274.

42 Mehl J. B., Moldover M. R., J. Chem. Phys., 1981, **74**, (7).

43 Ewing M. B., McGlashan M. L., Trusler J. P. M., J. Chem. Thermo., 1985, **17**, 549-559.

44 Ewing M. B., McGlashan M. L., Trusler J. P. M., J. Chem. Thermo., 1986, **18**, 511-517.

45 Colclough A. R., Acustica, 1976, **36**, 259-270.

46 Denardo B., Alkov S., Am. J. Phys., 1994, **62**, (4).

47 Giacobbe F. W., J. Acoust. Soc. Am., 1993, **94**, (3), Pt 1.

48 Carey C., Bradshaw J., Lin E., Carnevale E. H., Experimental Determination of Gas Properties at High Temperatures and/or High Pressures. (Arnold Engineering Development Center, Arnold Air Force Station, TN 37389, USA 1974) Report no. AEDC-TR-74-33.

49 Stewart J. L., Rev. Sci. Instrum., Vol.17, No. 2, 1946.

50 Trusler J. P. M., Ph.D. Thesis. University of London 1984.

51 Younglove B. A., Frederick N. V., International Journal of Thermophysics, Vol. 11, No. 5, 1990.

52 Trusler J. P. M., Physical Acoustics and Metrology of Fluids, Adam Hilger, 1991.

53 Colgate S. O., House V. E., Thien V., Zachery K., Hornick J., Shalosky J., International Journal of Thermophysics, Vol. 16, No. 3, 1995, 655-662.

54 Buxton A. J., Ph. D. Thesis. Univerity of London, 1997.

55 Jarvis G. K., Johnson K. A., Walmsley S. L., J. Chem. Eng. Data 1996, 222-230.

56 Morse P. M., Feshbach H., Methods of Theoretical Physics, Part II, NY: McGraw-Hill, pp1052-5, 1953.

57 Morse P. M., Ingard K. U., Theoretical Acoustics, NY: McGraw-Hill, 1969.

58 Encyclopaedia of Physics, Editor: S. Flugge; Volume XI/I, acoustics I, Springer Verlag 1961. Linear Acoustic Theory; Morse P. M., Ingard K.U.

59 Boyes S. J., Ph.D. Thesis. University of London 1992.

60 Van der Waals J. D. Thesis: Leiden 1873.

61 Holleran E. M., J. Chem. Thermo., 1970, **2**, 779.

62 Ewing M. B., Marsh K. N., J. Chem. Thermo. 1979, **11**, 793.

63 Scott R. L., J. Chem. Phys. 1962, **66**, 639.

64 Mayer J. E., Mayer M. G., Statistical Mechanics, second edition, Wiley: New York 1977.

65 Hall K. R., Canfield F. B., Physica 1967, **33**, 481.

66 Chemical Thermodynamics, Volume 1, Specialist Periodical Reports. A review of recent literature published up to Dec 1971. (1973)

67 Mehl J. B., Moldover M. R., J. Chem. Phys **77** (1), 1982.

68 Pires P. F., Guedes H. J. R., J. Chem. Thermo., 1999, **31**, 55-69.

69 Wilson D. A., Liebermann L. N., J. Acoust. Soc. Am. 1947, **19**, 286.

70 Kurtze G., Tamm K., Acustica, 1953, **3**, 33 - 48.

71 Moen C. J., J. Acoust. Soc. Am. 1951, **23**, 62 - 70.

72 Leonard R. W., J. Acoust. Soc. Am. 1947, **19**, 286.

73 Ohsawa T., Wada Y, Japanese J. App. Phys., Vol 6, **12**, 1351-1356.

74 Mehl J. B., J. Acoust. Soc. Am., 1982, **71**, (5).

75 Mehl J. B., J. Acoust. Soc. Am., 1986, **79**, (2).

76 Ewing M. B., McGlashan M. L., Trusler J. P. M., Metrologia, 1986, **22**, 93-102.

77 Goodwin A. R. H., Ph.D. Thesis. University of London 1988.

78 Ewing M. B., Pure and Applied Chemistry, **65**, no. 5, 1993, 907-912.

79 High Pressure Safety Code, High Pressure Technology Association, 1977.

80 BS 5500, 1990; Unfired Pressure Vessels.

81 BS 3580, 1964; Guide to Design Considerations on the Strength of Screw Threads.

82 Anderson H. L., Physics Vade Mecum, American Institute of Physics.

83 Harvey J., Theory and Design of Pressure Vessels, VNR, second edition, New York.

84 Bickell M. B., Ruiz C., Pressure Vessel Design and Analysis, Macmillan 1967.

85 Jawad M. H., Farr J. R., Structural Analysis and Design of Process Equipment, Wiley Interscience, second edition 1989.

86 Roark R., Young W., Formulas for Stress and Strain, McGraw-Hill Book Co., 1975.

87 Wentorf R. H., Modern Very High Pressure Techniques, London Butterworths, 1962.

88 Moss D. R., Pressure Vessel Design Manual, Gulf Publishing Company, 1987.

89 Azbel D. S., Cheremisinoff N. P., Chemical and Process Equipment Design - Vessel Design and Selection, Ann Arbor Science, 1982.

90 Blake A., Design of Mechanical Joints, Marcel Dekker Inc., 1985.

91 Juvinall R. C., Marshek K. M., Fundamentals of Machine Component Design, second edition, John Wiley & Sons, 1991.

92 Bickford J. H., An Introduction to the Design and Behaviour of Bolted Joints, second edition, Marcel Dekker Inc., 1990.

93 Editors: Spence J., Tooth A. S., Pressure Vessel Design, Concepts and Principles, E & FN SPON (an imprint of Chapman and Hall), 1994.

94 Isaacs N., Liquid Phase High Pressure Chemistry, Wiley Interscience 1981.

95 Bridgman P. W., The Physics of High Pressure, London G. Bell & Sons Ltd., 1952.

96 Editors: Spain and Pauwe, High Pressure Technology, Volume I.

97 Chuse R., Eber S. M., Pressure Vessels, the ASME Code Simplified, sixth edition, McGraw-Hill, 1984.

98 Megyesy E., Pressure Vessel Handbook, fourth edition, 1977.

99 Bednar H. H., Pressure Vesseel Handbook, Van Nostrand Reinhold, 1981.

100 Watts G. W., Lang H. A., Trans. ASME, Aug 1952, 1083.

101 Unfired pressure vessel code, Section viii, 1962.

102 Ledbetter, H. M., Weston W. F., Naimon E. R., J. Appl. Phys. **46**, 3855 (1975).

103 Kaye G. W. C., Laby T. H., Tables of Physical & Chemical Constants, sixteenth edition, Longman 1995.

104 Goodfellow's catalogue 1997, (Goodfellow Cambridge Ltd., Cambridge Science Park).

105 Schoessow G. J., Brooks E. A., Trans. ASME, Jul 1950, 567.

106 Kenny B., Moore G. G., Duncan J. P., J. Mech. Eng. Sci., Vol 5, no. 1, 1963, pp. 1 -14.

107 Tracy Hall H., Rev. Sci. Instru. Vol 29, no. 4, 1958, 267 -269

108 Mehl J. B., Moldover M. R., Physical Review A, Vol 34, no. 4, 1986, 3341-3344.

109 Boyes S. J., Ewing M. B., Trusler J. P. M., Unpublished work 1989.

110 Ewing M. B., Mehl J. B., Moldover M. R., Trusler J. P. M., Metrologia 1988, **25**, 211.

111 Ewing M. B., Trusler J. P. M., J. Acoust. Soc. Am., 1989, **85**, (4).

112 Quinn T. J., Temperature, Monographs in Physical Measurement: series editor Cook A. H., Academic Press Inc. (London) 1990.

113 Royal D. D, Sanchez Ochoa J. C., Calibration of 'SDL long' thermometer.

114 Ewing M. B., Sanchez Ochoa J. C., J. Chem. Thermo. 1998, **30** (2), 189 - 198.

115 Bevington P. R., Data Reduction and Error Analysis for the Physical Sciences, NY: McGraw-Hill, 1969.

116 Landau L. D., Lifshitz E. M., Course of Theoretical Physics: Volume 6. Fluid Mechanics, Pergamon Press, 1987.

117 Incropera F. P., Dewitt D. P., Fundamentals of Heat and Mass Transfer, second edition, John Wiley & Sons, 1985.

118 Knobler C. M., Pure and Appl. Chem., 1983, **55**, 455

119 Maitland G. C., Rigby M., Smith E. B., Wakeham W. A., Intermolecular Forces. Their Origin and Determination (Clarendon: Oxford, 1981).

120 Pitzer K. S., Lipman R. F., Curl R. F., Huggins C. M., Peterson D. E., J. Am. Chem. Soc. 1955, **77**, 3433.

121 Carnahan N. F., Starling K. E., J. Chem. Phys. 1969, **51**, 635.

122 Redlich O., Kwong J. N. S., Chem. Rev. 1949, **44**, 223.

123 Soave G., Chem. Eng. Sci. 1972, **27**, 1197.

124 Peng D. Y., Robinson D. B., Ind. Eng. Chem. Fundamentals. 1976, **15**, 59.

125 Beattie J. A., Bridgeman O. C., Proc. Amer. Acad. Arts Sci. 1929, **63**, 229.

126 Benedict M., Webb G. B., Rubin L. C., J. Chem. Phys. 1940, **8**, 334.

127 Schouten J. A., Michels J. P. J., Prins C., van der Gulik P. S., Trappeniers N., J. Report No. 8410-1, (van der Waals Laboratory: Netherlands, 1984)

128 Schouten J. A., ten Seldam G. A., Biswas S. N., Michels J. P. J., Trappeniers N., J. Report No. 8410-2, (van der Waals Laboratory: Netherlands, 1984)

129 Schouten J. A., ten Seldam G. A., Michels J. P. J., Trappeniers N., J. Report No. 8410-3, (van der Waals Laboratory: Netherlands, 1984)

130 Schouten J. A., Michels J. P. J., Report No. 8410-4, (van der Waals Laboratory: Netherlands, 1984)

131 Coulson J. M., Richardson J. F., Fluid Flow, Heat and Mass Transfer, Chemical Engineering, Volume 1, fourth edition, Pergamon 1990.

132 Buxton A. J., Bailey C., Ewing M. B., Unpublished work 1992.

133 Vasserman A. A., Litovchenko V. V., Tables of the transport properties of ethylene and propylene, Viniti. 1976, 2226, Deposited Document (Russian).

134 Clifford A. A., Kestin J., Wakeham W. A., Physica 1979, **97A**, 287.

135 Kestin J., Ro S. T., Wakeham W. A., Physica 1972, **58**, 165-211.

136 Gough D. W., Matthews G. P., Smith E. B., J. Chem. Soc. Faraday Trans. I, 1976, **72**, 645.

137 Byers W. H., J. Chem. Phys. **11**, 348 (1943)

138 Corran P. G., Lambert J. D., Salter R., Warburton B., Proc. R. Soc. London Ser. A **244**, 212 (1958).

139 Rubio R. G., Zollweg J. A., Palanco J. M. G., Calado J. C. G., Miller J., Streett W. B., J. Chem. Eng. Data, 1991, **36**, 171-184.

140 Douslin D. R., Harrison R. H., Moore R. T., McCullough J. P., J. Chem. Phys. **35**, 1357 (1961)

141 Shimanouchi T., Tables of molecular vibrational frequencies, Part I, Natl. Stand. Ref. Dat. Ser. 6 (US GPO, Washington DC) 1967, p11.

142 MacCormack K. E., Schneider W. G., J. Chem. Phys. **19**, 845 (1951).

143 Choy P., Raw C. J. G., J. Chem. Phys. **45**, 1418 (1966).

144 Itterbeek A. V., van Dael W., Physics of High Pressures and the Condensed Phase North-Holland Publishing Co., 1965.

145 Ewing M. B., Goodwin A. R. H., Trusler J. P. M., J. Chem. Thermo., 1989, **21**, 867-877.

146 Ewing M. B., Trusler J. P. M., Physica A., 1992, **184**, 437-450.

147 Ewing M. B., Owusu A. A., Trusler J. P. M., Physica A., 1989, **156**, 899-908.

148 Mehl J. B., Letters to the Editor, J. Acoust. Soc. Am., 1978, **64**, (5).

149 Ewing M. B., Goodwin A. R. H., McGlashan M.L., Trusler J. P. M, J. Chem. Thermo., 1988, **20**, 243-256.

150 Colclough A. R., Acustica, Vol. 23, 1970, pp.93-99.

151 Herzfeld K. F.,Fifty Years of Physical Ultrasonics, Review no. 4, Acoustical Society of America.

152 Ferrell R. A., Moldover M. R., Annalen der Physik 3, 1994, 195-206.

153 Bretz M., Shapiro M. L., Moldover M. R., Am. J. Phys., 1989, **57**, (2).

154 Mehl J. B., J. Acoust. Soc. Am., 1978, **64**, (5).

155 Edited by Schooley J. F., Temperature its Measurement and Control in Science & Industry, Vol. 6, Parts 1 & 2, American institute of Physics 1992.

156 Moldover M. R., Waxman M., Greenspan M.
High Temperatures, High Pressures, 1979, **11**, 15-86.

157 Campbell I. D., Acustica, Vol. 3, 1953, 395.

158 Gillis K. A., Moldover M. R., Goodwin A. R. H., Rev. Sci. Instrum., **62**, (9), 1991.